REPORT DOCUMENTATION PAGE

Form Approved OMB No. 0704-0188

1. AGENCY USE ONLY (Leave blank)	2. REPORT DATE	3. REPORT TYPE AND DATES COVERED
	21 Jan 2015	Dissertation

4. TITLE AND SUBTITLE

Numerical and experimental analysis of the load-carrying behaviour of laminated elastomeric bearings as seismic isolators

5. FUNDING NUMBERS

6. AUTHOR(S)

Toshihisa Mano

7. PERFORMING ORGANIZATION NAME(S) AND ADDRESS(ES)

UNIBW

8. PERFORMING ORGANIZATION REPORT NUMBER

9. SPONSORING/MONITORING AGENCY NAME(S) AND ADDRESS(ES

Universität für der Bundeswehr München
Werner-Heisenberg-Weg 39
D-85577 Neubiberg Germany

10. SPONSORING/MONITORING AGENCY REPORT NUMBER

11. SUPPLEMENTARY NOTES

Text in German.

12a. DISTRIBUTION/AVAILABILITY STATEMENT

12b. DISTRIBUTION CODE

ABSTRACT (Maximum 200 words)

Depending on the structural form and the strength of the vertical seismic force, a seismically isolated structure may experience a rocking motion during earthquake, which leads to the uplifting on one side and could cause the tensile force in the isolator bearing. The rubber isolator bearings are known to be capable of carrying a little tensile force but their tension capacity has not been utilized in practice because of the cavitation phenomenon which occurs when the rubber bearing is subjected to a certain degree of tension. Comprehensive research regarding this phenomenon on the rubber bearing is rarely found and therefore the aim of this dissertation is to provide an overview of the mechanism of cavitation phenomenon as well as the consequence of cavitation on the properties of the rubber bearing. For that purpose, different types of elastomeric bearings are analysed numerically and experimentally.

Machine assisted translation.

14. SUBJECT TERMS

UNIBW, German, Numerical and Experimental Analysis, seismic isolators

15. NUMBER OF PAGES

16. PRICE CODE

17. SECURITY CLASSIFICATION OF REPORT	18. SECURITY CLASSIFICATION OF THIS PAGE	19. SECURITY CLASSIFICATION OF ABSTRACT	20. LIMITATION OF ABSTRACT
UNCLASSIFIED	UNCLASSIFIED	UNCLASSIFIED	UL

der Bundeswehr
Universität München

Berichte aus dem Konstruktiven Ingenieurbau

Numerical and experimental analysis of the load-carrying behaviour of laminated elastomeric bearings as seismic isolators

Toshihisa Mano

18/1 Baukonstruktion – Baumechanik – Baustatik – Ing.-Informatik – Massivbau - Stahlbau

ISSN 1431-5122

der Bundeswehr
Universität München

Berichte aus dem Konstruktiven Ingenieurbau

Numerical and experimental analysis of the load-carrying behaviour of laminated elastomeric bearings as seismic isolators

Toshihisa Mano

18/1 Baukonstruktion - Baumechanik - Baustatik - Bauinformatik - Massivbau - Stahlbau

ISSN 1431-5122

Schriftleitung:
Univ.-Prof. Dr.-Ing. N. Gebbeken
Institut für Mechanik und Statik
Labor für Ingenieurinformatik
Universität der Bundeswehr München
Werner-Heisenberg-Weg 39
85577 Neubiberg
Tel.: 089-6004-3414
Email: norbert.gebbeken@unibw.de

ISSN 1431-5122

der Bundeswehr
Universität München

Numerical and experimental analysis of the load-carrying behaviour of laminated elastomeric bearings as seismic isolators

Toshihisa Mano

Vollständiger Abdruck der von der Fakultät für Bauingenieurwesen und Umweltwissenschaften der Universität der Bundeswehr München zur Erlangung des akademischen Grades eines

Doktors der Ingenieurwissenschaften

genehmigten Dissertation.

Gutachter/Gutachterin:

1. **Univ.-Prof. Dr.-Ing. Ingbert Mangerig**
2. **Univ.-Prof. Dr.-Eng. Akimitsu Kurita**
3. **Univ.-Prof. Dr.-Eng. Takashi Yamaguchi**

Die Dissertation wurde am 21.01.2015 bei der Universität der Bundeswehr München eingereicht und durch die Fakultät für Bauingenieurwesen und Umweltwissenschaften am 18.03.2015 angenommen. Die mündliche Prüfung fand am 19.08.2016 statt.

ACKNOWLEDGEMENT

First of all, I would like to thank my supervisor, Prof. Mangerig, Prof. Kurita and Prof. Yamaguchi. They are not only the supervisor for my dissertation but also key persons along with Prof. Albrecht who built and keep the very good relationship between German and Japanese universities. Without their pioneering achievement, I would not have even started Master study in Munich, let alone the doctor research. I hope I can do something to maintain this good relationship between engineers in both countries as a sign of gratitude.

I owe Mr. Nothaft many thanks for his support in all activities in the laboratory. Without his broad knowledge and various creative ideas about testing, my experiment would not have been carried out successfully. It is very painful for me that those words cannot be delivered to him.

I thank all of my colleagues during the time I worked at the University of German Armed Forces Munich (Universität der Bundeswehr München) as an assistant. I feel so lucky that I could work with such kind and intelligent people. They are teachers and friends to me at the same time.

I am very grateful for the company Maurer AG that they provided me with the elastomeric bearings for my research.

I also thank Prof. Lion and his colleagues from the faculty of Aerospace Engineering, Institute of Mechanics at the University of German Armed Forces Munich (Fakultät für Luft- und Raumfahrttechnik, Institut für Mechanik an der Universität der Bundeswehr München) for their support in material testing.

I acknowledge and thank the New Zealand GeoNet project and its sponsors EQC, GNS Science and LINZ, for providing data/images used in this study.

Last but not least, I thank my family and friends for their support during all those years.

Abstract (Deutsch)

Je nach Strukturform und Stärke der seismischen Vertikalkraft kann ein seismisch isoliertes Bauwerk bei einem Erdbeben einer Rüttelbewegung ausgesetzt werden, die auf einer Bauwerkseite zum Anheben führt und eine Zugkraft in den Isolator-lagern verursacht. Von den Elastomerlagern ist bekannt, dass sie in der Lage sind, eine geringe Zugkraft auszuhalten. Diese Zugfestigkeit ist in der Praxis wegen des Kavitationsphänomens, welches auftritt, wenn die Elstomerlager einem bestimmten Maß an Zugspannung ausgesetzt werden, bisher jedoch nicht ausgenutzt worden. Umfangreiche Forschungsarbeiten bezüglich dieses Phänomens an den Elastomerlagern sind selten zu finden. Das Ziel dieser Dissertation besteht folglich darin, einen Überblick über die Mechanismen des Kavitationsphänomens sowie über die Auswirkungen der Kavitation auf die Eigenschaften der Elastomerlager zu geben. Zu diesem Zwecke werden unterschiedliche Arten von Elastomerlagern numerisch wie auch experimentell analysiert.
Darüber hinaus wird ein Versuch unternommen, mittels Zeitverlaufsanalyse und linearer Antwortspektrumanalyse inklusive Modeüberlagerung ein besseres Verständnis für die Änderungen in der globalen Reaktion des Bauwerkssystems infolge der uneinheitlichen Vertikalsteifigkeit der Elastomerlager zu entwickeln. Diese Simulationsergebnisse deuten darauf hin, dass ein Einsturz des Bauwerks auch dann noch abgewendet werden kann, wenn ein übermäßiges Kippmoment des Bauwerks einen Kavitationsschaden an den Elastomerlagern verursacht, solange die Lager nicht völlig zerrissen sind. Außerdem ist erkennbar, dass der Vorteil aus einer Härtung der Lagerungen unter Hochdruckbedingungen zu einer Reduzierung dieses Kippmoments führt. Diese Tatsachen führen nun zu der Idee, dass einige zusätzliche Kompressionsfedern entlang der Außenkante des Bauwerks die oft problematische Zugverankerungskonstruktion ersetzen könnten, um eine übermäßige Rüttelbewegung zu verhindern. Diese zusätzlichen Kompressionsfedern sollten nur dann aktiviert werden, wenn ein hohes Maß der Rüttelbewegung auftritt und als Beispiel wären für solche Federn Elastomerlager geeignet, die auf ihrer Oberseite mit einer Gleitoberfläche mit geringer Reibung versehen sein können.

Abstract (English)

Depending on the structural form and the strength of the vertical seismic force, a seismically isolated structure may experience a rocking motion during earthquake, which leads to the uplifting on one side and could cause the tensile force in the isolator bearing. The rubber isolator bearings are known to be capable of carrying a little tensile force but their tension capacity has not been utilized in practice because of the cavitation phenomenon which occurs when the rubber bearing is subjected to a certain degree of tension. Comprehensive research regarding this phenomenon on the rubber bearing is rarely found and therefore the aim of this dissertation is to provide an overview of the mechanism of cavitation phenomenon as well as the consequence of cavitation on the properties of the rubber bearing. For that purpose, different types of elastomeric bearings are analysed numerically and experimentally.

Furthermore an attempt was made to comprehend the change in the global response of the structural system due to the varying vertical stiffness of the elastomeric bearing by means of the time history analysis and the linear response spectrum analysis with the mode superposition. These simulation results indicate that the collapse of the structure may be averted, even if the excessive overturning moment of the structure causes the cavitation damage in the elastomeric bearings, unless bearings are completely torn. Also the benefit from the hardening of the bearing under high compression is noticeable to reduce this overturning moment. This fact leads to the idea that some additional compression springs along the outer edge of the structure could replace the often troublesome tension anchoring construction in order to prevent the excessive rocking motion. These additional compression springs should be activated only when a higher degree of the rocking motion appears and as an example for this spring, the elastomeric bearing, perhaps with a low-friction gliding top surface, would be suitable.

Contents

1 INTRODUCTION

1.1 History And Development Of Seismic Isolation

Earthquakes are one of the most catastrophic natural disasters without any doubts. In the history of human civilization a number of earthquakes have destroyed cities, and they have taken countless lives. Therefore, protecting structures against earthquakes has been an important subject for the structural engineers of the countries that are often subjected to damaging earthquakes. Until recently, enhancing the earthquake resistance capacity of structures, by building them in a stiff and massive manner, was always the dominating countermeasure. In the cities where frequent earthquakes are expected, many bridges with gigantic piers and buildings with thick walls can be seen for this reason. With this method structures may be prevented from collapsing but not from partial destruction or damages, as in the design steel frames may yield or cracks in the concrete structures develop. This even expected to happen during a strong seismic action for the energy dissipation purpose [1]. Furthermore the natural frequency of the structure is increased by stiffening them and results in introducing a rapid shaking motion to the structure during an earthquake due to the resonance. Those effects can put human lives in jeopardy and high building costs have to be accounted for in the increase of structural elements.

A totally opposite concept, often referred as 'base isolation' or 'seismic isolation', appeared in the end of 19th century. This approach is characterised by decoupling the structure from its foundation in lateral movement. According to [2] a British professor of Mining Engineering John Milne built an example of an isolated building while he was at the University of Tokyo. He used balls between the superstructure and the foundation so that the lateral seismic force is not transferred to the structure. This building was seemingly experimented with the simulated seismic force. After some modifications decoupling of the building was reportedly successfully achieved. Almost certainly referring to this result, in August 1909 J.A. Calantarients, a medical doctor invented another seismic isolation concept where sand instead of balls was used in order to accomplish decoupling of the structure [2]. Some historical buildings that are isolated from the ground by means of a layer of sand or steamed rice between the superstructure and the foundation can be found in China and Japan [3], although it is not sure if it was intentionally so designed.

These historical developments had, however, been limited only in the theoretical field and the practical application of the seismic isolation building was still delayed for several decades. Tokyo Imperial Hotel completed in 1923, claims to be one of the first seismic isolation applications. This hotel was built on a soft alluvium ground and by using shallow footings the building was supposed to 'float' on the ground during earthquakes. Tellingly The Great Kanto earthquake happened in the same year that the building was erected and the hotel survived only with minor damages. Next the Heinrich Pestalozzi elementary school in Skopje Macedonia was built with elastomeric bearings as the first base-isolated building with isolator elastomeric bearings in 1969. For this application the elastomeric bearings had no reinforcing steel shims. Therefore the structure sank to a certain degree due to lateral bulging of the elastomer, although this structure still proved that elastomeric bearings can be an effective isolator.

Since then elastomeric bearings were further developed and the multilayered, laminated elastomeric bearing was invented in 1970s. This bearing consists of rubber layers and steel reinforcement shims alternatively. Due to the constraint to the bulging deformation of elastomer by steel shims the stiffness of the bearing in the vertical direction is highly enhanced while still possessing the same degree of flexibility in the horizontal movements.

Along with the development of the multilayered elastomeric bearings, the number of the applications of seismic isolation started increasing gradually. A major attention to this method was finally obtained after both the 1994 Northridge and 1995 Kobe damaging earthquakes which lead

many structures with the enhanced earthquake resistance capacity into collapse. Only limited number of the seismic isolation buildings existed at that time but those structures remained without serious damages or sometimes remained almost intact after those severe seismic motions. As a consequence the number of application of this technology in more important infrastructures such as hospitals, fire brigade buildings and bridges increased exponentially. This was particularly true in USA, New Zealand, Italy and Japan. Later the friction pendulum bearing was developed and this type of bearing is also gained popularity due to its high load-carrying capacity and high energy dissipating ability.

1.2 Focused Problem

The range of base-isolation applications covers ordinary houses, middle-height buildings and bridges. For the analysis of such structures, either the nonlinear time history method on the basis of numerical simulation or the response spectrum method is often employed in practice. The simplified single or multi-degree-of-freedom system, to which the structural stiffness and material characteristics are provided as inputs, is often sufficient for this purpose. In case of modelling a base-isolated building with elastomeric seismic isolator bearings, for instance, the shear stiffness of the bearings needs to be integrated to this global structural model at the isolation level as spring, (see Fig. 1.)

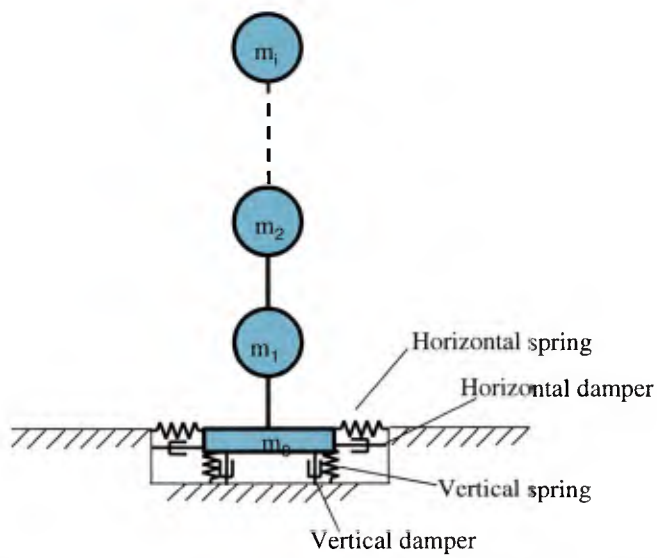

Figure 1: Multi-degree of freedom model with both horizontal and vertical springs [4]

In general those seismically isolated tall structures are specially designed with enhanced resistance against overturning so that tension does not appear in isolator bearings. Nevertheless depending upon the profile of the base-isolated structure, the strength of the seismic force and the distance from the active fault, there exists the possibility that the first several structural deformation modes (swinging motion) resonate with seismic motion and isolators undergo the tensile force despite the application of the seismic isolation. The laminated elastomeric bearing which is most commonly used as a seismic isolator can be designed to carry a little tensile loading unlike other isolator bearings such as sliding bearings, although that capacity is generally not utilized due to lack of knowledge on the behaviour of rubber bearing in tension. Internal damage, often referred to as "cavities" or "voids", may develop if a rubber material experiences a certain amount of tensile force in a high constraint condition and that damage is linked to an immediate softening in the tensile stiffness or may deteriorate the expected performance of bearings. Resulting change in the vertical

stiffness and the vertical damping of elastomeric bearings contributes, in turn, to a change in the structural dynamic behaviour. Hence in order to analyse a base-isolated building realistically the vertical stiffness along with the horizontal characteristics of the base-isolators should be integrated to the global analysis model. Even more accurate representations of the whole system can be achieved by using the simplified rubber bearing model introduced in [5], [6], [7] and [8], with which the stability limit of the bearings is also considered. Accurate evaluation of all the vertical and rotational stiffness as well as the shear stiffness of the seismic isolator bearings are important for this purpose and therefore evaluation formulae for the compression and shear stiffness provided by design standards such as Eurocode [9] [10], AASHTO [11] and Japanese specifications for highway bridges [12] are examined for their applicability by comparing with the existing test results and numerical results at first in the following Chapters. Evaluating tensile stiffness of elastomeric bearing is only partially possible due to the cavitation-induced softening which is not well defined in any design standards. This aspect will be examined, using a survey of existing research regarding cavitation phenomenon.

1.3 Research Goal

This dissertation aims to provide an overview of the cavitation mechanism of laminated elastomeric bearings. Furthermore prediction of cavity nucleation and influence of cavities on the performance of laminated elastomeric bearings will be investigated by means of experiments and numerical analysis. Finally changes in the dynamic behaviour of structures due to the cavity-induced softening is studied and existing regulations from various design standards against tensile force applied to elastomeric bearings will be discussed taking those results into consideration.

2 INTRODUCTION TO SEISMIC ISOLATION

2.1 The Principle of Seismic Isolation

As described briefly in the previous chapter, the mechanism of seismic isolation can be explained by the separation of the superstructure from the foundation or the substructure. The ideal, which is complete separation, cannot be achieved since the weight of the superstructure still has to be supported by the solid ground. What can be done is to lay a laterally soft or flexible structural layer between these super- and substructure so that the seismic force transferred to the superstructure is highly reduced. This flexible interlayer is namely comprised of isolator bearings. These bearings support the structure vertically while deforming or displacing (depending upon the type of isolator) horizontally with the ground during the earthquake, allowing the superstructure to remain almost in place. In the physical point of view the effect of seismic isolation can be interpreted as a shift in the natural frequency of the structure. A strong shaking motion is induced by the resonance when the natural frequency of the structure lies within the excitation frequency of the seismic ground motion. By applying the seismic isolation, the dominant deformation mode of the structure is replaced by the deformation or displacement mode of the isolator bearings which is corresponding to a much lower natural frequency, hence a longer natural period. The concept is sketched in Fig. 2, where ω and T are the natural circular frequency and the natural period, respectively and the subscripts 's' and 'b' denote 'structure' and 'base isolation', respectively.

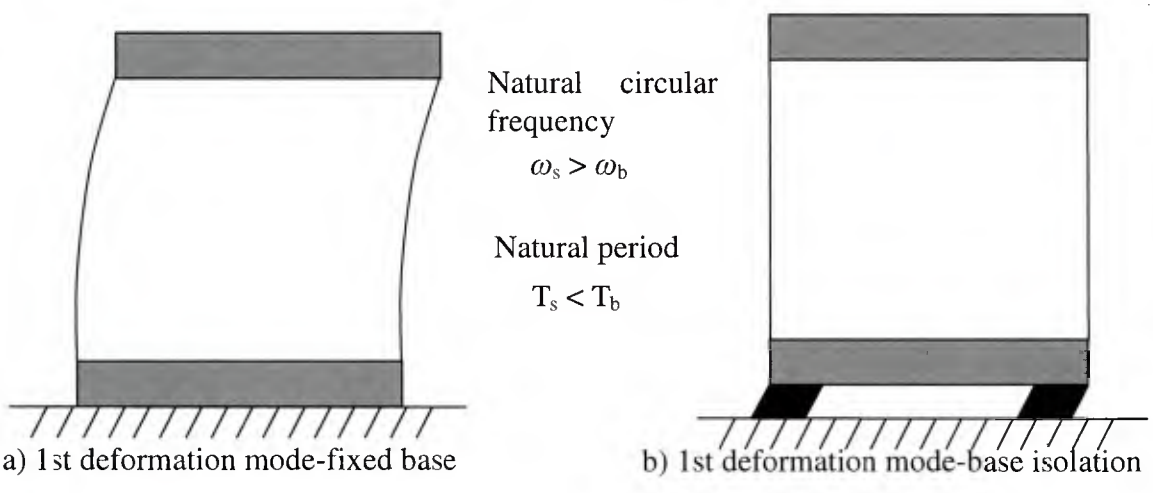

Figure 2: Primary deformation mode of the base-fixed and base-isolated structure

Structures with the natural frequency of 2 to 4 seconds are affected a lesser degree by earthquakes as the resonating seismic excitation frequency often ranges between 0.1 to 1.5 seconds unless the ground condition is soft as in the case of alluvium-type ground for instance. On such soft ground the seismic isolation is not the optimal counter-measure, as it can even induce the risk of resonance in a longer natural period. Design acceleration spectra in accordance with the different ground types are provided in the design standards, for instance [13], [14], and [15]. The period-shifting effect of the seismic isolation can be seen in the following acceleration and displacement response spectra (see Fig. 3).

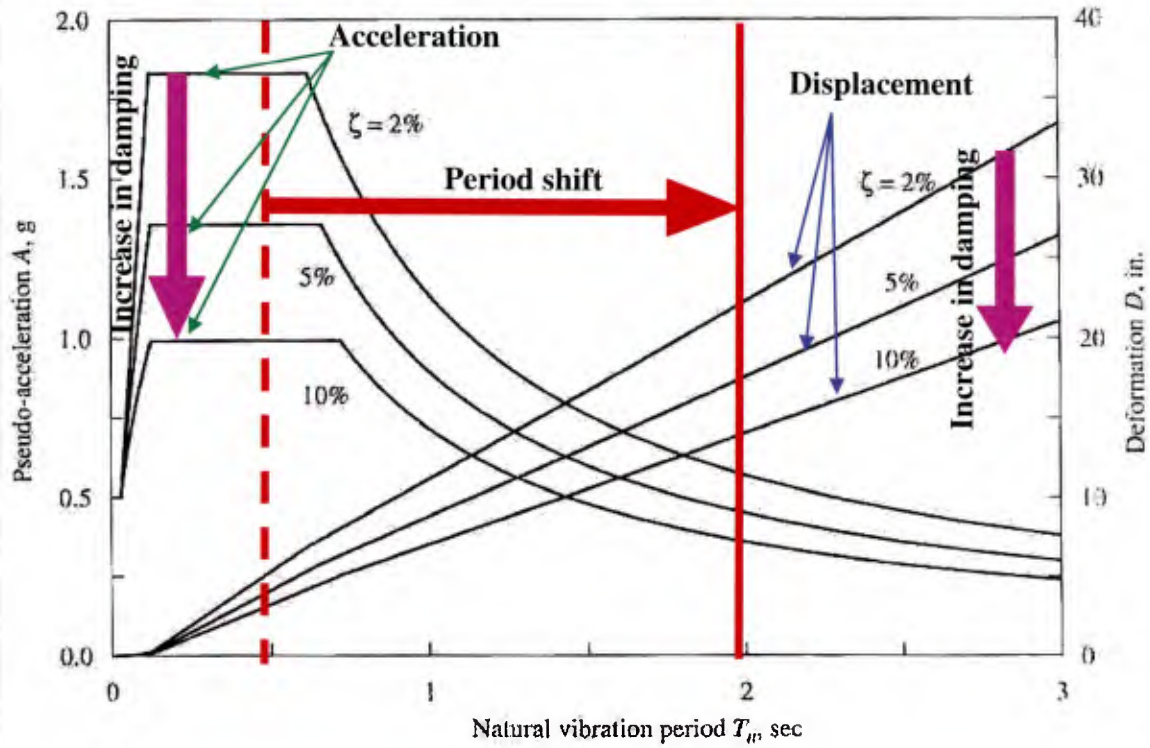

Figure 3: Acceleration and displacement spectra example with three different damping degrees [16]

Figure 3 demonstrates that the elongation of the period due to the seismic isolation can radically decrease the acceleration response of the structure. However, at the same time this period shift also results in a lager displacement. This displacement increase does not stem from the structural deformation as in the building without seismic isolation (shear or bending deformation of each storey, for instances) but mostly from the relative displacement between foundation (or the substructure such as piers for cases of bridge construction) and the superstructure. Ideally, in the application of the seismic isolation system, the whole superstructure moves together without deforming. This relative displacement has to be limited considering the displacement capacity of the isolator bearings and the available clearance around the structure.

A certain degree of damping is beneficial to the seismic isolation system to reduce both the peak acceleration as well as the displacement, although excessive damping brings a high nonlinearity to the structural response and hence the analytical method assuming the linear behaviour of the structures such as response spectrum analysis would become inappropriate. For the design purpose, the structural damping of 2 to 5 % is generally assumed for structural materials have their own energy dissipation mechanism or energy can be dissipated at the connection parts of structural members by large deformation due to friction. Often the structural damping is insufficient for the seismic isolation system to ensure the safety of the structure. In such situations additional damping can be obtained by extra dampers that will be briefly described in the next section. There are also some isolator bearings available which are equipped with a certain damping property, such as high damping rubber bearings (HDR), lead-plug rubber bearings (LRB) and sliding bearings.

2.2 Devices For Seismic Isolation

2.2.1 Isolator bearings

There are several types of the isolator bearings but the major specifications cover mainly rubber bearings, sliding bearings and sliding pendulum bearings. These three bearings types are in fact most commonly used as the seismic isolator.

Laminated elastomeric bearings

Laminated elastomeric bearings are most commonly applied seismic isolators due to their relatively reasonable cost and well-understood mechanical characteristics due their use in bridge bearings. Laminated elastomeric bearings can be further categorised into three groups according to its damping property, i.e. low damping rubber bearings (LDR), high damping rubber bearings (HDR) and lead-plug rubber bearings (LRB).

The low damping bearings with natural rubber or synthetic rubber material are widely used for the seismic isolation all over the world. They consist of alternating layers of rubber pads and steel shims and also generally include two steel flanges on the top and bottom of the bearing, which have to be anchored to the super- and substructure, respectively. Manufacturing this type of bearing is relatively simple. All rubber pads, steel shims and steel flanges are vulcanised together in a mould with a certain heat and pressure. LDR bearing has the equivalent damping ratio in the range of 2-10% (less than 6% defined in EN 15129, and 3-7% according to the test results given in the Japanese Bridge Bearing Specifications) to the critical value, and thus other additional damping devices are usually required. Against horizontal shear loading low damping bearings behave almost linear-elastically, possessing excellent position-restoring property. Furthermore the mechanical response is not much affected by aging or the loading-rate and history. Natural rubber is, however, vulnerable to the ozone, and thus it has to be covered with anti-ozone layer. For that purpose some of synthetic rubbers such as chloroprene are applicable alternatives since they are not affected by ozone. The low damping polychloroprene bearing produced by the company Maurer AG tested at the testing laboratory of the institute of construction engineering, the University of the German Armed Forces in Munich (Universität der Bundeswehr München) and its typical hysteresis loops are shown in the following Fig. 4.

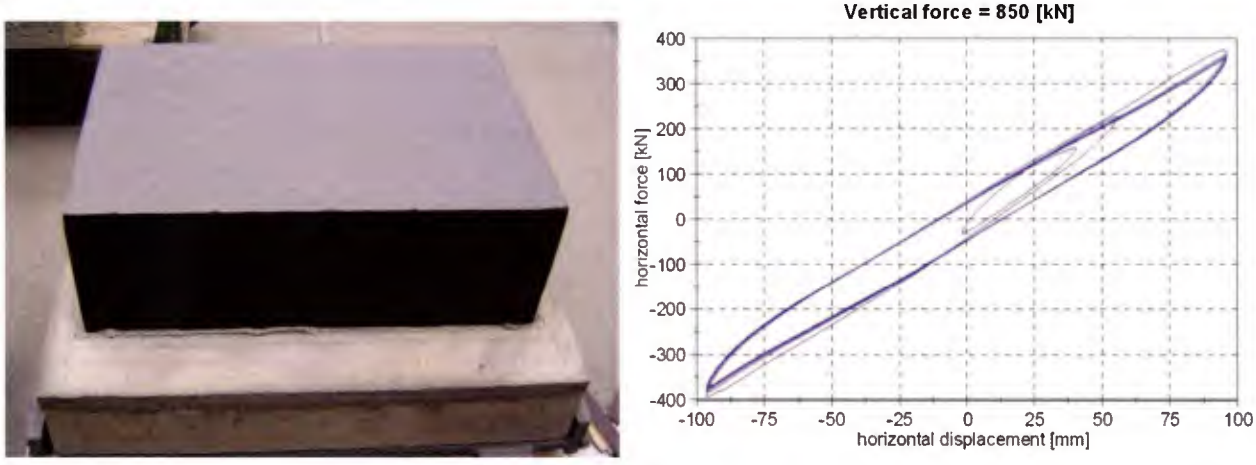

Figure 4: Low damping elastomeric bearing with chloroprene material and the typical hysteresis loops

In order to supplement damping without additional dampers the lead-plug elastomeric bearing was invented in 1975 in New Zealand [17]. To create lead-plug elastomeric bearings, one or more

cylindrical lead bars are inserted in the centre area of the laminated elastomeric bearing, which serve as a metal damper, -dissipating energy by a yielding mechanism in a relatively large displacement range. They also serve as a stiffener under the other service loading such as wind or traffic load in a small displacement range. Figure 5 shows an example of the lead-core elastomeric bearing manufactured again by Maurer AG. The hysteresis loops generated by this type of bearings exhibit a mixture of both viscoelastic and bilinear characteristics.

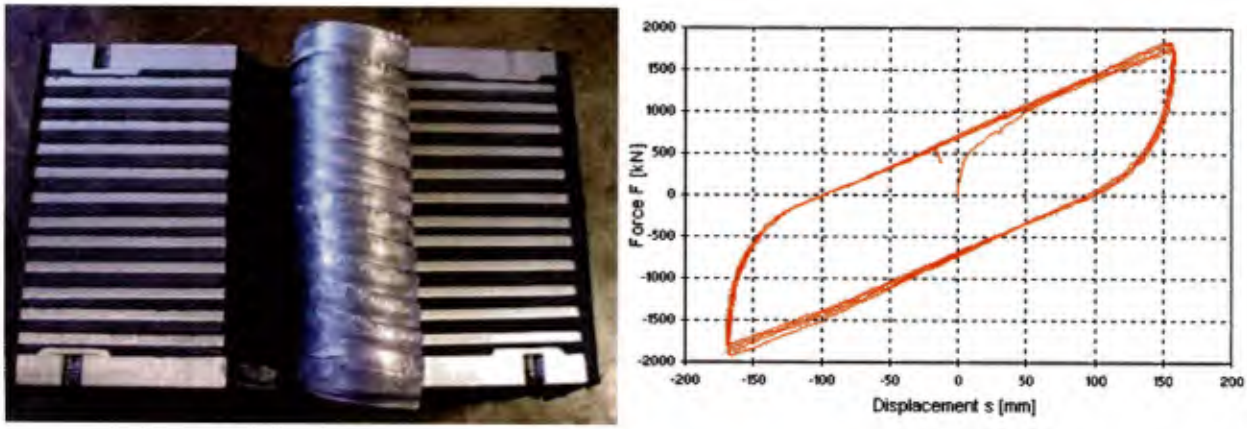

Figure 5: Lead-plug elastomeric bearing and the typical hysteresis loops [18]

High damping elastomeric bearings are another method to bring higher damping to the structural system without additional dampers. High damping rubber was developed by the Malaysian Rubber Producers' Research Association (MRPRA) of the United Kingdom in 1982 [2] and was applied to the seismically isolated building in California in 1984 for the first time [12]. A higher damping in this type of elastomeric bearing is achieved through the additional reinforcement material and fillers such as oil, resins and most importantly carbon black. A wide range of characteristics can be arranged by varying the ratio of compounds. The production process is exactly same as that of the low damping elastomeric bearings.
These laminated elastomeric bearings are described in further detail in the next chapter, as they are a main focus of this research and hereafter in this thesis they will be simply referred to as elastomeric bearings or rubber bearings.

Sliding bearings
The sliding isolation system is the classic concept of the seismic isolation as described in the first chapter. The currently common material combination for the sliding surface is stainless steel and unfilled or filled polytetrafluoroethylene (PTFE or known as the product name Teflon of the company DuPont). Seismic energy is dissipated through the friction between these contact surfaces. The concept sounds uncomplicated as long as the simple assumption of coulomb friction holds but determining the coefficient of friction is more elaborate task in reality. As the test results of MSM (Mauer Sliding Material) indicates [19], the sliding property of such polymer materials depends on the temperature, the roughness or cleanliness of the surface and, to a certain degree, the velocity of the sliding motion. Therefore these influence factors have to be carefully controlled. When the sliding bearing is referred to, conventionally its sliding surface is flat and therefore there is no restoring force available in the system. This inconvenience can be remedied by using them with other type of isolator bearings that provide the enough restoring force to the system. For instance the combination of low damping elastomeric bearings and flat sliding bearings is often found, so that they can complement what is missing in each system, by the restoring force and the energy dissipating property.

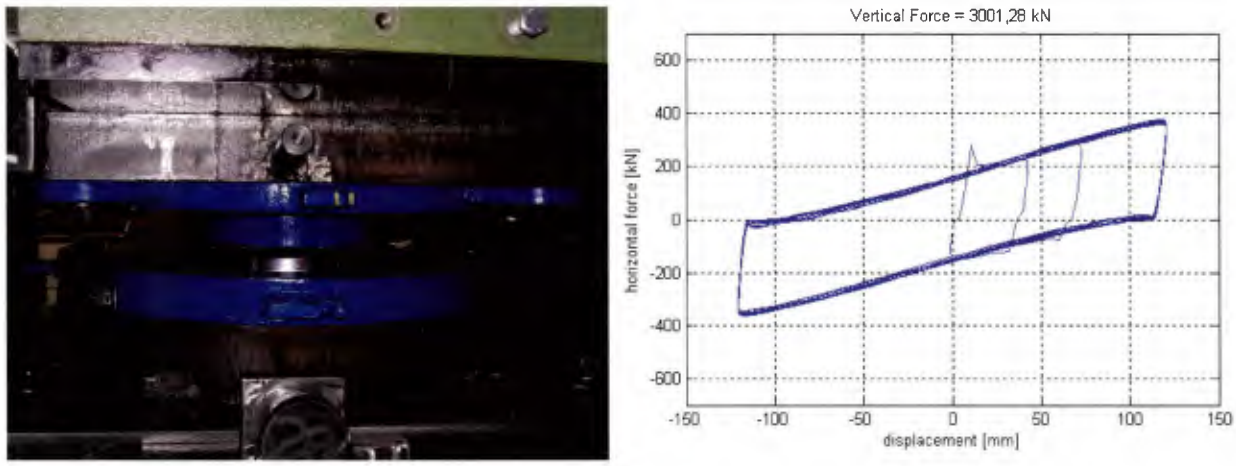

Figure 6: Friction pendulum bearing and its typical hysteresis loops

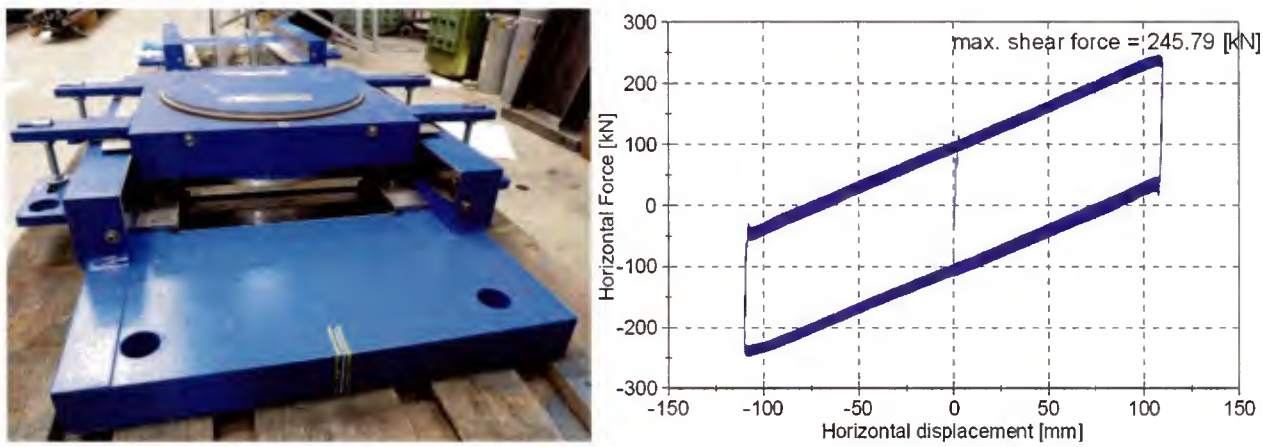

Figure 7: Uniaxial friction pendulum bearing and its typical hysteresis loops

In 1987 Zaya et al. [20] introduced the new sliding isolation bearing in which a concave sliding surface was employed instead of a flat one in order to supplement the position-restoring property. That bearing is called 'friction pendulum bearing' and quite a few seismically isolated structures with this type of bearing can be already found. The pictures of two types of friction pendulum bearings tested at the University of the German Armed Forces in Munich (Universität der Bundeswehr München) are shown in Figs. 6 and 7 with typical hysteresis loops obtained by these bearings. These bearings are also designed and manufactured by the company Maurer AG. The second example of Fig. 7 is the specially designed friction pendulum bearing one of whose lateral displacement is restrained especially for the application to seismic isolation bridges where the excessive displacement in the transverse direction is often not desired.
The restoring stiffness is calculated as

$$K_h = \frac{\mathcal{W}}{R} \tag{2.1}$$

where $\mathcal{W}$ and R are the weight of the structure and the curvature radius of the sliding surface, respectively [2].

The natural period of the isolation system with the gravitational acceleration g is then obtained as $T = 2\pi\sqrt{R/g}$. This indicates that the isolation period can be modified simply by varying the curvature of the sliding surface, independent of the structural weight above the isolation layer.
Figure 8 depicts the principle of the friction pendulum bearing schematically. The force equilibrium in the horizontal direction is kept by three force components, namely the friction force, the restoring force and the input external forces (service live loading or seismic excitation) as shown in the same figure. The inertial force of the horizontal drifting motion of the superstructure has to be taken into account in the equilibrium. The sliding system is not described further in this thesis since this type of bearing does not generally possess a tensile resistance, and thus is outside the bounds of the focus of this research purpose.

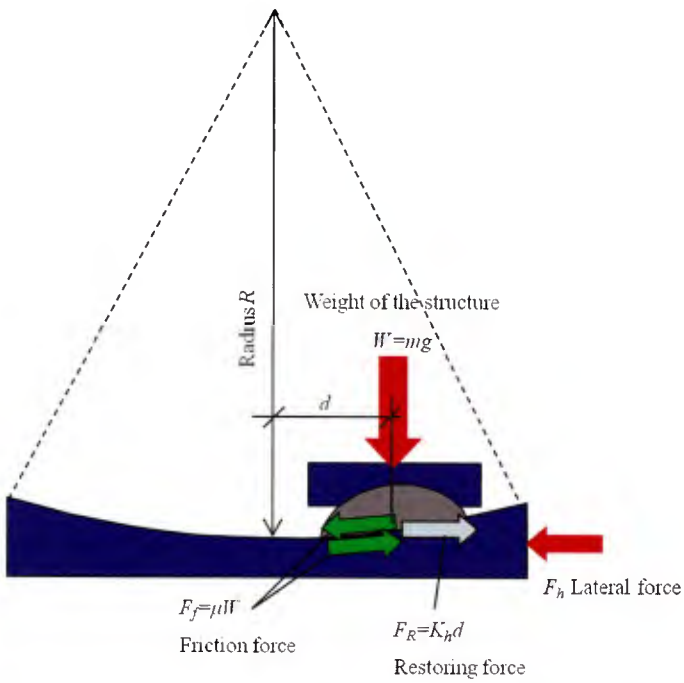

Figure 8: Principle of the friction pendulum bearing

2.2.2 Dampers

As shown in Fig. 3 the increase in damping for the seismic isolation system is beneficial to control the drifting displacement of the structure as well as to reduce the duration of the drifting motion of the superstructure. For this purpose dampers are installed on the isolation level where the isolator bearings are mounted whereas there are cases wherein they are installed between storeys of the building in order to reduce the shear deformation because the structural deformation modes can still appear in response of the seismically isolated structure. A number of the latter applications can be found independent of the seismic isolation in order to mitigate the shaking motion of the building. Conventionally the principle of the seismic resistance design has always been to increase the stiffness and the ductility of a building. There is, however, a certain limit to increase those properties and for that reason some inelastic deformation such as plastic hinges in the frame structure is intentionally designed to develop during the strong seismic motion for energy dissipation purpose. This inelastic deformation is still a kind of damage and, has to be limited to prevent the structure from collapsing. By applying dampers between storeys of a building the inelastic energy dissipation demand on the structure can be reduced. This concept has been long

known as 'passive energy dissipation system' and its implementation started increasing rapidly in the mid-1990s along with the seismic isolation implementation [21] [22]. For both systems (seismic isolation and passive energy dissipation systems) the commonly employed damping devices include viscous fluid dampers, friction dampers, and metallic dampers. Those dampers are briefly described referring to [17] and from [21] to [35].

Viscous fluid dampers

The viscous fluid dampers were originally invented for military applications and their performance was proven in that field [24] [25]. One advantage of the viscous fluid dampers is that they can be activated in a small stroke range since they are velocity dependent.

A viscous fluid damper typically consists of a hollow cylinder filled with fluid and a piston rod with one or more piston heads. As an example a viscous fluid damper explained in [25] is shown in Fig. 9. The stroke of piston rod moves the piston heads, inducing a flow of fluid through orifices either around or through piston heads. This flow causes the pressure difference across the piston heads and generates strong resistant force against the relative motion of the cylinder and the piston. Friction occurs between fluid particles and the piston head during this process. The seismic energy is converted into heat energy by this friction and in turn raises the temperature of the fluid. The fluid commonly used for this type of dampers is silicone-based oil but the choice of material depends on the required characteristics such as compressibility and viscosity [27].

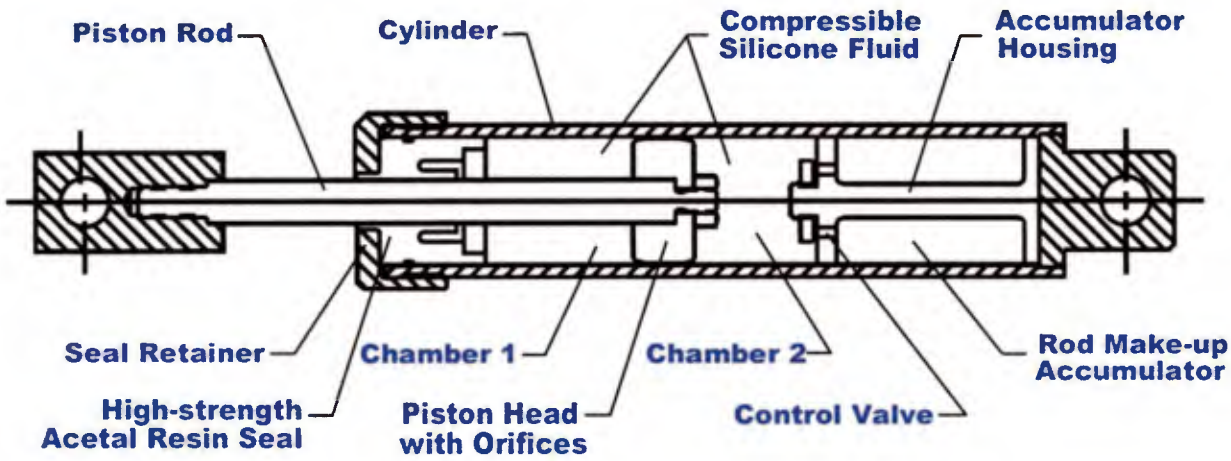

Figure 9: Example of a viscous fluid damper [25]

The damping force F(t) of viscous fluid dampers can be generally evaluated by the following expression [21][22][26][35].

$$F(t) = C_d \left|\dot{u}(t)\right|^{\alpha_d} \operatorname{sgn}[\dot{u}(t)] \tag{2.2}$$

where C_d is the damping coefficient, u is the relative displacement across the viscous damper and α_d is the exponent whose value is determined by the piston head orifice design. sgn[·] is the signum function and the overdot indicates the differentiation with respect to time t.

Equation (2.2) indicates that the viscous fluid damper has velocity-dependence unlike other damping devices such as friction or metallic dampers which have displacement-dependence. This can be physically interpreted as a nonlinear viscous dashpot. This option is appealing from the

design point of view because the velocity is out of phase with the displacement, which means that at the maximum displacement the viscous dampers do not add the damping force to the total structural elastic forces. This is, however, the ideal condition and in reality there is always a coupling effect to a certain degree. The total force to the structural system is indeed increased by the damping force [22]. Velocity (frequency) dependence of a viscous fluid damper is shown in Fig. 1C with the hysteresis loops.

For the passive energy dissipation system against earthquake, the exponent α_d has a value range generally from 0.3 to 1.0 [21] [22] [35]. The shape of force-displacement curves of a viscous fluid damper are ellipsoidal loops and this form approaches to the rectangular shape as the exponent α_d approaches zero as with the case of the friction dampers, see for instance [22].

The estimation of the energy dissipation per cycle of steady-state harmonic motion E_D, i.e. the area of the loop in each cycle, can be calculated by integrating Eq. (2.2) over the displacement as

$$E_D = 4F_{peak}u_{peak}2^{\alpha_d}\left(\frac{\Gamma^2(1+\alpha_d/2)}{\Gamma(2+\alpha_d)}\right) \text{ [21] [23] [26]} \tag{2.3}$$

where F_{peak} is the peak damping force, u_{peak} is the peak relative displacement across the damper and Γ is the gamma function.

In the case of α_d=1 (linear case) the Eq. (2.3) becomes the classical formula to calculate the area of an ellipse, i.e.

$$E_D = \pi F_{peak}u_{peak} \tag{2.4}$$

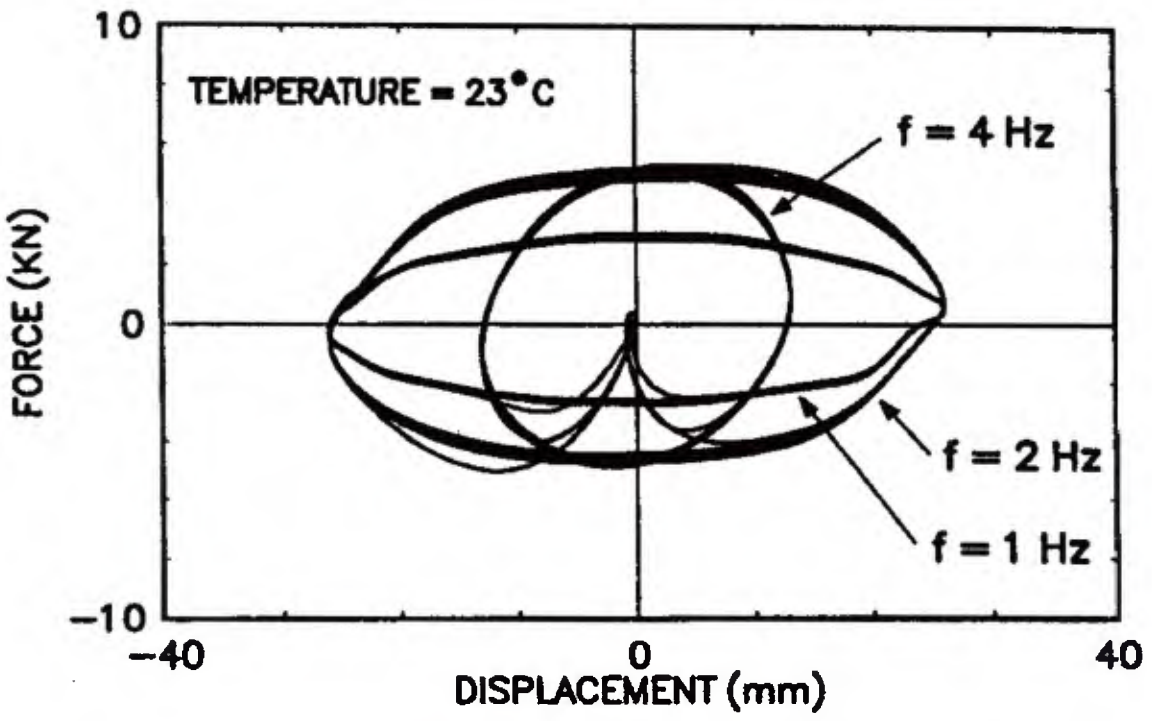

Figure 10: Typical hysteresis loops of a viscous fluid damper with different oscillation frequencies [26]

Wen-Hsiung and Chopra [35] studied the influence of the nonlinearity of the fluid viscous dampers on the seismic response of the single-degree-of-freedom system. Within their analysis the factor α_d

varied from 0.35 (highly nonlinear) to 1.0 (linear). The same damping ratio and the results showed that the nonlinear damper can reduce the seismic responses of the single-degree-of-freedom (SDOF) system with equivalent sufficiency as the linear damper. Furthermore the peak damping force introduced to the SDOF system becomes smaller as the nonlinearity of the damper increases [35] [26]. These findings indicate that the use of nonlinear dampers is advantageous in terms of the damping force and that the seismic response of the SDOF system with nonlinear dampers can be accurately evaluated by the same calculation procedure as in the case of the SDOF system with linear dampers. However, it should be noted that a higher nonlinearity of the damper disturbs the aforementioned ideal out-of-phase condition and as a result a certain amount of the damping force would be transferred to the structure at its maximum response as well. The same effect is observed by increasing the number of dampers [22].
Fluid viscous dampers can offer a relatively constant performance over the wide range of temperature but nevertheless temperature rise is still of concern for it can possibly damage the damper seals [21]. Markis et al. studied the mathematical model of the temperature rise in dampers [28] [29]. They concluded that the temperature rise is generally proportional to the pressure drop of the fluid in front of and behind the piston head. Based on this understanding they recommended that a larger piston diameter should be used to reduce the pressure difference when viscous heating is concerned. More interestingly temperature rise is also proportional to the velocity of the motion when small stroke-amplitude is concerned, whereas for large stroke-amplitude it is independent of the velocity.

Friction dampers
The friction damper typically consists of steel or other metal plates clipped together with a certain amount of force so that the desired friction force is obtained by the relative displacement between those plates during the seismic action. One example of the friction damper is shown in Fig. 11.

Figure 11: Example of the friction damper (Pall friction device) [30]

In mechanical sense the friction damper is equal to the sliding bearing with a flat surface whose friction force is calculated with the assumption of simple Coulomb friction as

$$F = \mu N \, \mathrm{sgn}[\dot{u}(t)] \tag{2.5}$$

where μ is the coefficient of friction and N is the normal force applied to clip metal plates together.

Hysteresis loops of a friction damper have a rectangular shape as shown in Fig. 12 and the energy dissipation per cycle is equal to the area of the hysteresis loops which is in design simply calculated as

$$E_D = 4F_{peak}u_{peak} \tag{2.6}$$

where F_{peak} is the peak damping force and u_{peak} is the peak relative displacement across the damper.

The sliding bearings can also be regarded as a friction damper in this sense. Due to the higher coefficient of friction in the initial phase of motion (static friction), the friction damper can be designed so that the damper will not be activated by the service live loads such as wind or the minor seismic motion. Furthermore, high amounts of damping can be achieved by this type of dampers and their force-displacement response is seemingly independent of loading frequency, amplitude and temperature [33]. Disadvantages of the friction bearing are that 1) performance is sensitive to the sliding surface condition, 2) the strongly nonlinear nature of this type of damper may excite higher deformation modes and 3) some restoring mechanism has to be provided because otherwise there would be residual displacement in the structure.

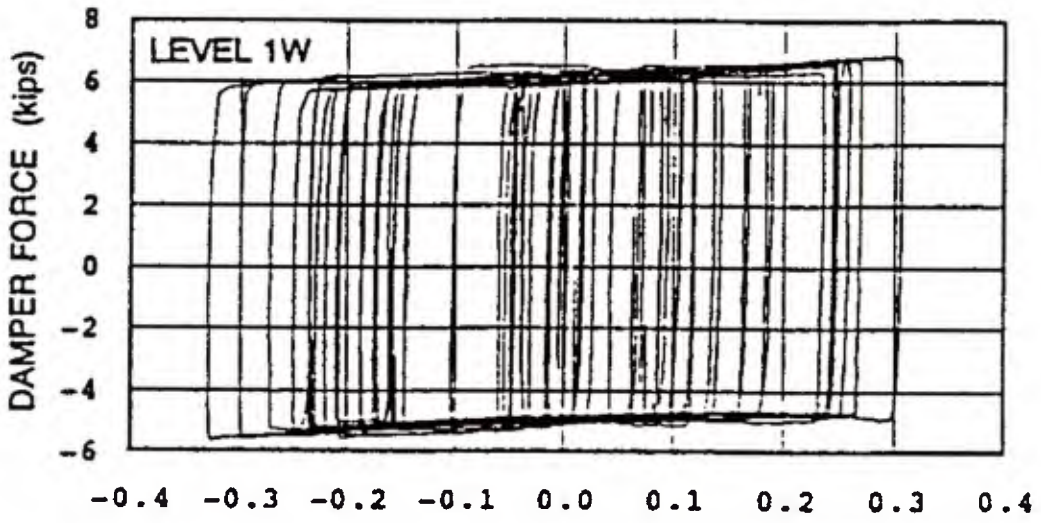

Figure 12: Typical hysteresis loops of a friction damper [33]

Metallic dampers

There are various types of metallic dampers available but the mechanism behind them is the same, i.e. energy dissipation is achieved by the plastic deformation of metals. Typically the steel with low-yielding strength or lead are the choice of materials for this type of dampers. They are configured to yield in bending, shear or axial compression/tension. The lead damper is mostly configured to yield in shear because of its low-stiffness.

The simplest configuration of the metallic damper in bending would be the steel bar damper. Both ends of the steel bars are fixed on the superstructure bottom and the foundation surface and as the relative motion across the isolation level occurs, those steel bars are bent and will yield when the seismic force exceeds a certain amount. Shear type dampers are configured analogously but yielding is not caused by bending but shear stress. After plasticization those steel bar dampers exhibit a nearly bi-linear hysteretic behaviour analogous to other metallic dampers. Other bending type of dampers such as Type-U and Type-T dampers [17] are available. They can be also installed between the top of the chevron bracing bars and the floor above. Metallic dampers that yield in bending or shear are often mentioned as 'adding damping and stiffness (ADAS) dampers'. Two examples are shown in Fig. 13.

Figure 13: Example of the ADAS dampers-left [31], right [32]

Axially yielding dampers are configured as diagonal braces. To ensure yielding will occur under compressive load as well as tensile load, those dampers are specially designed not to buckle. This is achieved by covering the core-steel of the damper with concrete-filled tube. For this reason, they are also called buckling-restrained brace (BRB) dampers. They are mostly applied to reduce the structural shear deformation but not to reduce the relative displacement across the seismic isolation level.

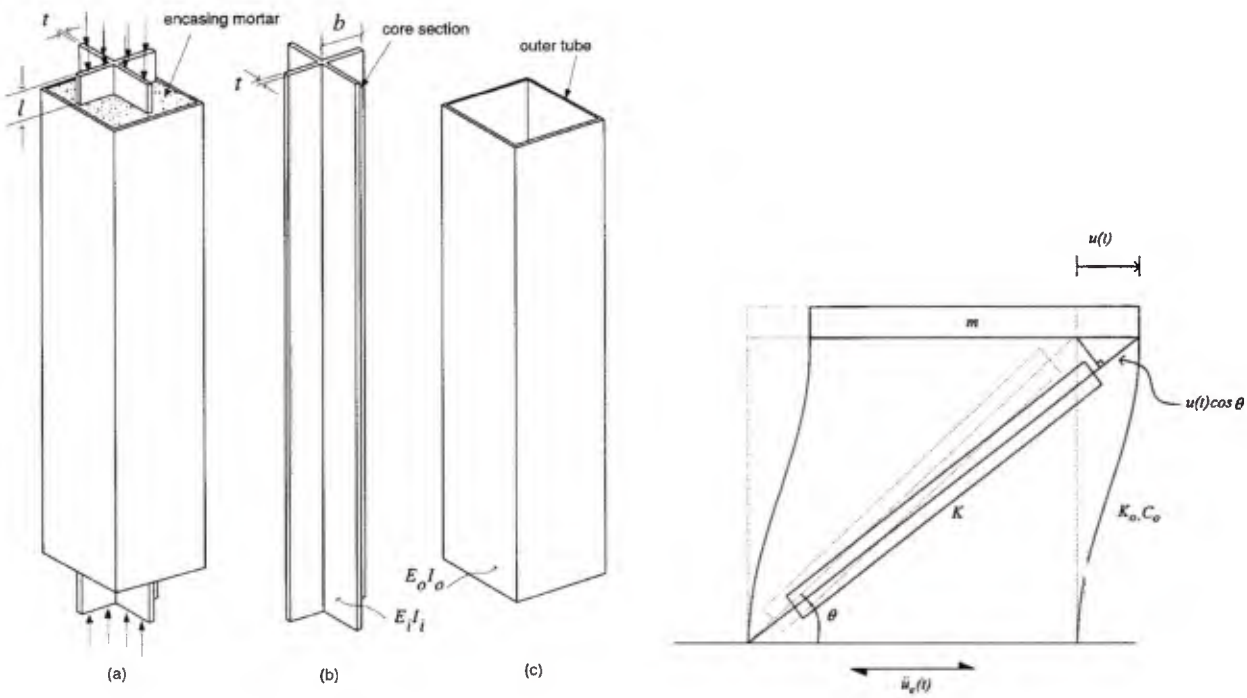

Figure 14: Example of the BRB damper [34]

In design the energy dissipation per cycle of the metallic damper is calculated by

$$E_D = 4F_y(u_{peak} - u_y) \tag{2.7}$$

where F_y is the yield strength of the metal, u_{peak} is the peak displacement and u_y is the displacement at the force F_y.

Steel dampers have a high initial elastic stiffness. Therefore they are not activated under the service loading or the minor seismic action. The ratio of the stiffness of the damper and the stiffness of the structure is an important parameter to determine the amount of damping and a higher stiffness of the former to the latter promises the higher amount of damping. In practice this ratio of greater than 1 is difficult to achieve, hence the realistic target would be the damping of the order of 10 % to 15 %. The effect of this ratio to the amount of damping is summarised in [22]. Further concern regarding the stiffness of damper has to be given for the design since this additional stiffness alters the structural response. As indicated above, the yielding dampers require a high stiffness and high yield strength in order to exert maximum effectiveness but that results in reducing the structural natural period. Another aspect of concern is the problem of fatigue. If the metallic dampers are constantly subjected to the dynamic service loads such as wind and traffic load then damages can be caused due to fatigue in a given long period of service. If that is the case damaged dampers may not achieve the desired function. Finally, a disadvantage regarding the metallic yield dampers (lead is exception since recrystallization process can take even at the room air temperature) is that they have to be replaced by new ones after they are activated by an earthquake because they may not resist stiffly against even relatively small dynamic service loads.

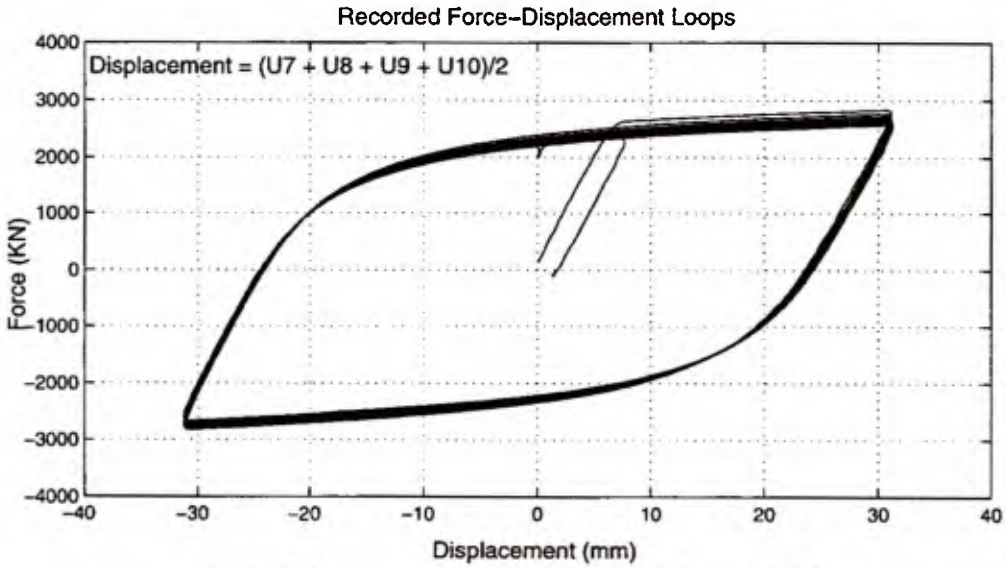

Figure 15: Hysteresis loops of a BRB damper [34]

2.3 Application Example And Response Data

Many application examples of the seismic isolation system are summarised in references, for instance [2] [3] [17] [36] and [37]. Naturally earthquake-prone countries such as Japan, Republic of China, Russian Federation, the United States, Italy, France and New Zealand are leading in the number of seismic isolation applications. Japan has by far the most application. The modern seismic isolation system started in New Zealand when the Motu Bridge which was equipped with sliding bearings in the North Island was completed in 1974 [3]. Moreover the stepping isolation concept [2] [17] and some seismic isolation devices with lead material were also invented in New Zealand. Already in the early1970s, Dr. Robinson invented the lead extrusion damper and in 1974 this technology was applied in two overbridges in the city of Wellington. In 1975 Robinson also invented the lead-rubber bearing [38] [3]. For this pioneering country of the modern seismic isolation, the number of application seems quite small but it is simply because her population is relatively small. As a matter of fact, if normalised by the population, the application number is just

next to Japan. The number of seismic isolation applications did not increase as expected in the United States despite the fact that quite a few well-informed engineers and researchers had cultivated this field in relatively early history of the seismic isolation-development. For instance the United States has the first seismic isolation application with high-damping rubber bearings or the first seismic isolation project for retrofitting purpose [2] [3] [39]. The friction pendulum system (FPS) was also invented and applied first in the United States [2] [20]. According to [2], the slow development in the application number is due to the elaborate design process. Italy is also a country whose number of seismic isolated buildings has not increased at the expected rate because of the absence of the design regulations and time-consuming, uncertain process to obtain the approval from the Ministry of Constructions. The situation in Italy was improved after the proper design regulations were introduced and the more seismically isolated buildings and bridges have been under construction currently according to [36]. Also other countries subjected to the earthquake hazard including China, Russia, Turkey, Greece, Portugal, Romania, and Armenia. Many other countries in South America will be likely to increase the number of seismically isolated structures in the future. Further information on the situation of the seismic isolation in these countries can be found in references from [40] to [44].

In the following tables, the seismic acceleration response of the seismically isolated buildings recorded during actual earthquakes are presented to clarify the effectiveness of the seismic isolation as well as to show the change in vertical motions. These are of interest in this research work for it can be considered as a criterion weather the isolator bearing is subject to tension or not. All data shown in the following chapter is exclusively from Japan because it has by far the most application examples and very frequent earthquakes. Hence there is more data available, naturally

For a comparison purpose the seismic response data of non-seismic isolated buildings are also presented. In Table 1 an overview of the measured buildings is provided. There, the abbreviations of the building type 'E.R.S.', 'D.S.' and 'S.I.S.' represent 'Enhanced Resistance System', 'Damping System' and 'Seismic Isolation System', respectively. The first one is the conventional building designed to resist against seismic forces with thick walls and large piers. The second one is the building with damping devices, namely the passive energy dissipation system. Only the building No.4 is this type where the tuned mass dampers are employed to mitigate mainly the wind-induced rocking motion. More information of buildings No. 1 to 7 can be found in [45] and No. 8 to 12 in [3]. Those buildings have been selected because the measurement data in the vertical direction is also provided. Further seismic response records on seismic isolated buildings can be found in [46] and [47].

Table 1: Overview of the measured buildings

Building No.	Storeys	Height [m]	Plan Dimension [m]	Aspect ratio	Type
1	3	11.3	15.9×92	0.73 / 0.12	E.R.S.
2	4	16.2	19.5×20.3	0.83 / 0.8	E.R.S.
3	9	34.4	33×72	1.04 / 0.48	E.R.S.
4	4	15	18×94.5	0.83 / 0.16	E.R.S.
5	33	145.5	25.6×51.2	5.7 / 2.8	D.S.
6	18	84.9	40.4×46	2.10 / 1.85	S.I.S.
7	13	38.2	13.6×27.6	2.81 / 1.38	S.I.S
8	11	56	72×109	0.78 / 0.51	S.I.S
9	5	22.2	34.5×34.9	0.64 / 0.64	S.I.S
10	9	35	25×50	1. 4 / 0.7	S.I.S
11	3	10.9	40.6×41.4	0.27 / 0.26	S.I.S
12	6	30	85.6×110	0.35 / 0.27	S.I.S

Measured seismic acceleration responses of the conventional structure (E.R.) are summarised from Table 2 to Table 5. The symbols $\ddot{u}_{h1}$, $\ddot{u}_{h2}$ and $\ddot{u}_v$ represent the maximum acceleration responses in the horizontal transversal direction (shorter side), the horizontal longitudinal direction (longer side) and the vertical direction, respectively. Note that in Japan '1F' denotes the ground floor. Those measurements were obtained during the earthquake near Miyagi prefecture in 2005. A magnitude of 7.2 on the moment magnitude scale was measured at the epicentre.

Table 2: Measured maximum acceleration response of the building No.1

Floor	$\ddot{u}_{h1}$ [cm/s^2]	$\ddot{u}_{h2}$ [cm/s^2]	$\ddot{u}_v$ [cm/s^2]
3F	584.9 (2.6)	318.6 (2.0)	289.5 (1.2)
1F	221 (1.0)	156.9 (1.0)	250.5 (1.0)

Table 3: Measured maximum acceleration response of the building No.2

Floor	$\ddot{u}_{h1}$ [cm/s^2]	$\ddot{u}_{h2}$ [cm/s^2]	$\ddot{u}_v$ [cm/s^2]
4F	271.3 (1.5)	328 (1.4)	164 (1.1)
1F	183.3 (1.0)	228 (1.0)	147.8 (1.0)

Table 4: Measured maximum acceleration response of the building No.3

Floor	$\ddot{u}_{h1}$ [cm/s^2]	$\ddot{u}_{h2}$ [cm/s^2]	$\ddot{u}_v$ [cm/s^2]
9F	329 (3.8)	287 (3.5)	133 (2.3)
1F	87 (1.0)	81 (1.0)	57 (1.0)

Table 5: Measured maximum acceleration response of the building No.4

Floor	$\ddot{u}_{h1}$ [cm/s^2]	$\ddot{u}_{h2}$ [cm/s^2]	$\ddot{u}_v$ [cm/s^2]
4F	338 (1.8)	299 (2.3)	90 (1.4)
1F	192 (1.0)	132 (1.0)	65 (1.0)

As can be observed from this data, the acceleration in all directions increased towards the top of the buildings. By enhancing the structural stiffness the natural frequency of the building often remains within a resonance range of the seismic excitation frequency. Therefore these results are typical for this type of building. In parenthesis the normalised ratio of the response acceleration to the ground acceleration is provided in order to compare the magnitude of the increase. From these values it can be seen that the increase in the vertical acceleration is less than horizontal ones and the degrees of the increase in the horizontal accelerations is similar. The vertical stiffness in general is very high in order to support the self-weight of the structure and hence the structural natural frequency in the vertical direction lies mostly a little higher than the resonance range of the seismic excitation. Any kind of damage in the structural elements may result in a reduction of the vertical stiffness which in turn brings the vertical natural frequency of the structure closer to this range. However such a consideration is generally of no importance since serious damages are caused not by the vertical motion but mostly by the horizontal shear or bending deformation.

Table 6: Measured maximum acceleration response of the building No.5

Floor	$\ddot{u}_{h1}$ [cm/s^2]	$\ddot{u}_{h2}$ [cm/s^2]	$\ddot{u}_v$ [cm/s^2]
32F	190.7 (1.8)	139.3 (2.3)	146.1 (2.6)
19F	162.1 (1.5)	104.4 (1.7)	109.1 (2.0)
5F	150.6 (1.4)	101 (1.6)	91.1 (1.6)
B3F	100.1 (1.0)	61.8 (1.0)	53.8 (1.0)

The maximum acceleration responses of the buildings with tuned mass dampers are summarised in Table 6. This damping device consists of the tuned mass and the spring elements, which is designed to have a natural frequency very close to the one of the first structural deformation mode so that this tuned mass reacts against the external forces such as wind-or earthquake-induced forces instead of the structure. Two these TMDs are installed at the top of the building. It is difficult to evaluate the damping effect because no comparison can be made. However, it should be noted that for this building, the increase in the vertical maximum acceleration response is higher than the horizontal one. Only the horizontal displacement is mitigated by the TMDs and therefore the horizontal maximum responses were probably reduced and the vertical one remained almost unchanged. It could also be either that the vertical natural frequency of the structure is coincidentally nearer to the one of the seismic excitation or that the tuned mass has a negative effect in the vertical motion. Nevertheless it would still be harmless considering the fact that the seismic excitation is generally much lower in the vertical direction than in the horizontal ones, and that the vertical stiffness is quite high.
The maximum acceleration responses of the seismically isolated buildings are summarised in table 7 to 13. Those buildings are located in several cities and the measurements were carried out during different earthquakes.

Table 7: Measured maximum acceleration response of the building No.6

Floor	$\ddot{u}_{h1}$ [cm/s^2]	$\ddot{u}_{h2}$ [cm/s^2]	$\ddot{u}_{v}$ [cm/s^2]
18F	121.9 (0.9)	85.5 (0.9)	161 (2.7)
10F	116.2 (0.8)	87.5 (0.9)	111.5 (1.9)
1F	121.4 (0.9)	59.2 (0.6)	58.3 (1.0)
B1F	139.1 (1.0)	94.5 (1.0)	59.4 (1.0)

Table 8: Measured maximum acceleration response of the building No.7

Floor	$\ddot{u}_{h1}$ [cm/s^2]	$\ddot{u}_{h2}$ [cm/s^2]	$\ddot{u}_{v}$ [cm/s^2]
13F	82 (0.4)	117 (0.4)	- (-)
1F	76 (0.3)	99 (0.4)	278.5 (1.4)
B1F	220 (1.0)	274 (1.0)	197 (1.0)

Table 9: Measured maximum acceleration response of the building No.8

Floor	$\ddot{u}_{h1}$ [cm/s^2]	$\ddot{u}_{h2}$ [cm/s^2]	$\ddot{u}_{v}$ [cm/s^2]
11F	112.1 (0.6)	93.7 (0.5)	446.5 (3.5)
5F	94.8 (0.5)	61.3 (0.3)	172.2 (1.4)
1F	81.8 (0.4)	47.7 (0.3)	132.3 (1.1)
B1F	84.9 (0.4)	45.1 (0.3)	153.7 (1.2)
Foundation	195.2 (1.0)	175.4 (1.0)	125.9 (1.0)

Table 10: Measured maximum acceleration response of the building No.9

Floor	$\ddot{u}_{h1}$ [cm/s^2]	$\ddot{u}_{h2}$ [cm/s^2]	$\ddot{u}_{v}$ [cm/s^2]
1F	198 (0.3)	205.2 (0.3)	749.4 (1.5)
Foundation	740.4 (1.0)	807.7 (1.0)	487.2 (1.0)

Table 11: Measured maximum acceleration response of the building No.10

Floor	$\ddot{u}_{h1}$ [cm/s^2]	$\ddot{u}_{h2}$ [cm/s^2]	$\ddot{u}_{v}$ [cm/s^2]
9F	120.6 (0.6)	93.8 (0.6)	183.6 (2.4)
1F	80.6 (0.4)	70.3 (0.5)	85.1 (1.1)
B1F	192.4 (1.0)	154.1 (1.0)	76.4 (1.0)

Table 12: Measured maximum acceleration response of the building No.11

Floor	$\ddot{u}_{h1}$ [cm/s^2]	$\ddot{u}_{h2}$ [cm/s^2]	$\ddot{u}_{v}$ [cm/s^2]
1F	155 (0.7)	123 (0.9)	145 (1.5)
Foundation	212 (1.0)	142 (1.0)	100 (1.0)

Table 13: Measured maximum acceleration response of the building No.12

Floor	$\ddot{u}_{h1}$ [cm/s^2]	$\ddot{u}_{h2}$ [cm/s^2]	$\ddot{u}_{v}$ [cm/s^2]
6F	74.6 (0.3)	102.6 (0.3)	377.3 (1.8)
1F	57.4 (0.2)	105.6 (0.4)	193.4 (0.9)
Foundation	262.9 (1.0)	299.9 (1.0)	213.2 (1.0)

The effectiveness of the seismic isolation in the horizontal responses is obvious but in the vertical direction the maximum response tends to increase because the seismic isolation is again concerned only with the horizontal directions. It is not clear if this increase was magnified due to the vertical stiffness of elastomeric isolation bearings. In some of those reports it is mentioned that no tension in bearings should have been caused because the measured maximum vertical acceleration values on the isolation layer (generally 1F) are still less than the gravitational acceleration. This statement is not entirely true since uplift is caused not only by the simple up-and-down motion but also by rocking motion and excessive horizontal drifting motion. The measurement data here show that all response accelerations are very low and indeed there would have been no uplift to the degree that the isolator bearings had to carry the tensile force. This raises questions regarding which factors increase the danger of uplifting and how the seismically isolated building responds when the isolator rubber bearings undergoes tensile forces. This topic is studied for instances in [6] [7] and is also discussed briefly in Chapter 7.

3 ELASTOMERIC BEARING

3.1 Rubber Material

3.1.1 Natural rubber

The rubber material which is most commonly used for the seismic isolator bearing is natural rubber vulcanisate. It is used because of its flexibility, high tensile strength and durability against cold environments. The usage of natural rubber has a long history, although the word "rubber" was coined only in late 1700s by an English chemist because in those days it was nothing useful except rubbing off pencil marks on paper [48] [49]. The recorded history of the usage of the rubber material goes back to 6th century in the Aztec empire, where rubber was used mainly as a form of currency. Before the twelfth century the latex from the ule tree was already known to the Mayan civilization in Central and South America where people call it as "caoutchouc" -meaning 'weeping wood'. The Maya utilized this material to coat fabric for water-proofing purposes. There was also ritual ball game called tlachtli [49], whose origin can be traced even back to between 1000 and 700 B.C., among the Mayan or other Mesoamerican folks. Since a rubber ball has been used in this game for centuries, it is assumed that rubber material was known to them already at that time [50].
Natural rubber is in chemical terms cis-1,4 polyisoprene (see Fig. 16), which can be collected from about 2000 different trees. However only a dozen tree types can generate enough polyisoprene to be beneficial, and today the Hevea brasiliensis produces by far the most amount of natural rubber. The sap of Hevea brasiliensis can be obtained by tapping its bark. Besides natural rubber the freshly tapped latex also contains water, sugar, resin and protein. Even after purification, natural rubber is not much of use as it is in the form of highly viscous liquid. In 1839 Charles Goodyear discovered that the material becomes a viscoelastic solid when natural rubber is mixed with sulphur and the two material are heated together. This process is known as 'vulcanization', and the solid material as natural rubber 'vulcanisate'. Later in 1845 Thomas Hancock and Robert William Thomson separately developed the fully solid tire and the pneumatic tire of natural rubber vulcanisate, respectively [50]. Demand for the rubber tire rose rapidly along with the automotive industry [50] and soon it was clear that natural rubber production which depended only on the wild trees in South America would not meet the ever increasing demand. Plantations were, therefore, initiated in some of South Asian and African countries. This provides an explanation as to why countries such as Thailand, Indonesia and Malaysia are leading in the natural rubber production today. Further information regarding natural rubber can be found in [48] and [50].

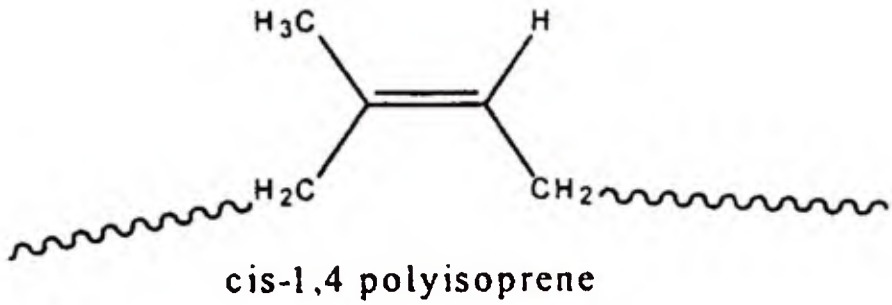

Figure 16: Chemical structure of natural rubber [48]

3.1.2 Chloroprene (Neoprene)

As rubber applications spread to a wider range and became essential to society, the necessity of developing synthetic rubber arose. This was in order to make sure that the rubber products could still be produced during international conflicts independent of natural material supplies coming only from countries in tropical climates such as Africa, South Asia or Central America. Various types of synthetic rubber are available today, but besides natural rubber only chloroprene seems to be used exclusively for the elastomeric bearings. This is due to its advantageous properties, for instance superior resistance against ozone, oil and fire. Chloroprene was developed by A.M. Collins in 1930 in the course of research work initiated by the company DuPont regarding the production of butadiene by dimerising acetylene. Therefore chloroprene is known as its trade product name "Neoprene". Chloroprene has five different configurations in the molecular chain as shown in Fig. 17 and they co-exist with different proportions. The most dominant configuration is trans 1,4-unit (I). The ratio of them varies with the polymerisation temperature, see more detail in [50].

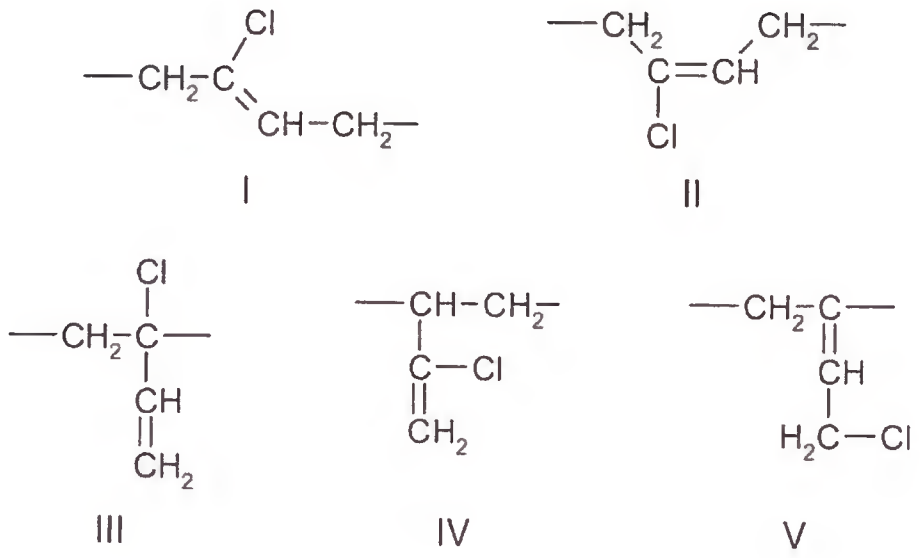

Figure 17: Chemical structure of polychloroprene [50]

3.1.3 Compound

Rubber is polymer material which possesses long molecule chains (typically 10,000 to 50,000 main-chain atoms) [49]. For practical use, these polymer chains have to be cross-linked into a three-dimensional network, by which the relative movement between chain molecules is limited and by that considerable stress can be supported by this material. In other words, it is a transformation process from highly viscous liquid into viscoelastic solid – the same process that Charles Goodyear discovered. This cross-linking process is often referred to as "vulcanization" or "curing" and the materials that facilitate cross-linking of the molecule chains are called curatives. For natural rubber the curative material is, as explained already, sulphur and for chloroprene metal oxides can also be used [51]. The degree of cross-linking has to be limited, typically with one crosslink site of every 100 to 1,000 main-chain atoms on average as overly frequent crosslinking prevents each chain molecule from stretching and as a result the material becomes rather inextensible and brittle. Limiting the degree of crosslink is, however, not simple as long rubber molecules tend to entangle

and create temporary physical cross-links additionally. This can be improved by diluting the material by adding so-called plasticizers such as petroleum-based oil so that the spacing between molecules is widened to reduce their entanglement. The plasticizers also have a function which reduces the viscosity of the uncured compound so that mixing or extruding processes can be accelerated.
There are some other ingredients which are necessary to improve properties of rubber. Among others, reinforcing agents, most commonly carbon black and silica, are of great importance. They enhance several rubber properties including tensile and shear strength. Many of elastomeric materials are in fact of no practical use without reinforcing agents. They also improve processability and hence contribute to reducing manufacturing cost.
Filler materials, typically clays, calcium carbonate and titanium dioxide are also often added in order to reduce cost and increase hardness. Improvement in properties is indeed possible but not as significant as the effect that reinforcing agents can achieve.
Other essential ingredients, (although their proportion to the compound is very small), are anti-degradants against ageing, i.e. oxygen and ozone attack. Exemplary compounds of the natural rubber vulcanisate and polychloroprene vulcanisate for general-purpose engineering use are shown in Tables 14 and 16. The physical properties of a typical natural rubber vulcanisate and chloroprene rubber vulcanisate are summarised in Tables 15 and 17, respectively.

Table 14: Carbon black-filled natural rubber formulation for general-purpose engineering use (table reproduced from [51])

Ingredient	Amount (phr*)
Natural rubber	100
Process oil	5
Stearic acid	2
Zinc oxide	5
N-550 carbon black	25, 50, 75
Phenylamine antioxidant	1.5
Sulphur	2.5
Cure accelerator: benzothiazyl disulfide	1
Cure accelerator: tetramethy thiuram disulfide	0.1

*Parts by weight per 100 parts by weight of rubber
Cure: 20 minutes at 150°C

Table 15: Properties of a typical natural rubber vulcanisate (table reproduced from [51])

	N550 carbon black (phr)		
	25	50	75
Shore A Hardness	51	62	72
300% Modulus (MPa)	7	9	11
Tensile Strength (MPa)	22	24	25
Breaking Elongation (%)	700	600	550

Table 16: Polychloroprene formulation for general-purpose engineering use (table reproduced from [51])

Ingredient	Amount (phr)
Polychloroprene	100
Process aid	5
N-550 carbon black	25, 50, 75
Stearic acid	2
Zinc oxide	5
Magnesium oxide	4
Antioxidant: octylated diphenylamine	2
Cure accelerator: activated thiadazine	1

Cure: 20 minutes at 150°C

Table 17: Properties of a typical polychloroprene rubber vulcanisate (table reproduced from [51])

	N550 carbon black (phr)		
	25	50	75
Shore A Hardness	53	64	78
300% Modulus (MPa)	9	11	14
Tensile Strength (MPa)	20	21	24
Breaking Elongation (%)	400	350	300

3.1.4 Dynamic properties

For rubber materials it is often difficult to define characteristic values such as shear modulus because of their viscosity and other time-dependent nature. As provided previously, the material properties can only be defined with some specific criteria and otherwise those values vary. This may depend, for instance, on the loading velocity, the loading history and the range of strain. In this section each of those specific properties is briefly explained.

Dynamic shear modulus and Payne effect

Due to its viscoelastic and entropic nature, rubber materials possess a varying shear modulus depending upon the loading speed as well as the strain level. Generally the dynamic shear modulus can be divided into two components, i.e. the storage (in-phase, elastic) and the loss (out-of-phase, viscous) shear moduli, *G'* and *G"*. The dynamic shear modulus G_{dyn} consists of these two moduli and can be expressed as

$$G_{dyn} = G' + iG'' \text{[52]} \tag{3.1}$$

where i is the imaginary number defined as $i^2=-1$.

Payne [52] [53] experimented on the dynamic shear modulus of rubber vulcanisates and discovered that both the storage and the loss moduli of filled butyl vulcanisates change rapidly within a relatively small strain range as shown in Figures 18 and 19. In these figures the different lines correspond to the different amount of the high abrasion furnace (HAF) carbon black filler in rubber vulcanisates, which are 9.2, 16.8, 20.2, 23.2 and 28.8 % to the rubber volume [52]. First from Fig. 18 it can be observed that the initial value of the storage modulus *G'* is the highest. The modulus decreases with increasing strain and appears to approach a limit value at sufficiently large strain. The initial and the limit values of the storage modulus and the degree of change between these two values clearly have some correlation with the concentration of the carbon black filler.

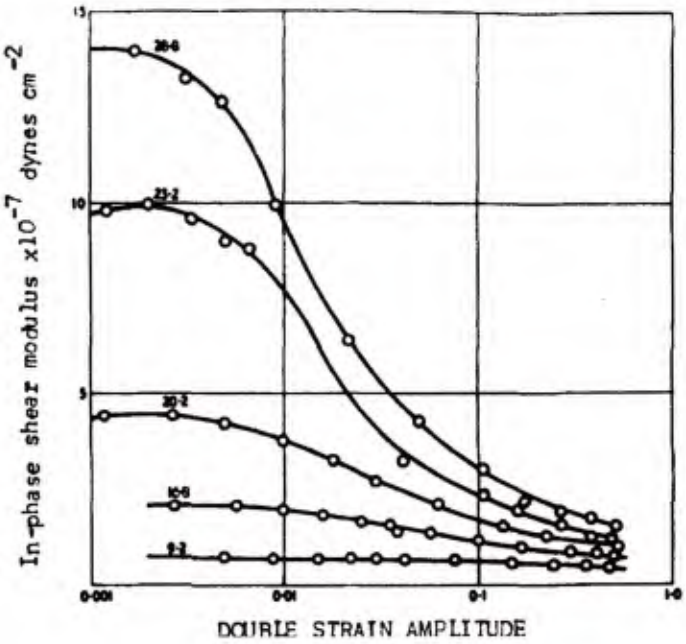

Figure 18: Change in the storage modulus along with strain amplitude [52]

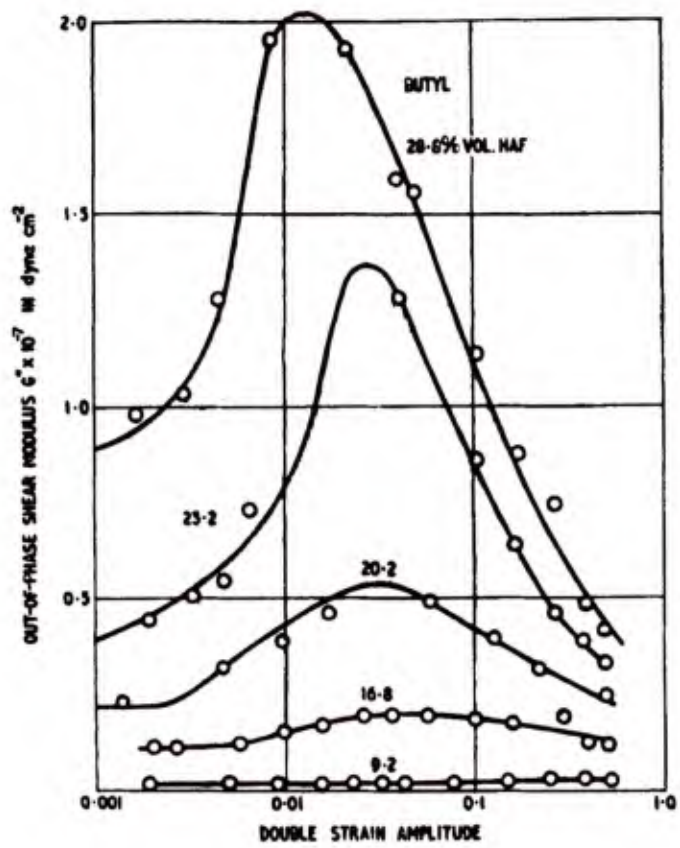

Figure 19: Change in the loss modulus along with strain amplitude [52]

As for the loss modulus *G"*, the maximum value is found where the highest inclination of the storage modulus appears. Analogous to the storage modulus, the maximum value and the degree of change in the loss modulus are related to the amount of the carbon black filler. Note in particular that the modulus approaches zero independent of the strain as the filler amount decreases. This is a clear indication that the viscosity of rubber vulcanisates is mainly attributed to the filler particle interaction.
In his other papers, Payne showed [54] [55] that the difference between G_0' and G_∞' is reduced by increasing the mixing time or breaking the aggregation of carbon black before mixing, i.e., by increasing dispersion of the filler particles. From these results concluded that the radical change in the dynamic shear modulus within a small strain range is caused by the breakdown or reformation of the aggregated carbon black filler clusters. Filler particle interaction can be categorized further and it is now generally accepted that those interactions with the molecular chain networks contribute to the shear modulus of filled polymer material. The dependence of modulus on strain amplitude is schematically shown in Fig. 20.

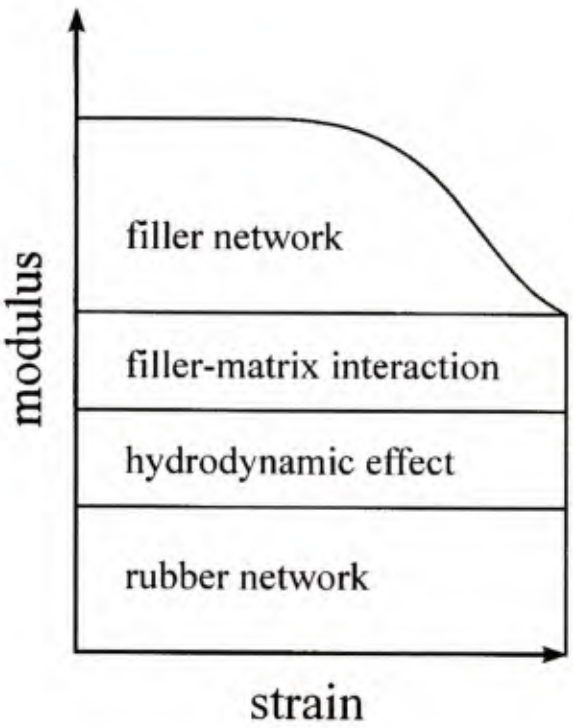

Figure 20: Change in the shear modulus with its strain-dependent and independent components [56]

Note that the proportion of three components shown in this figure is merely an example and it varies depending upon the amount, type and the processing method of the filler. Moreover the hardening due to the finite extensibility of molecular chains and the crystallization also has to be considered at the high strain range. This strong strain dependence of the dynamic shear (or elastic) modulus is called either 'Payne effect' or 'Fletcher-Gent effect'. In [54] and [55] it is also shown that there is a strong temperature influence on the initial storage modulus G_0' but almost no influence on the limit storage modulus G_∞'.
One aspect of the increase in the limit storage modulus with increasing amount of the carbon black filler is explained by the hydrodynamic interaction between the rubber vulcanisates and the filler particles. Einstein studied this phenomenon in his examination of the increase in viscosity of fluid

due to the dissolved spherical colloids [57] [58]. Increased friction (suspension) in flow due to the colloid particles is the cause of this hydrostatic effect and this increase in viscosity is expressed as

$$\eta_f = \eta_u (1 + 2.5 c_{fill}) \text{ [57] [58]} \tag{3.2}$$

where η_f and η_u are the viscosities of the filled and the unfilled system, respectively. c_{fill} is the ratio of the filler volume to the fluid (solvent) volume.

The validity of this Eq. (3.2) is, however, limited to a very small ratio of c_{fill}. In fact Guth and Gold claimed that it is necessary to include the interaction between spherical particles when the ratio c is higher [59]. They introduced an additional term, which takes this interaction between particles into account, to the Eq. (3.2) in order to take this interaction into consideration.

$$\eta_f = \eta_u (1 + 2.5 c_{fill} + 14.1 c_{fill}^2) \text{ [59]} \tag{3.3}$$

Smallwood theoretically showed in his paper [60] the validity of the Eq. (3.2) for the calculation of the elastic modulus of filled rubber vulcanisates. Again for a higher concentration of the filler particles the equation from Guth and Gold is more appropriate. Substituting the viscosity η to the shear modulus G'_f in the Eq. (3.3),

$$G_f' = G_u' (1 + 2.5 c_{fill} + 14.1 c_{fill}^2) \tag{3.4}$$

is obtained. Furthermore Guth [61] later pointed out that this expression can be used to predict the increase in characteristic values such as elastic modulus up to the volume concentration ratio of 0.1 since carbon particles more than this amount tend to form a chain-like cluster together and does not behave as a number of spherical particles. Therefore for a higher concentration ratio c_{fill} (from 0.1 to 0.3) Guth derived the following expression.

$$G_f' = G_u' (1 + 0.67 s_c \cdot c_{fill} + 1.62 s_c^2 \cdot c_{fill}^2) \text{ [61]} \tag{3.5}$$

s_c is the shape factor to capture the asymmetric proportion of the aggregated clusters defined as length/width of the aggregated cluster. Eqs. (3.4) and (3.5) deal only with the increase in shear modulus due to the hydrodynamic interaction effect between rubber and filler particles and hence they cannot predict the behaviour of rubber in small strain range.
The loss modulus is a function of both carbon black structure and carbon black specific area, while the storage modulus is independent of the latter. As for the loss modulus, Payne [52] pointed out that the maximum value of G'' is linearly related to the difference between the aforementioned initial and the limit values of G' such that

$$G_{max}'' = c_{in} + c_{out} (G_0' - G_\infty') \text{ [52]} \tag{3.6}$$

where G_0' and G_∞' are the initial and the limit values of the storage modulus, respectively. In his paper [52] c_{in} was called as the "out-of-phase" modulus of an ideally dispersed vulcanisates and c_{out} is the mix-dependent constant which ranges from 0.1 to 0.2 [52].

Later these expressions for both moduli were studied further by Kraus [62], who then suggested other phenomenological expressions which are now widely known as Kraus-model [56]. They are, under a periodic sinusoidal strain of the amplitude e_a at fixed frequency and constant temperature, expressed as

$$G'(e_a) = G_\infty' + \frac{G_0' - G_\infty'}{1 + (e_a / e_0)^{2c_G}} \text{ [56] [62]} \tag{3.7}$$

$$G''(e_a) = \frac{(G_0' - G_\infty')(e_a / e_0)^{c_G}}{1 + (e_a / e_0)^{2c_G}} \text{ [56] [62]} \tag{3.8}$$

where e_0 is the characteristic strain amplitude and c_G is the constant that varies depending on the polymer matrix.

Mullin's effect

When a rubber vulcanisate is stretched repeatedly, the stress-strain curve of each subsequent cycle does not follow the same path but a less force is required to reach the same elongation than the previous cycle. Figure 21 of experimental data from Holt [63] shows the force-strain curves of the tension test of a rubber unfilled vulcanisate (pure gum). In this test, the ring form specimen was stretched repeatedly with the same elongation amplitude. The softening can be clearly observed in this figure and the degree of softening is the highest between the first and second cycle. Another thing to notice is that the loading and unloading paths are significantly different as well. Additionally, the results of the cyclic stretching test in which the elongation amplitude of each cycle exceeds the previous cycle (Fig. 22) reveal another typical behaviour of the rubber vulcanisates.

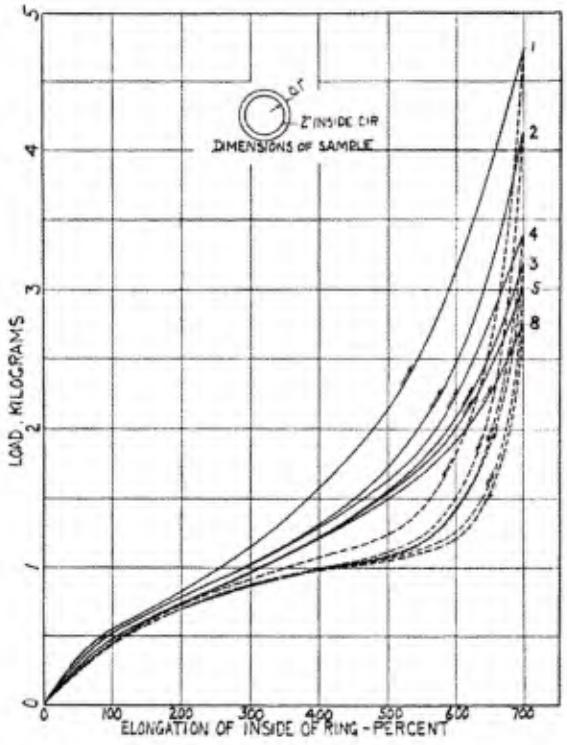

Figure 21: Load-elongation curve from one sample of unfilled natural rubber vulcanisate [63]

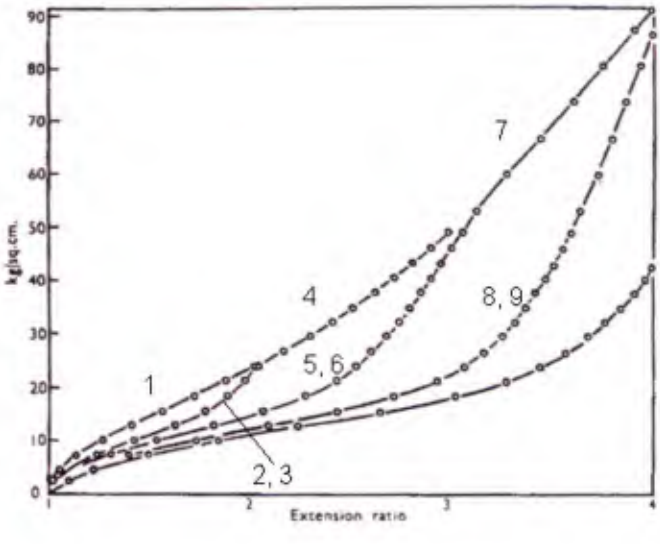

Figure 22: Load-elongation curve from one sample of natural rubber vulcanisate filled with MPC black [64] [65]

As indicated with numbers, the loading and unloading paths (1 and 2 respectively) differ and the second loading path (3) follows the first unloading path up to the maximum elongation of the first cycle. Then it goes on the path 4 which seems to be an extension of the first loading path. This

phenomenon is generally referred to as Mullins effect as Mullins was the first to investigate rubber vulcanisate extensively in 1948 [66], although as he mentioned, the softening behaviour had been already long known in industry. As for the causes of this phenomenon a general agreement has seemingly not met yet and several theories have been proposed [67]. For instance, Mullins has suspected that the cause of these phenomena involved some failure related to filler particles because the degree of observed softening seemed much higher for filled vulcanisates than pure gums. Bueche has also concluded that this softening behaviour is result of the detachment of the rubber molecular chains from filler particles upon stretching and developed the mathematical model based on this theory [68]. Other theories are based on concepts in which it is assumed that the slippage of molecular chains on the surface of filler particles during deformation causes the softening [69], rearrangements of linkages between the filler particles and polymer [70] or the rupture of the filler clusters. However as shown in Fig. 21, this softening behaviour is also observed for rubber unfilled vulcanisates and therefore these theories focusing only on rubber filled vulcanisates cannot fully explain the phenomenon. To answer this discrepancy Dannenberg and Brennan assumed that the softening of unfilled natural rubber vulcanisates involves the crystallization process (namely different mechanism from the case of filled rubber vulcanisates) since other unfilled synthetic rubbers exhibit no such softening behaviour within the tested strain range [70].
Harwood, Mullins and Payne carried out series of extension tests for various rubber vulcanisates and some of the results are shown in the following figures [71] [72].

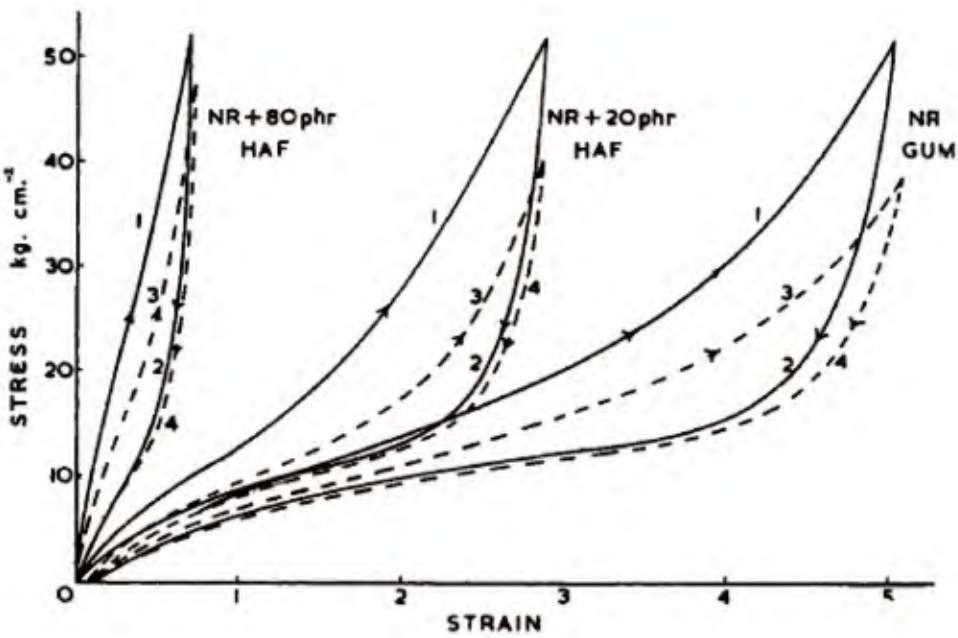

Figure 23: Stress-strain curves of rubber vulcanisates without or with different amount of carbon black filler [71]

The first Fig. 23, shows the Mullins effect on three different rubber vulcanisates categorized by the amount of carbon black filler in two loading cycles. From this figure an apparent difference in degree of softening can be seen. The next Fig. 24 is derived from the same result, however, here the stress level of the initial loading path is plotted against the stress of subsequent unloading (2, 4) and reloading (3) paths measured at the same strain. This normalized diagram reveals another insight of the Mullins effect. At the lower stress level the path of the rubber vulcanisates with 80phr HAF differs significantly from the other two. This difference must be caused by the aforementioned

breakage of the cluster of carbon black, since the larger amount of filler tends to increase the amount of clusters. However, the degree of softening of all rubber vulcanisates is more or less similar at a higher stress level. Based on these results, therefore, Harwood et al. came to the conclusion that the Mullins effect takes place due to the change in rubber phase rather than change in the bond structure between rubber molecules and filler particles [71] [72].

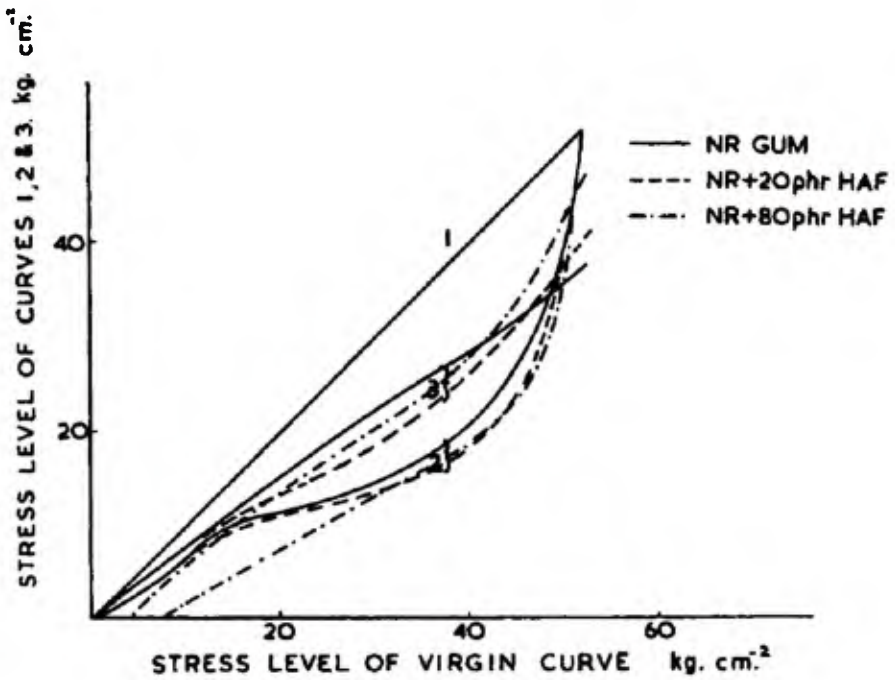

Figure 24: Stress vs. initial stress at the same strain level of figure 23 [71]

With their later publication [72], Harwood et al. explained that the existence of the filler carbon particles induces a local higher strain in the rubber vulcanisates. Due to this local high strain the degree of the change in the rubber vulcanisates is enhanced and thus the softening seems more pronounced for the filled rubber vulcanisates. They adopted the so-called strain amplification factor in order to estimate this locally increased strain so that the difference in "actual" softening degree between unfilled and filled rubber vulcanisates can be compared. The strain amplification factor is, in fact, the exactly same factor introduced earlier in Eqs. (3.3) and (3.4) for the calculation of the storage modulus considering the hydrodynamic effect. The generalized expression for the amplification factor is therefore

$$Z = \frac{X}{X_0} = 1 + 2.5c_{fill} + 14.1c_{fill}^2 \quad [59]\ [71]\ [72] \tag{3.9}$$

where X and X_0 are characteristic values of filled and unfilled rubber vulcanisates, respectively.

Mullins and Tobin [73] conducted a series of tension tests of rubber vulcanisates with different amount of carbon black filler and the stress-strain curves described by the Mooney-Rivlin relation were modified by this strain amplification factor. All curves except for those of the rubber vulcanisates with higher amount of carbon black ($c_{fill} > 0.1$) follow the similar paths and this tendency is in a good agreement with the theory of Guth. For a higher concentration ratio c_{fill} (from 0.1 to 0.3) the factor from the Eq. (3.5) would provide a better prediction.

$$Z = \frac{X}{X_0} = 1 + 0.67 s_c \cdot c_{fill} + 1.62 s_c^2 \cdot c_{fill}^2 \text{ [61]} \qquad (3.10)$$

The next Fig. 25 shows the stress-strain curves of natural rubber vulcanisates with different carbon blacks from the second extension, where the strain is normalised by the maximum strain value measured in the first extension as well as amplified with the strain amplification factor according to the volume concentration of each filler type. All curves of filled rubber vulcanisates trace in the vicinity of the path from the unfilled natural rubber vulcanisate (dotted line). This diagram indicates that for the most part Mullins effect indeed takes place due to changes in the rubber phase such as molecular chain scission or slippage. The same series of tests were carried out for Styrene-Butadiene synthetic (SBR) rubber and the results delivered the similar tendency, although unfilled SBR could not be compared because it was too weak to reach the stress level studied there. Those results imply that the assumption of Dannenberg and Brennan (that the softening of unfilled natural rubber involves the crystalline nature) is probably not entirely correct as SBR does not crystallize yet Mullins effect was observed. The recovering behaviour of Mullins effect was studied in [70], [74] and [75]. For unfilled natural rubber vulcanisates an almost full recovery was observed after resting them at high temperature (over 80 °C) but at the lower temperature such as the room temperature the recovery is negligible.

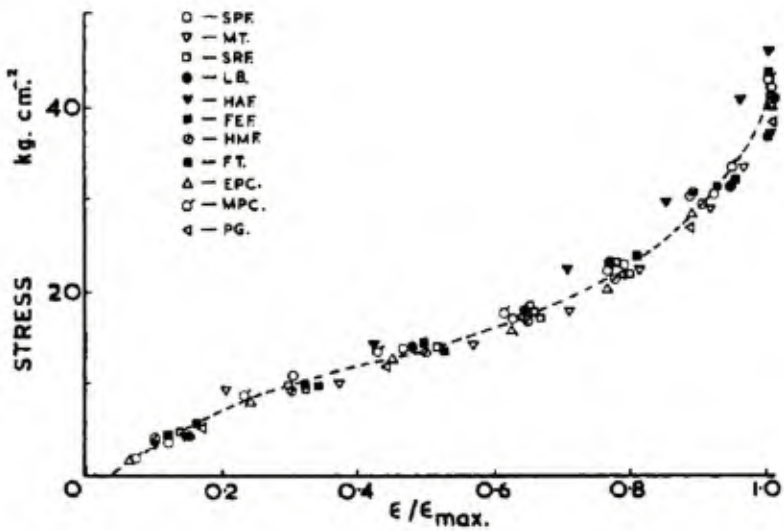

Figure 25: Stress–normalized strain curves of both natural rubber vulcanisates without and with various filler material from the second extension, using the strain amplification factor [71]

3.1.5 Other general properties

Environmental (weather) resistance

Natural rubber is especially vulnerable to ozone which exists only very small amount in the atmosphere (a few parts per hundred million) but enough to chemically react with natural rubber. This reaction appears in the form of crack, which develops rapidly by applying a relatively small strain, on the surface perpendicular to the loading direction. For natural rubber the critical strain is about 3 % [50]. Ozone reacts with carbon-carbon double bonds first together turning into an ozonide. Then this ozonide further changes into an instable zwitterion which provokes the chain scission. This process is schematically shown in figure 26.

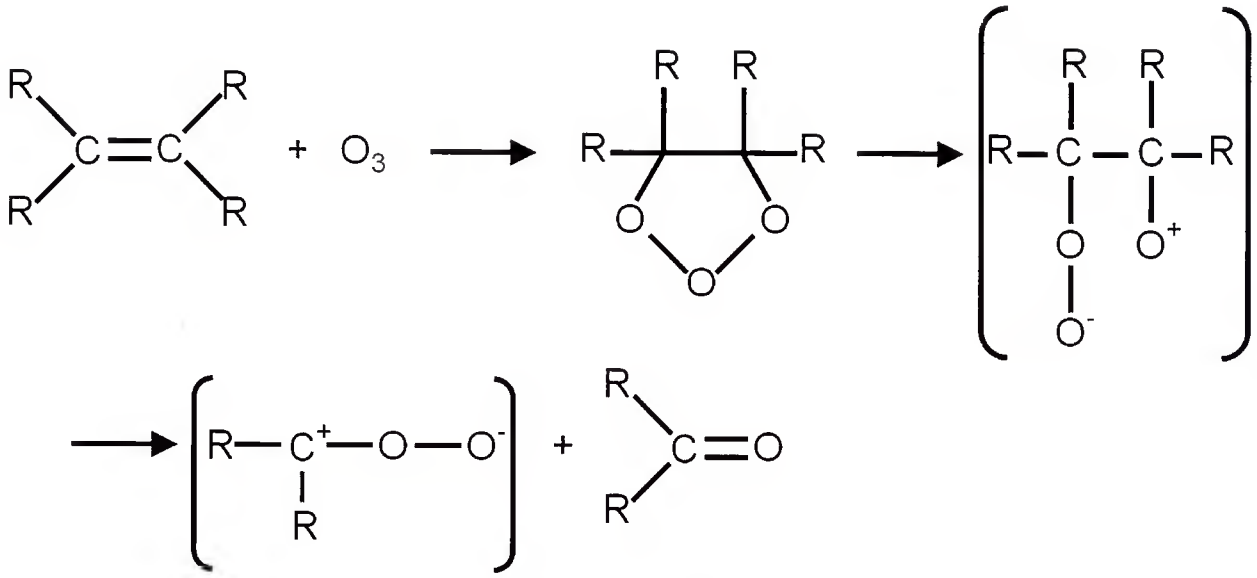

Figure 26: Chemical reaction of rubber with ozone (recreated from [50])

Complete remedies against ozone attack do not exist but ozone cracking can be reduced by adding Para-phenylenediamines (PPDs) which also chemically reacts with ozone competing with the chemical reaction between ozone and elastomer. Otherwise the natural rubber has to be covered with another elastomeric material which has ozone resistance.

The reaction of oxygen and elastomer has two opposite features. On the one hand the molecule chains of elastomer are cleaved by this reaction but on the other hand cross-linking is also facilitated. For the filled natural rubber the dominant reaction is the latter for the most technical elastomer [51] and therefore the elastomeric bearings are expected to become harder and brittle after years of their service. Oxidation process starts with the generation of peroxy radicals (ROO·) which in turn react with elastomer creating Hydroperoxides (ROOH) and polymer radicals (R·). The initiation can have different causes such as mechanical loading, heat and ultraviolet light. This process is an autocatalytic, free radical chain reaction and therefore propagates quickly. The decomposition of Hydroperoxides into radicals happens at a slower pace but can be accelerated by the catalytic heavy metals, notably copper, cobalt and manganese. As described above the chain reaction will be terminated by re-cross-linking, connecting the polymer radicals or deactivating the radicals by means of antioxidants. Antioxidants are applied to slow the oxidation chain reaction by letting them react with peroxy radicals and creating non-radical products [50]. The oxidation process is also somewhat slowed down by the already oxidized layer of elastomer and for this reason the speed of deterioration in the elastic characteristics is often not as acute as expected. Some test reports regarding the ageing of elastomeric bearings after a long period of service all of which indicate the oxidation took place only on the thin surface level and change in the material properties were negligibly small [51]. Nevertheless adding the antioxidants to elastomer vaulcanizates is recommended to secure a longer service life of the elastomeric bearing.

Temperature dependence

There is a certain temperature, below which polymer material becomes hard and brittle, and transform into a glassy material due to the restriction in the relative movement between molecular chains. This temperature (approximate mid-point of the transition range) is referred to as the glass transition temperature T_g and the surrounding temperature of elastomeric bearings has to be well above this value, otherwise the bearings cannot exert their flexibility as designed.

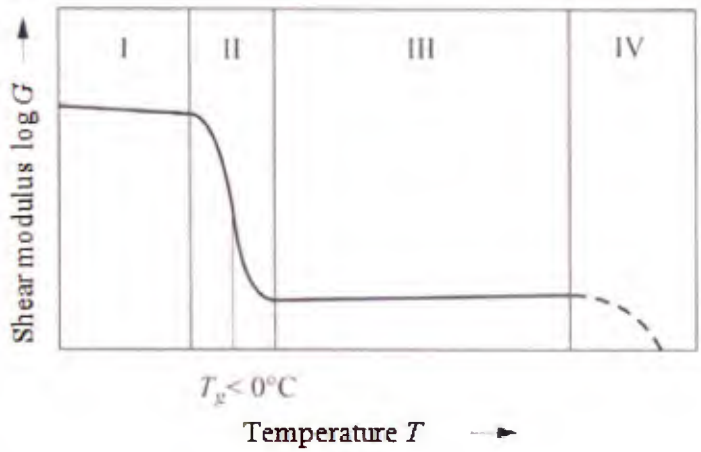

Figure 27: Temperature dependence of the shear modulus G of elastomer in accordance with DIN 7724 [50]

Unvulcanised rubber has a slightly lower glass transition temperature than vulcanised rubber since the vulcanization decreases the flexibility of the molecular chains. For instances the unvulcanised natural rubber has a glass transition temperature of -72 °C whereas the vulcanised one has a value about -68°C and the unvulcanised and vulcanised polychloroprene has a glass transition temperature of -50°C and -45°C, respectively [51]. Both of them still possess a sufficiently low glass transition temperature to keep them in the rubbery state for most of the cold regions. However even above the glass transition temperature a caution must be paid for the design, considering the changes in characteristics of the elastomer due to the crystallization, if these elastomer are expected to be used in a cold environment with extended period. Crystallization takes places slowly in contrast to the instantaneous glass transition process and causes hardening. The problem is that it can occur well above the glass transition temperature. Crystallization occurs when the condition $T \cdot \Delta\Psi < \Delta H$ is satisfied, where T, $\Delta\Psi$ and ΔH are the temperature, the change in entropy and the change in enthalpy, respectively [76] [77]. Change in the enthalpy is equivalent to the heat transferred to the system from the surroundings if the constant pressure is assumed. Then there exists the threshold temperature of crystallization (or melting point) defined as $T_m = \Delta H / \Delta\Psi$. If in the undeformed condition, it is known that the crystallization takes place with the maximum rates at -10 °C and -25 °C for polychloroprene (-12 °C for pure trans 1-4 Polychloroprene) and natural rubber, respectively [50] [51]. Therefore natural rubber has a greater resistance to low temperature crystallization. Crystallites begin to melt at temperatures 10°C above the crystallization point and this process is faster than crystallization. The crystallization can be induced at higher temperature in a largely deformed configuration. This phenomenon is often referred to as the strain-induced crystallization. Thermodynamically speaking the rise in the crystallization-initiating temperature is the consequence of the decrease in the conformational entropy due to the large deformation of rubber while change in entropy remains the same order. The excellent tear strength of natural rubber or polychloroprene is attributed to the strain induced crystallization since crystallites which develop at the crack tip reinforce those elastomers locally. The stress hardening is also rooted in the strain-induced crystallization, although the very high hardening observed in the maximum strain range occurs mostly due to the finite extensibility of the molecular chains. That is why the stress hardening can also be observed in noncrystallizable rubber such as Styrene-Butadiene-Rubber (SBR) near the maximum strain range. X-ray diffraction technology or dilatometry (measurement of change in volume) are frequently used for the monitoring the rate of crystallization [49]. It is

certainly a complicated phenomenon to comprehend and thus the complete mechanism is yet to be revealed despite of many years of research. The pioneering work of Flory [76] resulted in several crucial theories regarding the strain-induced crystallization and are still agreed today. One of them is the co-existence of the crystalline and the amorphous regions, namely the semi-crystalline rubber. Another is that the crystallites formed parallel to the stretched direction have an effect to the polymer network as extra giant cross-linkages. The second assumption was important to explain the "paradox" he encountered that the required tensile force should reduce as the rubber undergoes crystallization in the thermodynamical point of view but the quite opposite phenomenon, i.e. hardening is observed in reality. Considering the nucleation of crystallites at a certain strain as additional random cross-linkages between molecular chains, change neither in the conformational entropy nor in the applied tension should occur. However more tension will be required as the elongation is increased because more molecular chains connected by those additional cross-linkages resist the deformation. Recent research, for instance [78], show the simultaneous measurement of the rate of crystallization using modern apparatus so that the correlation to the stress-strain curve can be observed, see figure 28. The X-Ray intensity can be regarded as the degree of crystallization. In the same figure the possible configurations of the molecular chains at the different strain phases is also indicated. As reported in cases, not single form but various forms of the crystallites are observed in case of the strain-induced crystallization and their forming dependencies on the strain level [78] [79] [80].

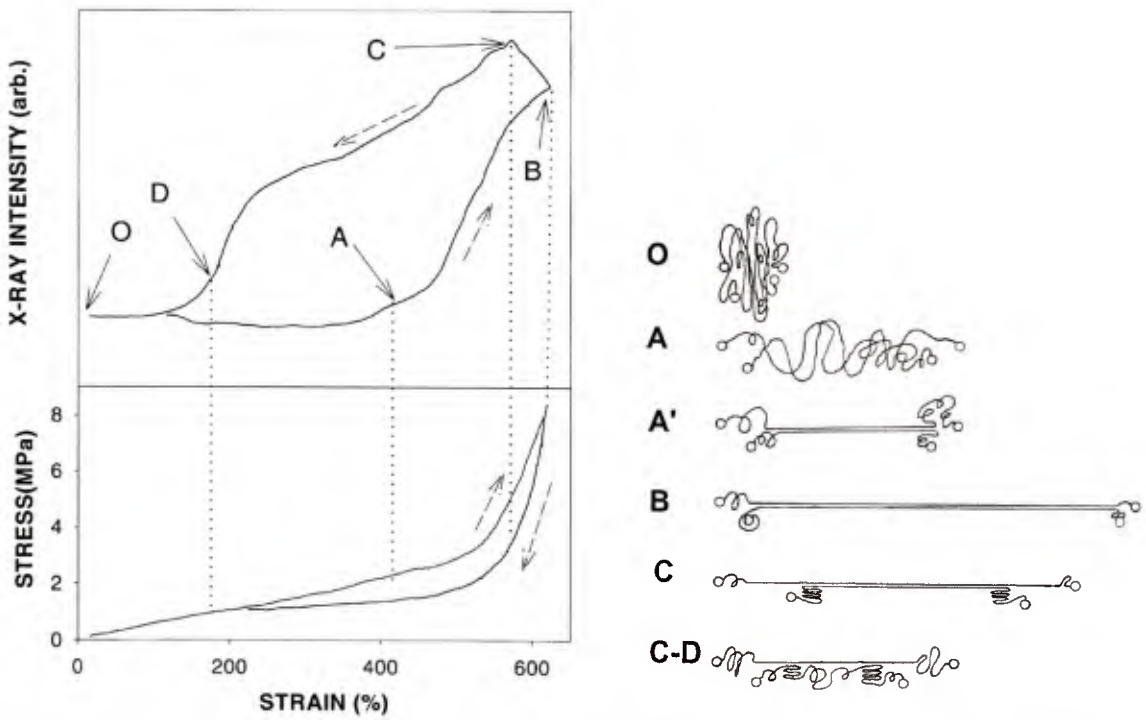

Figure 28: Comparison of the stress-strain and the X-ray intensity-strain curves with the proposed molecular chain configurations at each different phase [78]

Toki et al. [78] proposed two types of crystallization and their mixed configuration as denoted A', B, C and C-D above. From these curves it can be observed that crystallization starts first at a very high strain of about 400 % and while stretching until the maximum strain point B the extended chain crystallites are dominant. Upon unloading, most of those crystallites transform rapidly into the folded chain lamellae type that do not contribute to the stress. Toki assumed that this kind of transformation also occurs during the relaxation process. The point D where the loading and

unloading curves meets is assumed to be the melting strain point of all crystallites for this test and the rubber consists only of amorphous segments.
Another major concern for researchers is the influence of the filler materials. The onset of the crystallization-induced hardening is shifted to a lower strain range when the rubber material is filled with carbon black or other filler particles. In recent studies regarding the crystallization of filled rubbers, for instance [81], [82] and [83], it seems to be agreed that the cause of this shift is due to the increased local strain due to the existence of filler particles, although the strain amplification factor adopted in [82] and [83] is different from the ones introduced by Gold and Guth (Eq. (3.9) and (3.10)). Furthermore Rault et al. [82] support the theory of Flory that not only the crystallites but also the filler particles played a role as the giant cross-linkage between molecular chains, whereas Poompraub et al. [81] schematically described these stiffening and hardening effects of the crystallites and filler particles as the geometrical constraint which hinders the deformation of the molecular chain network, see Fig. 29.

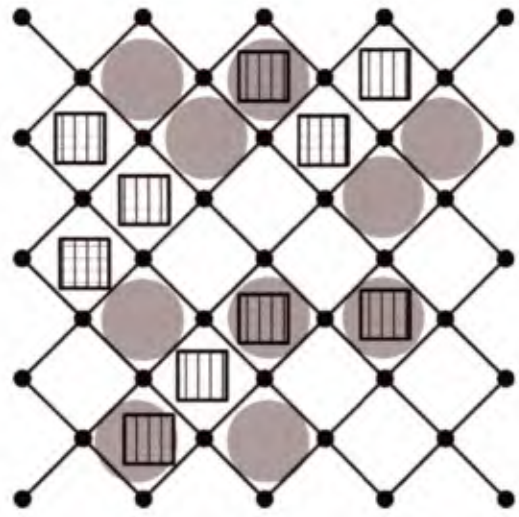

Figure 29: Mechanical model of the molecular chain network filled with crystallites (white square) and filler particles (grey circle) [81]

Assuming those theories are correct, the strain amplification factor would have to be modified to consider the increase in the elastic modulus or the constraint due to crystallization. That is, however, not focus of this thesis and hence it is not discussed further.

Time dependent effects
Elastomeric materials are prone to time-dependent effects such as creep, stress relaxation and set. The phenomena of creep and stress relaxation are caused in the same mechanism and each of their process rates can be deduced by another in practice. Therefore they are often just referred to as "relaxation" phenomenon in literature. There is both physical relaxation and chemical relaxation depending upon the causes. The changes in the molecular network under strain including rearrangement, rupture, and entanglement or disentanglement of the molecular chains contribute to the former. If the filled elastomer is considered, the breaking of bonds between fillers and elastomers can top up the effect. Physical relaxation takes place in a relatively short period and generally decreases proportionally with respect to the logarithm of time. The viscoelastic property of elastomer can mathematically describe this phenomenon. For instance, Maxwell-fluid model describes the stress relaxation and Voigt-Kelvin-solid model describes the creep. Physical stress relaxation can be expressed as

$$\text{Physical stress relaxation} = \frac{\sigma_0 - \sigma_t}{\sigma_0} = c_{re\_p} \log_{10}\left(\frac{t}{t_0}\right) \text{ [51]} \tag{3.11}$$

where c_{re_p} is the physical relaxation constant depending upon material in percent per decade of time (ppd), σ_0 is the nominal stress at time t_0 and σ_t is the nominal stress at time t, respectively

On the other hand, chemical relaxation takes place over a long period and is mainly caused by aforementioned ozone and oxygen attacks. Change in material properties due to the scission of the molecular chains or chemical cross-links caused by oxidation results in stress reduction within the material. This process is referred to as chemical relaxation. Unlike physical relaxation, the rate of relaxation increases almost linearly with time and is sensitive to the environmental temperature. Chemical relaxation rate is expressed as

$$\text{Chemical stress relaxation} = \frac{\sigma_0 - \sigma_t}{\sigma_0} = c_{re\_c}(t - t_0) \text{ [51]} \tag{3.12}$$

where c_{re_c} is the chemical relaxation constant depending upon material at constant temperature in percent per decade of time (ppd).

Total stress relaxation is then given by the sum of both Eqs. (3.11) and (3.12).
Some strain remains after releasing the load which depends on the material type, surrounding temperature, the degree of deformation and the loading duration. This permanent strain is called 'set' and under-cured elastomers exhibit especially excessive amounts of set due to the formation of extra cross-links in the compressed configuration [51]. Therefore, it is required that elastomeric bearings are examined for the degree of compression set (DIN 15129) in compliance with ISO 815, which serves as the quality control check for the cure condition.

3.2 Characteristics Of Elastomeric Bearings

3.2.1 Behaviour under shear loading

The flexibility of rubber materials enables a structure on elastomeric bearings to drift horizontally with little restriction. This property is crucial not only as a seismic isolator but also as a bridge bearing because the deformations induced by temperature change have to be more or less constraint-free at the supports in order to avoid possible accumulation damages, i.e. fatigue. Principally the elastomeric bridge bearing and the elastomeric seismic isolator bearing have the same structure, i.e. alternative layers of rubber pads and steel shims, apart from the fact that the first shape factor for bridge bearings are generally smaller than one for seismic isolators. Therefore the equation to calculate the shear stiffness of the bearing is the same for both cases, which is

$$K_h = \frac{G \cdot A}{h_{total}} \tag{3.13}$$

where G is the shear modulus of the rubber material, A is the plane area of the rubber pad and h_{total} is the total thickness of the rubber pads.

To be precise this Eq. (3.13) is merely the simplified version of the following Eq. (3.14) derived from the Haringx theory (for details, see [84] [85]) that takes the influence of the vertical load on the horizontal (shear) stiffness into consideration.

$$K_h = \frac{F_z^2}{2E_{\theta b} I \frac{H_b}{h_{total}} q \cdot \tan\left(\frac{qH_b}{2}\right) - F_z H_b} \tag{3.14}$$

And q is the function expressed as

$$q = \sqrt{\frac{F_z \cdot h_{total}}{E_{\theta b} \cdot I \cdot H_b}\left(1 + \frac{F_z \cdot h_{total}}{G \cdot A \cdot H_b}\right)}. \tag{3.15}$$

where F_z is the vertical force, H_b is the total height of the elastomeric bearing, I is the second moment of inertia and $E_{\theta b}$ is the bending stiffness that is explained later in this Chapter.

Equation (3.13) is obtained by considering only the shear stiffness of rubber layers, which is equivalent to letting the compression force approach to zero in Eq. (3.14). The degree of change in the horizontal stiffness due to the vertical pressure is small for the bearing with a high shape factor S_1 (first) and S_2 (second) so that this effect is nearly negligible. S_1 and S_2 are defined as

$$S_1 = \frac{\text{Loaded surface area}}{\text{Free surface area}}, \quad S_2 = \frac{\text{Diameter (or edge length)}}{\text{Total thickness of rubber}}. \tag{3.16}$$

In case of the round type elastomeric bearing, those shape factors are expressed with the diameter D as $S_1=D/4h_i$ and $S_2=D/h_{total}$. The elastomeric isolator used for buildings have often very thin layers of rubber and a large planar dimension to support the heavy weight of the structure, which means S_1 and S_2 are generally high. The elastomeric isolator bearings for bridge construction have smaller S_1 and S_2 but they are normally subject to a lighter dead load. This fact leads to the conclusion that the influence of the vertical pressure variation is smaller. Therefore the simplified evaluation formula (3.13) is adequate for both cases. The obtained stiffness value from this simple linear equation sufficiently represents the realistic behaviour of rubber bearings and the same equation is adopted for most design standards, see for instances [10] [12]. The flexibility against shear deformation depends on the total thickness of all rubber layers and the steel shims have little influence on it. One of the tests (shear deformation ±119mm which is equivalent to 83 % shear strain) of the isolator elastomeric bearing that was performed in the testing laboratory of the Institute of Structural Engineering at the University of the German Armed Forces in Munich (Universität der Bundeswehr München) is shown in Fig. 30 with the linear stress-strain line obtained from the evaluation formula given in (3.13). The tested elastomeric isolator bearing was to be installed for Highway, Utility and Trestle bridge structures at Khalifa Port, Abu Dhabi. The bearing was designed and manufactured by Maurer AG in accordance with the bridge construction specifications AASHTO LRFD. The shear stiffness is well evaluated by the formula except the maximum strain range where the hardening characteristics of elastomeric material appear.
The maximum shear strain during earthquake $\varepsilon_{s,ea}$ defined in [10] [12] and [15] is 250 %. According to [12], numerous test results indicated that the stress-strain behaviour of elastomeric bearings was stable up to 270 or 300 % and hence the maximum design value was set well below that. Assumingly other design codes reached a similar conclusion after a number of shear loading tests.

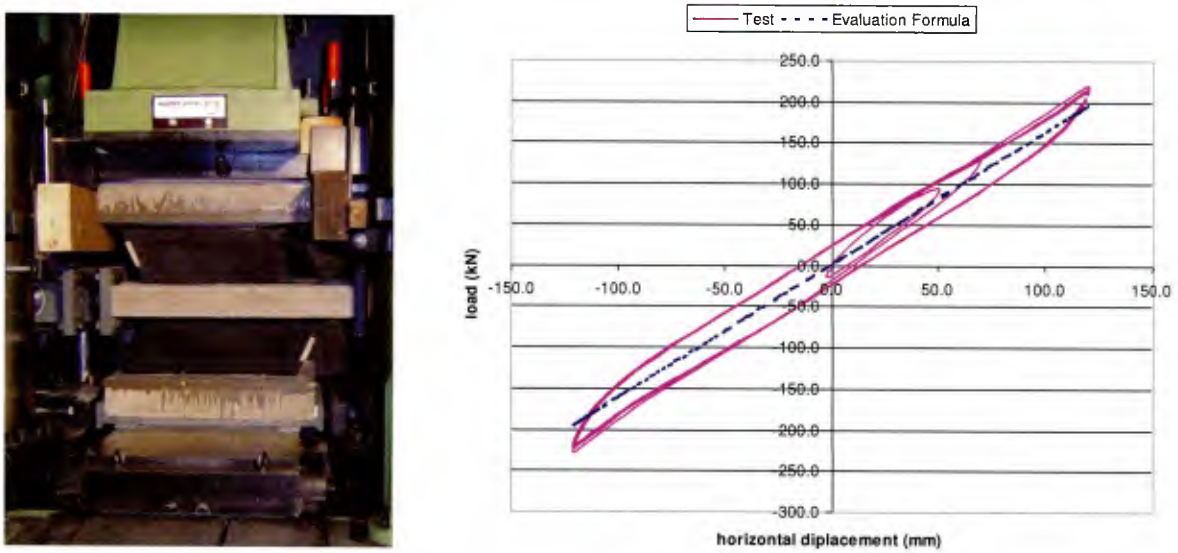

Figure 30: Tested laminated elastomeric bearing and their hysteresis curve [4]

The damping property in the horizontal direction is also another important parameter. Natural rubber-based bearings hardly possess this property (often less than 5 % of damping to the critical). Thus additional dampers are required if natural rubber bearings are applied for the seismic isolation system. High damping rubber bearings and lead rubber bearings dissipate much more energy than natural rubber bearings so that additional dampers may not be required.
The characteristics described here are subject to change by the cyclic loading, especially in the first several cycles. This phenomenon is probably caused by the same mechanism of the Payne effect and the Mullin's effect, namely the scission or reorganization of the molecular chains and the dispersion of carbon black particles. Considering this special property of rubber it is so stipulated in the design codes [9], [12] and [15] that those characteristic values are to be determined after several cyclic loading. In particular, the background of this consideration is described with some test results in the annex of [12]. According to that the effective horizontal stiffness can be considered as a stable after 3rd cycle and the equivalent damping after 10th cycle.

3.2.2 Behaviour under compression loading

The structure of elastomeric bearings, consisting of alternating layers of rubber pads and steel shims, enables the bearing to carry a heavier weight without undergoing an excessive amount of the vertical deformation. The deformation of each thin layer of a rubber pad is constrained by the bondage with steel shims in the both radial and tangential directions. Because of these constraints a high hydrostatic pressure is developed at the centre of the bearing when the bearing is vertically compressed. Rubber is a nearly incompressible material and exhibits a surprisingly strong resistance against volume change. This mechanism allows the laminated elastomeric bearing to have a smaller vertical deformation in comparison with the elastomeric bearing without steel shims even if the total thickness of rubber is same. For the calculation of the vertical stiffness, this constraint is taken into consideration with the first shape factor S_1. The compression stiffness of the elastomeric bearing is calculated by the following expression

$$K_v = \frac{E_{cb} \cdot A}{h_{total}} \tag{3.17}$$

where E_{cb} is the compression modulus of the elastomeric bearing taking the compressibility of the rubber into account.

This compression modulus E_{cb} consists of two parts; the apparent compression modulus of the elastomeric bearing E_c and the bulk modulus E_b. When the applied vertical pressure is high or the first shape factor S_1 is high, which is often the case for isolator bearings, the assumption of rubber being completely incompressible leads to an overestimation. Therefore E_{cb} can be calculated by the following expression considering two springs (E_c and E_b) in line.

$$E_{cb} = \left(\frac{1}{E_c} + \frac{1}{E_b} \right)^{-1} \tag{3.18}$$

The apparent compression modulus E_c is specified somewhat differently among international design codes. Evaluation formulae defined in various codes are presented in the followings.

$$\text{EN 15129: } E_c = 3G \cdot (1 + S_1^2) \text{ [9]} \tag{3.19}$$

$$\text{MCEER, Architectural Institute of Japan: } E_c = E_0 \cdot (1 + 2 \cdot \bar{k} \cdot S_1^2) \text{ [15] [86]} \tag{3.20}$$

$$\text{JP Specifications for highway bridges: } E_c = E_{cb} = \alpha_E \cdot \beta_E \cdot S_1 \cdot G \text{ [12]} \tag{3.21}$$

Equation (3.20) is based on the theory of Lindley [87], where k is the correction factor suggested by Lindley that modifies the apparent compression modulus depending upon the hardness (the shear modulus) of the rubber material affected by various compounds. Equation (3.19) seems to have a principally similar structure to (3.20) but rather simplified without the correction factor. Another difference among them is the definition of the relation between the elastic modulus E_0 and the shear modulus G of rubber material. With the Poisson's ratio υ, this relation is generally described as

$$E_0 = 2(1 + \upsilon)G \tag{3.22}$$

Then assuming the total incompressibility of the rubber material, i.e. υ=0.5, E_0=3G is obtained. However this is only an ideal case and as described before this assumption is not entirely correct for rubber materials. For instances, the reference value of Lindley is not E_0=3G, either [87] and it is mentioned in [15] that E_0=(3.8 to 4.4)G depending upon the hardness of the rubber. As for the bulk modulus, a range of values between 1000 to 3000 MPa is generally accepted [9] [15] [85] [87] [88] although the value might spread over even wider range since other compounds such as filler particles are not as incompressible as rubber material itself and thus the mixing with them would increase its compressibility.

Equation (3.21) is obtained by the regression curves of numerous experimental results [12]. Older version of Japanese specifications for highway bridges adopted another theoretically derived evaluation formula whose validity was limited for the low value of S_1. In earlier time the theoretically derived evaluation formula served its purpose adequately since there were hardly any bearings with a larger shape factor but demands for the larger dimension of bearings had been increased and accordingly the provided evaluation formula became less reliable. Experiments decided to conduct a number of tests in order to determine the evaluation formula for the compressive modulus based on those test results because no existing theoretically derived formulae provided an entirely satisfying corresponding value, especially if the high damping-rubber bearings and the lead-rubber bearings are concerned. Factors α_E and β_E in Eq. (3.21) are determined by the type and the shape of the bearing, respectively. This distinction is only partially possible in other two equations. Those evaluation formulae are compared later in Chapter 5 with the experimental results. Note that these formulae provide a constant compression modulus, although the

compression test of the bearing exhibits often nonlinearity in force-deformation curve. The hardening phenomenon is due to the characteristics of rubber material as explained in the previous Chapter and it should be also one of the causes for the hardening of the bearing under compression. It is doubtful, however, that this material-based hardening should play the main role here because the strain range in which the hardening starts appearing is normally not that high except the high local stretching strain along the outmost boundary edges between steel shims and rubber pads (read 3.3). Then the hardening of the rubber bearing under compression may be a result of domination swap in the components of the compression modulus. As expression (3.18) indicates, the compression modulus is always controlled by the constant value of the bulk modulus to different degrees. The apparent compression modulus E_c can be regarded as the geometry-based modulus because a change in the first shape factor. Hence the geometry of the bearing, radically alters the modulus E_c, whereas E_b is purely based on the material properties. When the first shape factor of the bearing is high, the deviatoric deformation of rubber is constraint to a great degree. As a result the volumetric deformation is less energy-requiring in relative sense and therefore the value of E_b is dominant. On the other hand, when the first shape factor is low, the dominant component (softer component) is E_c. In this case, however, there is a chance that the dominant modulus is swapped as deformation increased because rubber pads lose its deviatoric deformability. This means that the apparent compression modulus should increase along with the vertical strain, perhaps associated with the varying first shape factor S_1 considering that increase in the compression strain and the plane area due to bulging deformation is nearly equivalent to increasing the first shape factor. Building on this concept, E_{cb} should be a function also depending on the vertical strain with its asymptotic value of E_b. If the component E_c is greater than the bulk modulus E_b, then the E_{cb} is already dominated by the latter and therefore the bearing exhibits less nonlinearity. The necessity of the pressure/strain-dependent apparent compression modulus is also mentioned, for instance in [89] but no design standards offer such formulae. Furthermore the compression test results of the rubber bearing in Chapter 5 cast a doubt concerning the value of E_b since if E_b=2000 MPa is assumed, no evaluation formula among those named above can provide a good approximation. It can be that the bulk modulus of rubber compound depends strongly on its ingredients because other materials are not as incompressible as rubber itself. For better evaluation, those themes should be clarified.
The maximum capacity of the elastomeric bearing against vertical pressure can exceed even 150 MPa [85] depending upon its geometry and material. With the applied high pressure, steel shims at the centre area are first to fail due to a high tensile stress transferred from the hydrostatic pressure in rubber pads. This capacity depends, therefore, on the strength and thickness of steel shims and can be enhanced by increasing them. For designing steel shims the following expression is used. It is one of the criteria that determine the maximum capacity of the bearing.

$$\sigma_s = c_\sigma \sigma_n \frac{h_i}{h_s} \quad [12]\ [85][90] \tag{3.23}$$

σ_s and σ_n are the tensile stress in the steel shim and the nominal compression stress of the bearing, respectively. c_σ is the factor with which different pressure distribution in the rubber pad is taken into account. h_i and h_s are thickness of the single rubber pad and the single steel shim, respectively. The thickness t_s can be determined by setting the inequality $\sigma_s \leq \sigma_{s,y}$, where $\sigma_{s,y}$ is the yielding stress of the steel shim [9] [12]. This expression is derived from the equilibrium of the tensile stress in the steel shim and the hydrostatic pressure p in the rubber pad at the centre assuming $p=c_\sigma \cdot \sigma_n$. The hydrostatic pressure distribution within a rubber pad is nonlinear and varies with the first shape factor S_1. One example of the pressure distribution within an infinite rubber strip (plane strain case) is shown in Fig. 31.

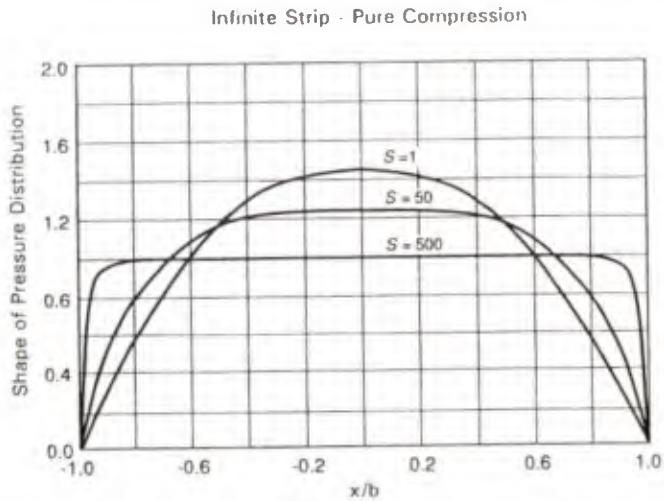

Figure 31: Hydrostatic pressure distribution within an infinite rubber strip [91]

In [9] and [12] the factor c_σ=2.0 for ring type bearings and c_σ=1.0 for other type is used. Furthermore [12] specifies another factor c_σ=3.0 for lead-rubber bearings.
The vertical pressure under the service condition should be limited to much lower than its maximum capacity because the bearing cannot deform flexibly in the horizontal direction under such high pressure. There is another concern regarding the stability of the bearing that is explained later in section 3.5. As for the vertical pressure, the stress range from 5 to 12 MPa under the service condition is commonly accepted [12] [85]. Tada mentioned in [85] up to 20 MPa pressure can possibly be applied if the bearing is designed well since there are test reports which have proved the high deformability of the elastomeric bearing (up to 400 % shear deformation) under 30 MPa pressure.

3.2.3 Behaviour against tilting motion

The rotational stiffness of the elastomeric bearing K_θ was derived by Gent and Meinecke [92] that is expressed as

$$K_\theta = \frac{E_\theta \cdot I}{h_{total}} \tag{3.24}$$

where E_ϑ is the rotational modulus and I is the moment of inertia.

E_θ is calculated by integrating the function of the pressure distribution with the whole plane area of a rubber pad as

$$E_\theta = (1+\frac{2}{3}kS_1^2)E_0 \text{ [92]} \tag{3.25}$$

where k is the same factor used for the compression modulus.

Same as the calculation of the compression modulus, it is suggested that this rotational modulus should be modified to $E_{\theta b}$ by considering the compressibility of the rubber [85] when the high compression is applied or the first shape factor S_1 is high.

EN 15129 provides the calculation method of the rotational stiffness based on the theory described here. Japanese Bridge specifications do not provide a similar calculation method. In MCEER recommended guidelines no definition of the rotational stiffness is found, although in the bridge design specifications [11] a similar expression to the Eq. (3.25) is provided.
This rotational stiffness is, however, likely to underestimate the actual behaviour of the elastomeric bearing since it does not take into consideration the influence of the vertical load. Block [89] studied the rotational stiffness experimentally and compared with the ones obtained by the evaluation formula in EN 1337-3 which is exactly the same as in EN 15129. His test results clearly show the dependence of the rotational stiffness on the vertical pressure and a nonlinear relationship between the tilting angle and the rotational stiffness. He derived expressions for the restoring moment from his experimental results taking those two facts into consideration.

$$M_{E_c} = E_c(\sigma_z) \cdot I \cdot \frac{\theta^{0.76}}{3.67 \cdot \sum_{i=1}^{n} h_i} (-0.037 S_1 + 0.956) \quad \text{if } 5.5 \le S_1 < 9.5 \text{ [89]} \tag{3.26}$$

$$M_{E_c} = E_c(\sigma_z) \cdot I \cdot \frac{\theta^{0.76}}{3.67 \cdot \sum_{i=1}^{n} h_i} (-0.01 S_1 + 0.695) \quad \text{if } 9.5 \le S_1 \le 14.5 \text{ [89]} \tag{3.27}$$

As for the compression modulus, one specific value of E_c obtained at σ_z from his other experiment results was applied here. He mentioned that further research is required to determine the pressure dependent expression for the apparent compression modulus $E_c(\sigma_z)$ in order to grasp the nonlinear restoring moment behaviour of the elastomeric bearing. These formulae are obviously limited for the bearings with the first shape factor within his test range which generally corresponds to the bridge elastomeric bearings.

3.3 Stability Of The Bearing And The Limitation Of The Local Shear Strain

Safety against buckling
The aforementioned maximum capacity of the elastomeric bearings cannot be exerted for two reasons. The first is that the horizontal flexibility is not available under the high pressure and another reason is the stability concern. During the seismic action, the elastomeric bearing has to support the structure with a lesser plane area due to the shear deformation. In its deformed configuration the bearing is, therefore, subject to a higher risk of the buckling. Equation (3.14) derived from the Haringx theory is applicable here again to define this limitation by setting the horizontal stiffness K_h equal to zero and approximating it as

$$F_{z,crit} = \varsigma G \cdot A \cdot S_1 \cdot S_2 \text{ [84] [85]} \tag{3.28}$$

where $\varsigma = \pi \sqrt{\frac{k}{8(1 + 2kS_1^2 G / E_b)}}$.

This determines the theoretical critical compressive force taking no shear deformation of the bearing into consideration. During the seismic action both the effective area resisting the vertical load and the critical force are reduced. Therefore the critical force has to be defined with the effective plane area A', which is equal to the overlapping area of the top and bottom flanges under the design seismic shear deformation, instead of the total plane area A in Eq. (3.28). For the

simplification of the design process ζ is given as a constant factor depending on the types of the bearing in both in EN 15129 and Japanese specifications for highway bridges.

Prevention of a local rupture

The local shear strain at the boundaries of steel flanges and elastomer pads can cause rupture in elastomer, either statically or dynamically due to fatigue. This local shear strain is contributed both the shear deformation resulting from the lateral loading such as traffic, temperature and seismic force and the compressive and tilting deformation. In order to prevent this damage, the sum of all these strain components should be lower than the experimentally determined maximum tensile strain at break γ_{crit} of the elastomer material [91] such that

$$\gamma_{t,s} = \gamma_{c,s} + \gamma_{s,s} + \gamma_{\theta,s} < \gamma_{crit} \tag{3.29}$$

where $\gamma_{t,s}$, $\gamma_{c,s}$, $\gamma_{s,s}$ and $\gamma_{\theta,s}$ are the total shear strain, the shear strain due to compression, the shear strain due to the shear deformation and the shear deformation due to the tilting deformation, respectively. Evaluation formulae defined in the major design standards are expressed as

$$\gamma_{c,s} = \frac{c_c S_1 F}{A' E_{cb}} \text{ [12][10]} \tag{3.30}$$

$$\gamma_{\theta,s} = c_\theta S_1^2 \theta \text{ [12][10].} \tag{3.31}$$

Apparently $\gamma_{s,s}$ can be calculated by the use of the shear stiffness defined by Eq. (3.13). Both expressions (3.30) and (3.31) are based on the design principles for elastomeric bridge bearings summarized by Rejcha [90]. The factors c_c and c_θ are determined by the shape and the ratio of the planar dimension by applying Fourier's series calculation to the pressure distribution.

A rubber pad glued between two steel plates under compression is illustrated in Fig. 32 to show schematically the relation between the local shear strain and the tensile strain.

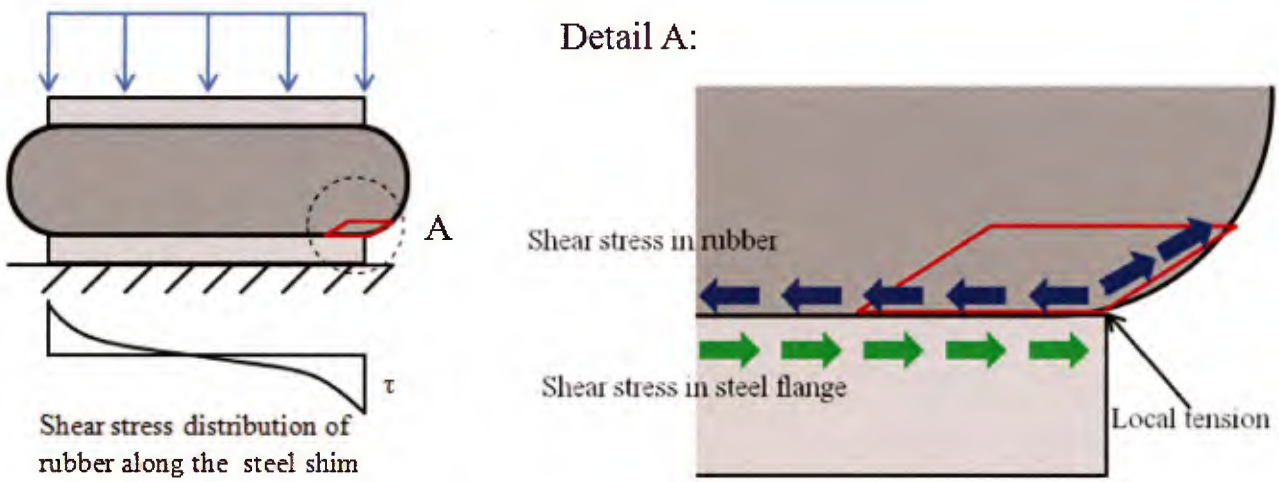

Figure 32: A high local tension due to the shear deformation caused by compression [94]

The tensile strain at break varies among the rubber materials. The harder the material is, the smaller this strain becomes. That difference stems presumably from the rubber-carbon black particles interaction described in the Section 3.1.4. Japanese bearing specifications for highway bridges specifies γ_{crit} according to rubber material where this strain value is divided by the safety factor of

1.5 for the design purpose. This safety factor is determined based on numerous cyclic tests of elastomeric bearings, see annex of [12]. On the other hand, MCEER recommended LRFD guidelines for the seismic design of highway bridges and EN 15129 set the only one constant value '5' and '7' for any rubber material as γ_{crit}, respectively. This definition seems rather radical since the extension strain at break for chloroprene-basis rubber is smaller than that of natural rubber. Observing the test results provided in the annex of [12], the allowable strain value defined in both standards can be still sufficiently safe under static loading. However, in the long run under dynamic effect, a fatigue crack might develop. Neither EN 15129 nor Japanese bearing specifications distinguish the strain along the inner circle and the outer circle of the ring type of rubber bearings. Large elastomeric bearings have often a hole at the centre (that type of bearings is generally referred to as the ring type bearing) in order to improve the heat distribution during the vulcanisation process by applying heat not only from periphery but also from the centre. A proper heat distribution has to be applied to ensure the bond strength between rubber pads and steel shims. This hole reduces the stiffness in both vertical and horizontal directions. What is often characterized as a disadvantage of this hole is the deterioration of the compression capacity of the bearing because the tensile stress in the tangential direction of the steel shims along the hole (inner edge) is increased. In fact rubber along inner edge undergoes a change in its stress state as well. A ring type bearing under compression is shown in Fig. 33.

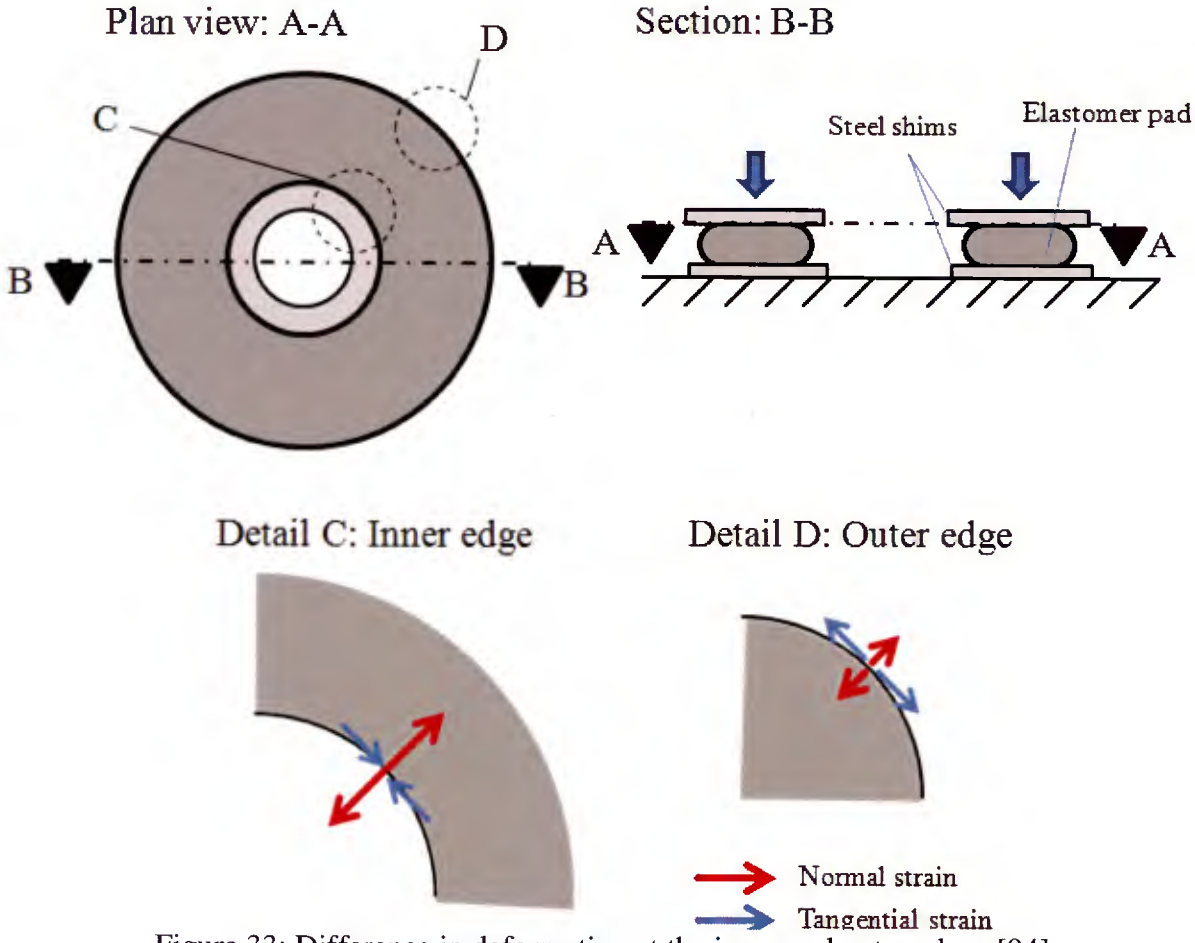

Figure 33: Difference in deformation at the inner and outer edges [94]

With detail C and D in this figure the difference in the strain conditions between the inner circle and the outer circle is described. In the vertical direction a constant strain distribution can be assumed all over the plane area but in other two directions this is not the case. Normally when rubber is

compressed in one direction, it then has to elongate in other two directions in order to keep its volume unchanged due to the nearly incompressibility. Along the outer edge of the ring type bearing in both the tangential and the radial (normal) directions the rubber can stretch almost constraint-free, whereas along the inner edge it cannot stretch or rather it is compressed in the tangential direction due to the geometrical constraint. As a result the stretch in the radial direction has to be increased to maintain the volume. Constantinou et al. [93] theoretically derived the strain along the inner circle. They compared the maximum strains of both circular rubber pads with and without a central hole whose outer diameter and thickness are the same and such compression is applied that the vertical compressive strain of the both pads is identical. The strain along the inner edge of the pad with a central hole is always higher to the magnification factor f than the shear strain along the outer edge of the pad without a hole. This factor varies depending on the first shape factor, the proportion of the outer and inner diameters or the proportion of the bulk to shear modulus. It can reach even 2.2 among their test range.

4 CAVITATION-INDUCED SOFTENING AND ITS INFLUENCE

4.1 Cavitation Process

A flat rubber disc which is constrained on the both plane surfaces (for instance glued between two steel plates) exhibits quite a different behaviour in tension than the dumbbell-shaped rubber sample which is commonly used to identify the stress-strain curve of rubber material, see Fig. 34.

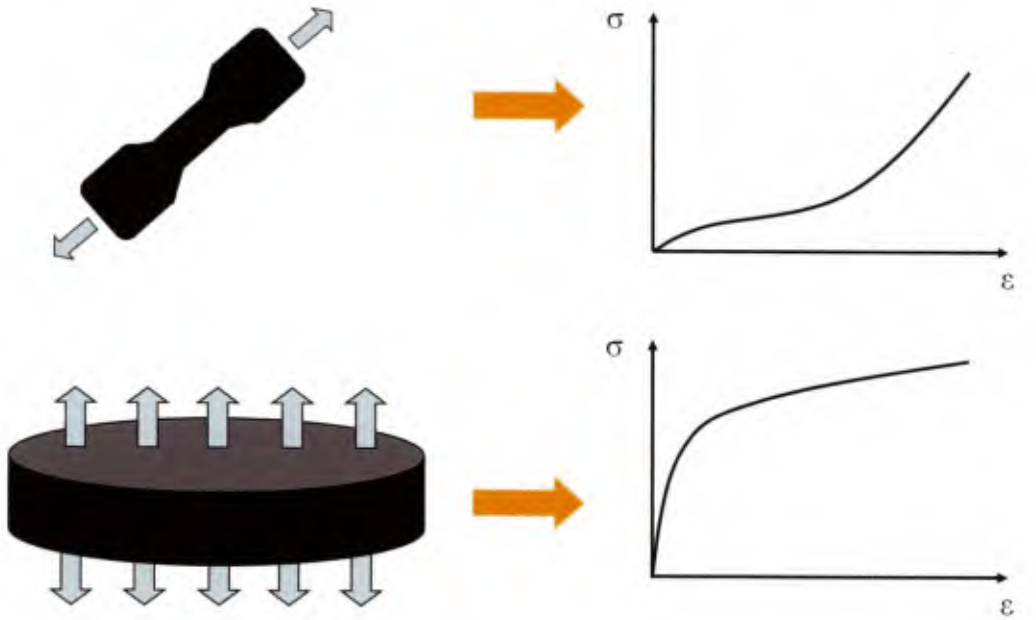

Figure 34: Typical stress-strain curves of a dumbbell-shaped rubber and flat disc-like rubber

This disc-like rubber represents the tensile behaviour of elastomeric bearings. As is indicated in this figure, relatively high tensile force is required to stretch such a rubber disc due to the constraint on the deformation of both surfaces but after reaching a certain stress the tensile stiffness gets significantly reduced. This softening occurs as a result of the internal damage which is often referred to as "cavities" or "voids" which develop through the expansion of the initially existing macroscopic holes such as air bubbles or dust trapped during manufacturing under a certain three axial tensile stress condition. For clarity in this thesis the term 'cavities' refers to this internal damage and the term 'voids' refers to the initially existing microscopic holes. This phenomenon has been well known and a number of theoretical and experimental studies can be found. For instance Pond [95] conducted a series of cyclic tensile loading tests using bonded rubber discs and observed the softening behaviour or rubber discs. Three kinds of compound are prepared for his test, which are all natural rubber base and either with or without carbon black filler. If filled with carbon black, the amount of filler is 20 or 80 p.p.h.r.. One of the stress-strain curves from the test of the unfilled natural rubber and the filled natural rubber with 20 p.p.h.r. carbon black are shown in Fig. 35. Noises in the curve start approximately at 0.9 MPa on the left and at 1.5 MPa on the right in Fig. 35 indicate at which loading level cavitation took place. Those discs are of the same dimension with the first shape factor S_1=2.5 and it infers that the resistance against cavity nucleation is enhanced by the carbon black. Furthermore another test disc made out of the rubber vulcanisate with 20 p.p.h.r. carbon black whose first shape factor S_1=5 (the same diameter and thinner disc) was also tested and again a higher force was required to initiate cavities. The reason of this difference should have something to do with the negative pressure distribution within the rubber disc. With a higher first

shape factor the pressure tends to distribute more uniformly over the plane so that the peak pressure value at the centre area is lowered and hence the cavity nucleation was delayed.

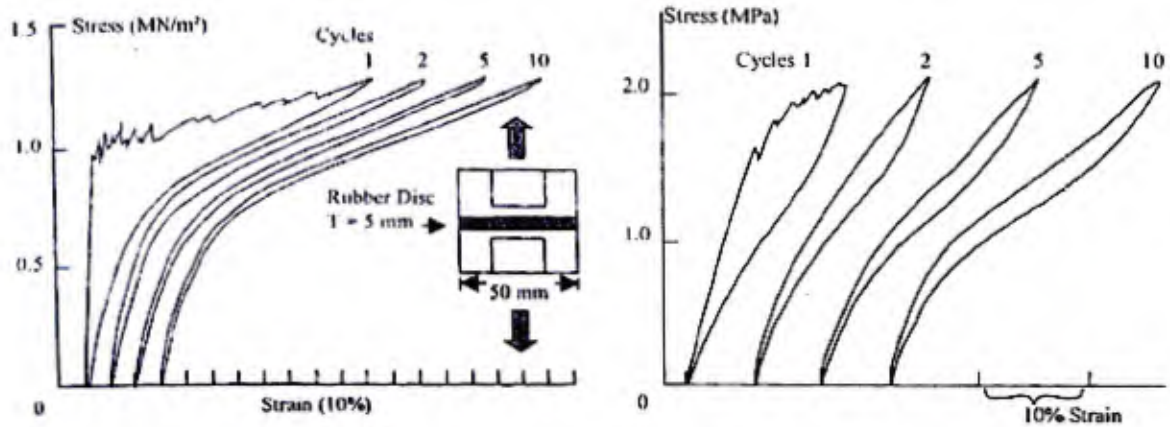

Figure 35: Unfilled rubber vulcanisate (left) and filled rubber vulcanisate (right) repeatedly pulled in tension to 1.25 MPa and test setup [95]

With the same compounds (filled with 20 p.p.h.r carbon black) Pond conducted another experiment, in which the maximum load was increased 0.025 MPa at each cycle and the 28 cycles starting from 1.4 MPa (just below the initial cavitation stress for the same compounds). In this case surprisingly no noise in the stress-strain curve was observed. Pond concluded that cyclic tension to less than the critical force may allow molecular chain entanglements to move or slip and crosslink to break and recombine. This rearrangement of molecular chains results in reducing the local stress concentration in a progressive manner within the heterogeneous rubber network tending to from a more homogeneously stressed structure thus reducing the risk of cavitations [95], see Fig. 36.

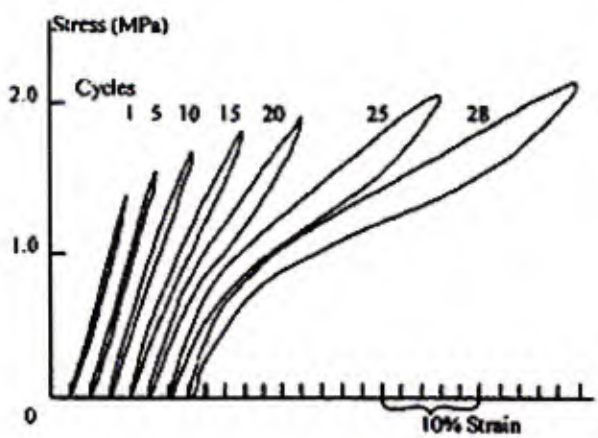

Figure 36: Reinforced rubber disk pulled in tension with increase in maximum stress per cycle [95]

Gent and Lindley [96] initiated the theoretical and experimental study of the cavitation process in rubber. In their experiment, several rubber cylinders whose diameter of 20 mm with various thickness were subjected to the same amount of tensile force. Different patterns of cavity formation were observed which seemed to be related to the thickness (therefore the first shape factor S_1) of the rubber cylinder. The cut surfaces of their test specimens are presented in Fig. 37. It is apparent that the thinner rubber cylinder has more cavities spreading all over the surface and their size is smaller, whereas the thicker cylinder has smaller amount of larger cavities concentrated near the centre.

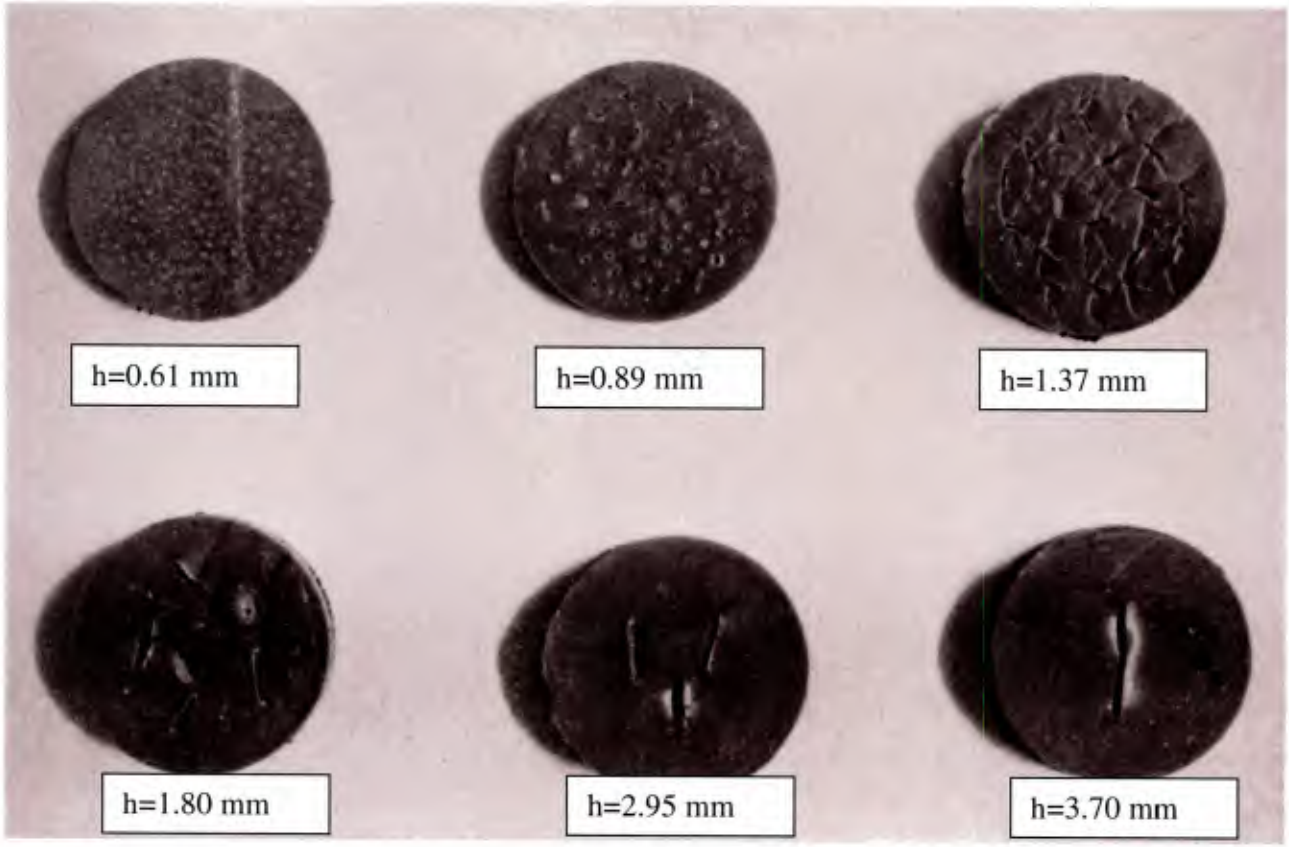

Figure 37: Cutting surfaces of rubber discs after the tension tests from [96]

From this observation Gent and Lindley assumed that the cavitation is induced by the negative hydrostatic pressure since the pressure distribution varies along with the ratio between the radius and the thickness of the rubber cylinder. For the relatively thick rubber cylinder, or lower first shape factor S_1, the pressure distribution is highly nonlinear and the peak value appears at the centre of the cylinder because rubber is constrained in all directions there. This is schematically depicted in figure 38.

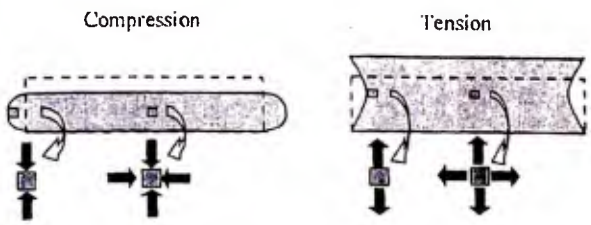

Figure 38: Deformed shapes of single rubber layer [97]

Gent and Lindley's test results indicated that there is a linear relation between the minimum nominal tensile stress applied to the rubber vulcanisate cylinder required to induce cavitation and the elastic modulus E. Based on the mathematical model described in [88] and [96], the maximum pressure value p_m at the middle of rubber cylinder can be expressed as a function of the nominal stress σ_n

$$\sigma_n = \frac{1}{2} p_m (1 + 2h^2 / R_r^2) \tag{4.1}$$

where h and R_r are the thickness and the radius of the rubber cylinder, respectively.

This equation indicates that the pressure value at the centre has its maximum value $2\sigma_n$ with the moderate thickness h. However as thickness decreases proportionally to the radius R_r, i.e. cylinder with a high first shape factor, the deformation becomes increasingly bulk dilatation dominant. In that case the pressure distribution is almost uniform throughout the cylinder and the pressure value is nearly equivalent to the nominal stress.
Gent and Lindley derived the pressure value at the circumference of an arbitrary cavity in a spherical Neo-Hookean body. In this case the strain energy density function W is expressed as

$$W = C_1 (I_1 - 3) \tag{4.2}$$

where C_1 is the material constant that is equal to 1/2 G or 1/6 E assuming the total incompressibility of rubber and I_1 is the first strain invariant.

If the considered spherical shell is infinitely thick and the void surface is force-free, the relation between the extension ration λ of the circumference of the void and the negative pressure at infinity is expressed as

$$p_m = C_1 \left(5 - \frac{4}{\lambda} - \frac{1}{\lambda^4} \right) [96]. \tag{4.3}$$

As λ increases, the pressure value gets closer to the asymptotic value of $5C_1$ which is equivalent to 5E/6 or 5G/2 assuming the total incompressibility of rubber. These both experimentally and theoretically derived critical pressures were found to be in fair agreement. This pressure value is, therefore, often assumed as the critical pressure to expand existing microscopic voids to visible cavities [85] [97]. However this is not always the case because the initial size of voids is not considered in this study. Gent and Tompkins [98] applied internal gas to the existed submicroscopic voids within rubber rather than a tensile stress to the rubber at infinity. These conditions are assumed to be equivalent due to the incompressibility of the rubber material. The minimum pressure values to expand the relatively large existing microscopic voids indeed correspond to the amount of 5E/6 but other smaller voids which were not expanded by even a higher pressure. Their conclusion was that the critical pressure 5E/6 is only a good approximation if the radius of the initially existing voids is larger than 5×10^{-4} mm. Other research such as [99] and [100] reached the same conclusion. In practice, however, the elastomer has always microscopic voids with a wide range of sizes and thus the aforementioned negative hydrostatic pressure value 5E/6 or 5G/2 can be assumed as the critical value of cavitation.
In the series of experiments of Notomi and others [101] the size influence is concerned, where he prepared rubber disks with a constant diameter D=40.56 mm and five different thickness values, 1, 3, 5, 7 and 10 mm, corresponding to the first shape factor of 10.14, 3.38, 2.21, 1.45 and 1.01, respectively. The same tendency as the experiment of Pond was observed. The higher the first shape factor is, the higher the tension force required to induce cavitation is, see Fig. 39.

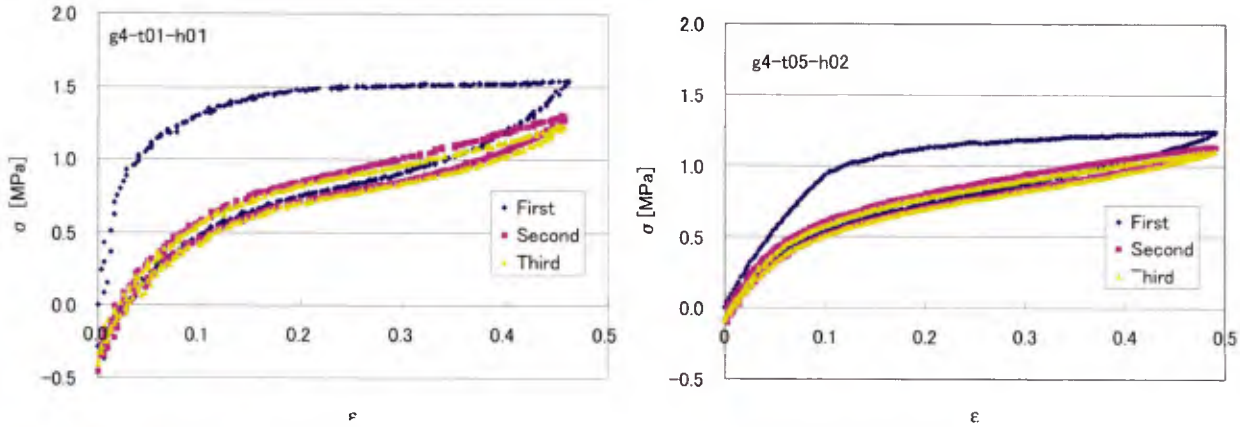

a) h=1 mm (S_1=10.14) b) h=5 mm (S_1=2.21)

Figure 39: Stress-strain curves of the rubber discs with different first shape factors [101]

Notomi et al. also carried out numerical analysis with the Mooney-Rivlin material model and compared both the test and FE results. They first obtained the necessary characteristic constants for the material model by curve-fitting and then confirmed that their numerical result and the test result were in good agreement. Then they built all FE models corresponding to all test specimens and compared those experimental and numerical results. Since their numerical simulation did not take into account the softening caused by cavities, load-displacement curves started to bifurcate at the point where cavities begin to develop. They took the pressure value p_m at this loading step as the critical negative pressure. As for the location the centre of the disc was selected because all cavities were observed only in a certain range from the centre. They concluded the critical negative pressure values are almost constantly independent of the thickness, see table 18.

Table 18: Thickness of rubber disk, displacement and critical negative pressure at onset of cavitation (recreated from [101])

Thickness h [mm]	Displacement u [mm]	Negative Pressure p_m [MPa]
1	0.04	1.33
3	0.14	1.36
5	0.48	1.68
7	1.04	1.59
10	-	No cavities up to 50 % strain

Note that cavities were not found in the test specimen of thickness 10 mm after the tension test, although the pressure at the centre could have been sufficient for cavitation to take place. They only provided the material constants for the Mooney-Rivlin body for their FE-model, which are obtained by the curve-fitting. From those values the shear modulus of the considered rubber here is estimated as 0.74 MPa and then the critical negative pressure becomes approximately 1.8 MPa. This is a little higher than those pressure values obtained by the FE calculation, but the first question is to conclude whether, it is possible to pick up the ambiguous threshold point of cavitation with this method accurately.

Their additional findings were that the thinner the thickness of the rubber disk is, the smaller the size of the cavities become and the more the number of cavities increases, which is consistent with the results of Gent and Lindley [96]

The number of studies regarding the elastomeric bearings in tension is limited yet nevertheless they can be found, in particular, among Japanese academic institutes and industries. For instance the series of experiments of the natural rubber bearing were performed by Shoji and the others [102].

Numerical and experimental analysis of the load-carrying behaviour of laminated elastomeric bearings as seismic isolators

One of the experiments was a simple tension test and the result is shown in Fig. 40. The bearing consists of three layers of rubber pads (h_i=8 mm) and two steel shims in between, and its planar dimension is 240×240 mm, with which the first shape factor amounts to 7.5. The shear modulus of the natural rubber is G=1.2 MPa.

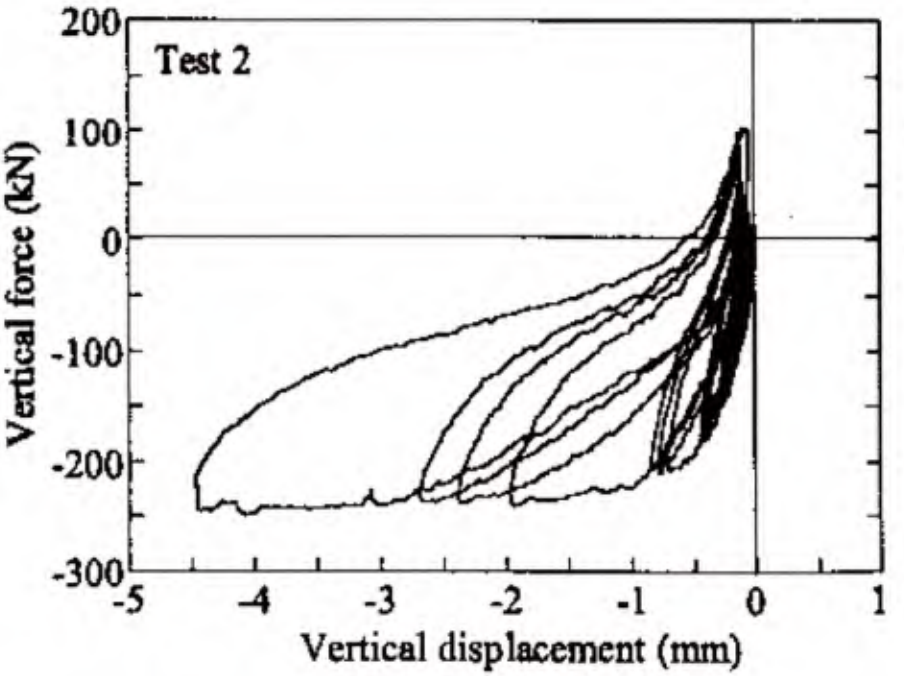

Figure 40: Stress-strain curves of the natural rubber bearing [102]

At tension force approximately of 200 kN a clear reduction in the stiffness is observed, which is nearly 3.5 MPa nominal stress. It can be assumed that this value is almost equivalent to the pressure value for the first shape factor of the tested bearing is sufficiently high. Theoretical critical pressure value is 5G/2=3 MPa. It seems that the estimation through this expression is acceptable.

For the simple tension tests the articles [103] and [104] can be referred to. Uryu and others investigated the influence of the number of rubber pad layers in their research [104] in which the simple tension test was performed for both one rubber pad and a bearing consisting of 26 layers of the same rubber pad. From the stress-strain curves of the bearings a more apparent softening is observed since the total stiffness of the bearing is lower than that of the single pad. The out-of-plane bending deformation of the flange plates were taken into consideration in the research work of Nishio and others [103]. They concluded that this bending deformation of flanges can reduce the pressure of rubber pads at centre depending on the size of the bearing and the flange. Considering their result, the flange plates should be modelled as well for the FE analysis of the tested bearing, if the flange plates are relatively thin and expected to be bent.

As described in Chapter 2, there are several possibilities that can cause the tensile force in elastomeric bearings during earthquakes. Among them the concern is often the case of proportionally tall and slim base-isolated structures where the unavoidable structural rocking mode causes the tension force in addition to the shear deformation, see Fig. 41.

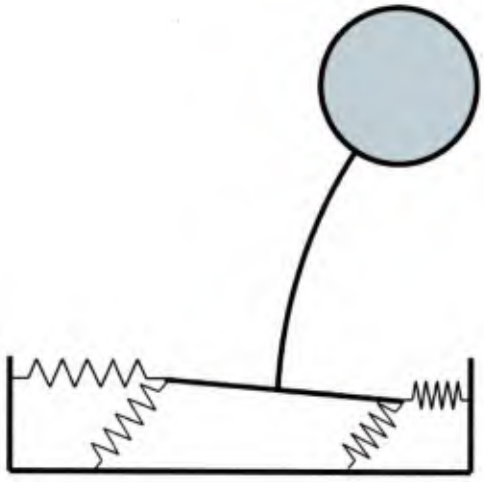

Figure 41: One possible scenario of the occurrence of tension in elastomeric bearings

Therefore if the more realistic situation during earthquakes is sought for, the shear deformation should be integrated with the axial tension. Kelly [105] and Takhirov [106] studied the possibility of the tension buckling of the elastomeric bearing theoretically and numerically. While they were deriving the critical buckling tension, they discovered that the simultaneous occurrence of tension and shear can even reduce the danger of cavitation in rubber. According to their theory the elastomeric bearing rotates with respect to the horizontal axis when the shear and tensile forces are applied at the same time and this rotation converts the uniaxial elongation into the shear deformation. As a result the hydrostatic stress condition is disturbed, which in turn reduces the risk of cavitation. Experiments concerning such a situation can be found, for instance, in [107] ~ [110] and [111], and Kelly's concept can be visually confirmed by the picture shown in Fig. 43.

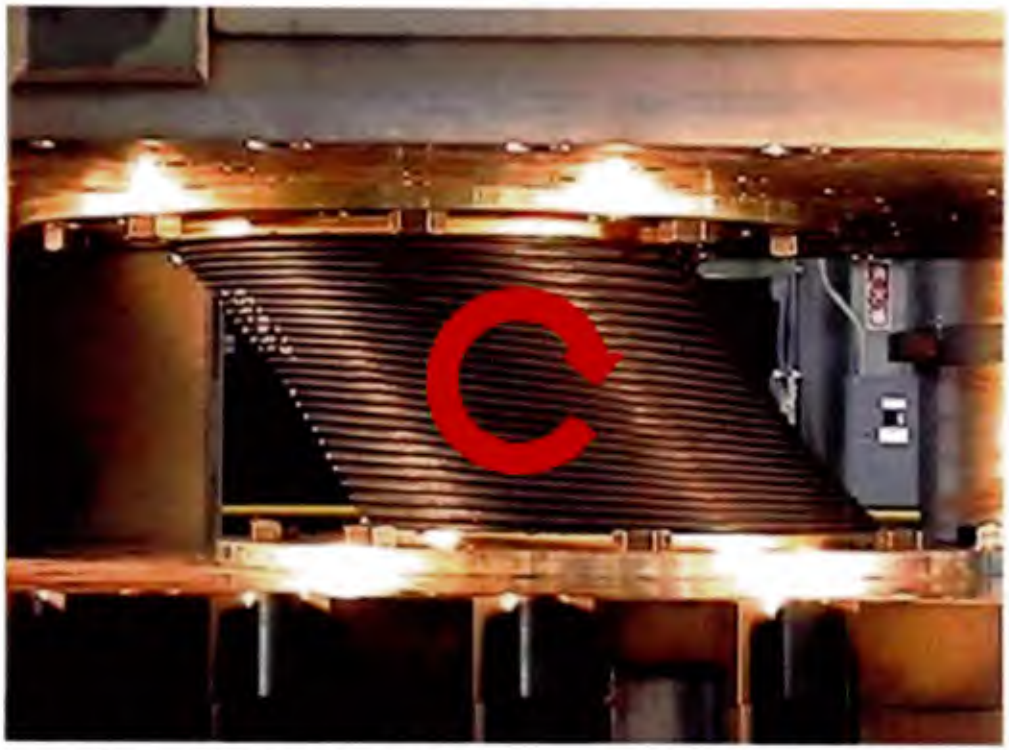

Figure 42: Offset tensile test of the natural rubber bearing [109]

However as for the statement "reducing the risk of cavitation due to the simultaneous shear deformation" [106], one cannot be certain. The stress-strain curves of the same elastomeric bearing under various shear strains from [109] are shown in Fig. 43. This result reveals the fact that cavitation starts earlier stage of tensile loading as the applied shear strain increases, although the degree of softening decreases as the shear strain increases. The similar tendency can be observed in other test results [107] [110].

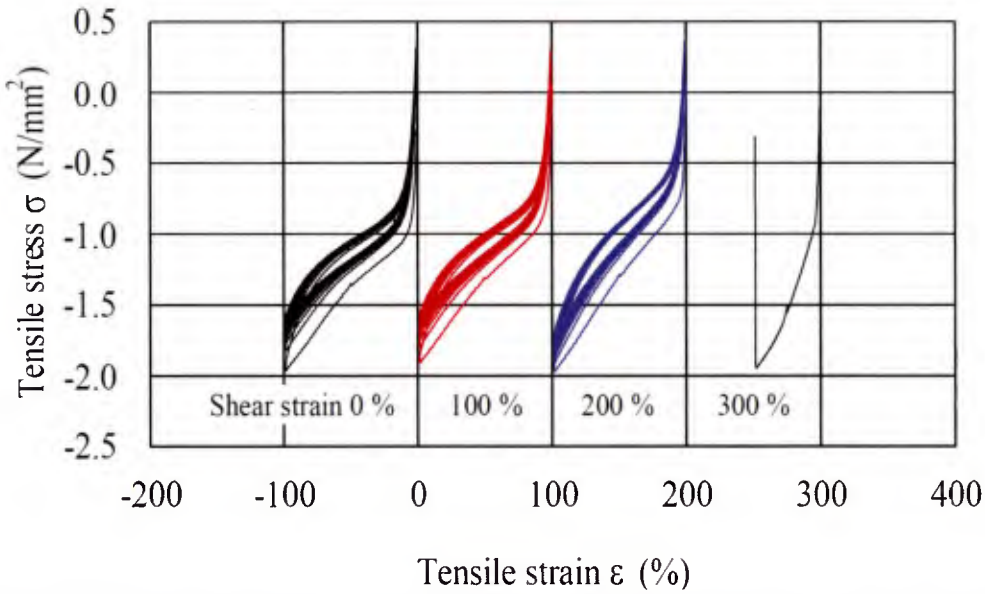

Figure 43: Stress-strain curves of the natural rubber bearing under various shear strain [109]

Bayraktar et al. [112] conducted a series of interesting experiments regarding the cavitation phenomenon in natural rubber and synthetic rubber. In these experiments, rubber cylinders were subject to torsion as well as unilateral tension. Smooth and notched specimens were prepared so that the influence of different first shape factor on cavitation could be observed. The radius R_r and thickness h of the all tested rubber discs were 50 and 5 mm, respectively with various notches, see Fig. 44. This combination of torsional and tensile deformations may not be common for the application of the seismic isolator bearings, but the theory of Kelly can be observed from a different point of view with those tests. The results of these tests are given in Figs. 45 (simple tension test) and 46 (tension with torsion of 20° tests). The notch reduces the effective area of the rubber disc at the notch level and the stress in the loading direction increases as the notch expands. Furthermore, expanding the notch is almost equivalent to increasing the height of the rubber disc (or decreasing the first shape factor) because the area constrained by the upper and lower flange plates is also reduced. The proportion between the maximum negative pressure at the centre of the disc and the nominal stress increases as the first shape factor decreases. These two facts can be understood as the reasons why the cavities develop earlier for the rubber disc with a larger notch. The ways of cavity development are comparable to those observed in the research work of Gent and Lindley [96], i.e. many small cavities are present when the first shape factor is large and a few large cavities at the centre when the factor is small. Decrease in the first shape factor influences on the tensile stiffness because over the surface the deviatoric part of deformation increases whereas the volumetric part decreases. Rubber is flexible against the former therefore the rubber disc can deform more when it has a lower shape factor. More importantly, the tensile stress to initiate cavitation is slightly higher for both rubber discs without notch and the degree of softening is lower when the torsional deformation is present, see Fig. 47.

Figure 44: Cutting section of a test sample with the notch length of 3 mm [112]

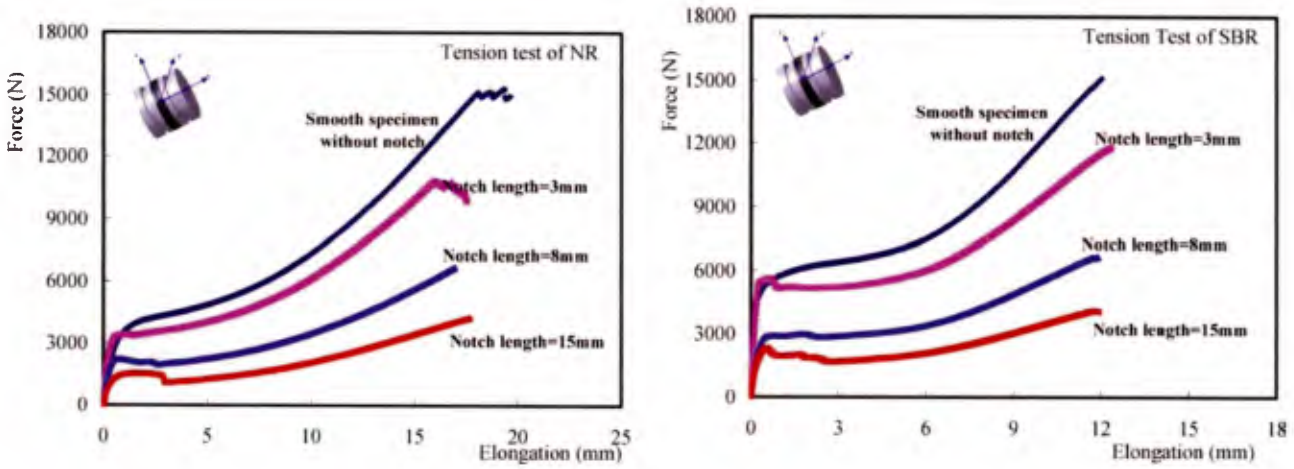

Figure 45: Tension test results of the cylinder specimens of NR and SBR [112]

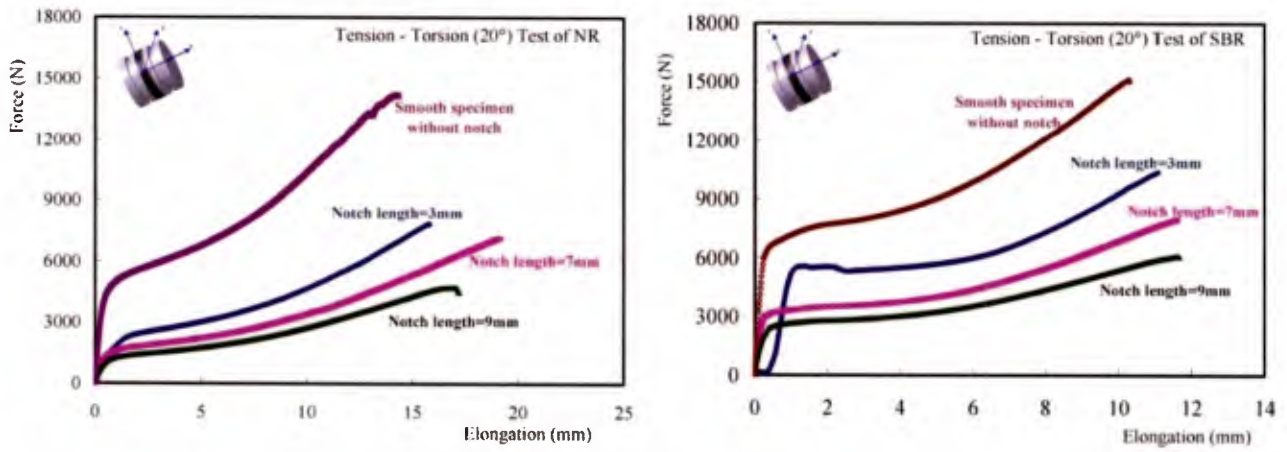

Figure 46: Tension-Torsion (20°) test results of the cylinder specimens of NR and SBR [112]

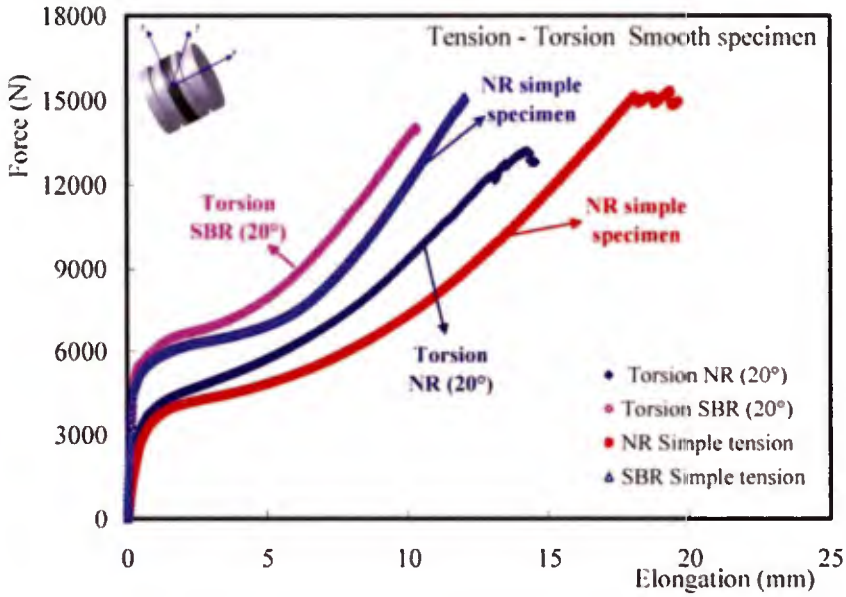

Figure 47: Comparison between results of the simple tension tests and the tension-torsion tests [112]

From Figs. 43 and 47 it can be assumed that the existence of shear stress lessens the cavitation effect. The reason for this is explained by the theory of Hou and Abeyrantne [114] [115]. They mathematically derived the so-called "cavitation instability surface" by representing the deformation field of the incompressible spherical Neo-Hookean body through the radius of the body and the three parameters that represent the size and the aspect ratio of a spherical cavity within the body. Then the principle of virtual work is applied for that body so that the relationship between the critical stresses and the form of cavity is obtained. This cavitation instability surface is an equality defined by the balance of three principal stresses, which is expressed as

$$(4\sigma_1-\sigma_2-\sigma_3)(4\sigma_2-\sigma_3-\sigma_1)(4\sigma_3-\sigma_1-\sigma_2)-125G^3=0 \text{ [114].} \quad (4.4)$$

where σ_i are the principal stresses

This equation defines the surface in the space based on the three axes that are $\sigma_1-\sigma_2$, $\sigma_1-\sigma_3$ and $\sigma_m=(\sigma_1+\sigma_2+\sigma_3)/3$, i.e. the difference between principal stress components and the volumetric stress component, respectively. Cavitation takes place if the left side of the equation is greater than zero. The critical pressure value converges into the minimum value of 5G/2 as all principal stresses become equal. In other words, in the hydrostatic condition the required pressure to induce cavitation is minimum and if the shear stresses disturbs this condition, cavitation can still take place but with higher pressure values. The cavitation instability surface normalized by the shear modulus G from Eq. (4.4) is shown in Fig. 48.

This theory can be optically explained using the model of the molecular chain network such as Fig. 29. In the centre region of a rubber disc, almost hydrostatic tensile pressure is built during by the uniaxial tension, which is equivalent to the attempt to expand the molecular network lattice in the all directions with the same force. In this way the molecular chain lattice cannot deform flexibly and will break when the force reaches the limited amount. Towards the edge the constraints of the molecular chain movement in the perpendicular direction to the loading become looser and thus the lattice can deform easier with lesser risk of breaking the molecular chains.

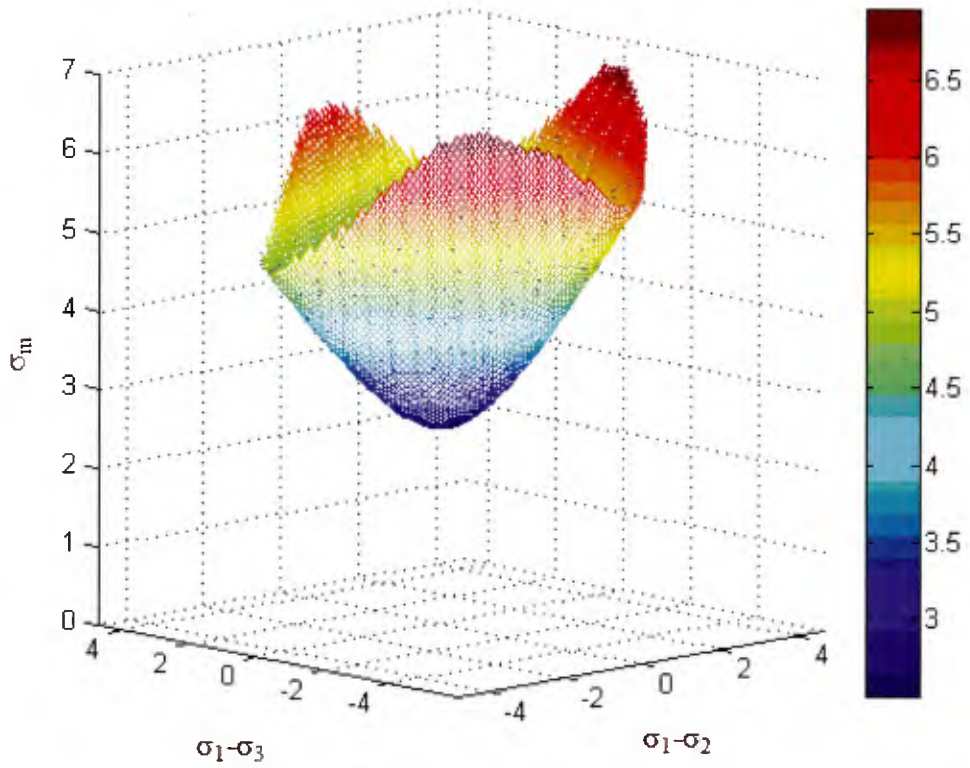

Figure 48: Cavitation instability surface

The cavitation instability curve was studied further by Chang et al. [116] and Ganghoffer and Schultz [117]. The former made an attempt to verify the validity of the cavitation instability surface by FE analysis with Neo-Hookean model. To simplify the model, an axisymmetric condition is assumed. The result aligns well when compressive stresses in two directions are applied, yet differs from the one theoretically obtained by Hou and Abeyrantne when all three principal stresses are tension under anisotropic condition. The cause of this discrepancy was not explained in the same paper.

Ganghoffer and Schultz investigated the behaviour of spherical shells subject to a combined far-field pressure and uniaxial tension. They derived the additional bifurcation instability curve and they concluded that the discrepancy shown by Chang can be explained by this extra curve. Fond [118] compared in his article those different cavitation instability surfaces under an axisymmetric condition. This comparison is shown in Fig. 49 for convenience, where σ_h is equivalent to σ_m. The cavitation instability surface of Hou and Abeyaratne is implemented in the finite element analysis in Chapter 6. There are a few concerns regarding the validity of this cavitation criterion since it is derived from the totally incompressible Neo-Hookean body. The assumption of total incompressibility can lead to an overestimation in analysis of rubber in some cases, and hence rubber is commonly treated as slightly compressible material. If this is the case the criterion is not known but the fact that minimum critical (hydrostatic) pressure corresponds to the experimentally obtained value is quite convincing. Besides such a high accuracy would not be necessary unless the body to be simulated is a part of the exquisite device. Another concern is if material models other than Neo-Hookena material model are applicable. In Chapter 6 several well-known hyper-elastic material models are introduced. They can be all reduced to the Neo-Hookean material model by neglecting higher order terms in the energy strain function defined in each model or rather the other material models were developed for the better representation of the hyper-elastic behaviour in a higher strain range. Cavitation takes place in a relatively low strain range where all material model including the Neo-Hookean model possess an almost identical load-carrying behaviour. Thus it can

be assumed that the cavitation instability surface is valid for the other material models. In reference [119], the slightly compressible Arruda-Boyce material model is compared with the incompressible Neo-Hookean material model for the critical hydrostatic pressure of the spherical body with a cavity by means of the FE analysis. Thus it can be concluded that both material models behave similarly if the locking stretch (see Chapter 6) is large enough.

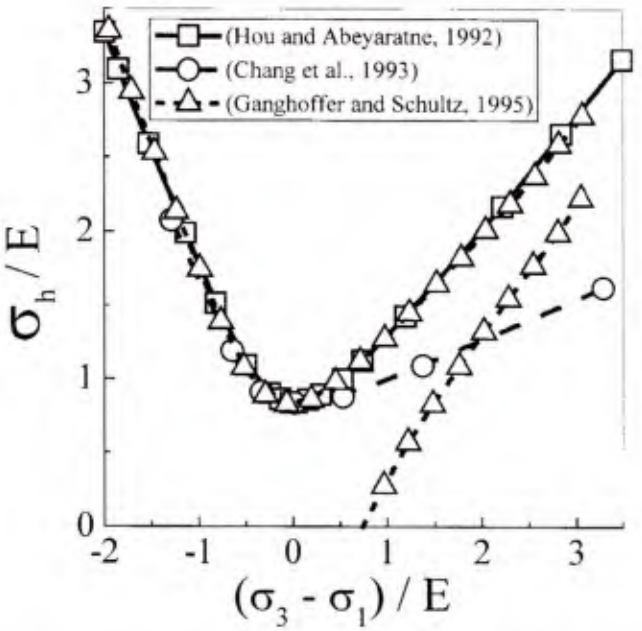

Figure 49: Comparison of various cavitation instability surfaces [118]

The last concern is that the cavitation instability surface is proportional to the shear modulus of the material but if the filled rubber is considered, this relationship seems illogical in the first sight. As already explained in Chapter 3 the increase in the shear modulus of rubber due to carbon black or any other filler particles can be explained by the locally augmented strains/stresses. Then due to locally high strains/stresses the cavitation should be induced at earlier loading stage than unfilled rubber. However, this is not the case, and a number of test results can confirm that higher pressure is indeed required to initiate cavitation as the shear modulus of rubber is increased by adding filler particles. The reason for this discrepancy could be: 1) filler particles are more compressible than rubber and therefore the pressure of rubber is somewhat absorbed by their deformation, or 2) hydrostatic pressure condition is not built due to the existence of other filler particles. Then higher stresses are required to develop cavities.

4.2 Influence Of Cavities On Rubber Properties

As described in the previous section, the tensile stiffness is reduced by the appearance of cavities. Then the important question is if those cavities have a great impact on the other main properties of the elastomeric bearings such as compression and shear stiffness or damping.

Iwabe and others [120] examined the tensile resistant characteristic of the natural rubber bearing (NRB), high damping rubber bearing (HDR), and natural rubber bearing with lead core (LRB). In their tests at first the shear strain was applied to the bearing to 200% and then cyclic stretching in the vertical direction up to 100% strain was performed. Softening was observed in all specimens and that indicates the cavities developed within rubber. The performance tests repeated after the offset tension tests showed no major sign of deterioration in their basic characteristics except the reduction in the compressive stiffness of HDR at the smaller range of compression However this

change should root in not only the cavitation but also the Mullins effect which can be observed in the force-displacement curves presented in their article [120]. It is generally difficult to filter out the Mullin's effect for tension tests because such high strain range would be reached only if the cavitation-induced softening is triggered.

Uno and others [121] also investigated the change in characteristics of NRB, HDR, and LRB after the tension shear test. The results are given in Table 19 and 20 where G8, G10, and G12 denote the shear moduli G=0.8, 1.0 and 1.2 MPa, respectively. Here LRB is not listed because two of the specimens were torn during tests. They failed at 2 MPa tension with 175% shear deformation. The numbers in parenthesis denote the proportion to the same characteristic values before test.

Table 19: Characteristics of natural rubber bearings before and after test (recreated from [121])

Natural Rubber		**NR-G8**	**NR-G10**	**NR-G12**
Before test	Compression stiffness K_v [kN/mm]	542.7	663.9	751.9
	Effective stiffness K_h [kN/mm]	2.0	2.5	3.3
	Equivalent damping ratio ξ [%]	6.0	7.3	6.2
After test	Compression stiffness K_v [kN/mm]	486.4 (0.90)	592.9 (0.89)	668.6 (0.89)
	Effective stiffness K_h [kN/mm]	1.8 (0.93)	2.3 (0.92)	3.0 (0.89)
	Equivalent damping ratio ξ [%]	6.1 (1.00)	7.3 (1.01)	6.1 (0.98)

Table 20: Characteristics of high damping natural rubber bearings before and after test (recreated from [121])

High Damping Rubber		**HDR-G8**	**HDR-G10**	**HDR-G12**
Before test	Compression stiffness K_v [kN/mm]	629.5	761.3	896.2
	Effective stiffness K_h [kN/mm]	2.1	2.6	2.9
	Equivalent damping ratio ξ [%]	14.6	14.1	13.9
After test	Compression stiffness K_v [kN/mm]	376.3 (0.60)	441.4 (0.58)	538.8 (0.60)
	Effective stiffness K_h [kN/mm]	1.9 (0.89)	2.1 (0.82)	2.4 (0.81)
	Equivalent damping ratio ξ [%]	14.1 (0.97)	14.3 (1.01)	13.7 (0.98)

Applied tensile stress was 2 MPa that is equivalent to the allowable tensile stress for elastomeric bearings during the seismic activity provided in the Japanese Specifications for Highway Bridges, except for G8 rubber whose allowable tensile stress is 1.6 MPa. The allowable tensile stress was determined by a number of the offset-tension tests and it is well below the ultimate strength of any types of the elastomeric bearings. No stress-strain curve was presented from the tension test and hence it is not clear whether cavities developed or not. Assuming a hydrostatic condition at the centre region of the bearing and considering that the pressure there is definitely higher than the

nominal stress, this applied tension force is therefore sufficient to induce cavitation for those tested bearings, especially for G8 rubber materials because 5G/2=2.0 MPa. Results of this experiment showed no significant change in the effective stiffness or the equivalent damping ratio of both NRB and LRB. As for the HDR, significant reduction of the compressive stiffness (up to 40%) was observed after tension shear test but again it is probably results both of cavitation and the Mullins effect. The equivalent horizontal stiffness of HDR was also more reduced than those of NRB and LRB.

Otsuka and others [122] examined the behaviour of the lead natural rubber bearings under tension. In their experiments rubber with the shear modulus G=0.98 MPa was used. Simple tension tests showed that mostly some reduction in the vertical stiffness was observed at around 2.45 MPa nominal tensile stress and this should be the indication of the threshold of cavitation within rubber. However, with the shear deformation, this behaviour varied. Typically, the smaller the shear deformation is, the higher the reduction in the vertical stiffness and the lower the cavitation initiating stress becomes. This is shown in Fig. 50. The symbol '×' in the same figure denotes the strain/stress at break. This tendency corresponds to the theory of Kelly [106] as well, i.e. the simple unilateral tension is the worst situation for cavitation.

Fig. 51 shows the hysteresis loops of the same type of LRB under various vertical load conditions. Clearly the lead rubber bearing can dissipate lower energy in tension than in compression. They described this is probably due to the absence of the constraint effect of the rubber to the lead plugs without high vertical compression.

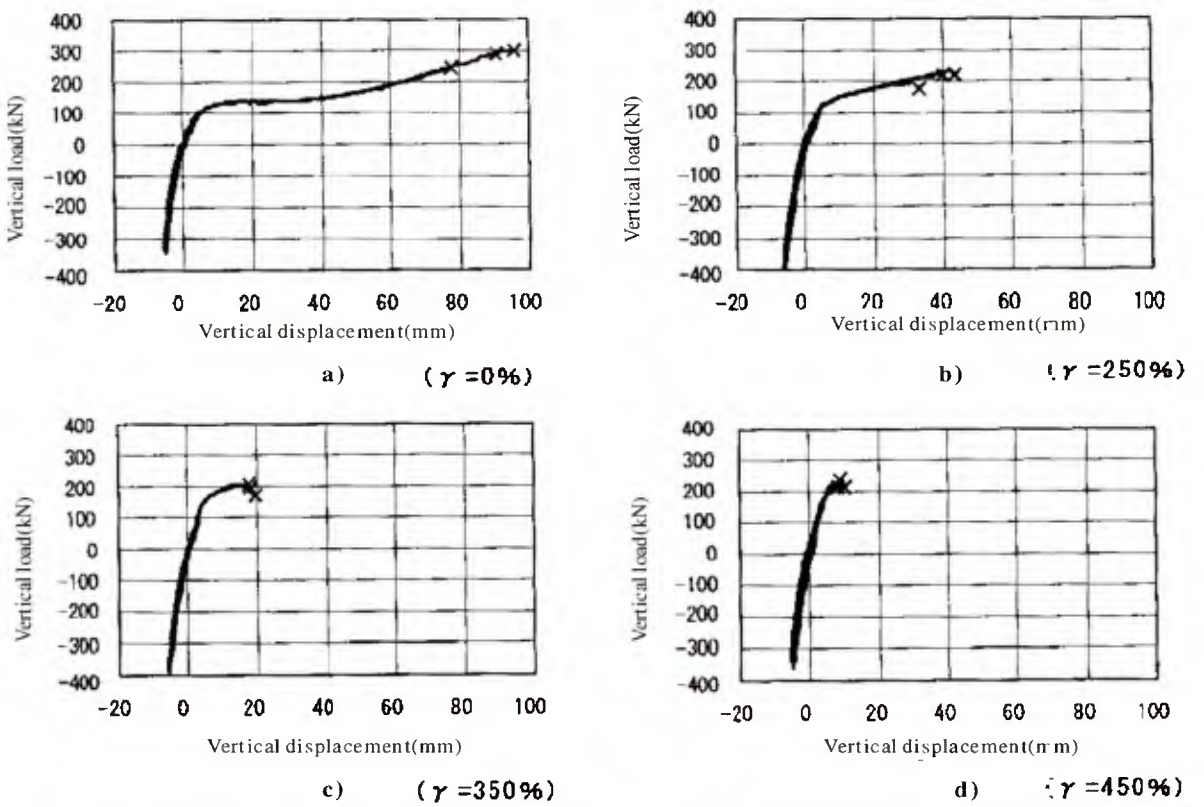

Figure 50: Vertical load-displacement curves of the lead rubber bearing [122]
(γ: Initial offset-shear strain, ×: breaking points of rubber specimens)

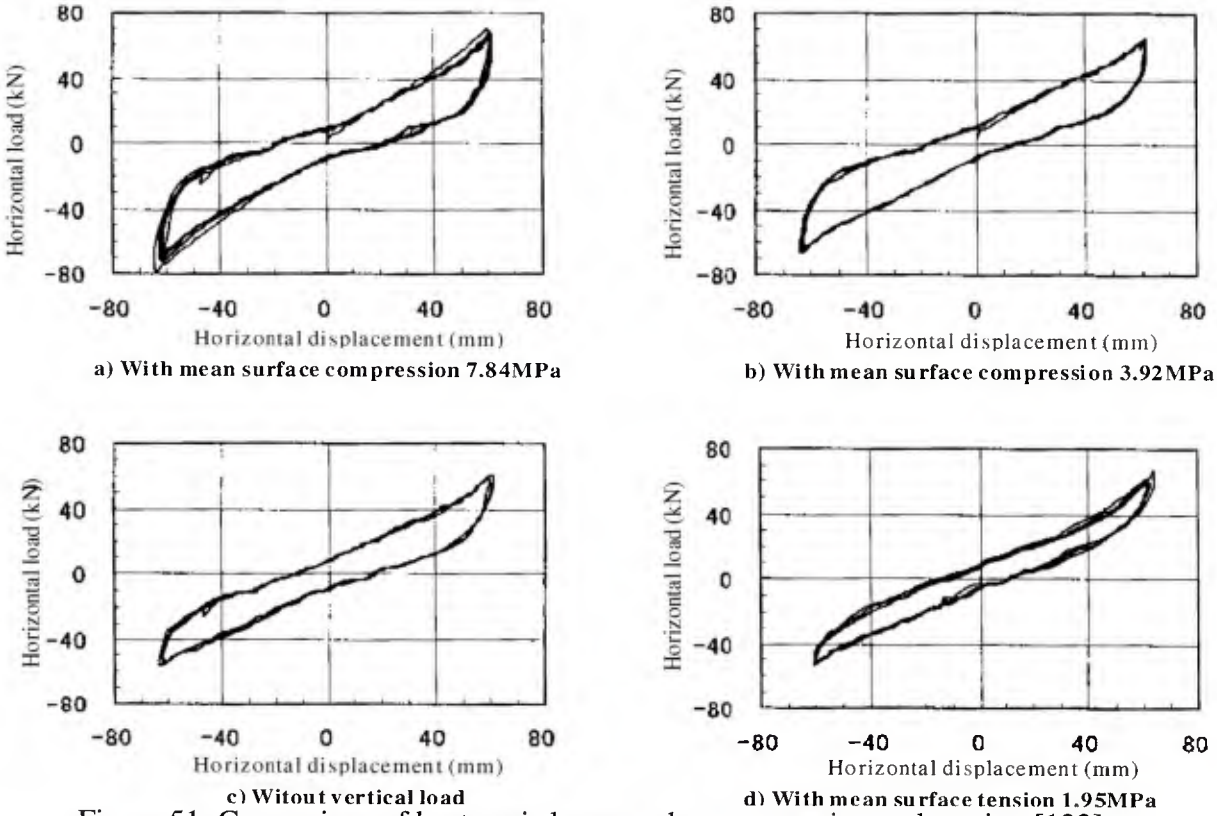

Figure 51: Comparison of hysteresis loops under compression and tension [122]

Matsushima and others [123] studied the cavities influence on the fatigue aspect of the natural rubber with up to 300 cyclic loading. Here the cavities were generated intentionally by pre-stretching uniaxially beforehand. Generally these tests did not exhibit any major influence of cavities on the fatigue characteristics of the rubber. However rubber disks with thickness 7 mm and 10 mm exhibited a notable reduction in the shear stiffness because the damage at the boundary of the rubber disk and the steel plate occurred during cyclic loading ($\gamma_{max} = 4$) and it expanded along with the number of cycles. It was more remarkable to the test piece with cavities as in shown in Fig. 52. This amount of shear deformation should not happen in real application frequently. Nevertheless this test result indicates that cavities could affect the fatigue resistance of rubber.

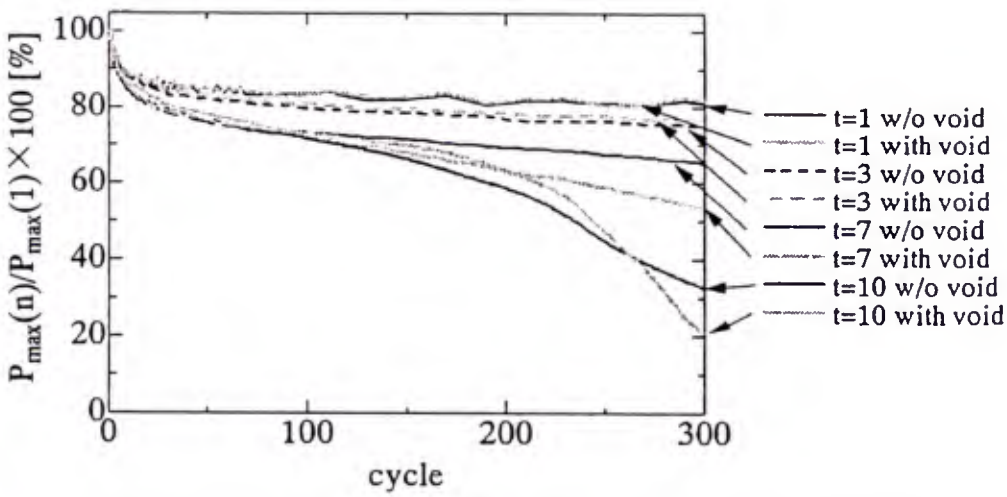

Figure 52: Rate of reduction of maximum load of each cycle [123]

5 EXPERIMENT

A series of elastomeric bearing tests were carried out at the laboratory of the Institute of Constructive Engineering, University of the Armed Forces Munich (Universität der Bundeswehr München). Twelve bearings with the first shape factor equal to 18.8 (S_1=18.8) and another twelve bearings of S_1=9.4 are prepared. For the convenience the former is named as the Type 1 bearing and the latter as the Type 2 bearing respectively. Those bearings were made out of low damping natural rubber and manufactured by Maurer Söhne GmbH. The sequence of the tests is as follows:

1) Compression and shear test in order to examine the initial properties of the bearings.
2) Either simple tension test, or shear and tension test aiming to cause the damage within rubber.
3) Compression and shear test to examine if any deterioration in their properties due to cavity-damage can be found.

Fig. 53 shows the dimension of both tested bearings. Both types have the same planar dimension and although the first shape factor differs, the total thickness of rubber pads is same. Bearings with a higher first shape factor (S_1>15) are likely used for the seismically isolated buildings and bearings with a shape factor up to 10 are for bridges. Type 1 bearing is for the application of the seismic isolation to building and Type 2 to bridges. Furthermore the same planar dimension and the same total thickness of rubber layers enable us to observe the difference in cavitation process due purely to different first shape factor.

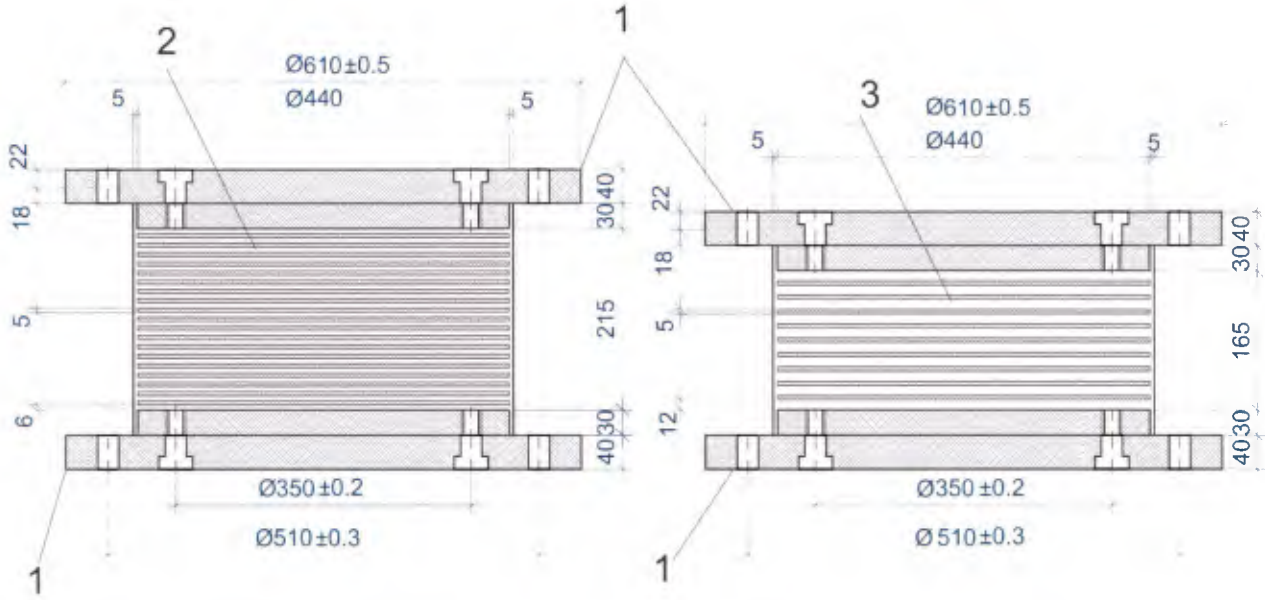

Figure 53: Dimension of the tested elastomeric bearings (left: Type 1, right: Type 2)

As described in the previous chapters, several similar tests were carried out in the past, mostly in Japan. The purpose of those tests is often to observe the cavitation-induced softening and its degree as well as to find out the influence on the cavitation due to various geometrical parameters but they seldom compared the test results with numerical analyses. Therefore the stress-strain curves of rubber materials or material constants, without which no proper numerical analysis can be performed, are rarely present in those researches. In this dissertation, however, both the implementing the numerical rubber-material model and understanding the cavitation phenomenon itself are of interest. For this reason dumbbell-shaped rubber samples have also been tested and their

stress-strain curves were used for the numerical simulation. Those results are presented with the FE analysis in the next Chapter.
In the following sections details of each test and the results are presented.

5.1 Test Setup And Devices

The setup of the test is shown in Fig. 54. This configuration is used for practically all series of tests. For the initial property test the vertical servohydraulic universal testing machine of "MFL und Zwick", type UPS 1000V is used to apply the vertical compression force to the tested bearings on top of the two horizontal actuators. The vertical actuator is controlled by a servohydraulic valve Moog 508K03DOJNO D101. The vertical load is calculated on the basis of the oil pressure in the actuator measured by a pressure transducer HBM P3MB-350 bar and the surface of the piston. The load measuring system is tested and recorded according to DIN EN ISO 7500-1 with Appendix 1 (Inv.No.: 43 1259 09–6 from November 11.2009), corresponding to accuracy class 1. For the horizontal load transfer, two actuators Schenck 630 kN with a stroke capacity of ±125 mm is used. The actuator is equipped with a displacement transducer and controlled by a servohydraulic valve SM250. The horizontal force of the actuator is measured by a calibrated load cell Schenck PM2,5Tn; No. 39904. Two actuators are mounted for general use in order to increase the shear displacement capacity. Each actuator is connected to the load-transferring plate that is lubricated with grease in order to reduce the undesired energy loss due to friction. However the hysteresis loops have still shown this extra energy loss. For the series of tests described here only the left actuator is activated and the right actuator is held at the original position. By this setting, the hysteresis loops due solely to the elastomer viscoelastic property can be obtained by depicting them with the displacement measured by the left actuator and the force measured by the right actuator.

Figure 54: Test setup for the property test

The left horizontal actuator is kept parallel to the ground by the bracing construction and is at the same time moveable in the vertical direction by means of the block and tackle mechanism so that pure shear deformation is assured independent of the vertical deformation of the elastomeric bearings, see Fig. 55.

Figure 55: Support construction for the left (upper) horizontal actuator

For the uniaxial tension test four additional actuators LUKAS LHC 60-35/25 were installed between two load-transferring plates as shown in Fig. 56. These actuators apply the compression force so that these plates are pulled away from each other. The forces were measured by the mounted load cells AST Gruppe KAF 250/500 kN. Displacement was measured at the two positions (see the same figure) by the displacement transducer that was calibrated by the Mitutoyo micrometer gauge.

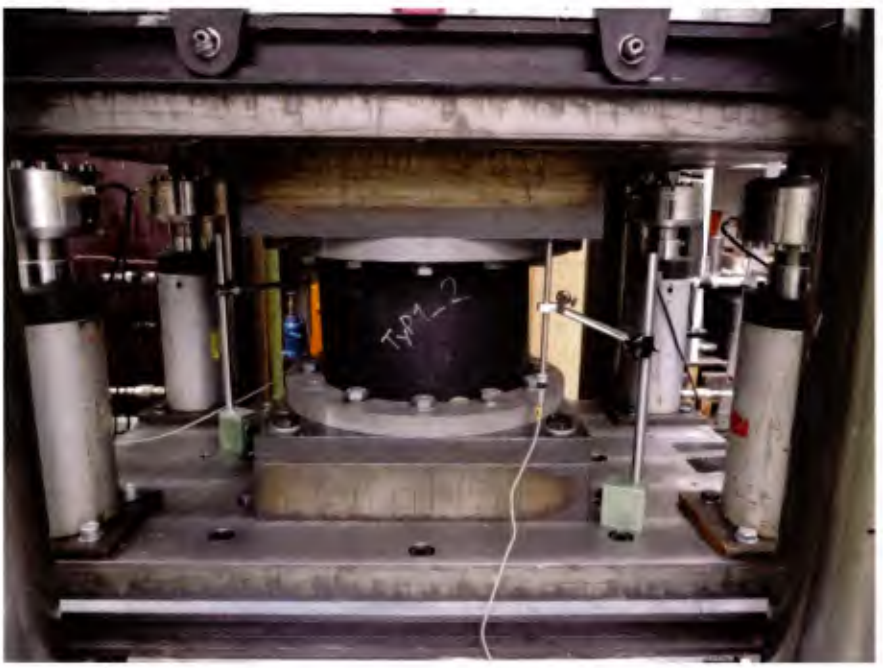

Figure 56: Test setup for the uniaxial tension test

This test configuration was slightly modified for the offset tension test. In order to prevent the bearing from rotating due to the initial shear deformation, a support construction was mounted which is indicated in the Fig. 57. A tension rod is installed on the other side for the same purpose.

Figure 57: Test setup for the offset tension test

Furthermore two actuators on the left side was replaced by only one actuator with ENERPAC P84 ULTIMA Hydraulic Steel Hand Pump since the required tensile force on this side is smaller due to the aforementioned rotation caused by the shear deformation. The two load-transferring plates were also kept parallel during the test by manually adjusting the loading on the left side by hand-pumping.

5.2 Initial Properties

The decisive properties of the elastomeric bearing are vertical and horizontal stiffness. As a seismic isolator, its damping property is also important although the tested bearing is the low damping natural rubber and therefore little energy dissipation is expected. Nevertheless those three properties are measured during this initial test and they are compared with the ones measured after all bearings are damaged by tension tests. As previously stated, the goal is to examine if there is any deterioration observable due to cavity damage. If damage is detectable in terms of such properties, bearings can be checked for their damage after seismic event without cutting it.
As for the procedure, the bearing is loaded vertically first and then the shear deformation is applied. The vertical force is calculated from the compression stress 6 MPa which is specified in [10] as the test procedure. This is also above the required minimum value and below the allowable maximum value defined in [9] [12]. Following the procedure of EN 15129 the maximum vertical load is applied to the bearing before measurement and kept for 5 to 10 minutes. Then the vertical force is unloaded and again loaded up to the maximum but this time in 5 steps. At each step the vertical force is held for at least 2 minutes. The vertical stiffness K_v of the elastomeric bearing is evaluated from this last force-displacement curve by the following expression:

$$K_v = \frac{F_{z2} - F_{z1}}{v_{z2} - v_{z1}} \tag{5.1}.$$

where

F_{z1} and F_{z2} : a third of the maximum load and the maximum load, respectively [kN]

v_{z1} and v_{z2} : the corresponding vertical deflections of the bearing at the two load levels provided above [mm]

The force-displacement curves from each bearing type are shown in Figs. 58 and 59.

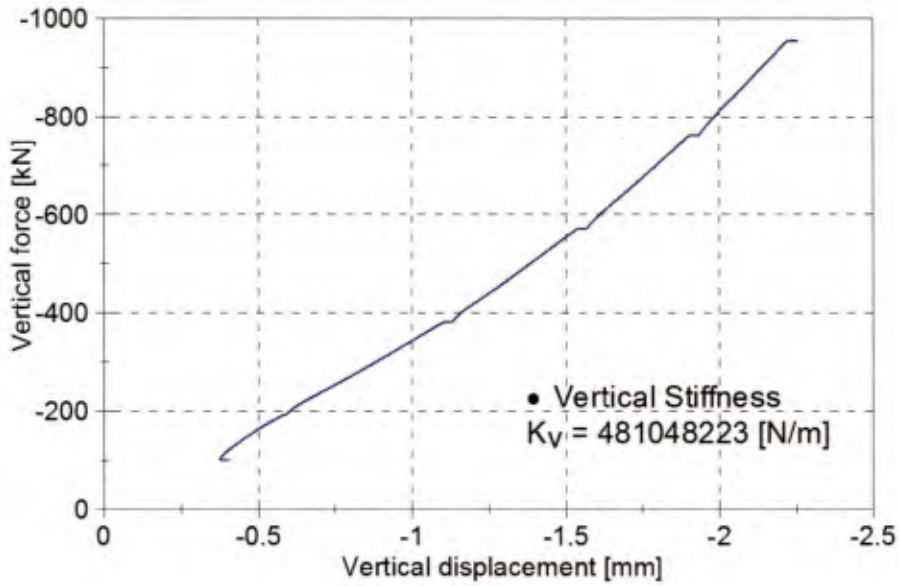

Figure 58: One of the vertical force-displacement curves of the bearing Type 1

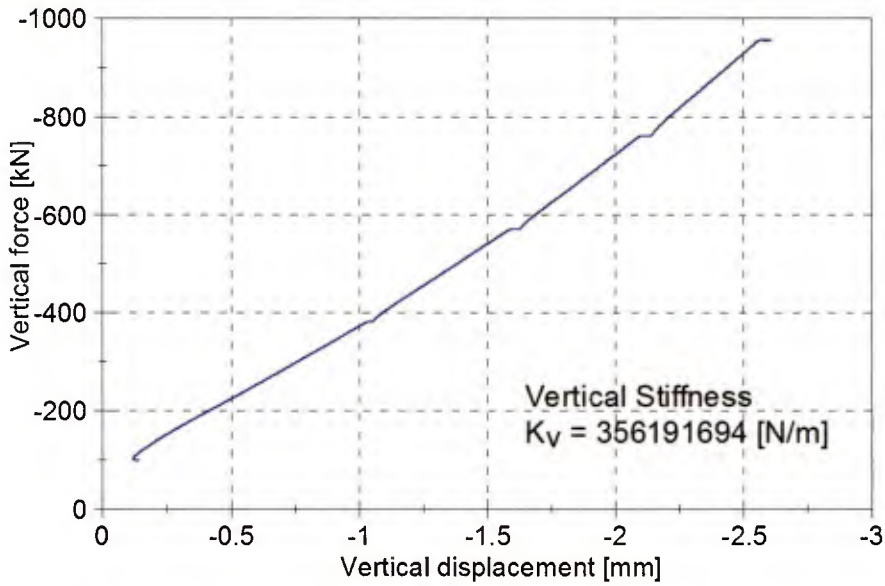

Figure 59: One of the vertical force-displacement curves of the bearing Type 2

With the vertical force kept at the maximum, the shear deformation of 100 %, which is the capacity of the horizontal actuator, is applied. The characteristic values of rubber stabilize when cyclic loading is applied because of rearrangement, re-crosslinking of the molecular chains or breakage of black carbon clusters occurring during the repeated loading. According to the annex of [12] ten cyclic loading is enough to obtain the stabilized shear stiffness. Hence these cyclic loading is applied to exclude this change in the characteristic values so that only the influence of cavity

damage can be examined at the comparison. However the characteristic values from the ninth cycle instead of the tenth cycle had to be compared because the hysteresis loop of the last cycle is not always fully closed. Hence the result could not be estimated properly. One of the hysteresis loops from each bearing type is exemplified in Figs. 60 and 61.

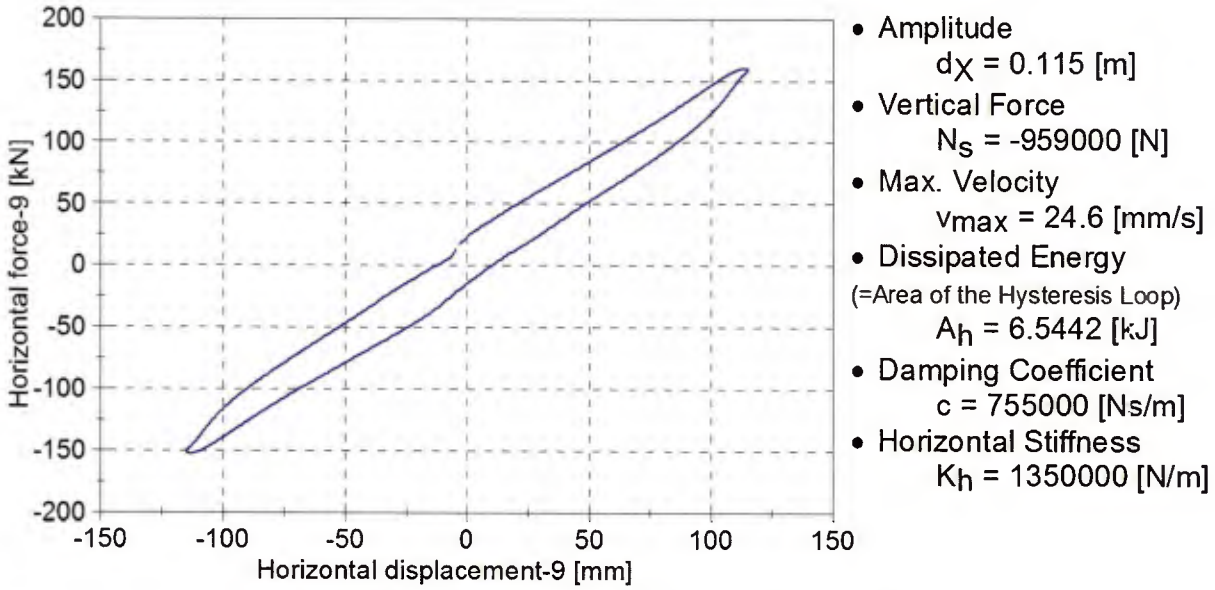

Figure 60: One of the hysteresis loops of the bearing Type 1

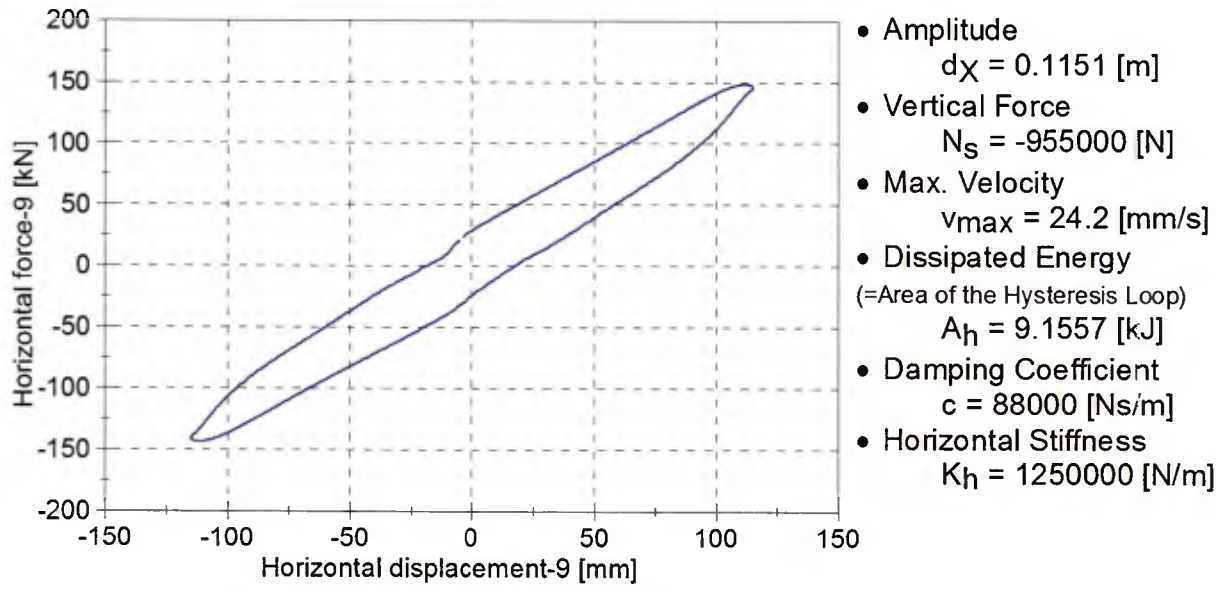

Figure 61: One of the hysteresis loops of the bearing Type 2

The horizontal displacement was applied with a sinus function with two different frequencies, 0.0332 Hz and 0.0664 Hz so that the dependence of the properties on the excitation frequency can be examined, if any exists.

The properties of tested bearings to be measured are the horizontal stiffness and the damping. The horizontal stiffness (effective stiffness) K_h is defined as:

$$K_h = \frac{F^+ - F^-}{u^+ - u^-} \tag{5.2}$$

where

u^+ and u^- : maximum and minimum values of displacement in the cycle

F^+ and F^- : corresponding forces at u^+ and u^-, respectively

The damping ratio is provided in the results as the measurement of damping that is expressed as:

$$\xi = \frac{2A_H}{K_h \pi (u^+ - u^-)^2} \simeq \frac{A_H}{2K_h \pi d^{+2}} \quad \because \text{abs}(u^+) \simeq \text{abs}(u^-) \tag{5.3}$$

where

A_H: the area within a hysteresis loop

The characteristic values of the Type 1 bearings are summarized in the following Tables 21 to 23. Originally six bearings of each type were to be tested. However, due to the failure of some bearings during the uniaxial tension test, three more samples of Type 1 bearings were tested.

Table 21: Measured horizontal properties of the Type 1 bearing from the ninth cycle (f=0.0332 Hz)

Bearing No.	Damping ratio ξ [%]	Measured K_h [N/m]×10^6	Shear modulus G [MPa]
1-01	5.8	1.35	1.02
1-02	7.8	1.33	1.00
1-03	7.8	1.34	1.01
1-04	7.1	1.26	0.95
1-05	7.0	1.33	1.00
1-06	6.7	1.37	1.03
1-07	7.9	1.29	0.97
1-08	7.0	1.29	0.97
1-09	7.6	1.18	0.89
Mean	**7.2**	**1.30**	**0.98**

Table 22: Measured horizontal properties of the Type 1 bearing from the ninth cycle (f=0.0664 Hz)

Bearing No.	Damping ratio ξ [%]	Measured K_h [N/m]×10^6	Shear modulus G [MPa]
1-01	5.7	1.32	1.00
1-02	8.3	1.30	0.98
1-03	7.0	1.31	0.99
1-04	7.5	1.23	0.93
1-05	8.0	1.29	0.97
1-06	5.9	1.34	1.01
1-07	8.0	1.26	0.95
1-08	7.3	1.26	0.95
1-09	8.5	1.16	0.88
Mean	**7.4**	**1.27**	**0.96**

The shear modulus given in the tables above are derived from Eq. (3.13) with the measured K_h. Evidently the damping ratio and the horizontal stiffness are virtually independent of the excitation frequency.

In the following Table 23 the measured vertical stiffness are compared with the design values based on three different design standards. For the calculation of design values, the mean values of two measured shear moduli are used and k factors are determined in accordance with [87] and [85]. The design compression stiffness calculated by Eqs. (3.19) and (3.20) amounts to almost twice as high as measured ones. They are practically no use for the evaluation of this bearing. The deviation between design stiffness values calculated by the Eq. (3.21) and measured ones are all within 30 % as should be according to the annex of [12], although it is still overestimation.

Table 23: Measured vertical stiffness of the Type 1 bearing and comparison with the design values

Bearing No.	Measured K_v [N/m]×10^8	Design K_v from Eq. (3.19) [N/m]×10^8	Design K_v from Eq. (3.20) [N/m]×10^8	Design K_v from Eq. (3.21) [N/m]×10^8
1-01	4.22	8.81	9.77	6.28
1-02	4.81	8.72	9.71	6.19
1-03	4.93	8.76	9.74	6.23
1-04	4.54	8.41	9.52	5.86
1-05	4.65	8.70	9.70	6.16
1-06	4.80	8.89	9.82	6.38
1-07	4.74	8.54	9.61	6.00
1-08	4.76	8.54	9.61	6.00
1-09	4.72	8.07	9.32	5.51
Mean	**4.69**	**8.60**	**9.64**	**6.07**

As explained in Chapter 3, this large gap between stiffness results might stem from the wrong bulk modulus. As an attempt, the evaluation formula (3.20) is recalculated with E_b=500 MPa and with that the results fit evidently better, see Fig. 62.

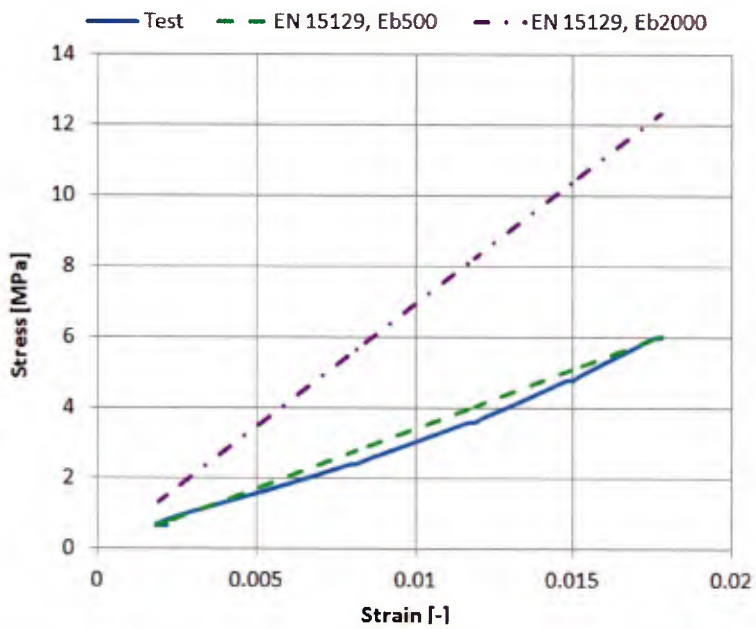

Figure 62: Comparison of the test and the evaluation formula (3.20) for the Type 1 bearing

The same sets of tables for the Type 2 bearing are given in the following Tables 24 to 26.

Table 24: Measured horizontal properties of the Type 2 bearing from the ninth cycle (f=0.0332 Hz)

Bearing No.	Damping ratio ξ [%]	Measured K_h [N/m]×10^6	Shear modulus G [MPa]
2-01	8.8	1.25	0.94
2-02	9.4	1.17	0.88
2-03	9.4	1.10	0.83
2-04	8.7	1.19	0.90
2-05	9.9	1.18	0.89
2-06	10.6	1.13	0.85
Mean	**9.5**	**1.17**	**0.88**

Table 25: Measured horizontal properties of the Type 2 bearing from the ninth cycle (f=0.0664 Hz)

Bearing No.	Damping ratio ξ [%]	Measured K_h [N/m]×10^6	Shear modulus G [MPa]
2-01	9.4	1.22	0.92
2-02	9.2	1.15	0.87
2-03	11.1	1.08	0.82
2-04	9.9	1.16	0.89
2-05	10.8	1.15	0.88
2-06	10.2	1.12	0.85
Mean	**10.1**	**1.15**	**0.87**

The measured mean horizontal stiffness of the bearing Type 2 is approximately 10 % lower than the Type 1 bearing, although theoretically they must be equal. The shear modului of the rubber derived from these measured K_h are, therefore, inevitably lower than those of Type 1 bearings as well. As explained in [124], a bending deformation increases as lowering the first shape factor, which in turn reduces the apparent shear modulus. The relationship between the actual and apparent shear moduli is also provided in [124] that is derived from the unit virtual load method, see Fig. 63.

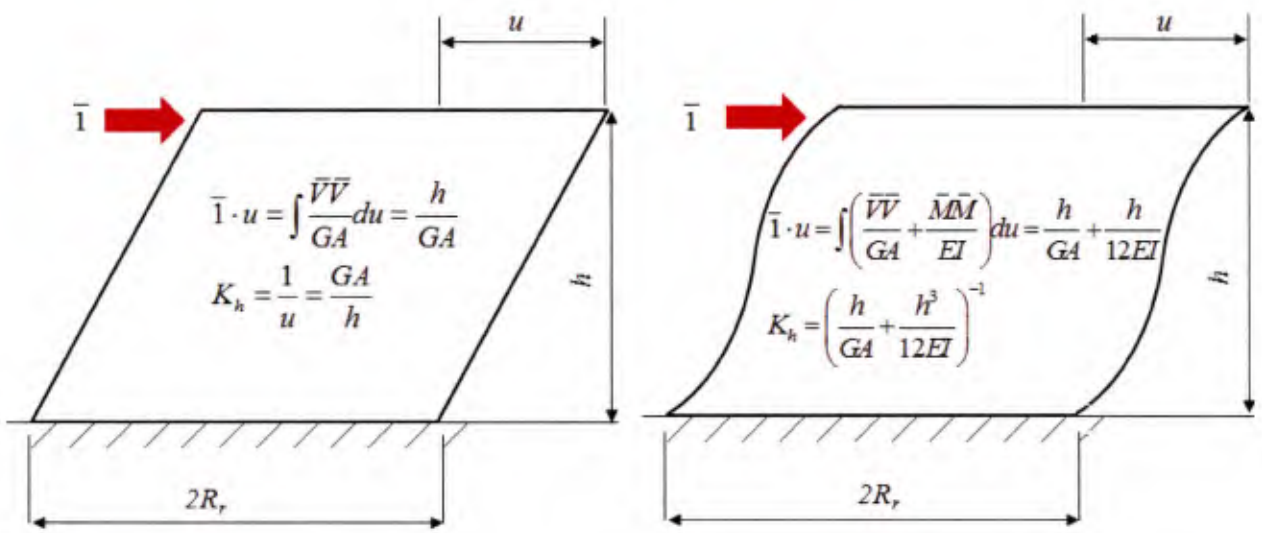

Figure 63: Work done by the unit virtual load involving only shear deformation (left) or both shear and bending deformation (right)

Assuming the total incompressibility of rubber, the elastic modulus is replaced by $\Xi=3G$. By substituting G for G_a (apparent shear modulus) of the equation in the right figure and equating both K_h, the following relationship is obtained for cylindrical rubber.

$$G_a = \frac{G}{1+\frac{1}{3}\left(\frac{h}{R_r}\right)^2} \tag{5.4}$$

By applying the same principle to the complete bearing and substituting EI in the equation in the Fig. 63 for $E_\theta I$ from, for instance, Eq. (3.25), the shear modulus of rubber is calculated as

$$G = \frac{K_h \sum h_i}{A}\left\{1+\frac{1}{\left(9+6kS_1^2\right)}\left(\frac{H_b}{R_r}\right)^2\right\} \tag{5.5}$$

where K_h, A and H_b are the horizontal stiffness, the plane area and the height including two flange plates of the rubber bearing, respectively. h_i is the thickness of each rubber pad, R_r is the radius of rubber pad and k is the same factor of Eq. (3.25).

Rubber pads of both bearing types are, however, flat enough so that the bending contribution is negligibly small and in fact the expressions above hardly help distinguish one from another. Then there is no other option than accepting the fact that the material characteristics are slightly different from each other, although the same rubber material should have been used for both bearing types. The difference in damping may also be explained by this hypothesis. A possible cause of these differences is, for instance, different degree of oxidization. Perhaps Type 1 bearings were manufactured before and they were exposed to the air a longer period than Type 2 bearings. Then the Type 1 bearings are more oxidized and oxidized natural rubber tends to possess higher shear stiffness, although oxidisation is normally a slow process and often only remains on surface level. A more plausible explanation would be the property change during the manufacturing process. Amount of heating and pressure during vulcanizing process as well as different curing conditions are responsible for the density of molecular chains cross-linking. Both explanation offer no evidence and are, therefore, mere hypotheses. The fact that the properties of the tested rubber bearing has altered is "confirmed" by the FE analysis in Chapter 6 in which it is demonstrated that the FE analysis cannot deliver the corresponding results to the test data if the same shear modulus is used for both bearing types.

Table 26: Measured vertical stiffness of the Type 2 bearing and comparison with the design values

Bearing No.	Measured K_v [N/m]×10^8	Design K_v from Eq. (3.19) [N/m]×10^8	Design K_v from Eq. (3.20) [N/m]×10^8	Design K_v from Eq. (3.21) [N/m]×10^8
2-01	3.14	2.80	3.32	2.91
2-02	3.56	2.65	3.22	2.73
2-03	3.36	2.50	3.12	2.56
2-04	3.53	2.68	3.24	2.76
2-05	3.22	2.66	3.23	2.74
2-06	3.34	2.58	3.18	2.65
Mean	**3.36**	**2.65**	**3.22**	**2.73**

Comparison of the measured and design compression stiffness is summarized in Table 26. All evaluation formulae provide a relatively good estimation for this bearing type in comparison with the bearing Type 1 and deviation between all design values and measured ones is within 30%. The closest estimation is generated by Eq. (3.20). For this bearing type, the bulk modulus of 2000 MPa provides a better fit as shown in Fig. 64, although the difference in two curves derived from the evaluation formula (3.20) based on two different bulk modulus is much smaller than that of the Type 1 bearing. This is because the apparent compression modulus E_c is highly dominant in the total compression modulus Ecb if the first shape factor S_1 is low and therefore the bulk modulus has less influence. Vice versa, the influence of the bulk modulus on E_{cb} becomes high as S_1 increases and hence more accurate E_b is required. Considering that, the value of 500 MPa for the bulk modulus seems more appropriate than 2000 MPa. For the FE simulation in the next Chapter, therefore, E_b is also set to 500 MPa.

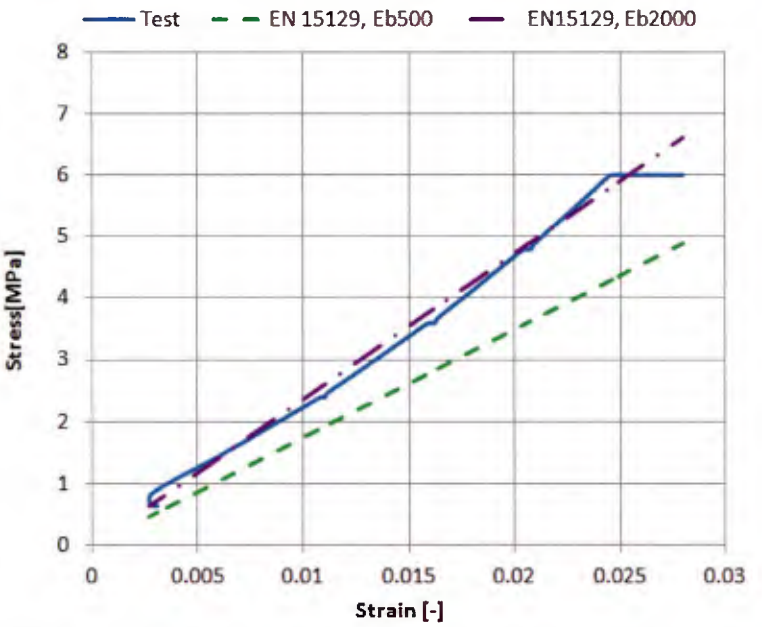

Figure 64: Comparison of the test and the evaluation formula (3.20) for the Type 2 bearing

5.3 Uniaxial Tension Test

The force-displacement curves from each bearing type are shown in Figs. 65 and 66 and all results of other bearings are provided in appendices. For both cases expected softening is observed, although its degree and onset point are different. The softening of the bearings Type 2 appears at a lower loading level than that of the bearings Type 1. As explained in Chapter 3 and visually shown by means of FE Analysis in the next Chapter, the distribution of the negative pressure in the radial direction is not constant and a higher pressure occurs in the centre region. This distribution is flattened towards constant distribution as the first shape factor increases, which means the Type 2 bearings experience a higher negative pressure there than the bearings Type 1 at the same loading level. Therefore cavities should develop in the bearings Type 2 earlier with a lower loading level than the bearings Type 1 and the test results support the theory.
The initial tensile vertical stiffness denoted in these figures are calculated between 100 kN and 300 kN since all tested bearing possess almost a linear behaviour in this range and there is no definition of the tensile stiffness provided by the design standards such as Eurocode or Japanese Specifications for Highway Bridges. The measured stiffness values are summarized and compared with their compressive stiffness in Tables 27 and 28.

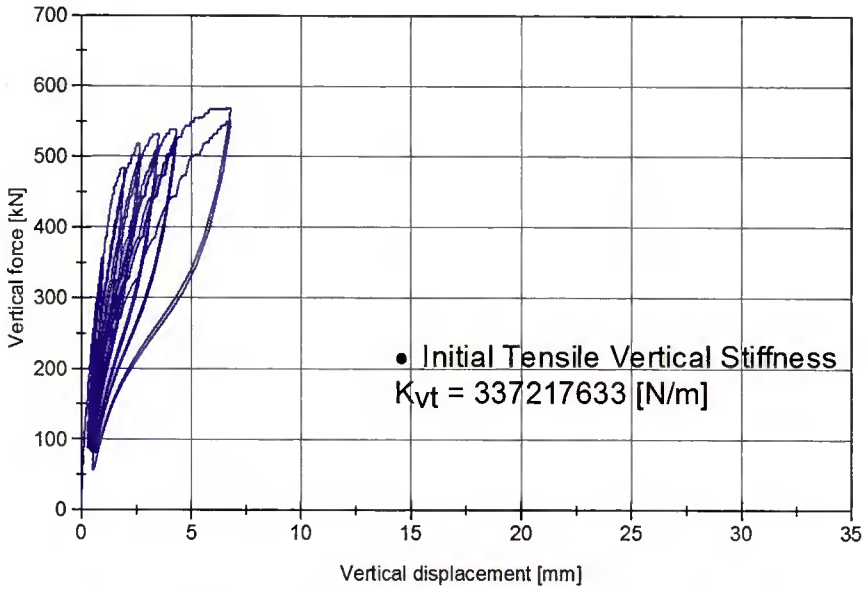

Figure 65: Force-displacement curves of the bearing 1-06

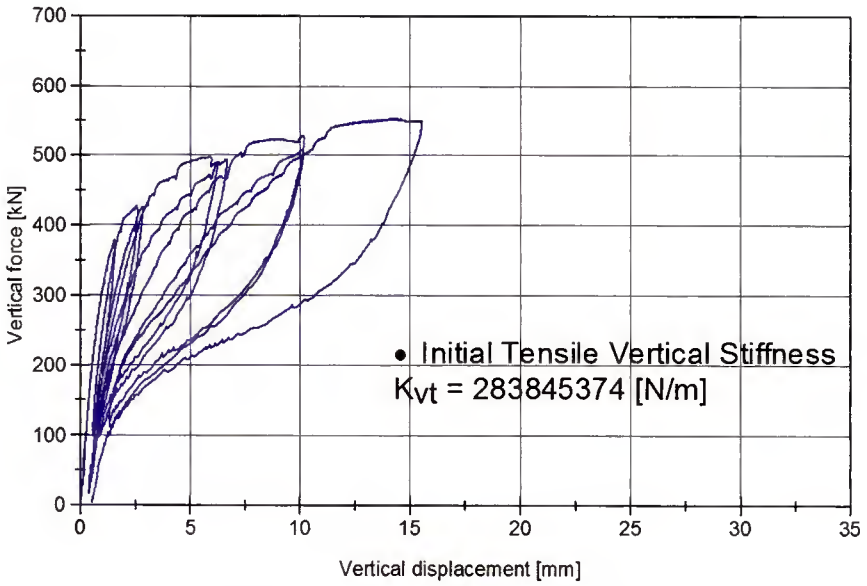

Figure 66: Force-displacement curves of the bearing 2-02

Six test pieces of Type 1 bearings and three of Type 2 bearings were tested for the uniaxial tension. After all initial property tests, more of Type 1 bearings were tested because among them the bearings 1-03 and 1-05 failed and the measurement of the bearing 1-04 was unsuccessful due to the hydraulic trouble during the test. Theoretically the compressive and tensile stiffness within a small strain range should be equivalent as described in [105] but the tensile stiffness of all tested bearings was more than 10 % lower than the compressive stiffness.

Table 27: Comparison of the compressive- and tensile stiffness of the Type 1 bearing

Bearing No.	Measured K_v * [N/m]×10^8	Measured K_{vt} [N/m]×10^8
1-01	2.60	2.93
1-02	4.13	2.90
1-03	4.01	3.51
1-04	3.79	3.85
1-05	4.19	3.10
1-06	-	3.37
Mean	**3.74**	**3.28**

*Compressive stiffness K_v measured between -100 kN and -300 kN for comparing

Table 28: Comparison of the compressive- and tensile stiffness of the Type 2 bearing

Bearing No.	Measured K_v * [N/m]×10^8	Measured K_{vt} [N/m]×10^8
2-01	3.11	2.31
2-02	3.16	2.84
2-03	2.79	2.32
Mean	**3.02**	**2.49**

*Compressive stiffness K_v measured between -100 kN and -300 kN for comparing

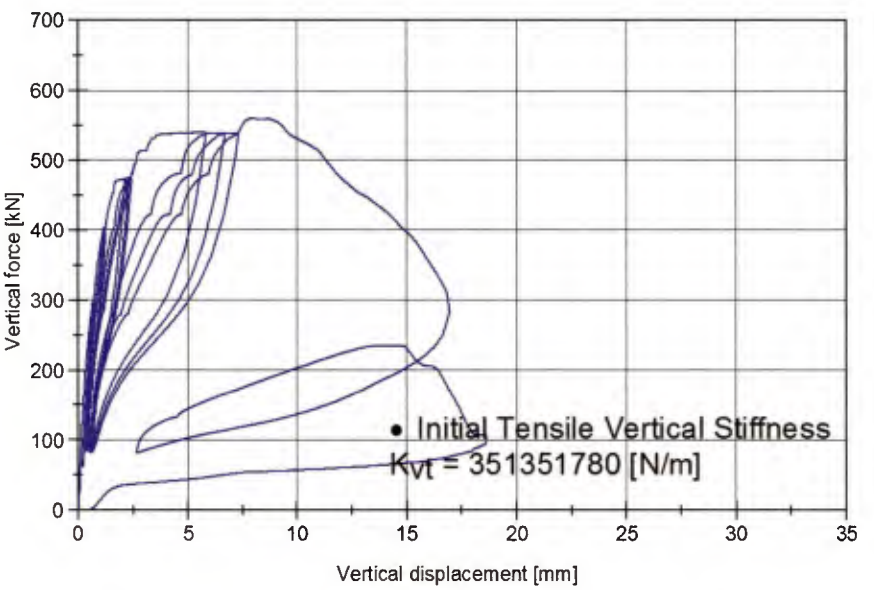

Figure 67: Force-displacement curves of the bearing Type 1-03

The force-displacement curve of the bearing 1-03 is shown in Fig. 67. At approximately 460 kN tensile force, the loading was briefly stopped since the deformation increased progressively. After that, at about 540 kN, the same phenomenon occurred. This time the deformation progressed more rapidly and the bearing lost its stiffness completely as the maximum tensile force reached 550 kN. The failure was caused most probably by delamination between a rubber pad and a steel shim. This assumption is deduced from the visible excessive concave deformation on the bearing surface, see Fig. 68.

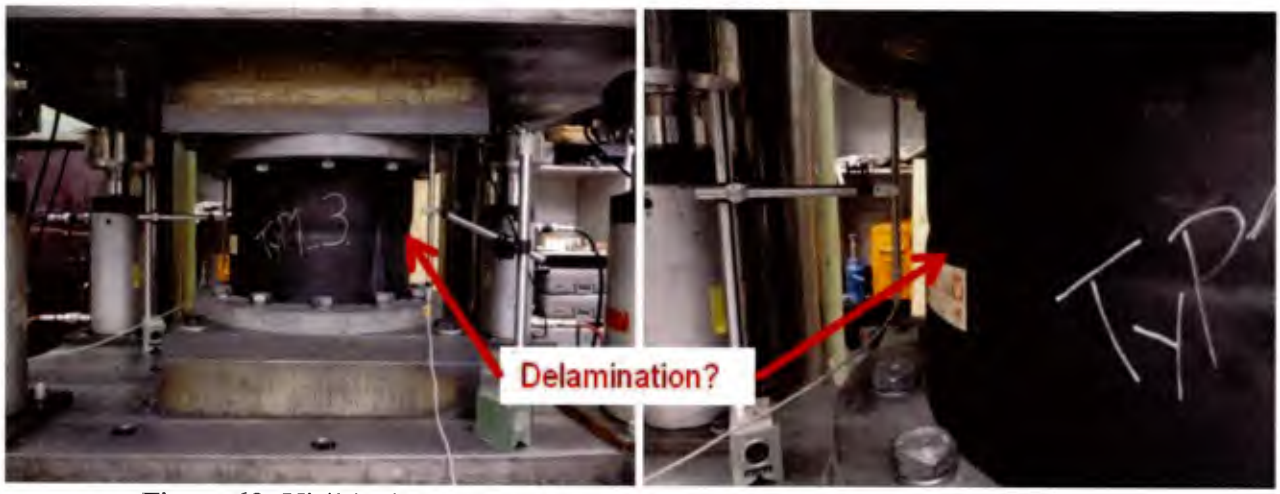

Figure 68: Visible damage of the bearing 1-03 during the uniaxial tension test

The same deformation was observed not only on the failed test pieces but also on some of the other Type 1 test pieces. This indicates that the delamination took place also in the other test pieces parallel to the cavitation. The one whose delamination was complete or almost complete was visible from the surface deformation. There was plateau in the force-displacement curves of the bearings 1-01 to 1-05 (see annex) as in Fig. 67. It has to be verified by cutting off the bearings if this excessive softening is caused by cavitation alone or that combined with the delamination.
As for the bearing Type 2, the same kind of deformation was difficult to detect since the surface of these bearings becomes a highly wave-like form (see Fig. 69) as a result of its higher deformability than Type 1. Moreover a clear plateau is not found in the force-displacement curves of these bearings, although the tensile vertical stiffness becomes also very low at higher displacement.
These cavitation- and delamination damages will be discussed in 5.6.

Figure 69: The bearing 2-02 during the uniaxial tension test

5.4 Offset Tension Test

The force-displacement curves from each bearing type are shown in Figs 70 and 71 and the force-displacement curves of all other bearings are provided in the appendices.

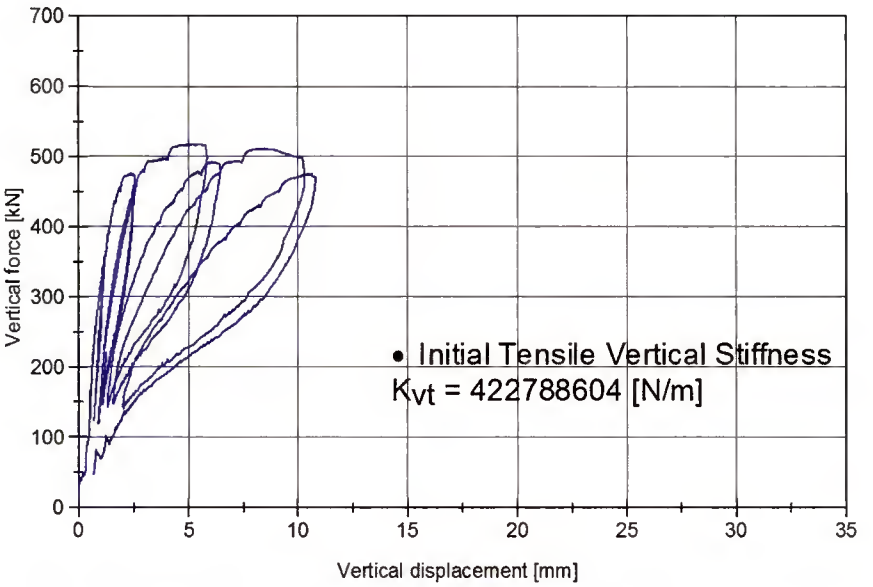

Figure 70: Force-displacement curves of the bearing Type 1-09

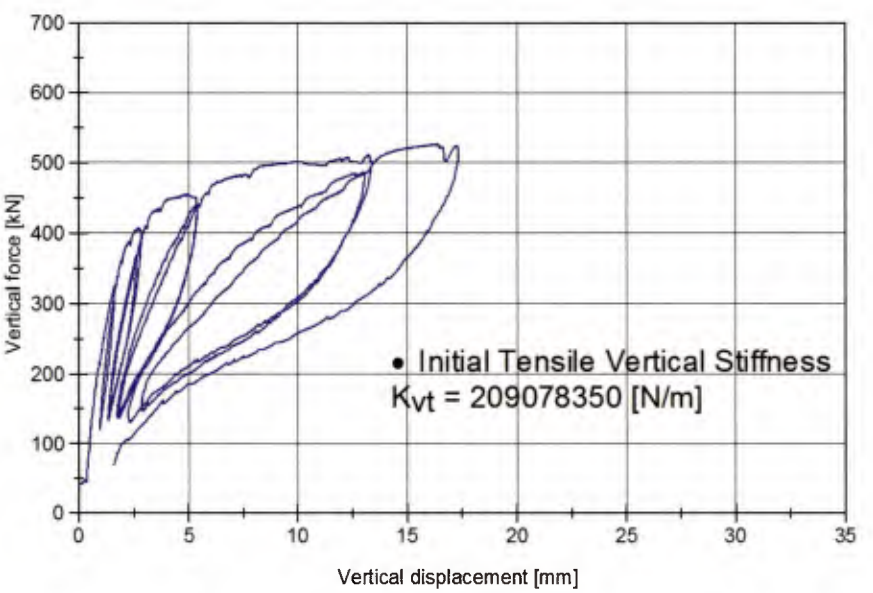

Figure 71: Force-displacement curves of the bearing Type 2-05

The load-carrying behaviours are similar to those of the uniaxial tension tests. Here however, the softening begins at lower loading levels and also the initial stiffness seems to be generally lower. The compressive stiffness is also lower when the shear deformation is present for the effective planar area resisting compression is reduced. This explanation is probably not valid for the tensile stiffness but the rotation within the bearing explained in [106] contributes to the lower stiffness. It is observed in all force-displacement curves of uniaxial tension- and offset tension tests that the required force to reach the same level of previously reached displacement is lower. This difference

in the required forces is most distinguished between the first and the second cycles. Furthermore cyclic force-displacement curves under small loading range in which they are nearly linear exhibit no such difference between consecutive loading cycles. From these observations, it can be deduced that the difference in the required force between consecutive loading cycles is caused mostly by the cavitation or perhaps delamination but not Mullin's effect.
During the offset tension tests the same local excessive deformation on the surface of the Type 1 bearings was also observed as shown in Fig. 72. Here as well, it is difficult to identify this kind of deformation on the Type 2 bearings but at the uppermost layer of rubber pad somewhat larger deformation was observed for all three tested bearings. As shown with the FE simulation in the next Chapter, the cavitation criterion was violated first in this area resulting in the damage, either cavities or delamination, might have developed there.

Figure 72: Visible damage of the bearing 1-09 (left) and 2-05 (right) during the offset tension test

5.5 Repetition Of The Property Test

Exactly the same series of property tests were carried out after either uniaxial tension tests or offset tension tests. Here only the changes in all properties are of interest and hence comparison of the properties before and after uniaxial- or offset tension tests is shown in the following tables.

Table 29: Change in the horizontal stiffness (9^{th} cycle) of the Type 1 bearing (f=0.0332 Hz)

Bearing No.	K_h before tension test [N/m]×10^6	K_h after tension test [N/m]×10^6	Deviation [%]
1-01	1.35	1.24	-8.1
1-02	1.33	1.23	-7.5
1-03	1.34	-	-
1-04	1.26	1.19	-5.6
1-05	1.33	1.26	-5.3
1-06	1.37	1.31	-4.4
1-07	1.29	1.24	-3.9
1-08	1.29	1.16	-10.1
1-09	1.18	1.11	-5.9
Mean	**1.30**	**1.22**	**-6.4**

Table 30: Change in the horizontal stiffness (9th cycle) of the Type 1 bearing (f=0.0664 Hz)

Bearing No.	K_h before tension test [N/m]×10^6	K_h after tension test [N/m]×10^6	Deviation [%]
1-01	1.32	1.28	-3.0
1-02	1.30	1.25	-3.8
1-03	1.31	-	-
1-04	1.23	1.18	-4.1
1-05	1.29	1.24	-3.9
1-06	1.34	1.30	-3.0
1-07	1.26	1.23	-2.4
1-08	1.26	1.16	-7.9
1-09	1.16	1.11	-4.3
Mean	**1.27**	**1.22**	**-4.1**

Table 31: Change in the damping ratio (9th cycle) of the Type 1 bearing (f=0.0332 Hz)

Bearing No.	ξ before tension test [%]	ξ after tension test [%]	Deviation [%]
1-01	5.8	7.1	-20.4
1-02	7.8	8.7	-11.5
1-03	7.8	-	-
1-04	7.1	7.8	10.0
1-05	7.0	7.5	7.1
1-06	6.7	7.1	6.0
1-07	7.9	7.7	-2.5
1-08	7.0	10.5	50.0
1-09	7.6	8.6	13.2
Mean	**7.2**	**8.1**	**6.5**

Table 32: Change in the damping ratio (9th cycle) of the Type 1 bearing (f=0.0664 Hz)

Bearing No.	ξ before tension test [%]	ξ after tension test [%]	Deviation [%]
1-01	5.7	5.8	1.2
1-02	8.3	6.4	-22.9
1-03	7.0	-	-
1-04	7.5	7.7	2.7
1-05	8.0	7.4	-7.5
1-06	5.9	7.3	23.7
1-07	8.0	8.1	1.3
1-08	7.3	9.4	28.8
1-09	8.5	8.2	-3.5
Mean	**7.4**	**7.5**	**3.0**

Table 33: Change in the vertical stiffness of the Type 1 bearing

Bearing No.	K_v before tension test [N/m]×10^8	K_v after tension test [N/m]×10^8	Deviation [%]
1-01	4.22	3.91	-7.3
1-02	4.81	4.49	-6.7
1-03	4.93	-	-
1-04	4.54	4.56	0.4
1-05	4.65	4.48	-3.7
1-06	4.80	4.79	-0.2
1-07	4.74	5.14	8.4
1-08	4.76	4.72	-0.8
1-09	4.72	4.54	-3.8
Mean	**4.69**	**4.58**	**-1.7**

The change in the horizontal and vertical stiffness is quite small despite the fact that the local excessive bulging deformation was observed on the surface of bearings where the delamination might have taken place during tension tests, see Fig. 73. The change in damping is diverse, and no logical pattern can be deduced weather there is some influence of cavities or not. The measurement and evaluation of such small damping is not quite accurate since admittedly the sampling frequency at measurement or rounding the number during the evaluation process can affect the results and might lead to an error. For this reason it is decided that the influence of cavities on the damping property are not evaluated.

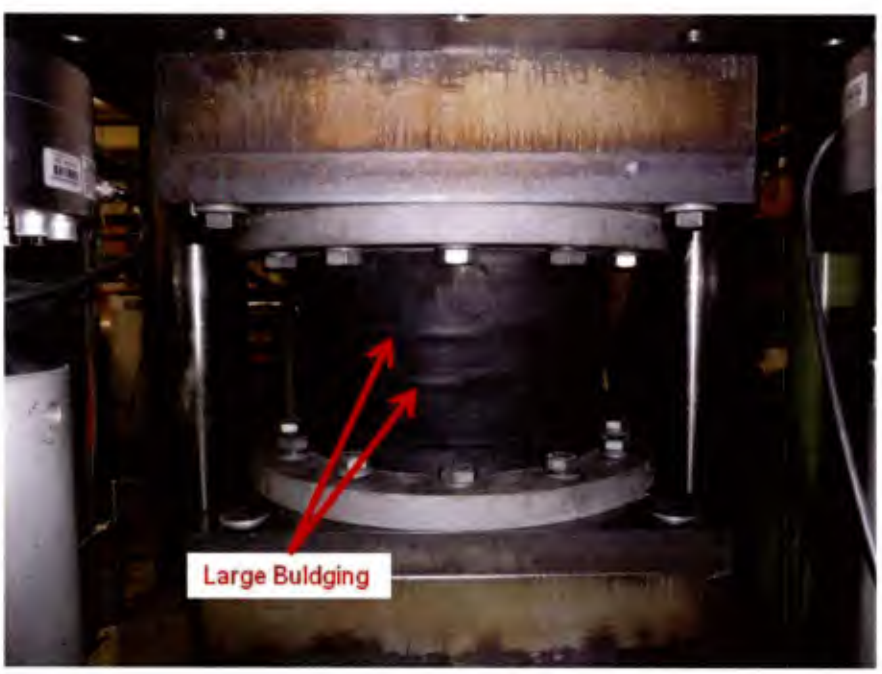

Figure 73: Bulging deformation of the bearing 1-05 during the compression and shear test

The same sets of tables for the Type 2 bearing are given in the followings
For the bearings Type 2, change in characteristic values is in the same order as bearings Type 1. It can be then concluded that the influence of cavities or delamination on the properties of both types of rubber bearings is minor within the tested loading or displacement range.

Table 34: Change in the horizontal stiffness (9th cycle) of the Type 2 bearing (f=0.0332 Hz)

Bearing No.	K_h before tension test [N/m]×10^6	K_h after tension test [N/m]×10^6	Deviation [%]
2-01	1.25	1.18	-5.6
2-02	1.17	1.12	-4.3
2-03	1.10	1.04	-5.5
2-04	1.19	1.12	-5.9
2-05	1.18	1.10	-6.8
2-06	1.13	1.07	-5.3
Mean	**1.17**	**1.11**	**-5.6**

Table 35: Change in the horizontal stiffness (9th cycle) of the Type 2 bearing (f=0.0664 Hz)

Bearing No.	K_h before tension test [N/m]×10^6	K_h after tension test [N/m]×10^6	Deviation [%]
2-01	1.22	1.18	-3.3
2-02	1.15	1.11	-3.5
2-03	1.08	1.04	-3.7
2-04	1.16	1.11	-4.3
2-05	1.15	1.10	-4.3
2-06	1.12	1.06	-5.4
Mean	**1.15**	**1.10**	**-4.1**

Table 36: Change in the damping ratio (9th cycle) of the Type 2 bearing (f=0.0332 Hz)

Bearing No.	ξ before tension test [%]	ξ after tension test [%]	Deviation [%]
2-01	8.8	9.9	12.5
2-02	9.4	10.0	6.4
2-03	9.4	10.8	14.9
2-04	8.7	9.7	11.5
2-05	9.9	10.2	3.0
2-06	10.6	10.4	-1.9
Mean	**9.5**	**10.2**	**7.7**

Table 37: Change in the damping ratio (9th cycle) of the Type 2 bearing (f=0.0664 Hz)

Bearing No.	ξ before tension test [%]	ξ after tension test [%]	Deviation [%]
2-01	9.4	8.8	-6.4
2-02	9.2	9.5	3.3
2-03	11.1	10.3	-7.2
2-04	9.9	10.3	4.0
2-05	10.8	11.2	3.7
2-06	10.2	11.3	10.8
Mean	**10.1**	**10.2**	**1.4**

Table 38: Change in the vertical stiffness of the Type 2 bearing

Bearing No.	K_v before tension test $[N/m]\times10^8$	K_v after tension test $[N/m]\times10^8$	Deviation [%]
2-01	3.14	3.03	-3.5
2-02	3.56	3.40	-4.5
2-03	3.36	3.11	-7.4
2-04	3.53	3.30	-6.5
2-05	3.22	3.05	-5.3
2-06	3.34	3.15	-5.7
Mean	**3.36**	**3.17**	**-5.5**

5.6 Cavity Inspection

Two of the bearings were cut so that cavities and other damages could be observed. Cutting the rubber layer in the plane direction is not a simple task without proper tools because of high deformability and friction. The cutting saw frequently was stuck and stopped while cutting and the fact that each rubber layer is thin made the process even slower. Eventually the cutting machine broke after the second bearings and hence only two bearings, 1-02 and 1-05 were cut. The cutting surface of the bearing 1-05 is shown in Fig. 74.

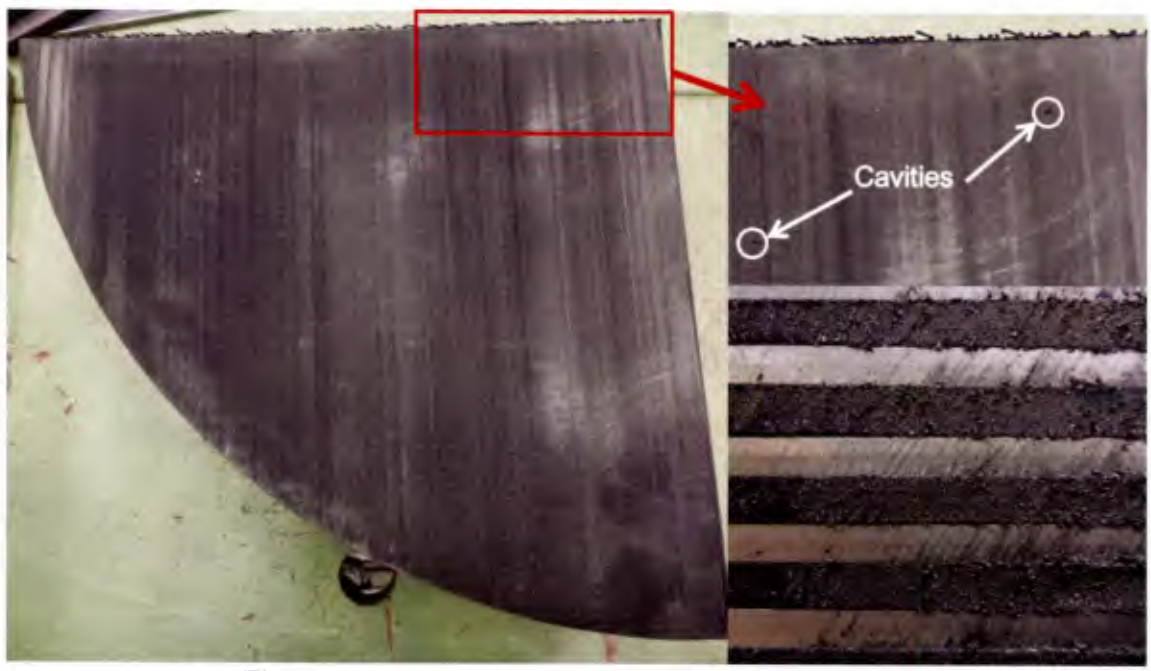

Figure 74: Cutting surface of the bearing Type 1-05

This bearing was selected to investigate the cause of failure since it lost most of its vertical stiffness during the uniaxial tension test at the lowest tensile loading level, see Appendices. Not many cavities were expected to appear in rubber pads due to this low applied tensile force and the radical change in the force-displacement curve which is not corresponding to the softening behaviour of other bearings. In fact the both planar and vertical cutting surfaces are smooth and there are only a few visible cavities in the centre region on this surface.

Another cutting surface near the boundary of a steel shim and a rubber pad is shown in Fig. 75 which revealed that delamination of approximately 20 mm in width took place along the whole

outer edge between steel shims and rubber pads. The excessive bulging deformation observed during the repeated property test (see Fig. 73) was caused by this delamination. The maximum shear stress should appear along the outer edge as in the case of compression where that would be the cause of delamination. The centre region is also delaminated approximately 150 mm in length and 20 mm in width. The steel shim in those areas was intentionally bent to show the delaminated part and as it was bent, it was observed that the glue between the steel shim and the rubber pad was not completely detached, but rather intermittently and the surface was rough whereas the delamination along the outer edge was complete and the surface was smooth. Centre region is where the highest hydrostatic stress condition is expected and therefore cavitation takes place first. Perhaps delamination occurred because of the same principal of cavitation there and this intermittent delaminated area spread until the size of the glued area became insufficient to sustain the applied force.

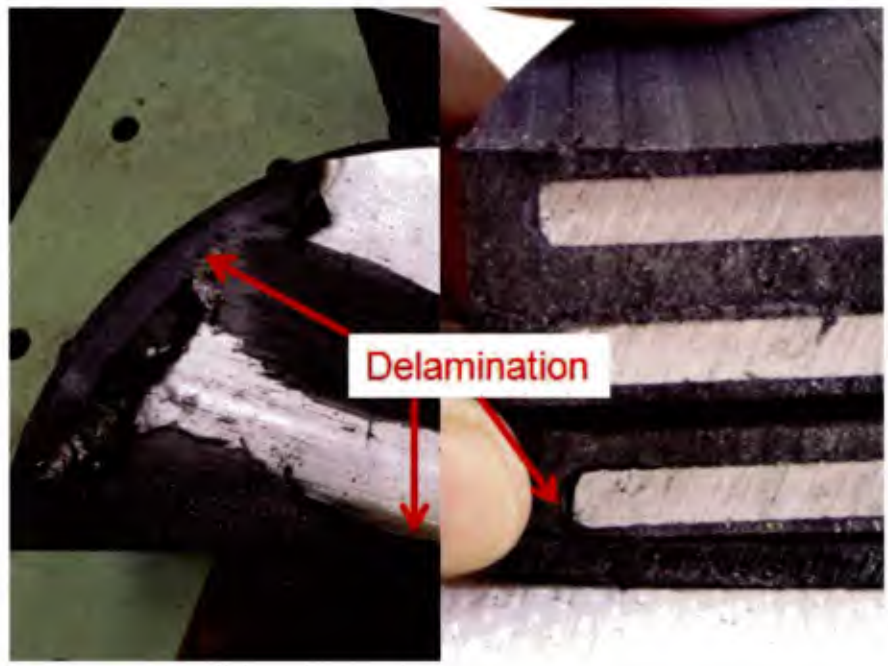

Figure 75: Delamination of the bearing Type 1-05

Fig. 76 shows the planar and vertical cutting surfaces of the bearing Type 1-02. There are more visible cavities on the planar surface, although their size is so small that they are barely recognizable with naked eye. On the vertical cutting surface they are easier to see and the difference between two bearings (1-02 and 1-05) is in this sense unambiguous. This bearing was subjected to the maximum tensile load among tested bearings and it did not fail during the tension test or at least it did not entirely lose the stiffness after experiencing the maximum force. From this cutting surface no sign of delamination was found. It is hard to believe that these small cavities reduce the stiffness of the bearing so radically, but as other studies such as [107] [108] [109] and [110] have shown, it is agreed upon that even the almost zero tensile stiffness (plateau in the force-displacement curves) can be caused solely by cavities. A plausible explanation of this radical degree of softening is due to the release of constraint on the deformability of rubber as cavities increase. Then those cavities would expand as the bearing is stretched further, which reduces the effective area and amplifies softening. The cavitation damage model described in the next Chapter is implemented based on this concept.

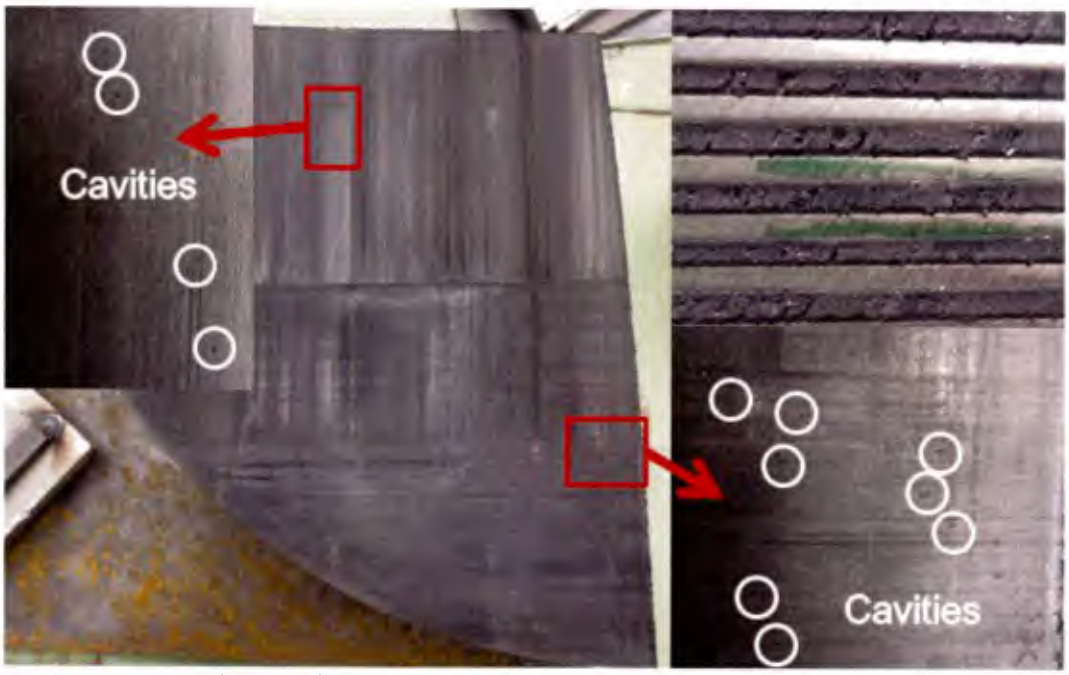

Figure 76: Cutting surface of the bearing Type 1-02

6 NUMERICAL ANALYSIS OF ELASTOMERIC BEARINGS

6.1 Preliminary

As explained in Chapter 3, it is quite a challenging task to comprehend the behaviour of rubber material. Unlike other solid material the rubber consists of flexible networks of long molecular chains. While these molecular chains are not fully stretched and the crystallization does not take place, its high elasticity is achieved by this molecular chain network structure. The undeformed chaotic network configuration possesses higher entropy and whenever it is deformed by external force, the network will return to the original chaotic configuration once this external force is gone. In other words, rubber returns to higher conformational entropy configuration (chaotic) from lower configuration (more organized). As molecular chains are stretched to their maximum length the conformational entropy is reduced almost to zero and the elasticity based on the force between atoms and molecules starts to be dominant. Under low temperature, rubber also behaves as a hard solid material because the entropy is reduced and as a result more inflexible organized network (crystallites) structure is formed. Both conditions coexist and the ratio of them changes depending upon the strain and the surrounding temperature. Therefore, the stress-strain curve of rubber material exhibits a highly non-linear behaviour. Moreover it is categorized as a viscoelastic material, which means the material behaviour also depends on the loading velocity. The energy loss, or the energy transition from the kinetic energy to the heat energy, has to be also taken into consideration. In the entropic elasticity-dominating condition, rubber is highly deformable and furthermore it is often referred to as an almost incompressible material. The problem for the simulation of rubber rises especially from this nearly incompressible characteristics because as it is explained in the next section the conventional displacement-based FE formulation, which is derived from the principle of virtual work, is not applicable. A high ratio of the bulk modulus to the shear modulus (or the Poission's ratio close to 0.5) results in generating unrealistically high stresses due to the so-called volumetric locking phenomenon. However this problem has been well known for long time and several alternative FE formulations have been suggested, which are proven as the effective remedies. In the next section the u/p formulation, one of the remedies for this problem introduced in [125] [126], is explained briefly, for this method is applied for analysis of (nearly) incompressible materials in the FE software ADINA, which is used for all simulation in this Chapter. Then some of the well-known hyperelastic material models that play a key role for the analysis of the highly nonlinear behaviour of rubber-like materials are described. Viscoelasticity and temperature-dependence of rubber, although they are also its important properties, are beyond the focus of this thesis. Mathematical formulation of such properties can be found in [113] for instance.

6.2 *U/P* Formulation

The name of u/p formulation stands for the fact that displacement u and pressure p are separately interpolated within this formulation as a remedy to avoid the volumetric locking. In this section the conventional displacement-based finite element formulation is first explained shortly for a comparison so that the advantages of u/p formulation can be better understood. The process of derivation of the finite element governing equation based on Hellinger-Reissner principle will follow.

Incompressible and nearly incompressible linear elastic solid

Here the variational finite element formulations are explained for the linear elastic body. The conventional displacement-based FE formulation is derived from the principle of virtual work as

described above. For the derivation of this principle, the external and the internal virtual works are equated and then its first variation with respect to displacements is obtained as

$$\partial\Pi(\mathbf{u}) = \int_{\Omega} \delta\mathbf{u}^{\mathrm{T}} \cdot \mathbf{L}^{\mathrm{T}} \cdot \mathbf{C} \cdot \mathbf{L} \cdot \mathbf{u} \mathrm{d}\Omega - \int_{\Omega} \delta\mathbf{u}^{\mathrm{T}} \cdot \bar{\mathbf{f}} \mathrm{d}\Omega - \int_{\partial\Omega_{\sigma}} \delta\mathbf{u}^{\mathrm{T}} \cdot \bar{\mathbf{F}} \mathrm{d}\partial\Omega = 0 \qquad (6.1)$$

where
u and δ**u**: displacement vector and its variation
L: differential operator matrix with respect to displacements
L*: differential operator matrix with respect to stresses
C: stress-strain material matrix
$\bar{\mathbf{f}}$: vector of the body forces
$\bar{\mathbf{F}}$: vector of the surface tractions
Ω: considered domain
$\partial\Omega_{\sigma}$: portion of the boundary of Ω with prescribed stresses

There can be more contributions of externally applied loading such as nodal concentrated loads and also the element initial stresses in this equation.
Discretisation of the displacement and the foces is performed by multiplying the same interpolation (trial) function matrix **N** such that

$$\mathbf{u} \simeq \mathbf{u}_{\mathrm{h}} = \mathbf{N}^{\mathrm{T}} \cdot \mathbf{U} \qquad (6.2)$$

$\mathbf{u}_{\mathrm{h}}$ is the discretised displacement vector and **U** is the nodal displacement vector. Hereafter subscript h denotes the discretised quantities. The discretised governing equation becomes

$$\begin{aligned} &\delta\mathbf{u}^{\mathrm{T}} \left(\left[\int_{\Omega} \mathbf{B}^{\mathrm{T}} \cdot \mathbf{C} \cdot \mathbf{B} \mathrm{d}\Omega \right] \mathbf{U} - \int_{\Omega} \mathbf{N}_{\partial\Omega_{\sigma}}^{\mathrm{T}} \cdot \bar{\mathbf{f}} \mathrm{d}\Omega - \int_{\partial\Omega_{\sigma}} \mathbf{N}^{\mathrm{T}} \cdot \bar{\mathbf{F}} \mathrm{d}\partial\Omega \right) = 0 \quad \because \mathbf{B} = \mathbf{N}^{\mathrm{T}} \cdot \mathbf{L}^{\mathrm{T}} \\ &\mathbf{K} \cdot \mathbf{U} = \mathbf{R} \quad \because \mathbf{K} = \int_{\Omega} \mathbf{B}^{\mathrm{T}} \cdot \mathbf{C} \cdot \mathbf{B} \mathrm{d}\Omega, \quad \mathbf{R} = \int_{\Omega} \mathbf{N}_{\partial\Omega_{\sigma}}^{\mathrm{T}} \cdot \bar{\mathbf{f}} \mathrm{d}\Omega - \int_{\partial\Omega_{\sigma}} \mathbf{N}^{\mathrm{T}} \cdot \bar{\mathbf{F}} \mathrm{d}\partial\Omega \end{aligned} \qquad (6.3)$$

$\mathbf{N}_{\partial\Omega_{\sigma}}^{\mathrm{T}}$ is the surface displacement interpolation (trial) function matrix which can be obtained from the displacement shape function matrix **N**.
This displacement-based finite element formulation is simple and straightforward, and is frequently adopted. The fact that the displacements are the only solution variables is, on the one hand, quite an attractive feature because other variables such as stresses and strains can be obtained once the displacements are calculated. On the other hand, this formulation lacks in flexibilities. The aforementioned locking problem stems from so-called "parasitic stresses" [127] which do not belong to the exact solution of the certain situation but nevertheless appear in a finite element based on the principle of virtual work as a result of a failure of interpolation of certain physical quantities. Interpolation of displacements is not necessarily wrong but parasitic stresses show up in some specific conditions due to the difference in integration order of displacements and strains, hence stresses. This phenomenon, which is mainly based on kinematic or geometric effects, can be categorized into transverse shear locking, shear locking and membrane locking according to their causes. The volumetric locking appears depending upon the material constant, i.e. Poisson's ratio *v*. The critical parameter is the volume change ratio, bulk modulus E_b=E/(3-6*v*). In linear elastic

theory it is assumed that the pressure is proportional to the bulk modulus and it goes to infinite as $\nu \rightarrow 0.5$, in case of total incompressibility. Thus the volumetric strain cannot be predicted as accurately as displacements if it is obtained by derivatives of displacements. That means that even if displacements are interpolated discreetly, errors might appear in the volumetric strain and that, in turn, becomes the root of enormous error in stresses. This mathematical ill-condition leads to a very high stresses and the total system would behave much stiffer than it should.
The first step of remedies to this problem is to "relax" the governing equation. In other words, other solution variables such as strains or/and stresses are introduced to the energy potential so that interpolation at different integration levels are achieved separately. One of the well-known "relaxed" formulations of finite elements is the Hu-Washizu functional.

$$\begin{aligned}\Pi_{\mathrm{HW}}(\mathbf{u},\boldsymbol{\varepsilon},\boldsymbol{\sigma}) = \int_{\Omega}\left[\frac{1}{2}\boldsymbol{\varepsilon}^{\mathrm{T}}\cdot\mathbf{C}\cdot\boldsymbol{\varepsilon}+\boldsymbol{\sigma}^{\mathrm{T}}\cdot\left(\mathbf{L}\cdot\mathbf{u}-\boldsymbol{\varepsilon}\right)-\mathbf{u}^{\mathrm{T}}\cdot\bar{\mathbf{f}}\right]\mathrm{d}\Omega \\ -\int_{\partial\Omega_{\sigma}}\bar{\mathbf{F}}^{\mathrm{T}}\cdot\mathbf{u}\,\mathrm{d}\partial\Omega-\int_{\partial\Omega_{\mathrm{u}}}\boldsymbol{\sigma}^{\mathrm{T}}\cdot\mathbf{n}\cdot\left(\mathbf{u}-\hat{\mathbf{u}}\right)\mathrm{d}\partial\Omega=\mathrm{stat.}\end{aligned} \tag{6.4}$$

Where $\hat{\mathbf{u}}$ is the prescribed displacements, $\boldsymbol{\sigma}$ is the Cauchy stresses and $\boldsymbol{\varepsilon}$ is the infinitesimal strains. $\partial\Omega_{\mathrm{u}}$ is the portion of the boundary of Ω with prescribed displacements

Invoking the stationary of Π_{HW} with respect to $\mathbf{u}$, $\boldsymbol{\varepsilon}$ and $\boldsymbol{\sigma}$, its first variation is obtained as,

$$\begin{aligned}\partial\Pi_{\mathrm{HW}}(\mathbf{u},\boldsymbol{\varepsilon},\boldsymbol{\sigma}) = \int_{\Omega}\left[\left(\delta\mathbf{u}^{\mathrm{T}}\cdot\mathbf{L}^{\mathrm{T}}\right)\cdot\boldsymbol{\sigma}-\delta\mathbf{u}^{\mathrm{T}}\cdot\bar{\mathbf{f}}-\delta\boldsymbol{\sigma}^{\mathrm{T}}\cdot\left(\boldsymbol{\varepsilon}-\mathbf{L}\cdot\mathbf{u}\right)-\delta\boldsymbol{\varepsilon}^{\mathrm{T}}\cdot\left(\boldsymbol{\sigma}-\mathbf{C}\cdot\boldsymbol{\varepsilon}\right)\right]\mathrm{d}\Omega \\ -\int_{\partial\Omega_{\sigma}}\delta\mathbf{u}^{\mathrm{T}}\cdot\bar{\mathbf{F}}\,\mathrm{d}\partial\Omega-\int_{\partial\Omega_{\mathrm{u}}}\delta\boldsymbol{\sigma}^{\mathrm{T}}\cdot\mathbf{n}\cdot\left(\mathbf{u}-\hat{\mathbf{u}}\right)\mathrm{d}\partial\Omega=0\end{aligned} \tag{6.5}$$

Unlike the principle of virtual work, here all equations, kinematic equation, material law, force and displacement boundary conditions and equilibrium, are satisfied in a weak (approximate) sense. This functional provides possibility to interpolate displacements, strains and stresses independently and hence is most flexible. Hu-Washizu functional is the basis of the enhanced assumed strain method for instance.
The basis of the mixed or hybrid methods is the Hellinger-Reissner principle, which is obtained by imposing the material law, namely $\boldsymbol{\sigma}=\mathbf{C}\cdot\boldsymbol{\varepsilon}$, to the Hu-Washizu functional. That means that the material law is satisfied in a strong (exact) sense and therefore it provides a little less flexibility in selecting the interpolation possibilities than Hu-Washizu principle. Assuming also that the displacement boundary conditions are satisfied exactly, the Hellinger-Reissner functional is expressed as

$$\Pi_{\mathrm{HR}}(\mathbf{u},\boldsymbol{\varepsilon}) = \int_{\Omega}\left[-\frac{1}{2}\boldsymbol{\varepsilon}^{\mathrm{T}}\cdot\mathbf{C}\cdot\boldsymbol{\varepsilon}+\boldsymbol{\varepsilon}^{\mathrm{T}}\cdot\mathbf{C}\cdot\left(\mathbf{L}^{\mathrm{T}}\cdot\mathbf{u}\right)-\mathbf{u}^{\mathrm{T}}\cdot\bar{\mathbf{f}}\right]\mathrm{d}\Omega+\int_{\partial\Omega_{\sigma}}\mathbf{u}^{\mathrm{T}}\cdot\bar{\mathbf{F}}\,\mathrm{d}\partial\Omega=\mathrm{stat.} \tag{6.6}$$

It would be straightforward to derive the first variation with respect to $\mathbf{u}$ and $\boldsymbol{\varepsilon}$ at this stage but instead the strains are divided into the deviatoric part $\boldsymbol{\varepsilon}_{\mathrm{D}}$ and the volumetric part $\boldsymbol{\varepsilon}_{\mathrm{V}}$ first for the mixed u/p formulation as

$$\boldsymbol{\varepsilon}=\boldsymbol{\varepsilon}_{\mathrm{D}}+\boldsymbol{\varepsilon}_{\mathrm{V}} \tag{6.7}$$

$\boldsymbol{\varepsilon}_V$ has only identical diagonal components with the value of $1/3\varepsilon_{ii}=\varepsilon_V$ and its trace is equivalent to the ratio of volume change $\mathrm{tr}(\boldsymbol{\varepsilon}_V)=\Delta V/V$. Then $\boldsymbol{\varepsilon}_D$ can be also defined as

$$\boldsymbol{\varepsilon}_D = \boldsymbol{\varepsilon} - \frac{1}{3}\varepsilon_V \boldsymbol{\delta} \tag{6.8}$$

$\boldsymbol{\delta}$ is the vector of Kronecker delta symbol. In linear elastic theory, the pressure p is calculated with the bulk modulus E_b as

$$p = -E_b \varepsilon_V = -\frac{\mathrm{tr}(\boldsymbol{\sigma})}{3} \tag{6.9}$$

Specializing the Hellinger-Reissner functional by separating strains into deviatoric and volumetric parts

$$\Pi_{HR}(\mathbf{u}, p) = \int_\Omega \left[\frac{1}{2}\boldsymbol{\varepsilon}_D^T \cdot \mathbf{C}_D \cdot \boldsymbol{\varepsilon}_D - \frac{1}{2}\frac{p^2}{E_b} - p\varepsilon_V \right] d\Omega + \int_\Omega \mathbf{u}^T \cdot \bar{\mathbf{f}}\, d\Omega + \int_{\partial\Omega_\sigma} \mathbf{u}^T \cdot \bar{\mathbf{F}}\, d\partial\Omega \tag{6.10}$$

where $\mathbf{C}_D$ is the stress-strain material matrix for the deviatoric stress and strain components.

The first variation of the functional with respect to the displacements and pressure is

$$\partial\Pi_{HR}(\mathbf{u}, p) = \int_\Omega \left[\delta\boldsymbol{\varepsilon}_D^T \cdot \mathbf{C}_D \cdot \boldsymbol{\varepsilon}_D + p\delta\varepsilon_V + \delta p\left(\frac{p}{E_b} + \varepsilon_V \right) \right] d\Omega + \mathcal{R} = 0 \tag{6.11}$$

where $\mathcal{R}$ is the virtual work of externally applied loads.

Now solution variables are displacements and pressure. Because of the condition (6.9), two sets of equations are obtained

$$\begin{aligned} &\int_\Omega \left(\delta\boldsymbol{\varepsilon}_D^T \cdot \mathbf{C}_D \cdot \boldsymbol{\varepsilon}_D + p\delta\varepsilon_V \right) d\Omega = \mathcal{R} \\ &\int_\Omega \delta p \left(\frac{p}{E_b} + \varepsilon_V \right) d\Omega = 0 \end{aligned} \tag{6.12}$$

Imposing the kinematic condition further on this set of equations, the discretisation takes the forms as follows

$$\mathbf{u} \simeq \mathbf{u}_h = \mathbf{N}^T \cdot \mathbf{U} \tag{6.13}$$

$$\boldsymbol{\varepsilon}_{Dh} = \mathbf{N}^T \cdot \boldsymbol{\varepsilon}_D = \mathbf{B}_D \cdot \mathbf{U}, \quad \boldsymbol{\varepsilon}_{Vh} = \mathbf{N}^T \cdot \boldsymbol{\varepsilon}_V = \mathbf{B}_V \cdot \mathbf{U} \tag{6.14}$$

$$p_h = \mathbf{N}_p \cdot \mathbf{P} \tag{6.15}$$

$\mathbf{N}_p$ is the shape (trial) function matrix for pressure and $\mathbf{P}$ is the pressure variables vector. Then the discretised governing equation finally becomes

$$\left[\int_{\Omega}\mathbf{B}_D^T\cdot\mathbf{C}_D\cdot\mathbf{B}_D\,d\Omega\right]\mathbf{U}-\left[\int_{\Omega}\mathbf{B}_V^T\cdot\mathbf{N}_p\,d\Omega\right]\mathbf{P}=\mathbf{R}$$
$$\left[\int_{\Omega}\mathbf{N}_p^T\cdot\frac{1}{E_b}\cdot\mathbf{N}_p\,d\Omega\right]\mathbf{P}-\left[\int_{\Omega}\mathbf{N}_p\cdot\mathbf{B}_V\,d\Omega\right]\mathbf{U}=0 \qquad (6.16)$$
$$\begin{bmatrix}\mathbf{K}_u & \mathbf{K}_{up}\\ \mathbf{K}_{pu} & \mathbf{K}_p\end{bmatrix}\cdot\begin{bmatrix}\mathbf{U}\\ \mathbf{P}\end{bmatrix}=\begin{bmatrix}\mathbf{R}\\ 0\end{bmatrix}$$
$$\because \mathbf{K}_u=\int_{\Omega}\mathbf{B}_D^T\cdot\mathbf{C}_D\cdot\mathbf{B}_D\,d\Omega,\quad \mathbf{K}_{up}=\mathbf{K}_{pu}^T=-\int_{\Omega}\mathbf{B}_V^T\cdot\mathbf{N}_p\,d\Omega,\quad \mathbf{K}_p=-\int_{\Omega}\mathbf{N}_p^T\cdot\frac{1}{E_b}\cdot\mathbf{N}_p\,d\Omega$$

Total incompressibility, i.e. ν=0.5 is treated as the special case of this formulation by setting $\mathbf{K}_p$=0. In his book [126] Bathe studied the efficiency and accuracy of this modified formulation for all possible combination of elements with various pressure interpolation functions numerically and theoretically. Bathe concluded that the element with 27 displacement nodes and 4 pressure nodes for a three dimensional element in which the linear interpolation function for pressure is adopted is optimal choice. In ADINA manual it is written that either that element or another element with 8 displacement nodes and 1 pressure node are recommended for the analysis of hyperelastic material. The latter element seems to predict reasonably good displacements but the constant pressure assumption may result in inaccurate stresses [125] [126]. The problem of 27/4-element is that the calculation becomes highly expensive and therefore the usage of the 8/1-elements with relatively fine mesh would be more reasonable in practise. For both element types, the pressure variables only pertain to the considered element because pressure nodes are located within the element not on the boundary nodes. Thus the pressure variables can be statically condensed out within each element level before assembling the elements.

Incompressible and nearly incompressible hyperelastic (nonlinear elastic) body

For the analysis of the nonlinear elastic body, the internal energy term is expressed with an incremental potential energy (strain energy function) in terms of the second Piola-Kirchhoff stresses and Green-Lagrange strains. This is expressed as

$$d\,{}_o^t\bar{W} = {}_o^t\bar{S}_{ij}\,d\,{}_o^te_{ij} \qquad (6.17)$$

where ${}_o^t\bar{S}_{ij}$ are the components of the second Piola-Kirchhoff stress tensor, ${}_o^te_{ij}$ are the components of the Green-Lagrange strain tensor, and ${}_o^t\bar{W}$ represents the strain energy per unit original volume. The left subscript 'o' denotes 'referred to the original configuration', the left superscript denotes the configuration at time t, and over bar denotes that the quantities are computed from the displacement field. Now incremental material tensor is

$${}_o\bar{C}_{ijrs}=\frac{\partial\,{}_o^t\bar{S}_{ij}}{\partial\,{}_o^t\varepsilon_{ij}}=\frac{\partial^2\,{}_o^t\bar{W}_v}{\partial\,{}_o^t\varepsilon_{ij}\partial\,{}_o^t\varepsilon_{rs}}={}_o\bar{C}_{rsij} \qquad (6.18)$$

Due to the symmetric property of the second Piola-Kirchhoff stresses, the potential-based u/p formulation generates symmetric element tangent stiffness matrices. The governing equation in terms of the potential is described as

$$\delta\left(\int_{{}^{0}\Omega} {}_{0}^{t}\bar{W}\,{}^{0}d\Omega\right) = {}^{t}\mathcal{R}. \tag{6.19}$$

Analogous to the linear elastic material case, the pressure obtained by the displacements and by separate interpolation must be related. A penalty function ${}_{0}^{t}Q$, which is equivalent of Eq. (6.9) for the linear elastic solid, is introduced for that purpose. Then the governing equation becomes:

$$\delta\left(\int_{{}^{0}\Omega}\left({}_{0}^{t}\bar{W} + {}_{0}^{t}Q\right){}^{0}d\Omega\right) = {}^{t}\mathcal{R}. \tag{6.20}$$

The determination of the additional function is based on the requirements that are imposed as the modification of the strain energy function is carried out so as to ensure that the possibly inaccurate pressure computed from displacements are removed, the separately interpolated pressure have the correct physical meaning. Thus the solution from the u/p formulation includes the displacement-based formulation as its special case if the pressure computed from the displacement field and the separately interpolated pressure are equal. Details of derivation can be found in [125] and [126]. The simplest function in case of an isotropic material suggested in [125] and [126] is

$${}_{0}^{t}Q = -\frac{1}{2E_b}\left({}^{t}\bar{p} - {}^{t}\tilde{p}\right)^2 \tag{6.21}$$

For the application to the finite element analysis the governing incremental equations of motion in matrix form are

$$\begin{bmatrix} {}^{t}\mathbf{K}_{u} & {}^{t}\mathbf{K}_{up} \\ {}^{t}\mathbf{K}_{pu} & {}^{t}\mathbf{K}_{p} \end{bmatrix}\begin{bmatrix} \hat{\mathbf{U}} \\ \hat{\mathbf{P}} \end{bmatrix} = \begin{bmatrix} {}^{t+\Delta t}\mathbf{R} \\ 0 \end{bmatrix} - \begin{bmatrix} {}^{t}\mathbf{F}_{u} \\ {}^{t}\mathbf{F}_{p} \end{bmatrix}, \tag{6.22}$$

where ${}^{t+\Delta t}\mathbf{R}$ are the nodal point forces corresponding to the external loading at time t+Δt, $\hat{\mathbf{U}}$ and $\hat{\mathbf{P}}$ are vectors which keep the increments in the nodal point displacements ${}^{t}u_i \simeq {}^{t}\hat{u}_i = N_i\,{}^{t}u_i$ and the pressure variables ${}^{t}p = N_{p,i}\,{}^{t}\hat{p}_i$. Other terms contain the entries such as

$${}^{t}F_{u,i} = \frac{\partial}{\partial {}^{t}\hat{u}_i}\left[\int_{{}^{0}\Omega}\left({}_{0}^{t}\bar{W} + \frac{1}{2E_b}\left({}^{t}\bar{p} - {}^{t}\tilde{p}\right)^2\right)d\,{}^{0}\Omega\right] = \int_{{}^{0}\Omega}\left(\frac{\partial\,{}_{0}^{t}\bar{W}}{\partial\,{}^{t}\hat{u}_i}\right)d\,{}^{0}\Omega = \int_{{}^{0}\Omega} {}^{0}S_{kl}\frac{\partial\,{}_{0}^{t}\varepsilon_{kl}}{\partial\,{}^{t}\hat{u}_i}d\,{}^{0}\Omega, \tag{6.23}$$

$${}^{t}F_{p,i} = \frac{\partial}{\partial\,{}^{t}\hat{p}_i}\left[\int_{{}^{0}\Omega}\left({}_{0}^{t}\bar{W} + \frac{1}{2E_b}\left({}^{t}\bar{p} - {}^{t}\tilde{p}\right)^2\right)d\,{}^{0}\Omega\right] = \frac{1}{E_b}\int_{{}^{0}\Omega}\left({}^{t}\bar{p} - {}^{t}\tilde{p}\right)\frac{\partial\,{}^{t}\tilde{p}}{\partial\,{}^{t}\hat{p}_i}d\,{}^{0}\Omega, \tag{6.24}$$

$${}^{t}K_{u,ij} = \frac{\partial {}^{t}F_{u,i}}{\partial\,{}^{t}\hat{u}_j} = \int_{{}^{0}\Omega} {}^{0}CUU_{klrs}\frac{\partial\,{}_{0}^{t}\varepsilon_{kl}}{\partial\,{}^{t}\hat{u}_i}\frac{\partial\,{}_{0}^{t}\varepsilon_{rs}}{\partial\,{}^{t}\hat{u}_j}d\,{}^{0}\Omega + \int_{{}^{0}\Omega} {}^{0}S_{kl}\frac{\partial^2\,{}_{0}^{t}\varepsilon_{kl}}{\partial\,{}^{t}\hat{u}_i\partial\,{}^{t}\hat{u}_j}d\,{}^{0}\Omega, \tag{6.25}$$

$$
\begin{aligned}
{}^{t}K_{up,ij} &= \frac{\partial {}^{t}F_{u,i}}{\partial {}^{t}\hat{p}_j} = \int_{{}^{o}\Omega} {}_{o}\frac{1}{E_b}\frac{\partial {}^{t}\bar{p}}{\partial {}_{o}{}^{t}\varepsilon_{kl}}\frac{\partial {}_{o}{}^{t}\varepsilon_{kl}}{\partial {}^{t}\hat{u}_i}\frac{\partial {}^{t}\tilde{p}}{\partial {}^{t}\hat{p}_j}\,d\,{}^{o}\Omega \\
&= \frac{\partial {}^{t}F_{p,j}}{\partial {}^{t}\hat{u}_i} = {}^{t}K_{pu,ji}
\end{aligned}
\quad , \tag{6.26}
$$

$$
{}^{t}K_{p,ij} = \frac{\partial {}^{t}F_{p,i}}{\partial {}^{t}\hat{p}_j} = -\int_{{}^{o}\Omega} {}_{o}\frac{1}{E_b}\frac{\partial {}^{t}\tilde{p}}{\partial {}^{t}\hat{u}_i}\frac{\partial {}^{t}\tilde{p}}{\partial {}^{t}\hat{u}_j}\,d\,{}^{o}\Omega . \tag{6.27}
$$

where functions ${}_{o}CUU_{klrs}$, and ${}_{o}^{t}S_{kl}$ are defined as follows:

$$
{}_{o}CUU_{kl} = {}_{o}\bar{C}_{klrs} - \frac{1}{E_b}\frac{\partial {}^{t}\bar{p}}{\partial {}_{o}{}^{t}\varepsilon_{kl}}\frac{\partial {}^{t}\bar{p}}{\partial {}_{o}{}^{t}\varepsilon_{rs}} - \frac{1}{E_b}\left({}^{t}\bar{p} - {}^{t}\tilde{p}\right)\frac{\partial^2 {}^{t}\bar{p}}{\partial {}_{o}{}^{t}\varepsilon_{kl}\partial {}_{o}{}^{t}\varepsilon_{rs}} \tag{6.28}
$$

$$
{}_{o}^{t}S_{kl} = {}_{o}^{t}\bar{S}_{kl} - \frac{1}{E_b}\left({}^{t}\bar{p} - {}^{t}\tilde{p}\right)\frac{\partial {}^{t}\bar{p}}{\partial {}_{o}{}^{t}\varepsilon_{kl}} . \tag{6.29}
$$

The following two conditions for all degree of freedom i assure that equilibrium is satisfied.

$$
0 = {}^{t}\mathcal{R}_i - \int_{{}_{o}V} {}_{o}^{t}S_{kl}\frac{\partial {}_{o}{}^{t}\varepsilon_{kl}}{\partial \hat{u}_i}\,{}^{o}dV \text{ and } 0 = -\int_{{}_{o}V}\frac{1}{E_b}\left({}^{t}\bar{p} - {}^{t}\tilde{p}\right)\frac{\partial \tilde{p}}{\partial \hat{p}_i}\,{}^{o}dV \tag{6.30}
$$

Eq. (6.30) is the detailed version of the governing equation (6.20) for u/p formulation. Left one represents the principle of virtual work with the modified stress tensor expressed by Eq. (6.29) which is basically computed from displacements but pressure computed from the displacements is subtracted. With this modification, the pressure calculated from this stress tensor is equal to the value obtained by separately interpolated pressure. The right hand side of Eq. (6.30) imposes the constraint condition on the governing equation relating the separately interpolated pressure to the pressure computed from displacements. This constraint condition ensures that the stress-strain relationship is satisfied on average within each element but not each point. In a sense this "weakens" the governing equation by increasing the flexibility in the stress-strain relationship.

6.3 Hyper Elastic Material Models

As the engineering rate of usage of rubber material increases the demand of capturing its actual behaviour becomes more and more important. However the material model that represents highly nonlinear characteristics of rubber remains a challenging task for researchers.

One of the first attempts was made based on the thermodynamic material concept of Guth and Mark [128], Kuhn [129]. As described shortly in Chapter 4, rubber materials are regarded as dominantly entropic in wide strain range before the strain-induced crystallization starts or the maximum extensibility of the molecular chains are reached. The deformation can be associated with the change in the conformational or configuration entropy $\Delta\Psi$ of molecular chains, which varies proportionally to the change in the Helmholz free energy ΔH for an isothermal process as

$$
\Delta H = -T \cdot \Delta\Psi \tag{6.31}
$$

In the aforementioned articles [128] [129] the conformational entropy is first calculated for a single molecular chain detached from the network system at the two cross-linked tie points. By the use of the Bolzmann's equation and the probability P(r) that the end-tie-point P_E lies within the infinitesimal volume element of size dv at P_E if the other tie point P_O is assumed to be a fixed original point, this entropy is expressed as

$$\Psi = \Psi_0 + k \ln P(r) \tag{6.32}$$

where Ψ_0 denotes an initial constant entropy in the reference configuration and k is the Bolzmann's constant.

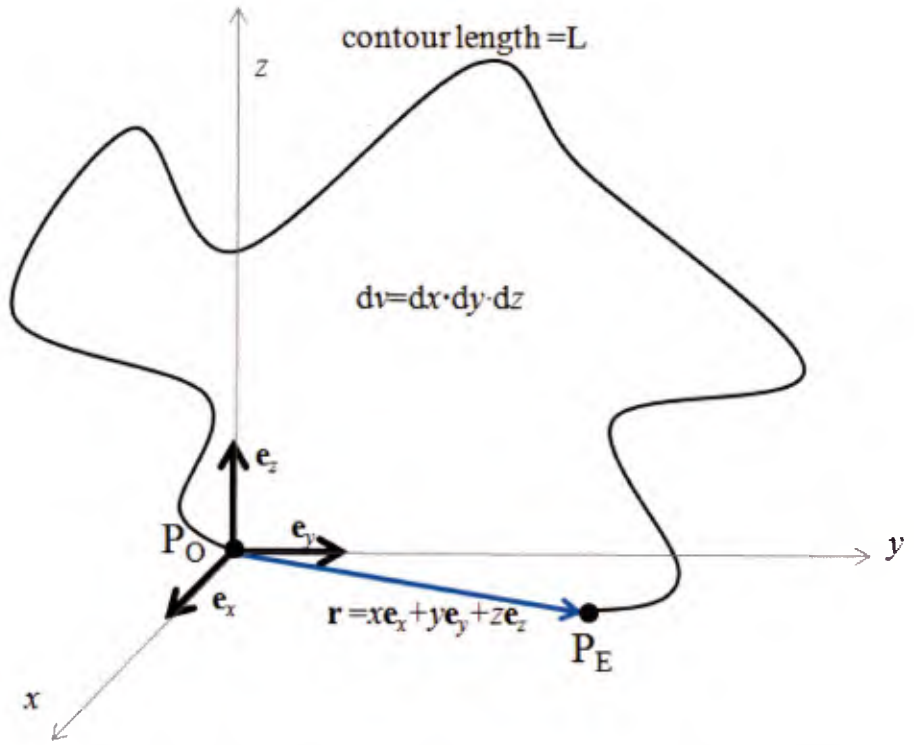

Figure 77: A representative single molecular chain detached out of the network at the two cross-linked point P_O and P_E

The probability is calculated by the Gaussian distribution function assuming that this end-to-end distance r is considerably less than the contour length L as

$$P(r)dxdydz = \frac{b^3}{\pi^{2/3}} \exp(-b^2 r^2)dxdydz \tag{6.33}$$

with which the change in the conformational entropy is obtained as

$$\Delta\Psi = \Psi_0 + k \ln P(r) - \{\Psi_0 + k \ln P(r_0)\} = k \ln P(\Delta r) \tag{6.34}$$

where b is the representative length of the considered Gaussian chain detached from the network defined as $b^2 = 3/(2\bar{r}_{out}^2)$ and r_0 is the end-to-end distance of the molecular chain in undeformed configuration. $\bar{r}_{out}^2$ is the mean-square value of the end-to-end distance of the un-cross-linked free molecular chain.

Numerical and experimental analysis of the load-carrying behaviour of laminated elastomeric bearings as seismic isolators

For the estimation of $P(\Delta r)$ in Eq. (6.34), only the term related to the change in r is necessary so that $\ln P(\Delta r)=-b^2\ \Delta r^2$. The original end-to-end distance r_0 in a three dimensional Cartesian coordinates field, for instance, can be expressed as $r_0^2=x_0^2+y_0^2+z_0^2$. In the deformed configuration, the position of one end of the chain is defined by multiplying the original position to principal stretches λ_i so that

$$\Delta r^2 = (\lambda_1^2 - 1)x_0^2 + (\lambda_2^2 - 1)y_0^2 + (\lambda_3^2 - 1)z_0^2 \tag{6.35}$$

Next this procedure is applied back to the body consisting of the whole cross-linked molecular networks where the deformation of the body is associated with the change in the length of the whole network or in other words, the change in the conformational entropy. With this method the entropic change for each segment of a molecular chain is obtained as mean value for all segments and all chains assuming affine motion and total incompressibility of the body. Then the total entropic change in a unit volume is obtained by multiplying the mean entropic change to the length of a molecular chain and the number of molecular chains consisting of this unit volume. If n_V molecular chains exist in that body, it can be assumed that the sum of end-to-end distance of each chain $\sum_1^{n_V} r_{0in}^2$ is equal to $n_V \bar{r}_{0in}^2$ and also

$$\sum_1^{n_V} x_0^2 = \sum_1^{n_V} y_0^2 = \sum_1^{n_V} z_0^2 = n_v \cdot 1/3\bar{r}_{0in}^2 \tag{6.36}$$

since in the undeformed configuration the molecular chains are arranged randomly without preference in directions (assumption of isotropy). Here $\bar{r}_{0in}^2$ is the mean-square value of the end-to-end distance r_{0in} for the whole assembly of chains in the body and it has to be distinguished from $\bar{r}_{out}^2$. Inserting these relationships into Eq. (6.34), the change in the conformational entropy in the whole assembly of cross-linked molecular networks in the unit body is expressed as

$$\Delta\Psi = -\frac{1}{2} n_V k \frac{\bar{r}_{0in}^2}{\bar{r}_{out}^2}\left(\lambda_1^2 + \lambda_2^2 + \lambda_3^2 - 3\right) \tag{6.37}$$

The term $\bar{r}_{0in}^2 / \bar{r}_{out}^2$ can be considered as a conversion factor from the single chain system to the whole system since some constraint must be applied to account for the difference in the end-to-end distances of a molecular segment (between two cross-linked points) out of the free single chain system and the whole networks of cross-linked chains.
Inserting (6.37) into the relationship (6.31), the following expression of energy based on the thermodynamic theory and the Gaussian statistical theory is finally obtained.

$$H = \frac{1}{2} n_V kT \frac{\bar{r}_{0in}^2}{\bar{r}_{out}^2}\left(\lambda_1^2 + \lambda_2^2 + \lambda_3^2 - 3\right) \tag{6.38}$$

This expression is the strain energy function of the classical Neo-Hookean material model by setting

$$G = n_V kT \frac{\bar{r}_{0in}^2}{\bar{r}_{out}^2} \tag{6.39}$$

When a single parameter, such as the shear modulus, controls the material behaviour, it is very practical material model. However the Gaussian distribution function includes increasing error as the end-to-end distance r of the molecular chain segment approaches its full contour length and hence it delivers reliable results only within a small strain range. For instance in a typical S-shaped stress-strain curve of rubber material, this strain range refers to the region below the second curve starts where an acute increase in stress is observed. Physically this is the turning point from "entropic region" to "elastic region". In his book [130], Treloar mentioned that this acute increase in stress occurs because the network structure of molecular chains reaches its maximum extensibility and therefore the behaviour of rubber is dominantly elastic from this point on. The crystallization contributes to the hardening but it occurs first at much higher strain and therefore the effect can be taken as secondary one. In the same book [130] he referred to the former region "Gaussian region" and the latter "Non-Gaussian region" indicating the validity of the Gaussian statistical theory. The derivation of (6.38) described here is based on the reference [113] and thus please refer to the book for further details.
Various constitutive equations for hyperelastic materials have been proposed to obtain better fitting including this non-Gaussian region. Unlike the theory explained above the majority of them are based purely on mathematical reasoning. One of the earliest phenomenological models which had been further developed by different researchers is the Mooney model. Again assuming the total incompressibility of the body, the strain energy density function is defined by two constants and first two strain invariants as

$$W = C_1({}_o^tI_1 - 3) + C_2({}_o^tI_2 - 3) \tag{6.40}$$

where C_i are material constants which have to be determined experimentally and. I_i are invariants defined as.

$$I_1 = \lambda_1^2 + \lambda_2^2 + \lambda_3^2 \tag{6.41}$$

$$I_2 = \lambda_1^2\lambda_2^2 + \lambda_2^2\lambda_3^2 + \lambda_3^2\lambda_1^2 \tag{6.42}$$

$$I_3 = \lambda_1^2\lambda_2^2\lambda_3^2 \text{ (=1 in case of incompressibility).} \tag{6.43}$$

Rivlin, pursuing the basic assumption of Mooney that the material is incompressible and that it is isotropic in the unstrained state, added the higher order terms which can be generalised as

$$W = \sum_{i=0,j=0}^{\infty} C_{ij}({}_o^tI_1 - 3)^i({}_o^tI_2 - 3)^j \tag{6.44}$$

with $C_{00}=0$

This is therefore often named the Mooney-Rivlin material model. There are a number of other suggested material models on the basis of the concept of Mooney with these strain invariants [130][113] but they are not explained further here. For this material model within a small strain range the material constants and the shear modulus or Young's modulus assuming the total incompressibility of the material has the relation

Numerical and experimental analysis of the load-carrying behaviour of laminated elastomeric bearings as seismic isolators

$$G = 2(C_1 + C_2) \tag{6.45}$$

$$E = 6(C_1 + C_2)\,. \tag{6.46}$$

Another well-known phenomenological material model was introduced by Ogden [131]. Instead of restricting the strain energy density function in terms of strain invariants, that of Odgen's material model is based on the principal stretches themselves.

$$W = \sum_{n=1}^{\infty}\left(\frac{\mu_{o,n}}{\alpha_{o,n}}(\lambda_1^{\alpha_{o,n}} + \lambda_2^{\alpha_{o,n}} + \lambda_3^{\alpha_{o,n}} - 3)\right) \tag{6.47}$$

where $\alpha_{o,n}$ and $\mu_{o,n}$ are material constants which have to be determined by fitting the experimental results.

Apart from these purely phenomenological material models, there exist some models such as three-chain model and four chain model whose formulation was motivated by the theoretical insight of the molecular structure of rubber. These models have been studied, compared and discussed in [130], [132], [133] and [134]. In the three-chain model concept three molecular chains are arranged in a cubic element along with three perpendicular axes, whereas in the four-chain model concept four of them are arranged in a tetrahedral element from each corner to the junction point within the element. The configurational entropy is again calculated based on the statistical theory depending upon the deformation of these three- or four chains, respectively. Here a more suitable representation of the probability density function than Gaussian statistical theory is used. If fitted to a single deformation state (either uniaxial tension, equi-biaxial tension or shear) both of them can represent the non-Gaussian behaviour of the same deformation state [130] but in [133] and [134] it is argued that neither of them can actually captures the real relation of the three principal strains of the element from these chain configurations. They suggested an improved material model with a new configuration whose cubic element has eight chains connected from the centre to each corner of the element. Following the Langevin statistics by Kuhn and Grün [135], the change in entropy is expressed as

$$\Delta S = -n_V k \frac{\bar{r}_{0in}^2}{\bar{r}_{out}^2}\left[n_l\left(\frac{r}{n_l l}\beta_L + \ln\frac{\beta_L}{\sinh\beta_L}\right)\right];\quad \beta_L = L^{-1}(r/n_l l)\,, \tag{6.48}$$

where r is the current length of a stretched chain, n_l is the number of statistical segment of length l in a chain between chemical crosslinks, β_L is the inverse Langevin function. Langevin function is defined as

$$L(r/n_l l) = \coth(r/n_l l) - 1/(r/n_l l) \tag{6.49}$$

The work of deformation is proportional to the change in configurational entropy and the temperature. Hence

$$W = n_V kT \frac{\bar{r}_{0in}^2}{\bar{r}_{out}^2}\left[n_l\left(\frac{r}{n_l l}\beta_L + \ln\frac{\beta_L}{\sinh\beta_L}\right)\right]. \tag{6.50}$$

Using the series of expansion form for the inverse Langevin function and the relationship (6.39), the final form of their proposed strain energy function in the first five terms is

$$W = G\left[\frac{1}{2}(I_1 - 3) + \frac{1}{20n}(I_1^2 - 9) + \frac{11}{1050n^2}(I_1^3 - 27) + \frac{19}{7000n^3}(I_1^4 - 81) + \frac{1}{673750n^4}(I_1^5 - 243) + \cdots\right] \tag{6.51}$$

This material model is also available in ADINA as Arruda-Boyce material model. Its input parameters are only two, i.e. the initial shear modulus G and the locking stretch $\lambda=n^{0.5}$. If only the first term is considered, the classical Neo-Hookean material based on Gaussian chain statistic is obtained.

All of material models described above are based on the assumption of the total incompressibility of rubber, i.e. $I_3=1$ is assumed. However this strict assumption does not always align with the real behaviour of rubber and thus it is important to take slight volumetric change into account for the analysis of filled rubber materials that are often used in engineering purposes since they exhibit often more compressibility than unfilled rubber materials. This strict incompressible condition can be released by substituting the strain invariants I_i to the reduced strain invariants J_i where $J_1=I_1I_3^{-1/3}$, $J_2 = I_2I_3^{-2/3}$ and $J_3=I_3^{1/2}=\det {}_0^t\mathbf{X}$, and by adding the volumetric potential ${}_0^tW_V$. $\mathbf{X}$ is the deformation gradient tensor in Cartesian coordinates, $x_{i,j} = X_{ij} = \partial x_i / \partial x_j$.

$$W = W_D(J_1, J_2) + W_V(J_3). \tag{6.52}$$

The pressure must be calculated by the derivative of the total potential with respect to the volume change ratio $\det\mathbf{X}=J_3$ and only the volumetric part of the strain energy function should contribute to the pressure. Hence the use of the reduced invariants J_i is necessary in order to eliminate the contribution of the deviatoric part of the strain energy function to the pressure.

A number of the deviatoric strain energy functions are available and some of them are explained above. Assuming the linear relationship between the pressure and the volume change ratio, the pressure function adopted in ADINA is expressed as

$$p = -E_b(J_3 - 1) \tag{6.53}$$

Integrating this pressure with respect to J_3 the volumetric strain energy function is obtained.

$$W_v = \frac{1}{2}E_b(J_3 - 1)^2 \tag{6.54}$$

According to [134] a nonlinear pressure function instead of the linear one above (6.53) is more appropriate and another function W_v is obtained by integrating the nonlinear pressure function accordingly. However when the User-Supplied Material is used, ADINA seems to calculate the pressure with the linear expression above. If the nonlinear function is adopted, an inconsistency appears between the subroutine and the source code. To avoid inconsistency in the calculation, users have to compromise and use linear expressions (6.53) and (6.54) as in [97].

6.3.1 Cavitation-damage model

To include the aforementioned softening phenomenon caused by cavities, the material model provided by ADINA has to be modified. Its so-called User-Supplied material model enables users

to develop their own subroutine. Some of the material models such as Mooney-Rivlin and Ogden materials are provided as examples and hence users have to implement only the damage criterion and all changes in stiffness matrix after cavitation is activated within the subroutine. As for the Arruda-Boyce material, users have to modify the strain energy density function additionally. For the definition of the post-cavitation-behaviour of the hyperelastic body, the work of Dorfmann and Burtscher [97] is cited, due to its rather simple formulation where the cavity-induced softening is associated with a significant reduction of the bulk modulus to 1/200 of its original value. This factor of 1/200 seems merely an empirical value determined during their private discussion with Muhr [97] and most probably has to be varied according to rubber material, the degree of molecular cross-linking, and the amount or the type of reinforcement filler material. This must be the case since the degree of softening are affected by those factors as, for instance, seen in the experiment of Pond [95]. A more general form of the modified bulk modulus $E_{b,cav}=E_b/\kappa_{cav}$ is used with an arbitrary reduction factor κ_{cav} in this dissertation. This reduction in the bulk modulus affects the volumetric part of the strain energy density and its derivative with respect to the ratio of the volumetric change J_3, namely pressure p. They modified the volumetric part of the strain energy density function as

$$W_v = \frac{1}{2}E_b\left(J_{3,crit}-1\right)^2 + \frac{1}{2}E_{b,cav}\left(J_{3,cav}\right)^2 \tag{6.55}$$

where: $J_{3,crit} = J_3, \quad J_{3,cav} = 0 \quad \text{when } p < p_{crit}$

$$J_{3,crit} = \frac{p_{crit}}{E_b}+1, \quad J_{3,cav} = J_3 - J_{3,crit} \quad \text{when } p \geq p_{crit}$$

$$E_{b,cav} = E_b / \kappa_{cav}$$

Analogously the pressure function is modified to:

$$p = -\left(E_b\left(J_{3,crit.}-1\right) + E_{b,cav}J_{3,cav.}\right) \tag{6.56}$$

Finally the second derivative of W_v with respect to J_3 becomes

$$\begin{aligned}\frac{\partial^2 W_v}{\partial J_3^{\,2}} &= E_b \quad \text{when} \quad p < p_{crit} \\ &= E_{b,cav} \quad \text{when} \quad p \geq p_{crit}\end{aligned} \tag{6.57}$$

In Dorfmann and Burtscher's work the critical pressure p_{crit} was set to a constant value of 5G/2 [97]. Their model worked well for simulating the simple tension test of a rubber pad from Pond and the elastomeric bearing. With this damage criterion, however, it is feared that the onset of cavitation would not be predicted correctly where elements are subject to non-hydrostatic negative pressure. In this dissertation the cavitation instability surface that is implemented in the User-Supplied material subroutine for the damage criterion. The principal stresses are calculated in the main code and sent to the subroutine and with these stress values, the following expression determines weather damage function is triggered or not. Unless this condition is violated, softening does not occur.

$$(4\sigma_1-\sigma_2-\sigma_3)(4\sigma_2-\sigma_3-\sigma_1)(4\sigma_3-\sigma_1-\sigma_2)-125G^3<0 \tag{6.58}$$

The mean stress value σ_m is calculated with the principal stresses at the moment when this condition is violated and is set as the critical pressure value of the considered element. The element in which cavitation is activated remains soft, once this criterion is violated unless the pressure of the element goes back to a positive (compressive) value. Implementing this condition is necessary especially when analysing the offset tension test of rubber bearings. It is observed in FE results that with high shear deformation the negative pressure of some elements after violating the criterion is reduced again to below the critical level due to the interaction between neighbouring elements. When that happens, the stress distribution becomes inconsistent between those elements.
Another important finding from the observation of the test result in Chapter 5 or test results of [136] is that cavitation-induced softening can be categorized into two phases. At the onset of cavitation, the degree of softening is mild and after some further increment of loading, a more radical softening follows. The first stage is probably attributed to the development phase of cavities and in this phase the softening is mild because not majority of rubber is cavitated. Volume change is low and therefore developed cavities cannot be expanded. The second phase begins when the most part of rubber is cavitated and a larger volume change occurs. With enough cavities the constraint to the rubber deformability is released and then cavities have possibility to expand further. In this phase the size of cavities increases rather than the number of them. As a result, radical softening occurs due to the much reduced effective planar area. The concept of the two-phased cavitation is based purely on the observation of the test and FE results and thus it is mere a hypothesis. However the stress-strain curves obtained by this implemented model correspond to the measured ones by experiments convincingly well. For simplicity the same principle is applied for the second phase and then the modified functions of the volumetric strain energy and pressure in the second phase are calculated as

$$W_v = \frac{1}{2}E_b\left(J_{3,crit}-1\right)^2 + \frac{1}{2}E_{b,cav}\left(J^*_{3,cav}\right)^2 + \frac{1}{2}E_{b,exp}\left(J_{3,exp}\right)^2 \tag{6.59}$$

where: $J_{3,crit} = \frac{p_{crit}}{E_b} + 1, \quad J^*_{3,cav} = J_{3,crit2} - J_{3,crit}, \quad J_{3,exp} = J_3 - J^*_{3,cav}$

$E_{b,cav} = E_b / \kappa_{cav}, \quad E_{b,exp} = E_{b,cav} / \kappa_{exp}$

Analogously the pressure function is modified to:

$$p = -\left(E_b\left(J_{3,crit}-1\right) + E_{b,cav}J^*_{3,cav} + E_{b,exp}J_{3,exp}\right) \tag{6.60}$$

The second derivative of W_v with respect to J_3 in the second phase is therefore

$$\frac{\partial^2 W_v}{\partial J_3^{\,2}} = E_{b,exp}. \tag{6.61}$$

This concept is schematically shown in figure 78. Note that $J_{3,crit2}$ and κ_{exp} are additional input parameters and have to be adjusted according to the material. Especially the second critical volume change ratio $J_{3,crit2}$ is here the criterion for the second softening phase and can be determined by checking the volume change ratio in the FE model when the cavitation development phase is completed. Alternatively if the result of the uniaxial test of a rubber disc or a rubber bearing is available, the axial strain at the onset of the second softening phase can be directly used as input value because the axial strain is very close to the volume change ratio at the centre. It is elaborate procedure and it would be useful when the range of the critical volume change ratio is

approximately known. From the simulation carried out in next sections $J_{3,crit2}$=1.05 (5 % volume change) could be a good start.
Hereafter the implemented cavitation model is referred to as "two-phase softening model" or simply "two-phase model".

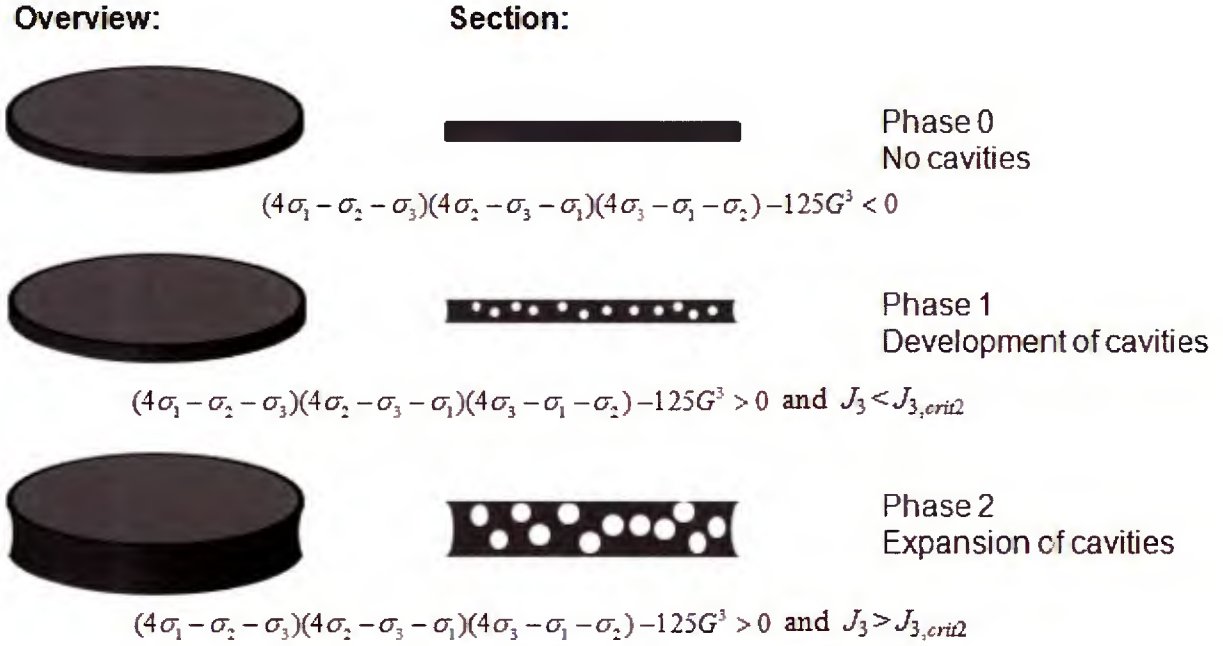

Figure 78: Three phases of the cavitation criterion

6.4 Performance Check

The performance of the implemented Cavitation Damage model is examined in this section. As for the base material models, Mooney-Rivilin material and Arruda-Boyce material have been adopted. The classical Neo-Hookean material can be recovered from both material models by limiting material constants. For the first step, the Neo-Hookean based model is verified with experimental data from Pond since the important material constants were not available for the tested rubber material. For the analysis, 8-noded cubic 3D solid element with 1 pressure variable or 27-noded cubic element with 4 pressure variables are recommended in the reference [125] as already explained in 6.2. Here, the former was chosen because the latter requires an extensive calculation time and enormous size of the output data. Only a quarter of the rubber disc is modelled to save the calculation time. Sensitivity analysis was carried out beforehand and the fineness of meshing was determined. The given shear modulus G=0.533 and 0.866 MPa for natural rubber with and without carbon black filler, respectively and bulk modulus E_b=2500 MPa are selected for the material inputs referring to Pond and Dorfmann [95], [97].
In Fig. 79 the stress-strain curve of the natural rubber with carbon filler from Pond is compared with the results obtained by FE analysis with and without cavitation damage model. As can be observed, within small strain range all curves show almost linear behaviour and they correspond to each other. However, at a certain strain the curves of the experiment begin to show a less neat path due to cavities nucleation and the stiffness drops dramatically at that point. The Neo-Hoookean based cavitation damage model can represent this behaviour fairly and this result is almost identical to the one from Dorfmann and Burtscher [97]. Note that for this analysis the second softening phase is deactivated since the tested strain range was limited and it seems that the second phase is not

reached for this test. Figure 80 shows the pressure distribution within the rubber pad. High negative pressure appears near the centre of the pad as predicted.

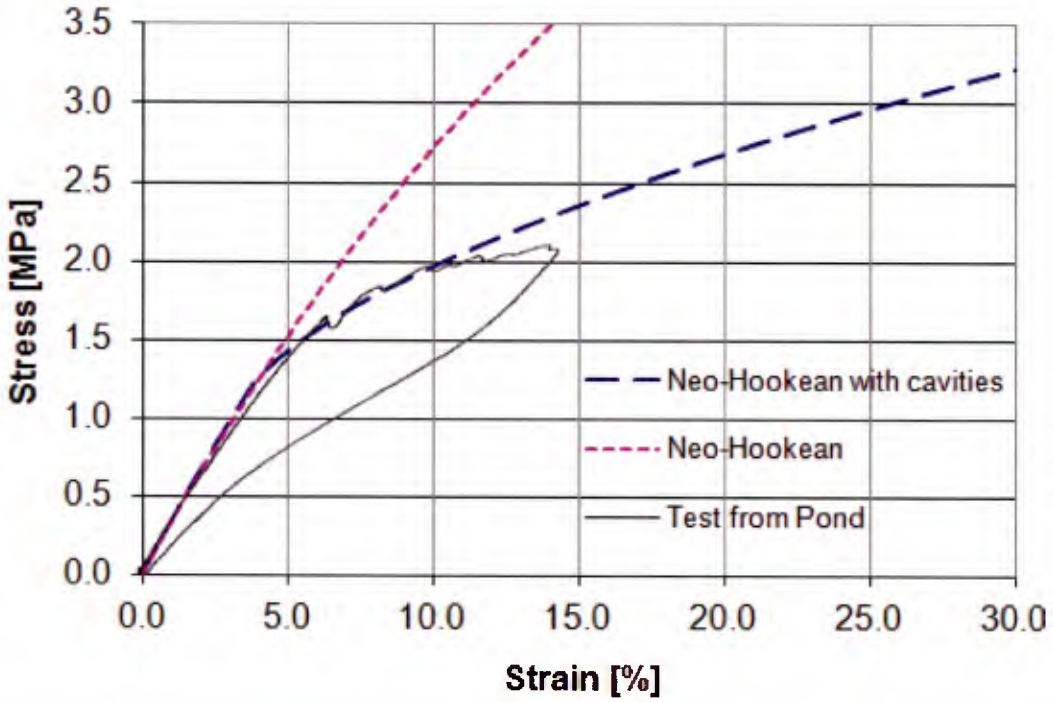

Figure 79: Comparison of experimental and numerical stress-strain curves (NR with CB) [95]

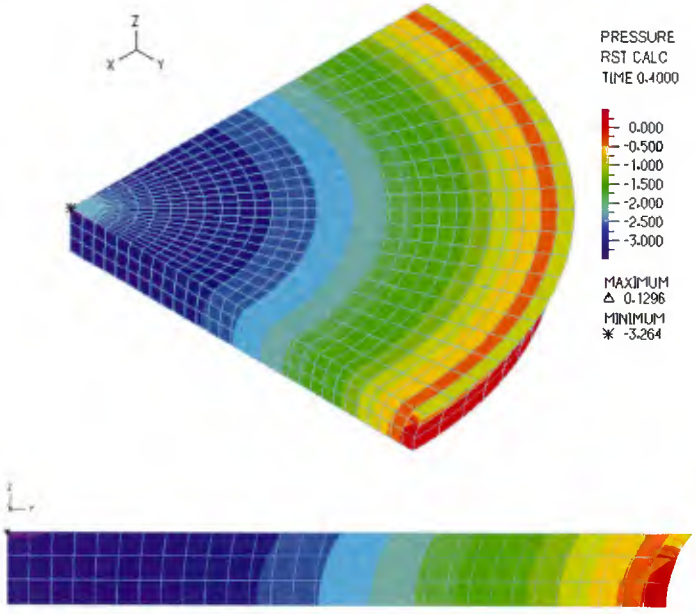

Figure 80: Pressure distribution within a rubber pad

Figure 81 is the plot of the critical pressure values under the nominal tensile stress of 4 MPa. The purple colour represents zero which means there is no cavities in elements with this colour. Cavitation takes place first at the centre of the rubber pad as predicted and proceeds further in the radial direction. This expansion of the damaged area stops at the certain stress level and the outer intact area remains even with further loading. In this area the hydrostatic condition cannot be

achieved since elements there are a less deformable (or less constrained) in the radial direction. As the cavitation instability surface shows, a much higher stress is required to cause cavities when three principal stresses are not equivalent to each other.

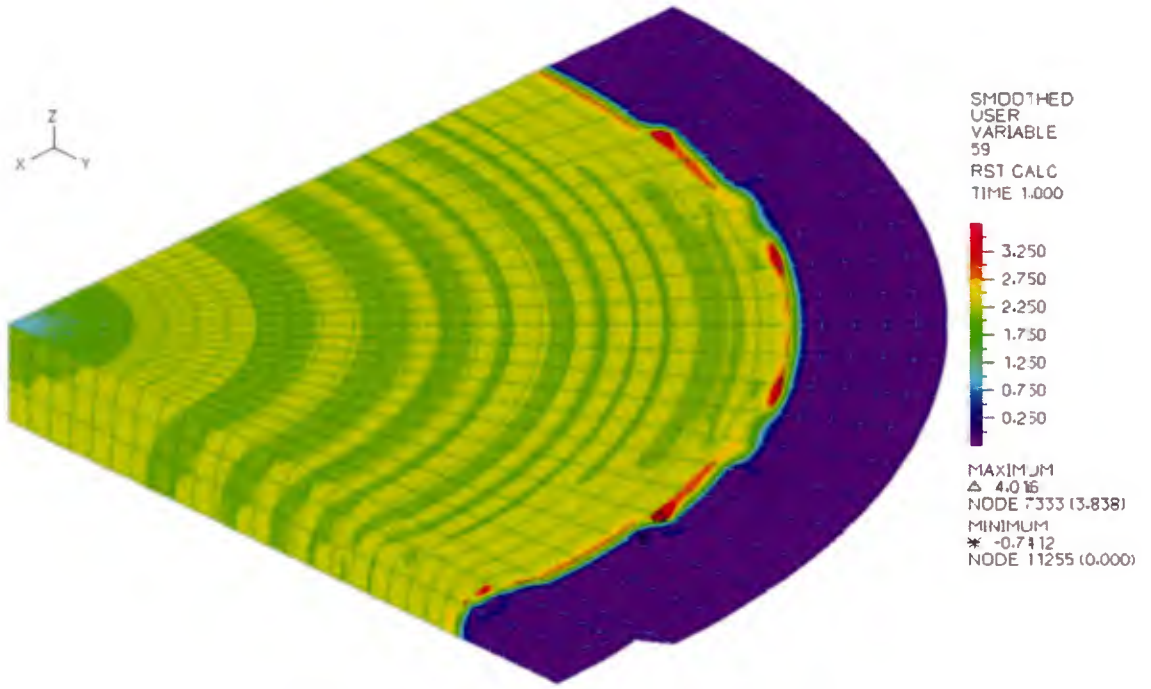

Figure 81: Plot of the critical pressure values

The critical value fluctuates very little around 2.2 MPa, very close to the value of 5G/2, which indicates that all damaged elements are all in nearly hydrostatic condition.

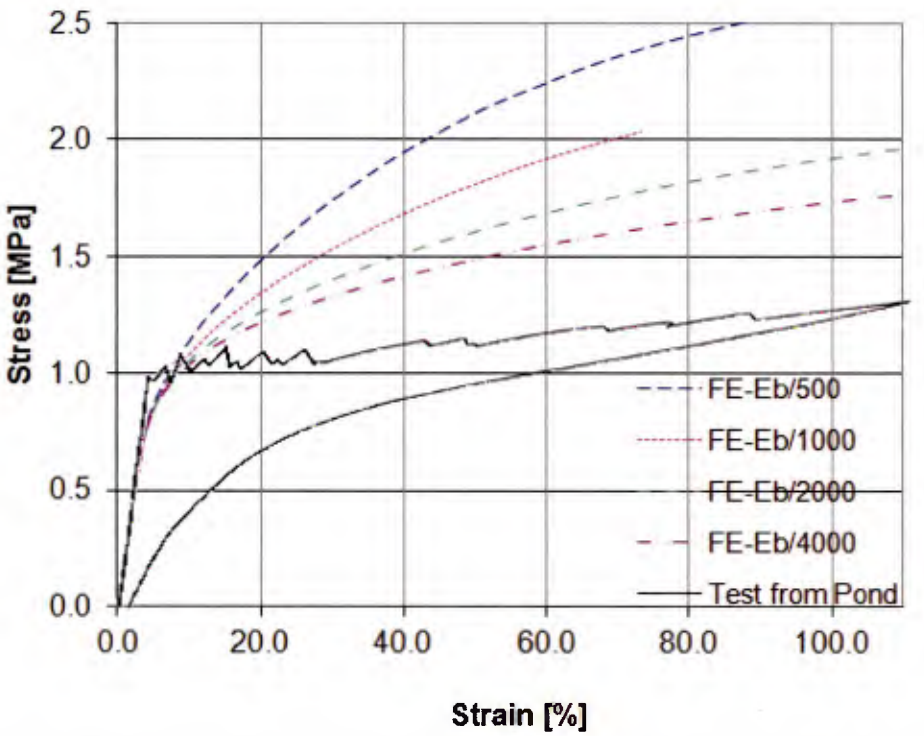

Figure 82: Comparison of experimental and numerical stress-strain curves (unfilled NR) [95] [137]

In Fig. 82, experimental and numerical stress-strain curves of the natural rubber without carbon black are compared. Here the softening begins at a radical degree. As an attempt, a parametric study with respect to the reduction factor κ_{cav} to the bulk modulus is carried out. Even with a reduction factor of as high as 4000 this high degree of softening was not realized. It is not realistic to think that this degree of softening is caused solely by cavities because the tensile stiffness drops to virtually zero value. The explanation of this significant reduction in the stiffness could be either delamination between rubber pad and steel plates or development of relative large rips It can be assumed that either or both of phenomena were triggered briefly after the development of cavities because they are an imperfection in a sense. Perhaps that is the reason why the onset of softening corresponds to the simulation but a degree of softening is not well captured.
Next the experiment results from [136] are referred to. That is one of the rare articles in which the stress-strain curve of rubber material used for their series of tests is provided, although only as a diagram. This stress-strain curve is recreated in the following Fig. 83 with black solid line together with stress-strain curves of Mooney-Rivlin model as well as Arruda-Boyce model obtained by the curve fitting function in ADINA.

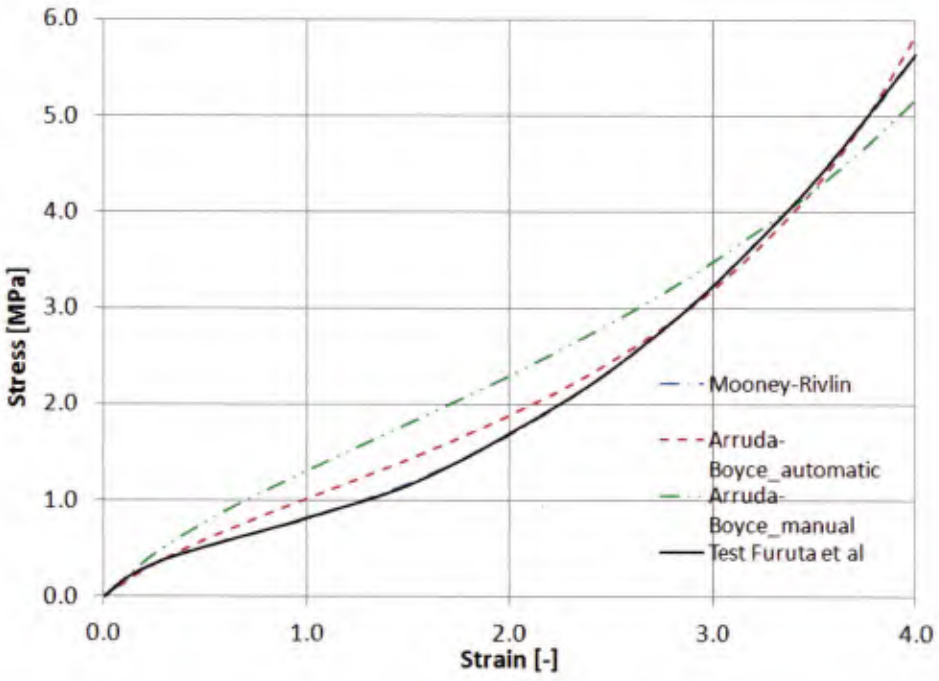

Figure 83: Comparison of experimental and numerical material properties [136]

The stress-strain curve of the Mooney-Rivlin material is almost identical to the test curve. For the curve-fitting, the approximation order of two, i.e. five terms with material constants from C_1 to C_5 in Eq. (6.44), is used. This is because higher order approximation causes instability in calculation sometimes and for this specific case the fitting with higher approximation order generates a worse result. The dotted red line (Arruda-Boyce_automatic) is obtained by the automatic curve-fitting for Arruda-Boyce material by ADINA. Due to a rather simple formulation of this material model, its curve-fitting can capture only approximately the real behaviour of the material, although difference seems insignificant. The double-dotted green line (Arruda-Boyce_manual) is obtained by manually setting the material constants to obtain a better fit of the initial material behaviour (see Fig. 84) because cavitation takes place within a very low tensile strain range and the material model should grasp the real behaviour there to adopt the instability criterion correctly. The overall behaviour is, however, not captured well by this model.

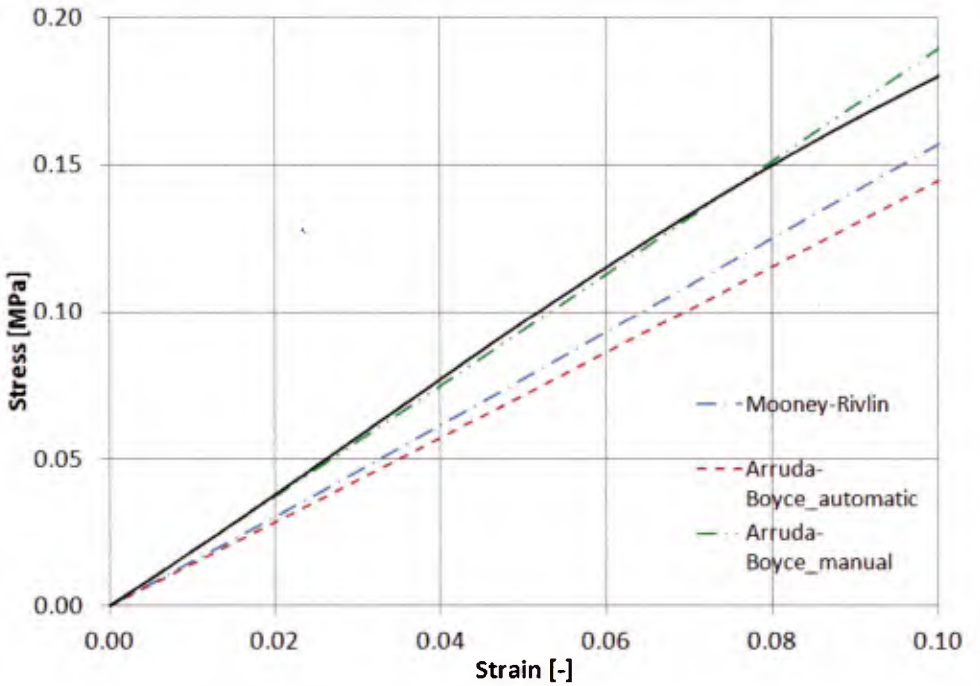

Figure 84: Comparison of experimental and numerical material properties in small strain range [136]

The shear modulus of 0.4 MPa is provided for this material in [136] whereas 0.74 MPa, 0.49 MPa and 0.71 MPa for Mooney-Rivlin model, Arruda-Boyce_automatic and Arruda-Boyce_manual, respectively are obtained. The bulk modulus is an unknown parameter. Generally the value is assumed to be between 1000 and 2000 as already described in Chapter 3 yet it is not necessarily true for all rubber material. For instance, the rubber used for bridge- or seismic isolator bearings contains other compounds which are more compressible and thus the rubber as a compound becomes slightly more compressible. The bulk modulus is determined in the numerical analysis by the following expression.

$$E_b = \frac{2G(1+\nu)}{3(1-2\nu)} \tag{6.62}$$

where ν is the Poisson's ratio.

Incompressibility is determined by the Poisson's ratio where ν=0.5 means totally incompressible. In their analysis the Poisson's ratio of 0.495 was assumed and with this value the bulk modulus becomes nearly 100G by applying the following relationship, whereas ADINA [138] assumes ν=0.499 as default for the hyperelastic materials. It is not clear which value is suitable for the analysis and thus the parametric study was carried out with E_b=200, 500, 1000 and 2000 MPa. For the following simulation, E_b=500 MPa was selected as the best fit.
The tested bearing is the ring type with an outer diameter is 800 mm and an inner diameter of 40 mm. The bearing consists of 36 layers of 4.45 mm rubber pads and 35 layers of 4.3 mm steel shims. For the steel component, the plastic multilinear material model is employed, see Fig. 85.

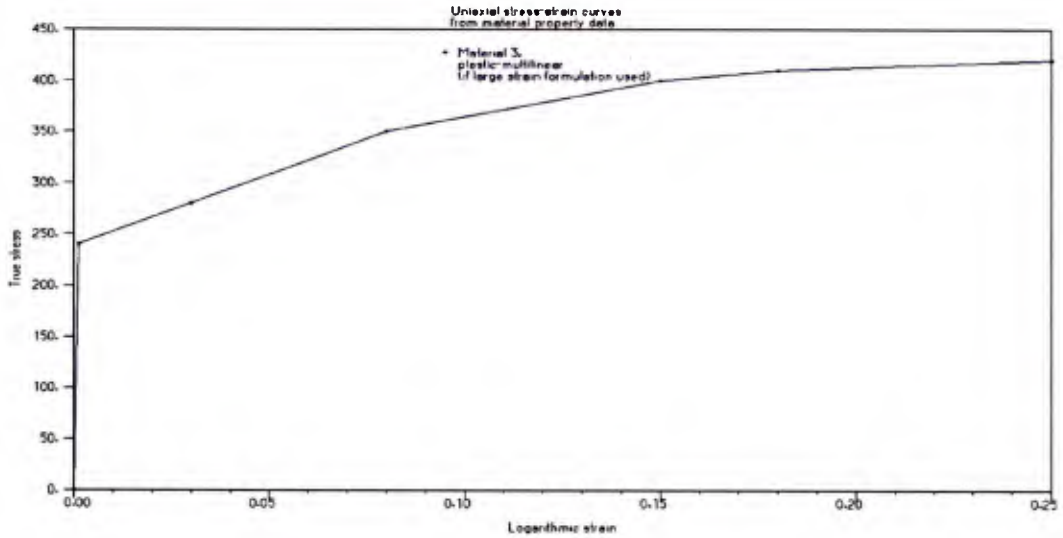

Figure 85: Stress-strain curve of the steel material for FE simulation

Only the half bearing is modelled in order to reduce the calculation time. The lower flange is not included for the same purpose. The number of division is, after sensitivity analysis, determined as in the following Table 39. Again 8-noded cubic 3D solid element with 1 pressure variable is selected for the analysis.

Table 39: Number of division of the FE model

Model component	Number of division
Rubber pads	16×16×3
Steel shims	16×16×2

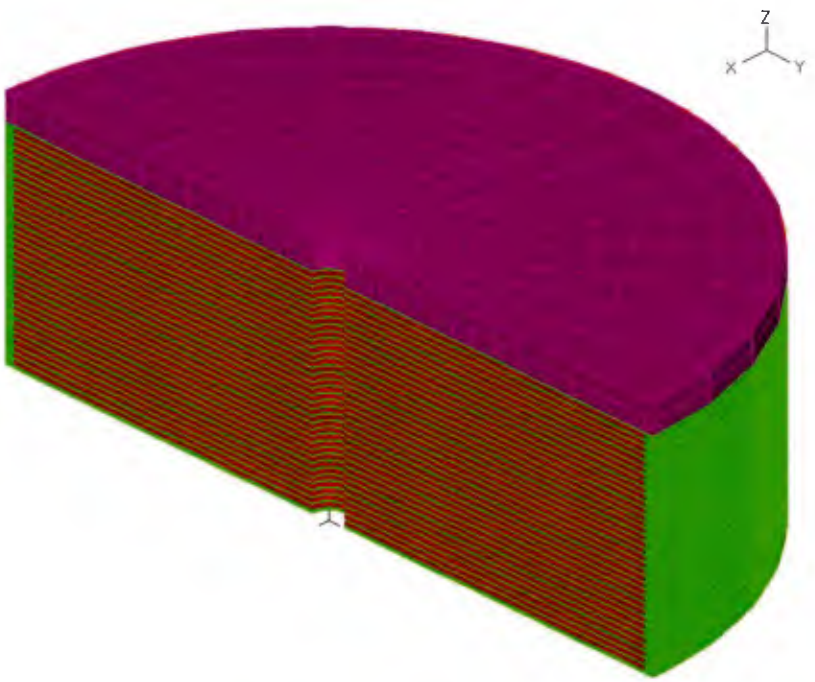

Figure 86: Simulation model

The simulation model is shown in Fig. 86. The bearing was subjected to shear deformation up to 250 % and then pulled in the vertical direction. The reduction factor of the bulk modulus κ_{cav}=200, the second critical volume change ratio $J_{3,crit2}$=1.08 and the second reduction factor of the bulk modulus κ_{exp}=5 are selected for the two-phase softening model.
The test results and numerical results are compared in Fig. 87. The Mooney-Rivlin material model did not work for 250 % offset. The material constants are determined only by the tensile stress-strain curve and that is seemingly not sufficient for the Mooney-Rivlin material since the shear stiffness of this material is unrealistically high and most cavities are initiated already only by a small shear deformation and the model collapsed shortly after that, even before applying the tensile load. On the other hand, the Arruda-Boyce material possesses the shear stiffness in the same order of its tensile stiffness and cavitation is also initiated by shear deformation but only in very high strain range. Arruda-Boyce whose material constants are obtained through the automatic curve-fitting by ADINA is not able to predict the onset point of cavitation, whereas the Arruda-Boyce_manual material captures the real behaviour well in this sense, although without activating the second softening phase the overall behaviour of the simulation is far too stiff (red line). From this observation, the aforementioned assumption that capturing the material behaviour within the smaller strain range is important is confirmed because that part determines the shear modulus of the material model, which in turn is the crucial parameter of the cavitation instability criterion. Furthermore more reliable simulation results of the bearing under compression or shear loading can be obtained by the manually determining the material constants as shown later in Section 6.4.1. The two-phase softening model (green line) captures the real bearing behaviour in the whole range well, even though elements are distorted in the very high strain range. The threshold of the second softening phase is not recognized from the simulation result because the criterion for the cavity expanding phase is already violated for some elements only by the high shear deformation and within the bearing both phases are mixed from the beginning of cavitation.

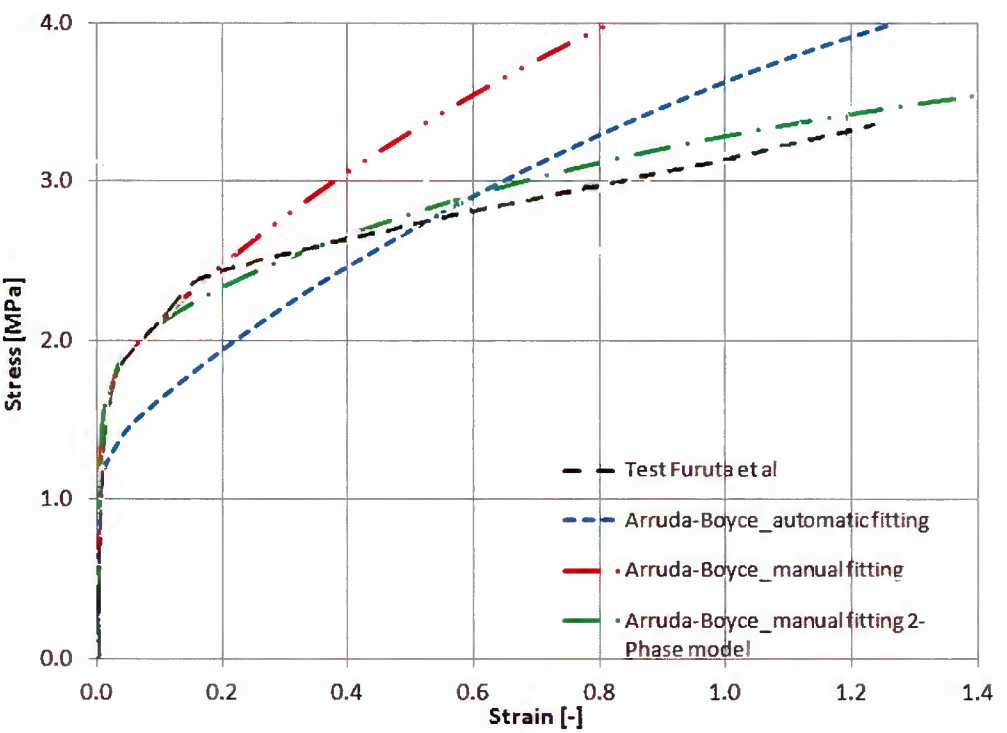

Figure 87: Experimental and numerical results of offset (250%) tension test [136]

The deformed configuration of the simulation bearing "Arruda-Boyce_manual fitting" with the two-phase softening model is shown in Fig. 88 (250 % offset). As indicated in [106] [136], the bearing rotates internally with respect to the x-axis of the figure. From this deformed configuration it can be also observed that the steel shims are bent. At approximately 3.5 MPa of tensile stress, the steel shims began yielding, although this softening due to the plasticised steel can be hardly recognized in the stress-strain curve. The second change in the stiffness was explained by this steel yielding in [136] but it contradicts the simulation result here.

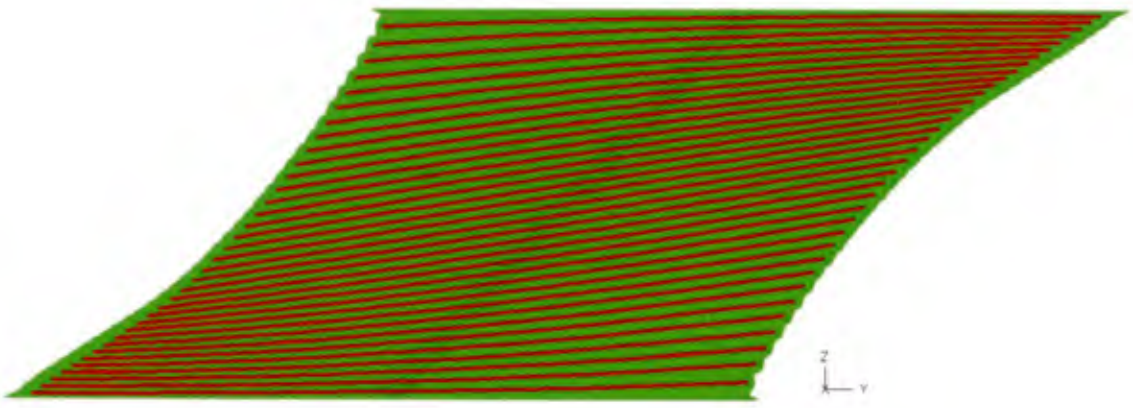

Figure 88: Deformed configuration of the simulation model at the vertical strain of 1.3 (Arruda-Boyce_manual two-phase softening model)

The following Fig. 89 shows the development of cavities. Purple colour denotes the intact elements and other colours denote the critical pressure values of the corresponding elements.

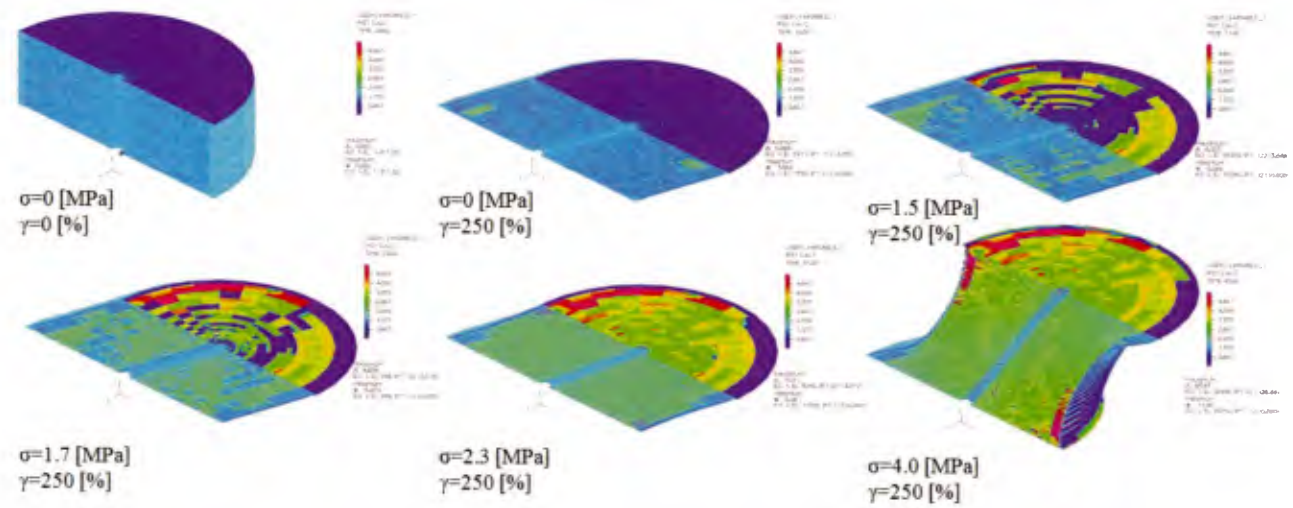

Figure 89: Development of cavities and the distribution of the critical pressure

The light green colour represents the minimum critical pressure (=5G/2) and other colours represent higher critical pressure values. As can be seen, cavities already develop by mere shear deformation (γ=250 %) but due to the non-hydrostatic condition, the critical value is higher there. These cavitated areas expand instantaneously by the first vertical loading step, approximately 0.1 MPa and remain unchanged up to 1.5 MPa tension. However, the second cavity-expanding phase starts

already there almost simultaneously because the volume change ratio exceeds the input critical value of 1.08 already by the shear deformation. By increasing the vertical tensile force, cavities propagate further, and the majority of elements seem to undergo the hydrostatic stress condition despite high shear deformation and the internal rotation of the bearing. At about nominal 2.3 MPa stress the number of cavitated elements stop increasing and from that point on the bearing starts deforming rapidly.

6.5 Simulation Of The Tested Bearing

The series of experiments described in the Chapter 5 are simulated with the implemented two-phase softening model.

6.5.1 Rubber material test

In order to obtain the material constants of rubber for the numerical analysis, the tension test of rubber was carried out in January 2012 with the generous help of Prof. Lion and his colleagues from the faculty of Aerospace Engineering, Institute of Mechanics at the University of German armed forces Munich (Fakultät für Luft- und Raumfahrttechnik, Institut für Mechanik an der Universität der Bundeswehr München). Their universal testing machine Zwick Roell TC-FR020 TH.A50 with the temperature chamber and the Videoextensometer was appropriate for the rubber material testing in compliance with ISO 37 [139] or DIN 53504 [140]. The videoextensometer is necessary to measure the extension between two lines in the central region (see Fig. 91) where the actual stress-strain behaviour of rubber is obtained as shown in Fig. 92. The initial gauge distance is specified as 25 mn in the aforementioned standards but 5 mm distance was selected instead in order to increase the strain-measurement-range within the limited measurement capacity. The temperature was kept constant at 25°C which is within the specified temperature range, namely 23±2°C in those standards during the test. The dumbbell-shaped sample ISO 37 Type 1 (Dumbbell type S1) was selected, for it is most commonly used [124].

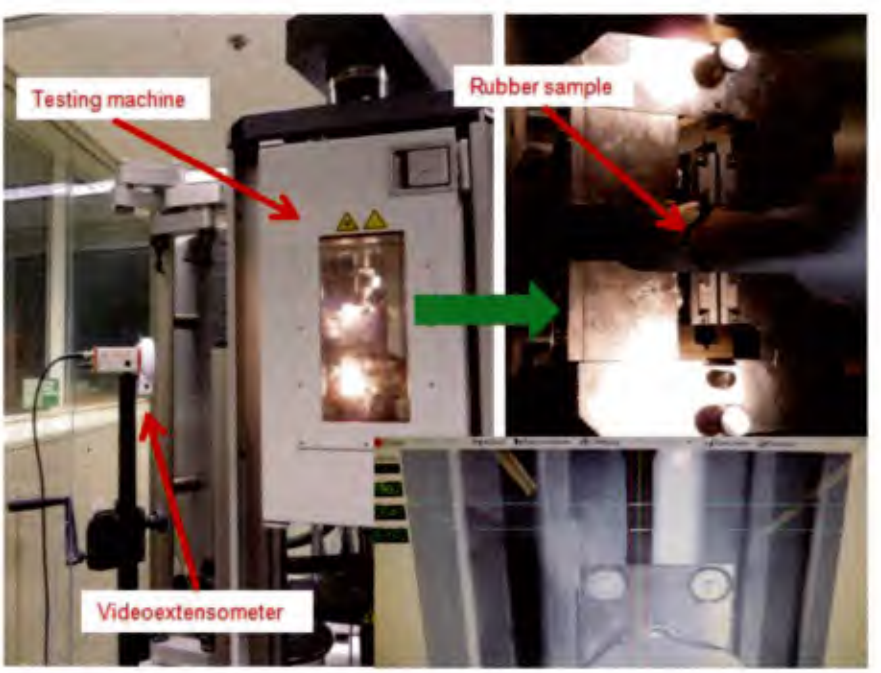

Figure 90: Test rig for rubber material test

Before measurement, the test specimen was stretched once to the planned maximal strain so that a majority of the Mullins effect would be excluded. The loading was carried out stepwise with deformation control and at each elongation step the deformation was kept for some time until the relaxation in stress stopped proceeding. The loading velocity was set to a very slow speed. These procedures were not required neither in [139] or [140] but are necessary because the purpose of the material test is to determine the material constants for the numerical simulation in which no viscoelastic behaviour of rubber is taken into consideration.

Figure 91: Dumbbell-shaped rubber specimens

Three test pieces were tested as required in [139] and [140]. One of the stress-strain curves is shown in Fig. 92.

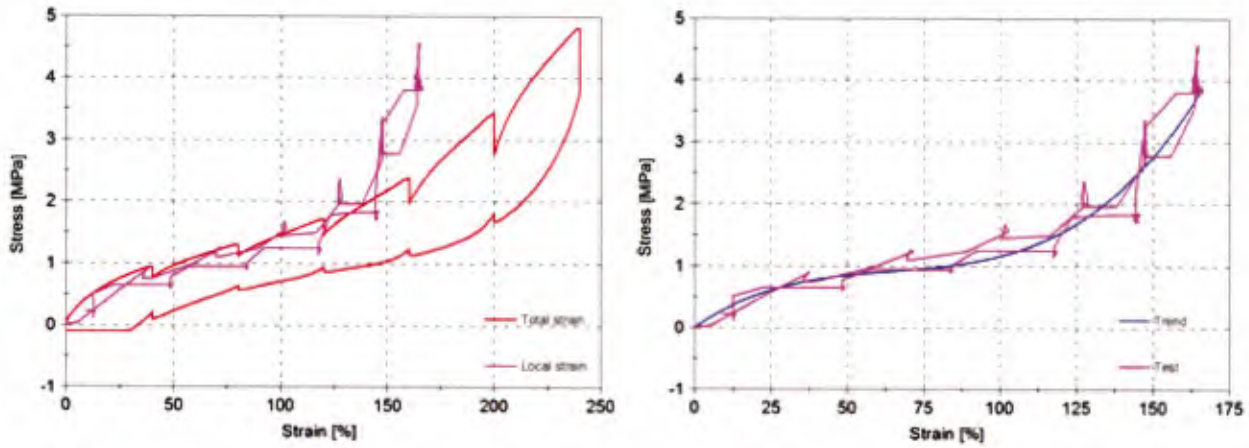

Figure 92: Stress-strain curve of the dumbbell-shaped rubber specimen

The red line is the stress-strain curve measured by the testing machine and the pink line is the stress-strain curve at the centre area of the specimen. As can be observed, local strain is lower than overall strain. The blue trend line that is used for the curve-fitting in ADINA for the FE analysis is generated by the DIAdem. The Arruda-Boyce material is applied and the manual curve-fitting is

carried out as described in 6.3. As for the material constants such as shear modulus and locking stretch, the mean values of three test pieces are used.

6.5.2 Determination of parameters

For the FE analysis the material constants are to be determined on the basis of the stress-strain curve described in Section 6.5.1. For its simplicity and stability, Arruda-Boyce material was selected. A special attention must be paid for the curve-fitting since it became clear in Section 6.4 that the automatic curve-fitting carried out by ADINA may generate inaccurate material constants, although it seems well-fit if the whole strain range is considered. Here again both automatic and manual curve-fitting were performed and the simulation results based on material constants obtained by these two different fitting methods are compared. As for the steel material, the plastic-multilinear model analogous to Fig. 85 based on the steel properties of S235 is used.
First, sensitivity analysis in terms of the mesh size was performed and stable results were obtained by the mesh size summarised in Table 40 and the simulation models for the Type 1 and Type 2 bearings are shown in Fig. 93. With this meshing size the aspect ratio of each element of rubber pads was not optimal. In fact the sensitivity analysis of the bearing Type 1 exhibited a little fluctuation as the number of division in rubber thickness increases but at least three divisions in this direction is necessary for elements to represent the real deformation. Therefore the minimum number of division was used. For the whole analysis in the followings, the same simulation models are used.

Table 40: Number of division of the FE model

Bearing type	Model component	Number of division
Type 1	Rubber pads	12×12×3
	Steel shims	12×12×2
Type 2	Rubber pads	12×12×3
	Steel shims	12×12×2

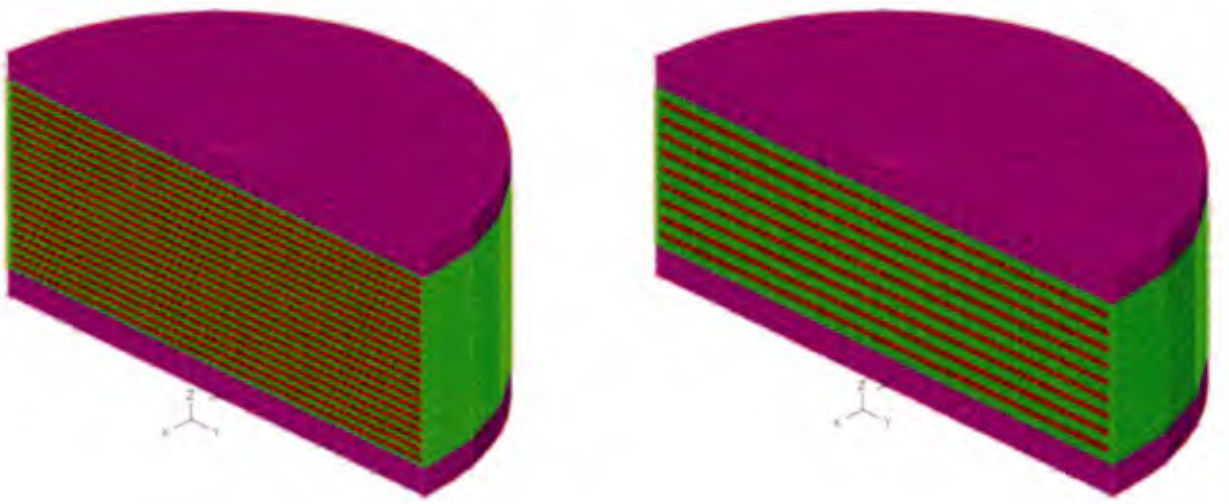

Figure 93: Simulation models, Type 1: left, Type 2: right

In order to verify the validity of the material constants of Arruda-Boyce model, in particular the shear modulus and the locking stretch, both experimental and numerical results of the compression and shear test are compared, see Fig. 94. The aforementioned two curve-fitting methods are

compared with the results from the Type 2 bearing. As it is clearly observed in this figure, the shear stiffness of the simulation model is too low when the material parameters are determined by the automatic curve-fitting. With the manual curve-fitting, the shear modulus of 0.96 MPa and the locking stretch of 2.8 were obtained and the simulation model captures the real behaviour of the Type 2 bearing. As for the bearing Type 1, the model with these material constants exhibits a lower shear stiffness (see left one in Fig. 94).

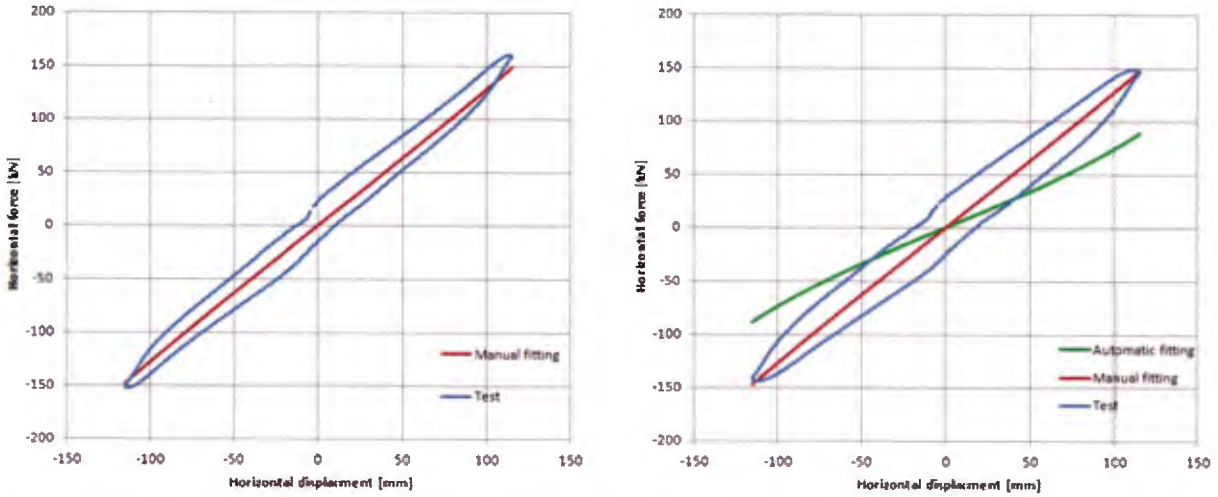

Figure 94: Comparison of test- and numerical results of the compression and shear test, Type 1: left, Type 2: right

In Chapter 5 the difference between the shear stiffness roots in the geometry of the bearing and the material shear stiffness itself has already been discussed. From these FE results, it is obvious that the different geometry of the bearings does not contribute to the shear stiffness and therefore an attempt is made to adjust the input shear modulus in FE. With the shear modulus G=1.05 MPa, a better fit is obtained as shown in Fig. 95.

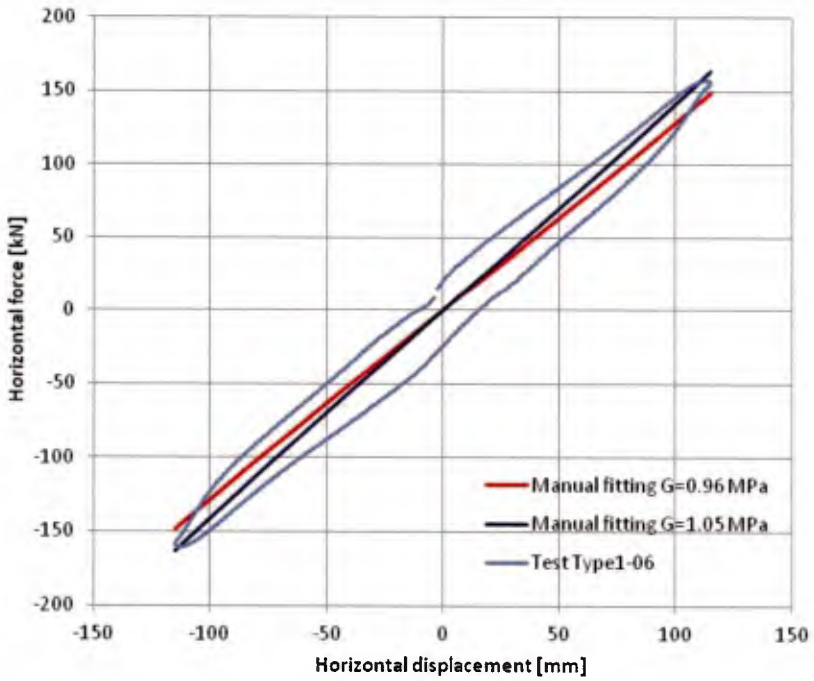

Figure 95: Adjustment of the input shear modulus in FE analysis to the test results of the compression and shear test, Type 1-06

Apart from the test bearing Type 1-09, the adjustment result in a better fit and therefore the shear modulus of 1.05 MPa is set for the analysis of the bearing Type 1. For the bearing Type 2, only for the Type 2-03 the shear modulus should be reduced a little but the shear modulus of 0.96 MPa is used for the analysis since most of the test results are in good agreement with FE results with this value. Interestingly the Arruda-Boyce material with these material constants generates a quite similar stress-strain curve to the measured one by the testing machine (red line on the left in Fig. 92). The dimension of each rubber element in this FE models is larger than the dimension of the measured part of dumbbell specimens. This fact might indicate that more appropriate stress-strain curves for this series of analysis could have been achieved if the measurement distance of the material test had been wider as specified in [139], although it was not possible due to the testing machine capacity.

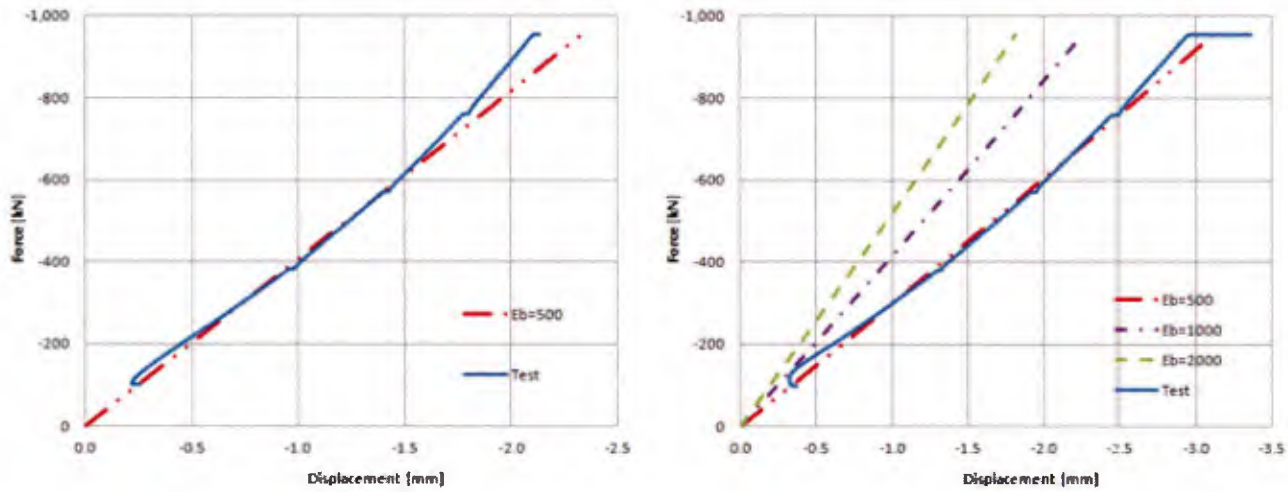

Figure 96: Comparison of test and simulation results of the compression test, Type 1: left, Type 2: right

The numerical and test results of the compression test are compared in Fig. 96. Here the purpose is solely to adjust the bulk modulus. This sequence of the validity examination is necessary since the horizontal properties of the bearings are almost exclusively determined by the shear modulus and the locking stretch, while the vertical property of the bearing is determined not only by those two parameters but also the bulk modulus. The shear modulus and the locking stretch values obtained by the manual fitting remain and parametric study with various bulk moduli was performed to seek the best fit to the initial compressive stiffness analogous to the previous Section 6.4. As a result the bulk modulus of 500 MPa was selected. This value also corresponds to the one with which the evaluation formula provides a better fit to the test results in Chapter 5.
With these material parameters the simulation is further performed for tension tests in the following Sections.

6.5.3 Simulation of the uniaxial tension tests

The performance of the implemented cavitation model with two softening phases is studied by comparing the tension test results. Before presenting the results, it should be noted that all force-displacement curves from the experiment have been shifted by the amount of -40 kN because several steel plates and half weight of the horizontal actuator, which are estimated to weigh approximately 4000 kg all together, were loaded on the bearings during tests. In FE analysis those weights are not taken into account and thus this modification in the test data is done for more accurate simulation.

The comparison of test- and FE results of the bearing Type 1-06 is shown in Fig. 97. The reduction factor κ_{cav}=25 is used and here the second softening phase is deactivated. The influence of the difference in the shear modulus on the simulation result can be seen. As in Fig. 95, a better fit is obtained with the heightened shear modulus. For all the Type 2 and Type 1-09 bearings, the shear modulus obtained by the manual curve-fitting (G=0.96 MPa) is used. In order to distinguish them, in this and the next section, the red line always represents the result with the shear modulus G=0.96 MPa and the green one represents the result with G=1.05 MPa.

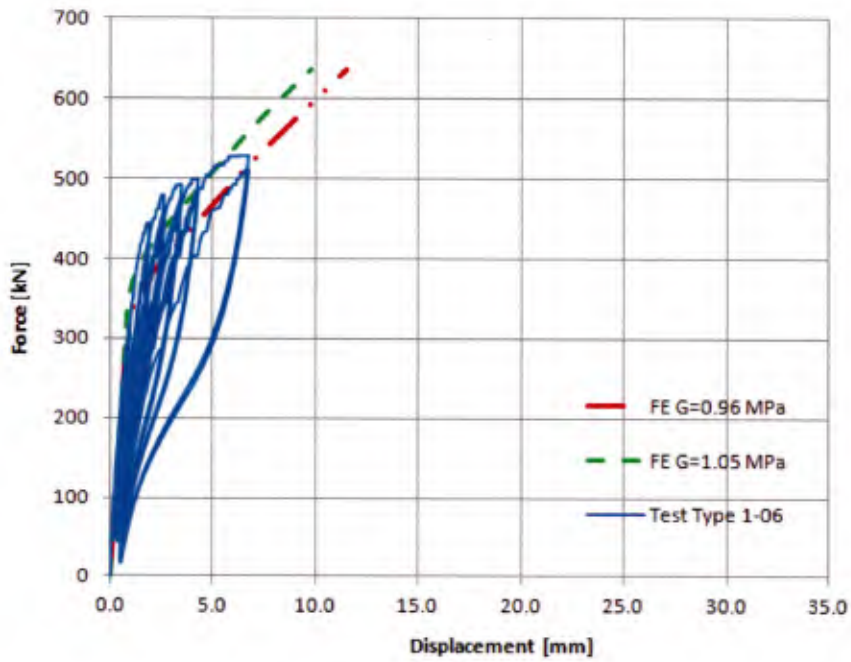

Figure 97: Comparison of test and simulation results of the bearing Type 1-06

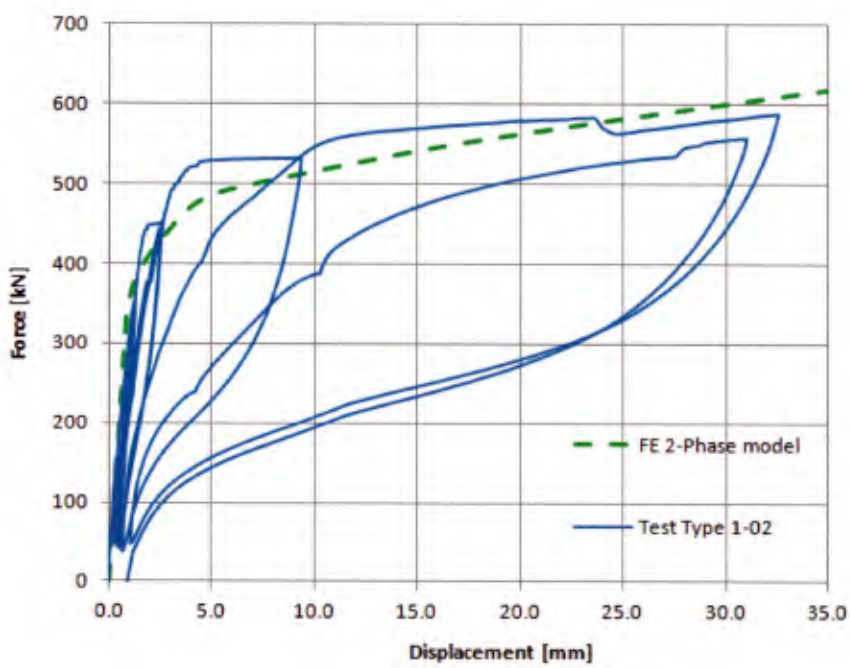

Figure 98: Comparison of test and simulation results of the bearing Type 1-02

The force-displacement curves of the bearing Type 1-02 from the test and FE results are compared in Fig. 98. The second softening phase is activated at the critical volume change ratio $J_{3,crit2}$=1.03 and the second reduction factor of the bulk modulus κ_{exp}=10 is selected. The former parameter is determined first roughly by the deformation where the second softening phase seems to begin. Observing all the results of uniaxial tension tests, that deformation point is approximately 5 mm (see annex) when the vertical stretch ratio 1.04 is obtained. As explained in Section 6.3 this strain should be nearly equal to the volume change ratio due to the highly constrained rubber configuration in all three principal directions. The FE result shows that J_3 value is about 1.03 at the time step when the most part of rubber is cavitated. These two values are very close to each other as expected and the best fit to these curves is obtained with $J_{3,crit2}$=1.03. These all parameters hold for all simulation here.

The same comparison for the bearing Types 2-02 and 2-03 are shown in Figs. 99 and 100. Both results are in good agreement as well. Note that the force-displacement curves calculated by FE analysis almost coincide with the path generated by connecting the peaks of second cycles of each loading level and this tendency is also true for the offset tension case in the next section. As already discussed in Section 5.4, the difference in forces between the first and the second cycle of each loading level roots in cavitation-induced softening. It is assumed that the "delay" of cavitation is due to the viscoelastic property of rubber. In the FE analysis this viscoelastic property is not taken into consideration and thus this delay does not occur. If the tests had been conducted very slowly or if the viscoelastic property of rubber was considered in FE analysis, the curves would be closer to each other.

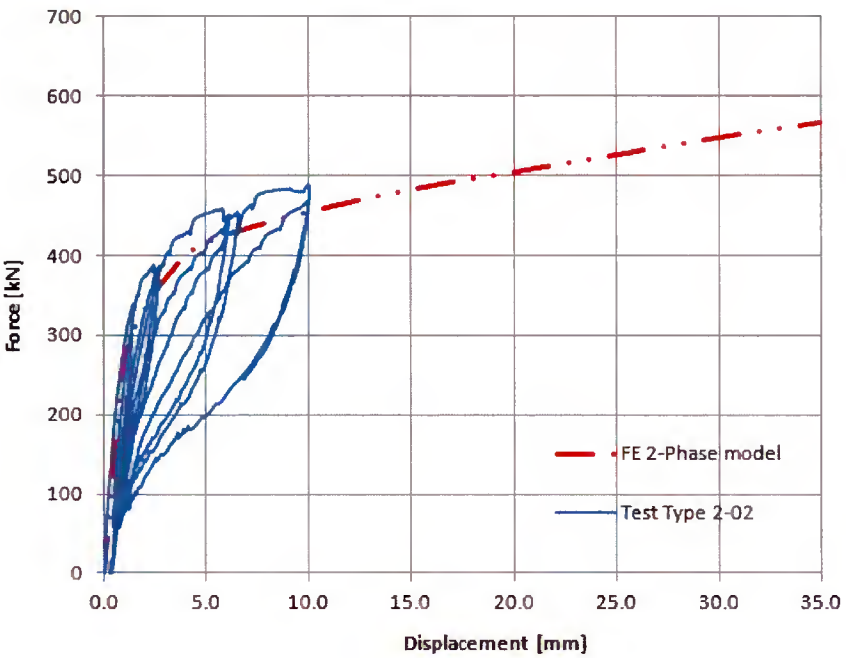

Figure 99: Comparison of test and simulation results of the bearing Type 2-02

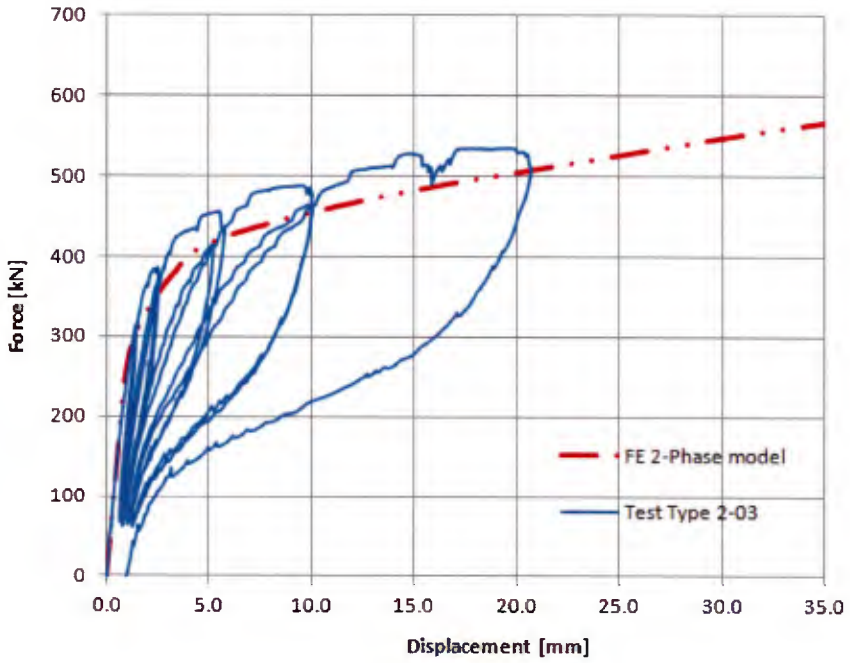

Figure 100: Comparison of test and simulation results of the bearing Type 2-03

Figure 101 plots of the critical pressure for both bearing types under the maximum tensile load of 636 kN. The yellow colour denotes the critical pressure range from 2.7 to 3.0 MPa and the light green colour denotes the critical pressure range from 2.4 to 2.7 MPa. Pressure 2.7 and 2.4 MPa are nearly equivalent to the pressure obtained by 5G/2 for the bearing Type 1 and Type 2, respectively. From these plots it is clear that almost all cavitated elements are subjected to the hydrostatic pressure. The bearing Type 2 has more intact areas along the outer edge because of a higher deformability there than the bearing Type 1.

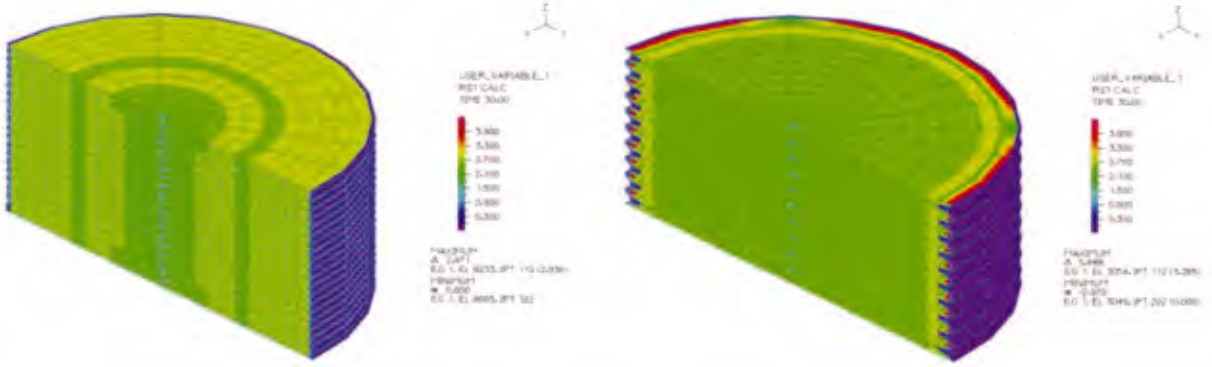

Figure 101: Plots of the critical pressure p_{crit}, left: Type 1, right: Type 2

6.5.4 Simulation of the offset tension tests

The force-displacement curves of the bearing Type 1-07, 1-09 and 2-05 from the tests and FE results are compared in Figs 102, 103 and 104.
Note that shear modulus of 0.96 MPa is used for the FE analysis of the bearing Type 1-09 since the shear modulus obtained by the compression and shear test is exceptionally lower than those of the other Type 1 bearings and almost equivalent to those of the Type 2 bearings. By comparing with FE analysis it can be assumed that this bearing failed at the loading level of approximately 450 kN.

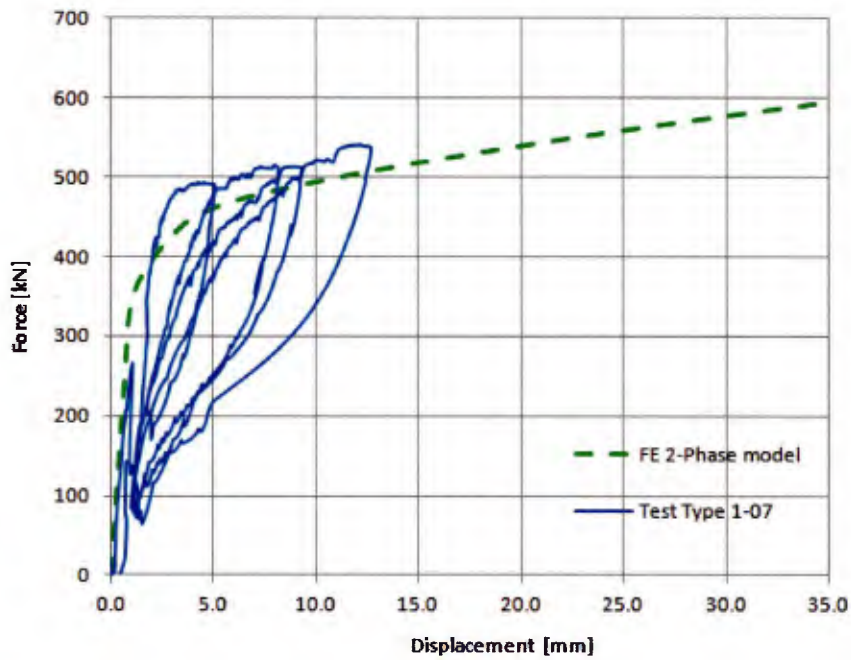

Figure 102: Comparison of test and simulation results of the bearing Type 1-07

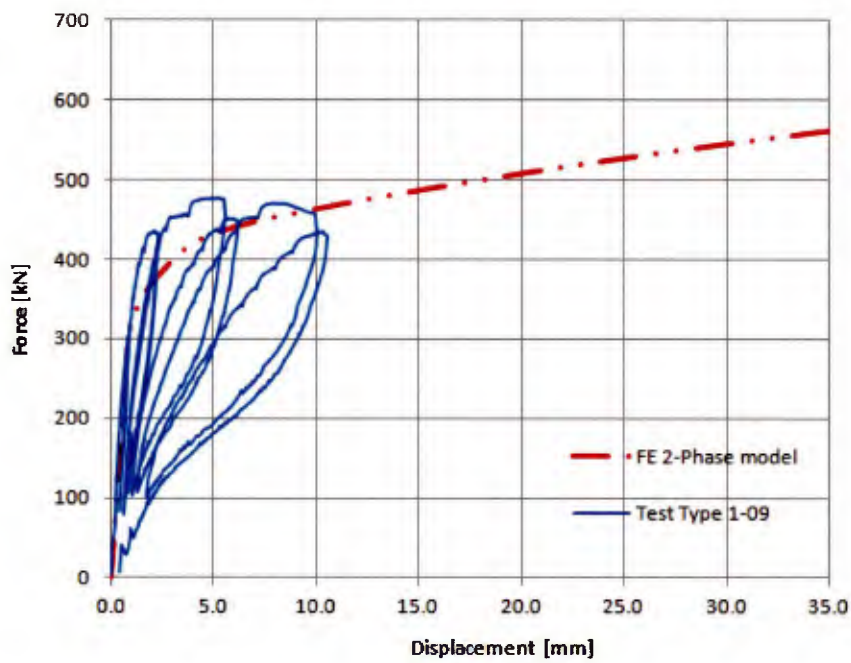

Figure 103: Comparison of test and simulation results of the bearing Type 1-09

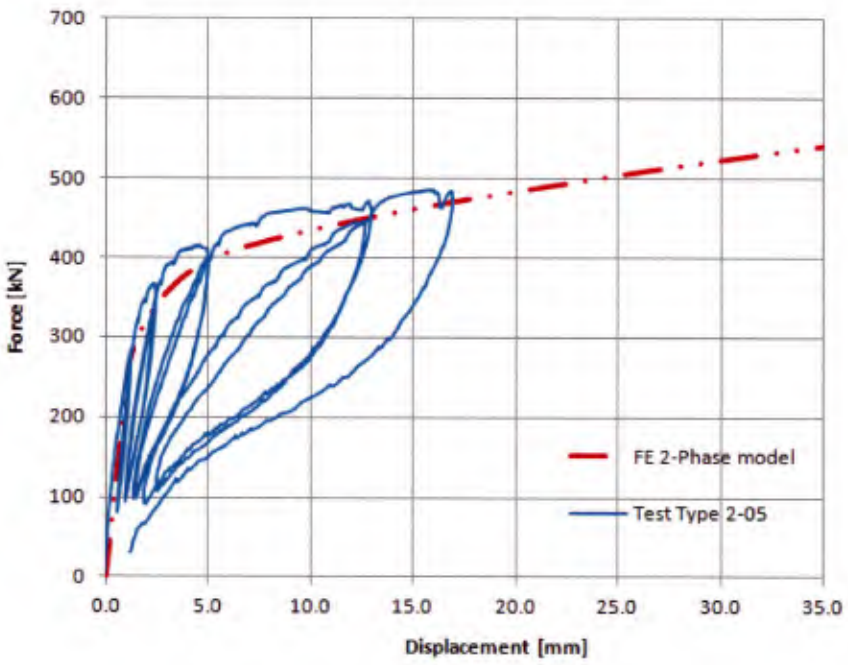

Figure 104: Comparison of test and simulation results of the bearing Type 2-05

Figure 105 plots of the critical pressure for both bearing types under the maximum shear deformation of 100 mm and the maximum tensile load of 636 kN. The same band plot as in Fig. 101 is applied. Here again the critical pressure values of the bearing Type 1 are generally higher than those of the bearing Type 2 because of the difference in the shear modulus. The critical pressure distribution is not uniform and the critical values are also higher than ones in Fig. 101. The hydrostatic condition is disturbed with the existing shear deformation and therefore it requires a higher pressure to initiate cavitation. That is also why the intact areas are slightly larger than the uniaxial tension case. However if the overall behaviour is compared the vertical stiffness in these cases are lower than the cases of uniaxial tension. That is probably because of the reduced effective area resisting the tensile force due to the shear deformation.

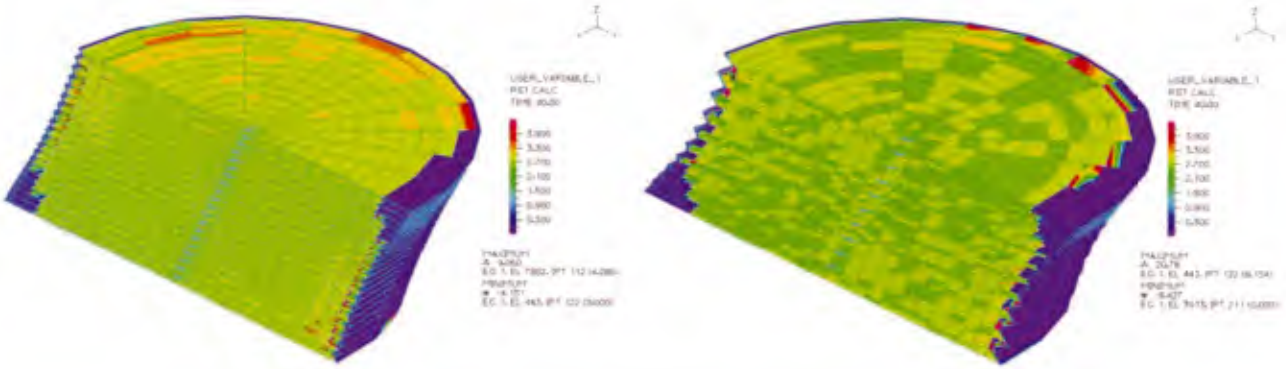

Figure 105: Plots of the critical pressure p_{crit}, left: Type 1, right: Type 2

The same parameters are used for the both bearing types and the results are all in good agreement. This means that the critical parameters are all material dependent. Then only one uniaxial tension test of a small bonded rubber disc is needed to determine those required parameters and with them very accurate simulation results for any other geometrical configuration can be expected.

Before closing this section, the FE results are compared in the next Fig. 106 that helps recognize the influences of the first shape factor and the simultaneous shear deformation on cavitation process.

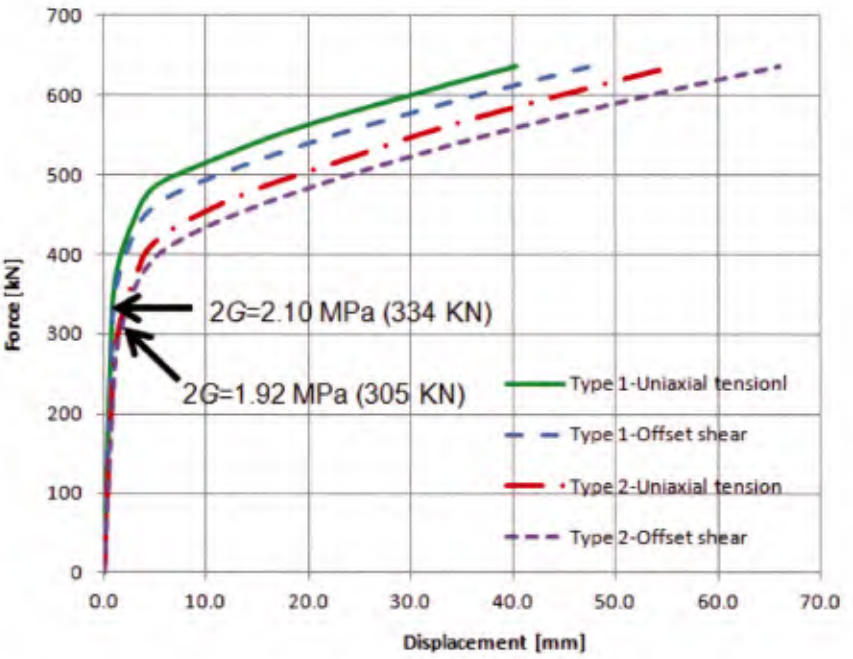

Figure 106: Comparison of all force-displacement curves

Indeed, the shear deformation of 100 mm has an influence on the cavitation process but it is not as significant as the influence of the first shape factor. In the same figure the "allowable" tensile stress specified in [10] and [12] that is equivalent to doubled shear modulus is indicated. For the bearing Type 1 this limit line seems below the onset of softening and then perhaps all bearings with even a higher first shape factor would be safe enough, although this may be a conservative statement. Thus it can be concluded that seismic isolator rubber bearings are on the safe side with this criterion because bearings with such high first shape factors are frequently used for the seismic isolation-purpose. For the Type 2 bearings, cavities develop before reaching this allowable stress level so that criteria for seismic isolator rubber bearings with lower first shape factors that are often used for seismically isolated bridges or simply as bridge bearings may need to be reconsidered.

6.6 Further Concerns

Apart from the combination with shear deformation, there are some other additional deformation modes that could accelerate the cavitation process. Examples of such modes are the torsional rotation with respect to the vertical axis or tilting. To realize these configurations by experiments is not an easy task and experiments are always time-consuming as well as expensive. In this last section of Chapter 6, an attempt is made to study those aspects with the help of FE analysis since the simulation results presented in the previous sections are convincing and so the other deformation modes can be predicted by the same model with certain credibility. However, it should be noted that the two-phase softening model works well only if all material constants and the parameters required for the cavitation criterion are available. For instance, FE analysis failed to provide a reasonable result when the shear strain is increased to 200 % for the models in Section 6.5 because the material behaviour was determined by the stress-strain curve within the strain range of 175 % and even at 150 % strain the stress value obtained by this model with those material

parameters is extremely high. The cavitation is induced but due to this high stress condition, expected softening is not obtained.
To begin with a parametric study with various first shape factors was carried out for a rubber pad model whose diameter is 440 mm since this factor seems most influential on the development of cavities. The result is shown in Fig. 107.

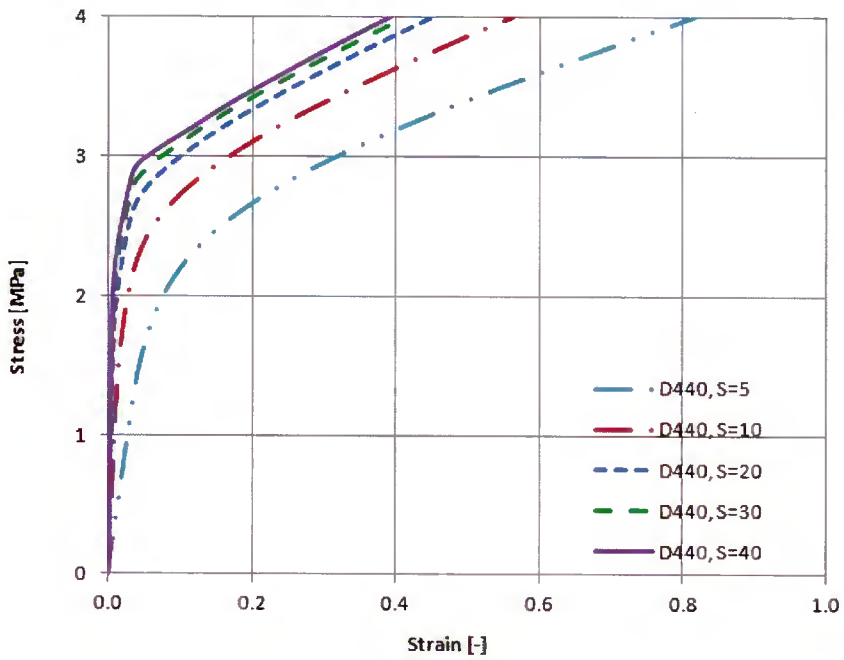

Figure 107: Force-displacement curves of the rubber discs with various first shape factors

The difference in force-displacement curve becomes insignificant as the first shape factor increases. When S_1 is higher than 20, all curves are almost identical, indicating that the critical volume change ration $J_{3,crit2}$ can be more accurately estimated merely with the vertical strain value in such cases. Seismic isolator rubber bearings often possess such a high value of S_1 in order to support a heavier superstructure. It is clear that only the second phase of softening is significant and the limit value should be determined by that phase. In this sense the currently adopted criterion $\sigma_{limit}=2G$ ensures the safety of the bearing sufficiently and could even be increased a little for the seismic isolator rubber bearings.

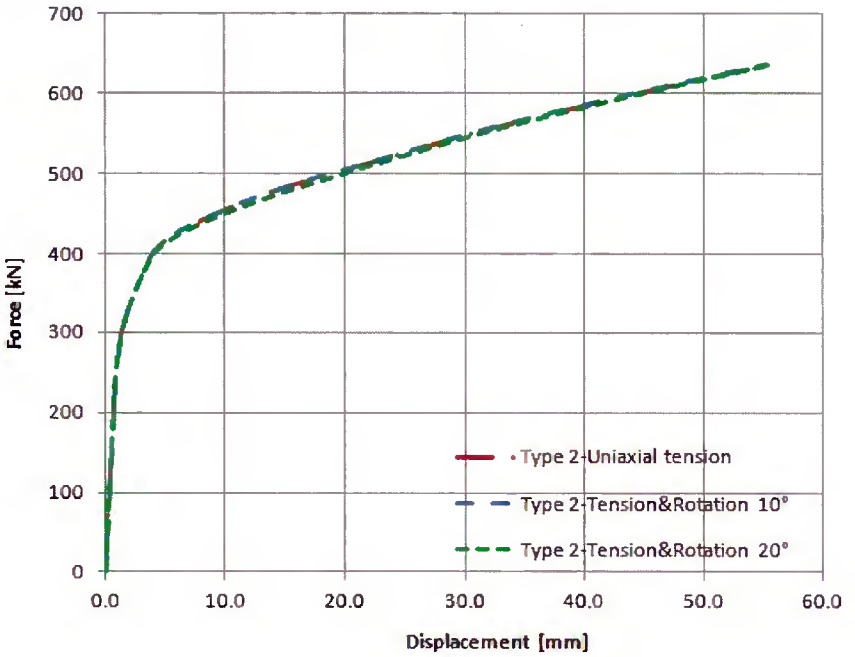

Figure 108: Comparison of force-displacement curves with/without torsional rotation

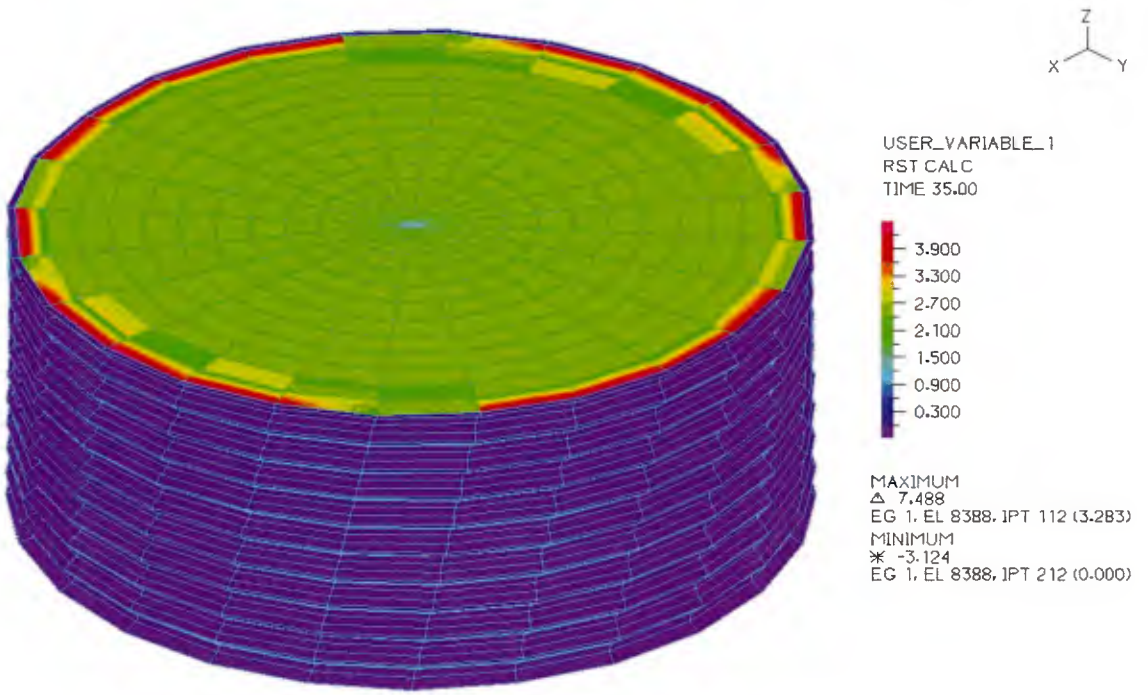

Figure 109: Pressure distribution of the bearing Type 2 under tension and torsion

Next the comparison of force-displacement curves of the Type 2 bearings under the uniaxial tension with/without torsinal rotation with respect to the vertical axis is shown in Fig. 108. Difference in the force-displacement curve due to the torsion is hardly recognized. The influence of the torsional deformation on cavitation process seems negligibly minor. The pressure distribution of the rubber in the deformed configuration is shown in Fig. 109.

Finally, the tilt deformation on top of the vertical compression was studied. The simulation model is first compressed with the amount of 6 MPa with which the vertical deformation of -3.0 mm reaches

and then inclination on the surface is increased. This simulates a situation where the bearing supports the dead load of the super structure and then is forcefully tilted by overturning the superstructure. Generally such a combination of deformation is not primary interest because each individual bearing should not experience excessive tilting if enough bearings are arranged on the same horizontal level. For bridge bearings, however, such situation may occur during earthquakes or due to the deformation of the superstructure caused by the temperature change. The pressure distribution of the bearing Type 2 is shown in Fig. 110.

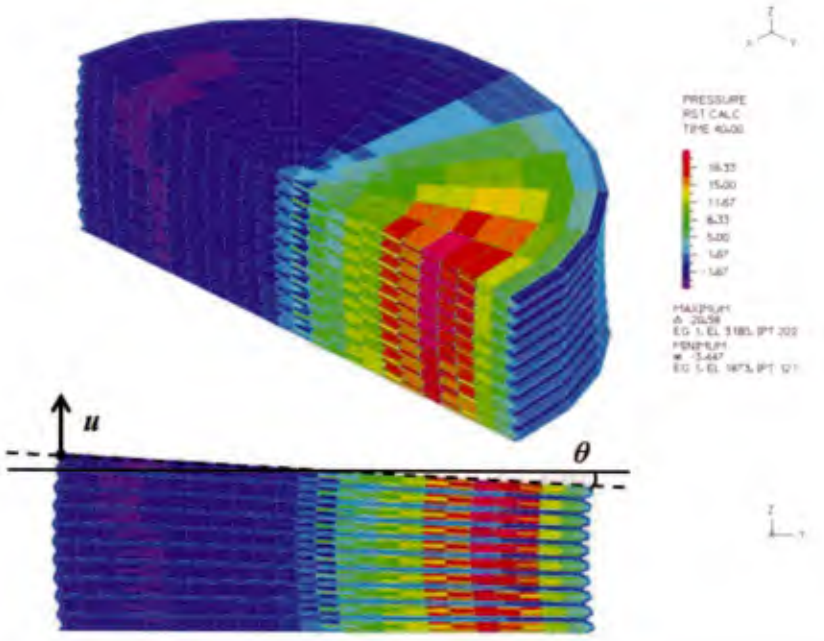

Figure 110: Pressure distribution of the bearing Type 2 under compression and inclination

This plot is made at the calculated maximum rotation angle θ_{max}=0.0717 radian with which the maximum displacement at the corner on the tension side u_{max}=17.0 mm. Those u and θ are also indicated in the same figure. In the annex of the Japanese specifications of bridge bearings [12], it is experimentally shown that no negative pressure appears unless the deformation u exceeds 0, and therefore the following condition under live loads is imposed for bridge rubber bearings in [12].

$$u_r \leq u_c / c_v \tag{6.63}$$

where u_r and u_c are deformation caused by inclination and compression, respectively and c_v is the safety factor concerning the deviation of the bearing properties.

The FE result corresponds to the experimental result of [12] that no negative pressure appears in rubber as long as the deformation u<0. The question is raised, however, of whether the precaution of (6.63) can be more relaxed. Propagation of cavitation is shown in Fig. 111 where it is observed that the cavities start developing first with very high inclination. This tendency is also true for the Type 1 bearing, although the minimum inclination required to trigger cavitation is half as much φ=0.0169 radian (u=2.5 mm). Hence it is assumed that doubling the limit value of (6.63) would still be safe enough and the capacity of the bearing can be fully utilized.

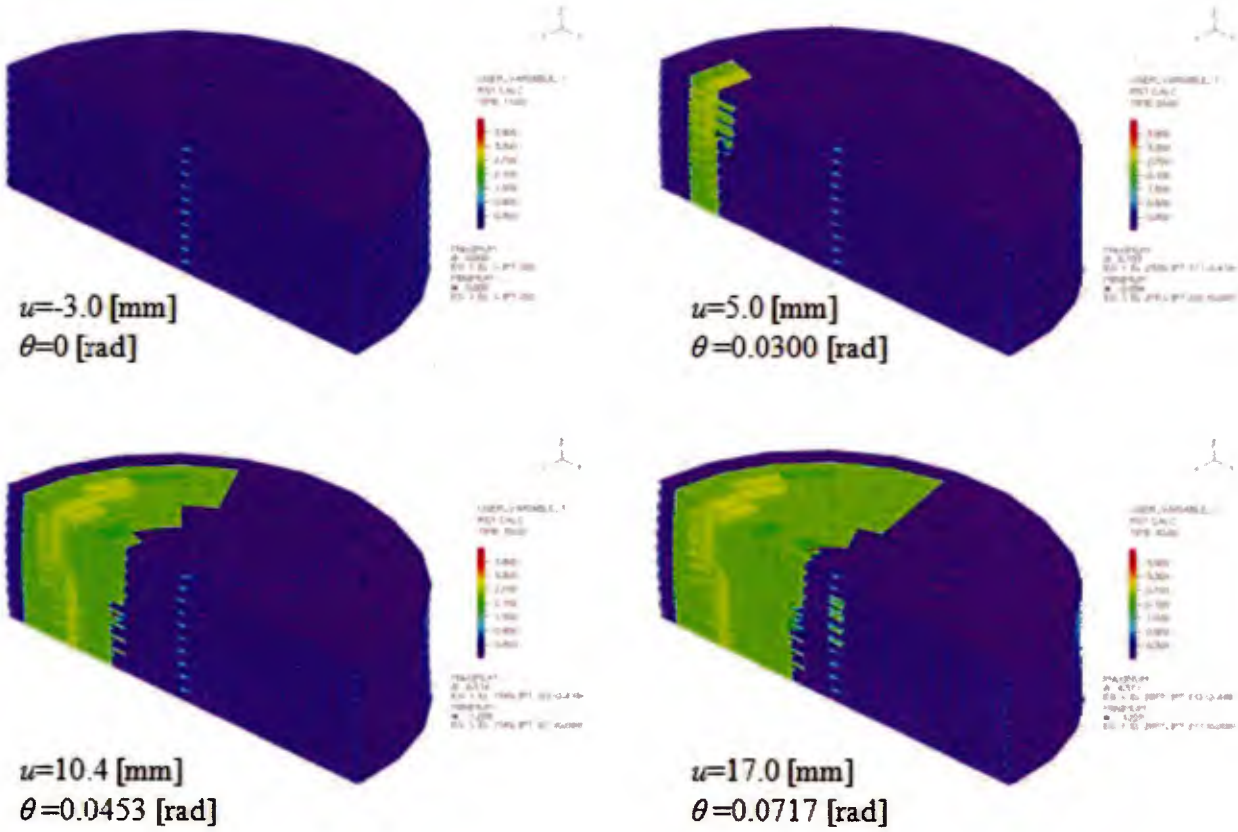

Figure 111: Development of cavities in the bearing Type 2 under compression and inclination

7 SOFTENING INFLUENCE ON THE GLOBAL STRUCTURAL SYSTEM

7.1 Preliminary

In this chapter the possibility of uplifting on the seismically isolated buildings at the isolation layer is studied. Uplifting is caused not only by the vertical seismic force but excessive isolation drifting deformation mode as well as structural rocking motion. In fact the latter two causes are main concerns and the influence of the vertical seismic force is often negligible unless the building stands relatively near an active fault. For the design of the seismically isolated buildings, it is generally suggested that no tension should occur in the seismic isolation layer, i.e. the isolator bearings should carry no tension during earthquakes, although international design standards of isolator bearings such as [10] and [12] specify the allowable tensile stress, which is frequently defined as 2G. In order to ascertain this "zero tension" condition at the design stage, there is a simplified criterion based on the response spectrum analysis available [85]. The horizontal force F_Q calculated by the structure weight $\mathcal{W}$ and the response acceleration S_a is applied to the structure at the centre of mass assuming that only the isolation deformation (drifting) mode of the ideal solid structure is present. Then creating the moment equilibrium at the base level considering that the bearing at the end of one side carries no force, the following expression is derived.

$$\alpha_{b,total} = \frac{1}{3} \cdot \frac{n_b + 1}{n_b - 1} \cdot \frac{B_s}{H_s} \qquad \because n_b \geq 2 \text{ [85]} \tag{7.1}$$

Where B_s and H_s are the width and the height of the building and n_b is the number of equally spaced bearings along the width direction. $\alpha_{b,total}$ is the base shear coefficient defined as $F_Q/\mathcal{W}$

This equation helps structural designers to determine the aspect ratio limit. It indicates that a relatively high and slim structure can be seismically isolated without causing the isolator bearing undesired tension as long as the horizontal seismic force is sufficiently reduced by seismic isolation. It is also clear from this expression that increasing the number of bearing reduces the limit of the aspect ratio. From these reasons it is recommended that the least amount of large bearings should be used so that the chance of uplifting is minimized. A large horizontal deformation capacity as well as a high vertical load carrying capacity are achieved. Tada mentioned in [85] that the optimal natural period of the seismically isolated building would be four seconds or longer with which a very low base shear coefficient is easily achieved. In turn the seismic isolation can be employed for taller buildings of the aspect ratio as high as six. In reality however, the rocking motion of the structure cannot be completely eliminated and the component of the overturning moment from this motion becomes more pronounced when the structural is tall and slim since the natural period of the rocking mode approaches the natural period of the isolation mode. Moreover the vertical deformation of the isolator bearings contributes to the rocking motion as well, see Fig. 112. K_s and K_r are the structural stiffness and the rotation stiffness due to the vertical springs, respectively. The structural stiffness K_s is determined by the elastic modulus and the moment of inertia of the wall and the height of the structure. The stiffness of the rocking motion due to the vertical stiffness K_v of isolator bearings is expressed as

$$K_r = \frac{1}{6} \cdot \frac{n_b + 1}{n_b - 1} \cdot K_v \cdot \left(\frac{B_s}{H_s} \right)^2 \qquad \because n_b \geq 2 \tag{7.2}$$

The stiffness K_r is much larger than K_s so that this component is virtually negligible for the most cases. However from this equation it is again clear that increasing the number of bearings elongates the natural period of the rocking motion, deteriorates the performance of the seismic isolation and therefore results in the danger of uplifting.
In the next section the criterion (7.1) is examined for arbitrary multi-degree-of-freedom systems by a comparison with the numerical analysis. Then Section 7.3 will focus on the influence of the cavitated isolator rubber bearings on the global dynamic behaviour of the seismically isolated structure.

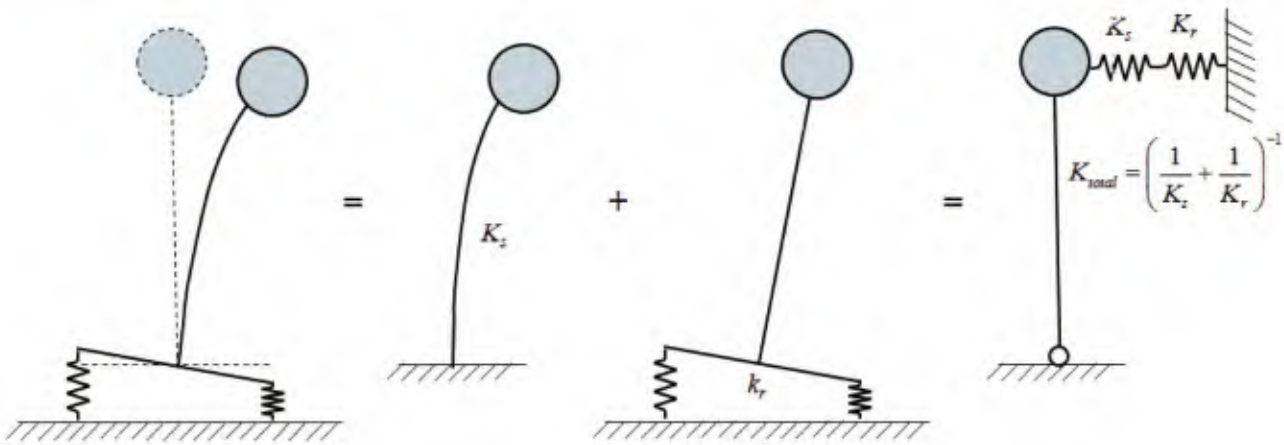

Figure 112: Components of the rocking motion

7.2 Examination Of The Uplift

The criterion of the uplifting limit for the seismically isolated structure is examined by means of the FE analysis and the modal superposition analysis combining with the response spectrum analysis. ADINA is employed for the FE analysis and a simple program is implemented for the modal superposition analysis with Visual Basic in Microsoft Excel. Two analysis methods are adopted in order to verify the performance of each method. The seismic data of the Christ Church earthquake (New Zealand in 2011) in the north-south component at the site code PRPC available on the GeoNet homepage is applied for the both analyses. This earthquake is selected since the seismic wave possessed relatively high acceleration response in longer period range (3 sec.~), which means that the uplift risk of seismically isolated buildings was higher. The time-acceleration plot of this seismic wave is shown in Fig. 113.

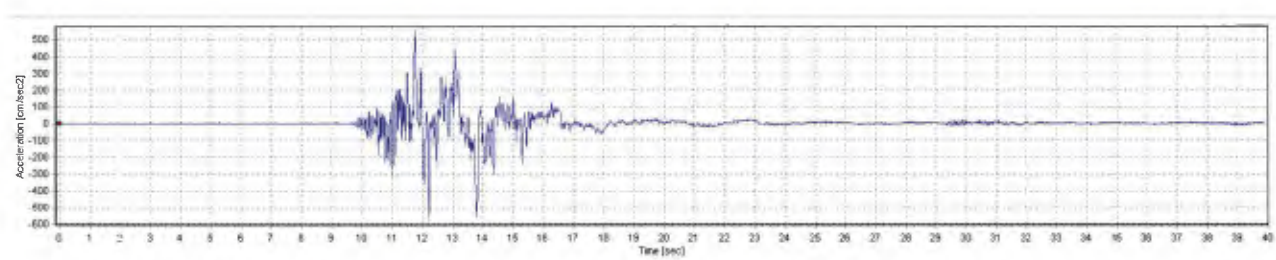

Figure 113: Time-acceleration plot of the NS component from 2011 Christchurch earthquake

7.2.1 Finite element analysis

The several MDOF system models (seven, thirteen and nineteen masses) were prepared and computed with the commercially available software ADINA. The simulation models consist of multiple concentrated masses, beam elements, and horizontal spring elements with dash pots and

vertical spring elements. These models represent a part of an arbitrary base-isolated building as shown in Fig. 114. Viscous damping (dash pot) is selected for the horizontal spring because other types of damping add their damping force to the maximum structural response and as a result the base shear coefficient in the criterion (7.1) cannot be evaluated exactly. As for the dimension of the buildings, the width is set to either 10 m or 20 m and the height is varied from 20 m to 60 m. The number of bearings n_b is varied from two to four but the sum of all vertical stiffness is kept at a constant value independent of n_b for each MDOF system. As for the vertical stiffness, the value is determined so that the vertical deformation of the springs due to the structural weight amounts approximately to 2 mm. The stiffness of the building itself is determined from its first natural period based on the evaluation formula $T_s=0.02H_s$ for RC frame structure provided in the notification No.1793 of the Japanese Construction Ministry (issued in 1980 and final revision in 1987 as the notification No. 1918). In [13] another expression for an approximate evaluation is given as $T_s=0.075H_s^{3/4}$ for the same type of structure but this evaluation formula is limited to the structure height of 40 m and also generates longer structural natural periods, which is unfavourable for the effectiveness of the seismic isolation. Hence the evaluation formula of Japanese Construction Ministry is adopted. Assuming the linear increase in the structural stiffness towards ground to carry the equally increasing shear force, the stiffness of each storey is computed approximately from the Dunkerley's formula. For a further simplification the stiffness of floors is set to a very high value so that no influence of the bending deformation of floors has to be considered. All masses are assumed to be equal including the base floor.

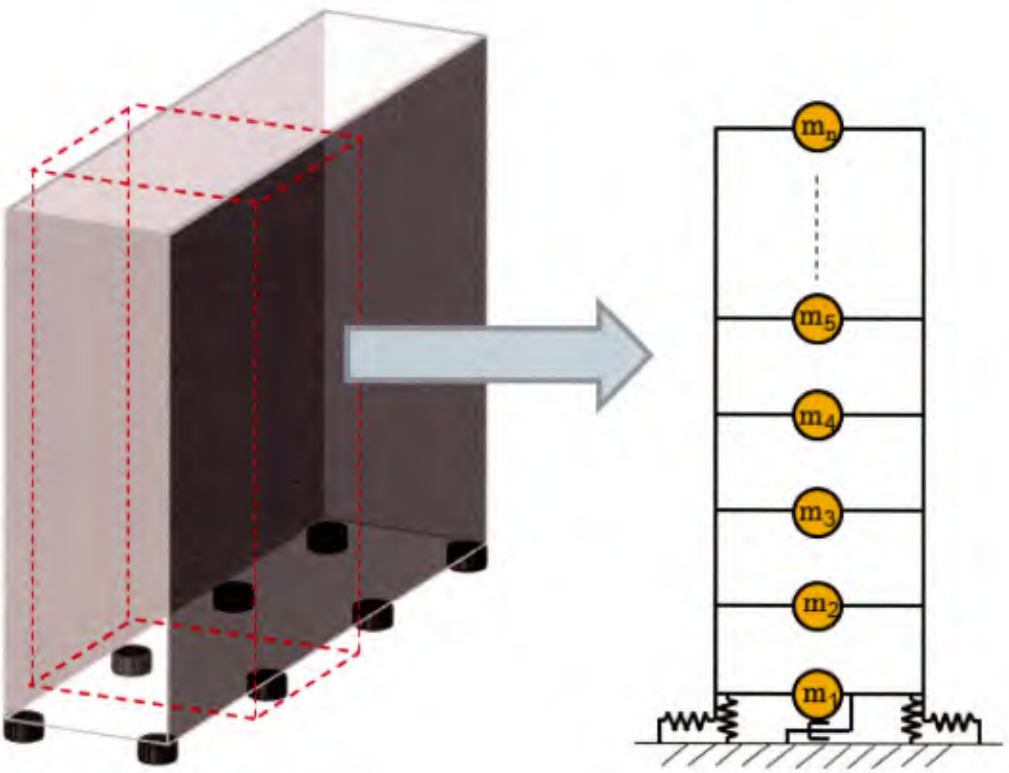

Figure 114: FE model of the MDOF system

According to [8] such simple models can sufficiently represent the dynamic structural behaviour unless the compression buckling failure of the isolator bearings is of concern. The characteristic values for each MDOF system are summarized in the following Table 41.

Table 41: MDOF system model parameters

Simulation model	7 masses	13 masses	19 masses
Height H_s [m]	20	40	60
Width B_s [m]	20	10 or 20	10 or 20
Aspect ratio	1	4 or 2	6 or 3
First natural period without seismic isolation T_s [s]	0.4	0.8	1.2
Natural period of seismic isolation T_b [s]	3.0	3.5	4
Structure damping ratio ξ_s [%]	5	5	5
Isolation damping ratio ξ_b [%]	10 or 20	10 or 20	10 or 20

These parameters are valid for the modal superposition analysis with the response spectrum analysis as well.

For the dynamic analysis the equations of equilibrium at each time step have to be solved by means of time integration. Two major types to solve such a system are offered by ADINA, namely the direct integration methods and the mode superposition. Both types should reach the same solution within the calculation error. For the direct integration methods the selection of the time step size is the main cause of error and for the mode superposition method the accuracy of the solution is determined by how many deformation modes are considered. The mode superposition method can be quite effective considering the main structural deformation modes that have major impact on the response are only first several modes but the spring damping elements, that represent the elstomeric isolator rubber bearings, are not feasible for this method. Therefore the direct integration method is selected and the concept of the modal superposition is used with the linear response spectrum analysis for comparison/verification instead.

The direct integration methods can be carried out with either explicit or implicit integration scheme. For the former the central difference integration scheme and for the latter the Wilson ϑ scheme and the Newmark scheme are available in AIDNA. Bathe [126] and ADINA manual [138] recommend the implicit integration schemes as an optimal choice in case of slow-speed structural dynamic problems such as earthquake response since they are 'unconditionally stable' and hence more efficient. Concerning this 'stability' of the integration method, the term 'conditional stability' or 'unconditional stability' can be understood by the following quote from [126]:

> "An integration method is unconditionally stable if the solution for any initial conditions does not grow without bound for any time step Δt, in particular when $\Delta t/T$ is large. The method is only conditionally stable if the above only holds provided that $\Delta t/T$ is smaller than or equal to a certain value, usually called the stability limit."

In this sense the explicit scheme is conditionally stable and if this scheme of the earthquake response problems is selected, the required time step size to obtain the stability would be, first of all, very small and furthermore to obtain the accurate responses even a much smaller time step size would be required. Therefore the implicit scheme is selected for the following analyses. This scheme is called implicit because some manipulation in the governing equation is necessary in order to obtain a solution at the next time step from the current time step. Both Wilson θ and Newmark schemes a function of the acceleration between the current time step and the next one is assumed as the first procedure. For the Newmark scheme, that is $(1-\delta)^t\ddot{\mathbf{U}}+\delta^{t+\Delta t}\ddot{\mathbf{U}}$. With this assumption the velocity and the displacement at the next time step can be written as

$$^{t+\Delta t}\dot{\mathbf{U}} = {}^t\dot{\mathbf{U}} + \left[(1-\delta)^t\ddot{\mathbf{U}} + \delta^{t+\Delta t}\ddot{\mathbf{U}}\right]\Delta t \quad [126] \tag{7.3}$$

$$^{t+\Delta t}\mathbf{U} = {}^{t}\mathbf{U} + {}^{t}\dot{\mathbf{U}}\Delta t + \left[\left(\frac{1}{2}-\alpha\right){}^{t}\ddot{\mathbf{U}} + \alpha\, {}^{t+\Delta t}\ddot{\mathbf{U}}\right]\Delta t^2 \text{ [126]} \tag{7.4}$$

where α and δ are factors to be selected, which determine the acceleration function within the time step Δt.

Equation (7.4) is first converted into the form such that the equation is solved for $\ddot{\mathbf{U}}^{t+\Delta t}$. Then by inserting it to Eq. (7.3), both equations can be expressed with all known terms from the previous time step and $\mathbf{U}^{t+\Delta t}$. Those for acceleration and velocity are inserted into the equilibrium equation at time step $t+\Delta t$ and $\mathbf{U}^{t+\Delta t}$. Then again using Eqs. (7.3) and (7.4) with the obtained displacement, the acceleration and the velocity are calculated. For the Wilson θ scheme, the assumed relationship of the acceleration between two sequent time steps is different from the Newmark scheme but the procedure is analogous. In fact both of them generate an equivalent result by setting certain values for factors α, δ and θ. The Newmark scheme is applied for the analysis with the factors α=0.25 and δ=0.5 since it is proven to be more stable and accurate than the Wilson θ scheme with an arbitrarily given time step size. The comparison of these two schemes can be found in [126]. With the factors above the average constant acceleration is assumed [126] [141].
Even if the Newmark method is unconditionally stable, it does not mean the result is always accurate with a randomly chosen time step size. For an accurate result, the time step size must be smaller than a specific value and the recommendation from [126] states that

$$\Delta t < \frac{T_p}{10} \text{ [126]} \tag{7.5}$$

where T_p is the period of the highest response mode considered.

Ordinarily very high frequencies do not have to be taken into consideration since those corresponding deformation modes contribute little in the structural responses. In this dissertation, however, the vertical motion during earthquakes is also of interest, which can correspond to higher frequencies since the vertical stiffness of the structures is very high in comparison with the shear stiffness or bending stiffness. If such shaking motions had to be simulated accurately, quite a small time step size would be required and as a result the calculation becomes expensive. To minimize this time-consuming computation, some reasonable limit in the frequency should be set.

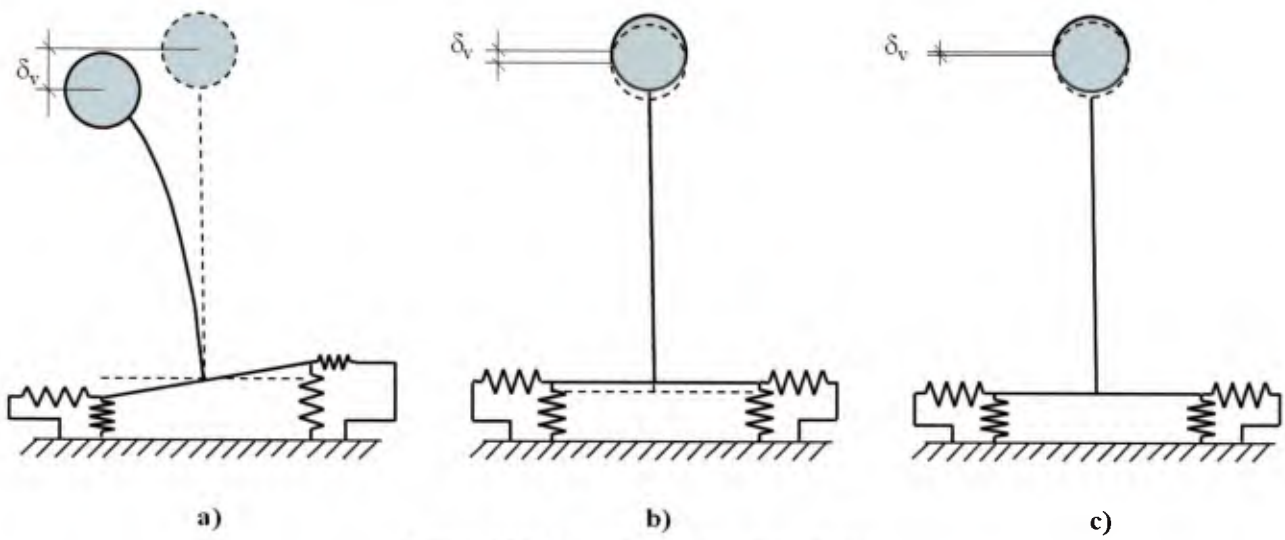

Figure 115: Possible vertical motions

The possible vertical motions of the seismically isolated building are sketched in Fig. 115. The case a) is the vertical displacement as a result of the rocking motion whose natural frequency should be equal to that of the rocking motion or twice as high depending on where the measurement takes place. The case b) is the simple vertical motion due to the elasticity of the elastomeric bearings. Finally the case c) represents the vertical motion due to the elasticity of the structural members of the building itself.

The natural frequencies of the modes b) and c) are apparently much higher than the mode a) since the vertical stiffness of the elastomeric bearings and the structure itself are high since the weight of the structure has to be supported by those vertical structural elements. A distinction must be made, however, between the modes b) and c). The structural vertical stiffness should be even much higher than that of b), since the design of the building itself should not be so different from conventional buildings where the walls and piers should be capable of enduring the shear and bending deformation. In order to achieve that, those structural elements possess a certain dimension, and therefore strength, which contributes to quite a high vertical stiffness. It is not possible to generalize the structural stiffness but considering the ratio of the structural elements and the mass supported by them, the natural frequency of the mode c) would be well beyond other two modes. Deformation would not reach even a millimetre between two sequent floors. Then even if the resonance is induced, the impact on the interior objects and human residing within the building are negligible. For these reasons, the mode c) is not considered here. The mode b), although it has still a higher natural frequency, is to be taken into account since the elevated vertical acceleration measured on the seismically isolated buildings (see Chapter 2) is most certainly caused by the isolator units. It is again difficult to specify the natural frequency range of the mode b) but there are design recommendations and some limitations in the compression loading on the elastomeric bearing. With these presumptions and by controlling the height and the plane area of the bearing considering the balance of the horizontal and the vertical stiffness, the range of the natural frequency can be roughly estimated. Generally speaking the range between 5 to 15 MPa of compressive stress is applied to each bearing and bearings with a higher S_1 tend to carry a heavier load. This estimation leads to the frequency range approximately from 8 to 15 Hz, which is close to the one mentioned in [91], from 8 to 12 Hz. Therefore if the motion of its natural frequency 15 Hz can be accurately simulated, the mode b) and hence a) as well are assumed to be adequately simulated. The recommended time step size by Eq. (7.5) is then 0.005 s. This time step size is also sufficiently small in order to avoid the aliasing problem for the discrete Fourier transformation of the same frequency range. In fact, this time step size, which is equivalent to the sampling time step and therefore determines the sample frequency, even the motions of frequency from 50 to 100 Hz can be evaluated. This indicates that the frequency analysis can be possibly carried out to pick up the frequency of the mode c) as well, although it is not of main interest as explained already. Hence in the following analysis Δt =0.005 s is used unless otherwise mentioned.

As for damping, there is specific information available on the equivalent damping coefficient for each construction material and construction component in the design standards [23] [14] or more detailed in [142], for instance. In the following sections, however, damping 5 % and 10 % for the superstructure and the horizontal springs, i.e. isolator bearings, respectively are assumed for convenience. The vertical motion of the spring is undamped. The damping of the isolator bearings is simply integrated in the spring element, whereas in order to mitigate the different deformation modes of the superstructure simply and effectively, the Rayleigh damping is applied. For the direct integration method, that is of the form

$$\mathbf{C} = \alpha_d \mathbf{M} + \beta_d \mathbf{K} \tag{7.6}$$

where α_d and β_d are factors that determine the damping amount.

Numerical and experimental analysis of the load-carrying behaviour of laminated elastomeric bearings as seismic isolators

With eigenvector $\boldsymbol{\phi}_i$ and the damping matrix $\mathbf{C}$ the damping coefficient ξ_i can be expressed in the relation

$$\boldsymbol{\phi}_i^T \mathbf{C} \boldsymbol{\phi}_j = 2\omega_i \xi_i \delta_{ij} \tag{7.7}$$

Equating these two equations and considering the M-orthonormal property of the eigenvector, the ξ_i can be expressed only by the factors α_d and β_d, and the angular natural frequencies ω_i as

$$\alpha_d + \beta_d \omega_i^2 = 2\omega_i \xi_i \tag{7.8}$$

The system of equations has two unknowns to be determined and hence only two different eigenmodes are necessary to obtain these two factors. For the analysis here the two factors are determined based on the first eigenmodes and the eigenmode corresponding to the vertical motion due to the isolator bearings. As for the damping coefficient, the amounts of 0.05 and 0.07 are given for the former mode and the latter, respectively so as to minimize the fluctuation of damping for the other modes between these two.

7.2.2 Response spectrum analysis

If the structure ought to be investigated for the criterion (7.1), only its maximum response has to be known. For approximation the conventional linear response analysis should be sufficient to examine if the bearing would be subject to tensile force since the vertical springs behave almost linear-elastically within relatively a low compression stress range. Aforementioned time history analysis is the most commonly adopted method to observe the dynamic structural behaviour but the effort for building up the simulation models and evaluation of the results is time-consuming. Therefore the simple program is implemented for MDOF systems by the use of Visual Basic with Microsoft Excel by which the natural frequencies of the MDOF systems and the linear elastic responses of each mode are computed. In general, the natural period of the base-isolation deformation mode (drifting displacement of the superstructure on the isolator bearings) is highly dominant and other structural deformation modes hardly contribute to its response. As already explained, however, the contribution of those other deformation modes can become a little more pronounced if the structure is slim and tall, i.e. if the stiffness of the structure is low. Hence it is necessary to include a few more deformation modes for a higher accuracy. The same attempt is made by Hino et al. [6] in which MDOF system is converted to the equivalent SDOF system or two-degree-of-freedom system to evaluate the overturning moment at the isolation level and the linear elastic response spectrum analysis is performed for those equivalent systems. Only the first and the second deformation modes were taken into account. However, they seem to deliver adequately accurate results. In this dissertation, the first three deformation modes are taken into account for the possibility of resonance in the frequency range of those deformation modes is non-zero and also there is no difference in effort whether more deformation modes are included or not once programming is completed.

For the computation of the natural frequencies and deformation modes, the vector inverse iteration method is employed. The starting point of this method is the relationship of the stiffness matrix, the mass matrix, and the assumed mode shape vector.

$$\mathbf{K}\boldsymbol{\phi} = \rho \mathbf{M}\boldsymbol{\phi} \tag{7.9}$$

Multiplying $\mathbf{K}^{-1}$ on both terms from the left, the following expression for iteration is obtained.

$$\boldsymbol{\phi}_{i+1} = \rho \mathbf{K}^{-1} \mathbf{M} \boldsymbol{\phi}_i \tag{7.10}$$

where i is the number of iteration.

As the first iteration step, an arbitrary vector $\boldsymbol{\phi}_1$ has to be defined and Eq. (7.10) is solved with that vector for the first iteration solution $\boldsymbol{\phi}_2$. Mathematically it is proven that the $\boldsymbol{\phi}_{i+1}$ converges to the first mode shape of the system. The eigenvalue ρ also converges to the square of the first natural circular frequency. More effective algorithm is described in [126] for this method and referring to it the following iteration procedures are carried out for i= 1, 2,···,

$$\mathbf{y}_1 = \mathbf{M}\mathbf{x}_1 \tag{7.11}$$

$$\bar{\mathbf{x}}_{i+1} = \mathbf{K}^{-1}\mathbf{y}_i \tag{7.12}$$

$$\bar{\mathbf{y}}_{i+1} = \mathbf{M}\bar{\mathbf{x}}_{i+1} \tag{7.13}$$

$$\lambda_{i+1} = \frac{\bar{\mathbf{x}}_{i+1}^{T}\mathbf{y}_i}{\bar{\mathbf{x}}_{i+1}^{T}\bar{\mathbf{y}}_{i+1}} \tag{7.14}$$

$$\mathbf{y}_{i+1} = \frac{\mathbf{y}_{i+1}}{(\bar{\mathbf{x}}_{i+1}^{T}\bar{\mathbf{y}}_{i+1})^{1/2}} \tag{7.15}$$

As i $\rightarrow\infty$, ρ converges to the eigenvalue of the system and once an arbitrary tolerance criterion is fulfilled, the first natural mode shape is obtained as

$$\boldsymbol{\phi} = \frac{\bar{\mathbf{x}}_{n_{last}+1}}{(\bar{\mathbf{x}}_{n_{last}+1}^{T}\bar{\mathbf{y}}_{n_{last}+1})^{1/2}} \tag{7.16}$$

where n_{last} is the number of the last iteration.

For the first iteration vector $\mathbf{x}_1$, all values are set to one since any arbitrary vector can be used. With these values the first iteration vector is equivalent to the ideal first mode shape of the seismically isolated building and thus the convergence would be achieved faster. For these procedures, more detailed description is found in [126] for instance.
Further natural deformation modes and natural frequencies are computed using the orthogonal property of the eigenmodes. Orthogonality between two eigenmodes is expressed as

$$^{(i)}\boldsymbol{\phi}^{T}\mathbf{M}^{(i+1)}\boldsymbol{\phi} = 0 \tag{7.17}$$

where the superscript (i) on the left denotes i-th modes.

After the iteration procedures described from Eqs. (7.11) to (7.16) the first eigenmode vector $^{(1)}\boldsymbol{\phi}$ is available and now using the relationship (7.17), the next eigenmode vector $^{(2)}\boldsymbol{\phi}$ can be computed. Provided that $^{(1)}\boldsymbol{\phi}$ is known and the degree of freedom is n, then the relationship (7.17) in matrix form is

$$ {}^{(1)}\left[\phi_1\ \phi_2 \cdots \phi_n\right]\begin{bmatrix} m_1 & 0 & \cdots & 0 \\ 0 & m_2 & \cdots & 0 \\ \vdots & \vdots & \ddots & 0 \\ 0 & 0 & \cdots & m_n \end{bmatrix}^{(2)}\begin{bmatrix} \phi_1 \\ \phi_2 \\ \vdots \\ \phi_n \end{bmatrix} = 0 \tag{7.18} $$

From Eq. (7.18) the following relationship is obtained

$$ m_1\,{}^{(1)}\phi_1\,{}^{(2)}\phi_1 + m_2\,{}^{(1)}\phi_2\,{}^{(2)}\phi_2 + \cdots + m_n\,{}^{(1)}\phi_n\,{}^{(2)}\phi_n = 0 \tag{7.19} $$

By setting ${}^{(2)}\phi_1=1$, ${}^{(2)}\phi$ can be rewritten as

$$ {}^{(2)}\begin{bmatrix} \phi_1 \\ \phi_2 \\ \vdots \\ \phi_n \end{bmatrix} = {}^{(2)}\begin{bmatrix} 0 & -\frac{m_2}{m_1}\,{}^{(1)}\left(\frac{\phi_2}{\phi_1}\right) & \cdots & -\frac{m_n}{m_1}\,{}^{(1)}\left(\frac{\phi_n}{\phi_1}\right) \\ 0 & 1 & \cdots & 0 \\ & & \cdots\cdots & \\ 0 & 0 & \cdots & 1 \end{bmatrix}^{(2)}\begin{bmatrix} \phi_1 \\ \phi_2 \\ \vdots \\ \phi_n \end{bmatrix} = {}^{(2)}\mathbf{S}\,{}^{(2)}\boldsymbol{\phi} \tag{7.20} $$

Again setting all ${}^{(2)}\phi_j=1$ as the first trial vector for iteration, the whole right hand side of Eq. (7.20) is inserted into the vector $\mathbf{x}_1$ of Eq. (7.11) and the iteration procedures are repeated from Eqs. (7.12) to (7.16) until the second eigenvalue ${}^{(2)}\rho$ converges. The so-called 'sweep matrix' ${}^{(i)}\mathbf{S}$ is modified with the general term of Eq. (7.19) to compute the further sequence of eigenmode vectors. For instance, Eq. (7.19) and the following equation are solved in terms of ${}^{(3)}\phi_1$, ${}^{(3)}\phi_2$ and then added to the second row in the sweeping matrix above in order to compute the third eigenmode vector.

$$ m_1\,{}^{(2)}\phi_1\,{}^{(3)}\phi_1 + m_2\,{}^{(2)}\phi_2\,{}^{(3)}\phi_2 + \cdots + m_n\,{}^{(2)}\phi_n\,{}^{(3)}\phi_n = 0 \tag{7.21} $$

The obtained natural frequencies and the natural mode shapes are employed for the response spectrum analysis.

The linear elastic acceleration response spectrum of the NS component of Christchurch earthquake on February 21st 2011 in New Zealand, computed by the commercially available software SeismoSignal is shown in Fig. 116. With the corresponding acceleration values from this diagram, the floor displacement of each mode is computed as

$$ {}^{(i)}u_j = {}^{(i)}\psi\,{}^{(i)}\phi_j\,{}^{(i)}\hat{\ddot{u}} / {}^{(i)}\omega^2 \tag{7.22} $$

where the modal participation factor ψ is defined as

$$ {}^{(i)}\psi = \frac{{}^{(i)}\varphi}{{}^{(i)}M} \qquad {}^{(i)}\varphi = \sum_{j=1}^{n} m_j\,{}^{(i)}\phi_j \qquad {}^{(i)}M = \sum_{j=1}^{n} m_j\,{}^{(i)}\phi_j^2 \tag{7.23} $$

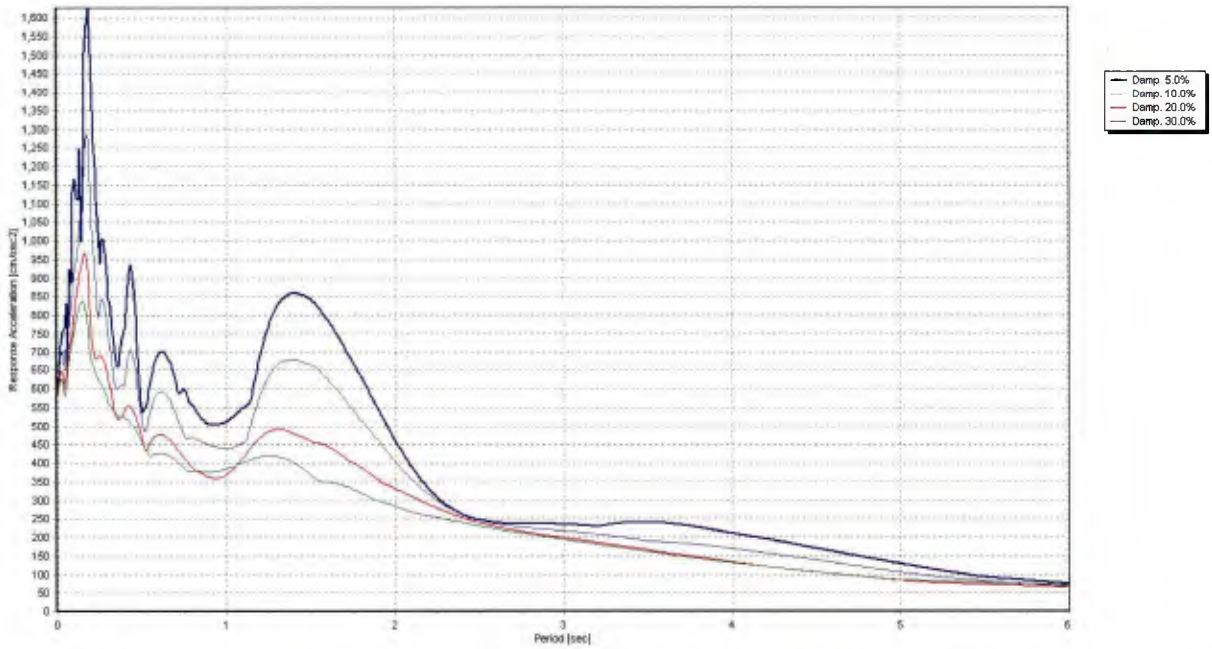

Figure 116: Linear acceleration spectrum of the NS component from 2011 Christchurch earthquake

The corresponding static forces related to the nth-mode peak response are

$$^{(i)}F_j = {}^{(i)}\psi m_j \, {}^{(i)}\phi_j \, {}^{(i)}\hat{\ddot{u}} \tag{7.24}$$

The total responses of the first three eigenmodes are computed by the square-root-of-sum-of-squares (SRSS).

$$u_{total,j} = \left(\sum_{i=1}^{3} {}^{(i)}u_j \right)^{1/2} \qquad F_{total,j} = \left(\sum_{i=1}^{3} {}^{(i)}F_j \right)^{1/2} \tag{7.25}$$

The sum of all these equivalent static forces is the base shear, namely

$$V = \sum_{j=1}^{n} F_{total,j} \tag{7.26}$$

and the overturning moment at the isolation level is computed as

$$M = \sum_{j=1}^{n} F_{total,j} h_j \tag{7.27}$$

Additionally the gravity-induced overturning moment is taken into consideration, which is computed as

$$\Delta M = \sum_{j=2}^{n} (u_{total,j} - u_{total,1}) m_j g \tag{7.28}$$

where g is the gravitational acceleration g=9.81 m/s^2.

[16], [126] and [143] are referred to for the implementation described in this section. Read them for more details.

7.2.3 Comparison of two analysis methods

The two analysis methods described in the previous sections are compared here. First the first three natural frequencies of all simulation models are summarised in Tables 42 to 46.

Table 42: Comparison of natural frequencies-7 mass model, aspect ratio 1

Analysis method	FE			Modal superposition		
No. of bearings n_b	2	3	4	2	3	4
First natural frequency f_1 [Hz]	0.330	0.329	0.329	0.330		
Second natural frequency f_2 [Hz]	2.820	2.803	2.793	2.858		
Third natural frequency f_3 [Hz]	5.242	5.234	5.229	5.267		

Table 43: Comparison of natural frequencies-13 mass model, aspect ratio 2

Analysis method	FE			Modal superposition		
No. of bearings n_b	2	3	4	2	3	4
First natural frequency f_1 [Hz]	0.267	0.267	0.267	0.268		
Second natural frequency f_2 [Hz]	1.145	1.141	1.139	1.153		
Third natural frequency f_3 [Hz]	2.157	2.156	2.155	2.159		

Table 44: Comparison of natural frequencies-19 mass model, aspect ratio 3

Analysis method	FE			Modal superposition		
No. of bearings n_b	2	3	4	2	3	4
First natural frequency f_1 [Hz]	0.222	0.221	0.221	0.222		
Second natural frequency f_2 [Hz]	0.717	0.715	0.715	0.721		
Third natural frequency f_3 [Hz]	1.277	1.276	1.276	1.279		

Table 45: Comparison of natural frequencies-13 mass model, aspect ratio 4

Analysis method	FE			Modal superposition		
No. of bearings n_b	2	3	4	2	3	4
First natural frequency f_1 [Hz]	0.266	0.266	-	0.268		
Second natural frequency f_2 [Hz]	1.121	1.109	-	1.153		
Third natural frequency f_3 [Hz]	2.150	2.147	-	2.159		

Table 46: Comparison of natural frequencies-19 mass model, aspect ratio 6

Analysis method	FE			Modal superposition		
No. of bearings n_b	2	3	4	2	3	4
First natural frequency f_1 [Hz]	0.220	0.219	-	0.222		
Second natural frequency f_2 [Hz]	0.705	0.701	-	0.721		
Third natural frequency f_3 [Hz]	1.271	1.268	-	1.279		

The first and the third natural frequencies computed by both analysis methods are almost identical with little deviation from each other. There is, however, slight difference in the second natural

frequencies, although it is still minimal and influence on the responses would be minor. This can be attributed to the fact that the response spectrum analysis includes no rocking stiffness contributed by the vertical springs explained in Section 7.1 with Fig. 112 and Eq. (7.2). From the same equation it can be understood that the aspect ratio of the building has more influence on the dynamic behaviour than the number of bearings and indeed the difference in the second natural frequencies between two methods is more accentuated for the higher aspect ratio (H_s/B_s=4 and 6). Still, the maximum deviation is approximately 4 % from each other and hence it can be considered that both analysis methods are verified for their performance in computing natural frequencies.
Next the maximum horizontal displacements u_1 and u_n and uplift z obtained by both analysis methods are summarised in the following tables.

Table 47: Comparison of maximum displacement and uplift-7 mass model, aspect ratio 1

Analysis method	No. of bearing n_b	Damping ratio [%]	Base shear coefficient	Max. u_1 [m]	Max. u_7 [m]	Max. uplift z [m]
FE	2	10	0.216	0.483	0.506	0.461×10^{-3}
		20	0.181	0.404	0.424	0.411×10^{-3}
	3	10	0.216	0.483	0.506	0.692×10^{-3}
		20	0.181	0.404	0.424	0.616×10^{-3}
	4	10	0.216	0.483	0.507	0.830×10^{-3}
		20	0.181	0.404	0.425	0.739×10^{-3}
Response spectrum	2	10	0.221	0.494	0.516	0.505×10^{-3}
		20	0.201	0.450	0.470	0.460×10^{-3}
	3	10				0.757×10^{-3}
		20				0.690×10^{-3}
	4	10				0.931×10^{-3}
		20				0.848×10^{-3}

Table 48: Comparison of maximum displacement and uplift-13 mass model, aspect ratio 2

Analysis method	No. of bearing n_b	Damping ratio [%]	Base shear coefficient	Max. u_1 [m]	Max. u_{13} [m]	Max. uplift z [m]
FE	2	10	0.198	0.603	0.769	0.858×10^{-3}
		20	0.149	0.452	0.581	0.722×10^{-3}
	3	10	0.198	0.603	0.771	1.290×10^{-3}
		20	0.149	0.452	0.582	1.085×10^{-3}
	4	10	0.198	0.603	0.772	1.550×10^{-3}
		20	0.149	0.452	0.583	1.304×10^{-3}
Response spectrum	2	10	0.186	0.567	0.713	0.894×10^{-3}
		20	0.153	0.466	0.587	0.737×10^{-3}
	3	10				1.342×10^{-3}
		20				1.105×10^{-3}
	4	10				1.651×10^{-3}
		20				1.360×10^{-3}

Table 49: Comparison of maximum displacement and uplift-19 mass model, aspect ratio 3

Analysis method	No. of bearing n_b	Damping ratio [%]	Base shear coefficient	Max. u_1 [m]	Max. u_{19} [m]	Max. uplift z [m]
FE	2	10	0.163	0.649	0.947	1.173×10^{-3}
		20	0.124	0.491	0.755	1.097×10^{-3}
	3	10	0.163	0.648	0.950	1.766×10^{-3}
		20	0.123	0.490	0.759	1.649×10^{-3}
	4	10	0.163	0.648	0.953	2.124×10^{-3}
		20	0.123	0.490	0.761	1.981×10^{-3}
Response spectrum	2	10	0.140	0.556	0.858	1.088×10^{-3}
		20	0.107	0.427	0.661	0.858×10^{-3}
	3	10				1.632×10^{-3}
		20				1.286×10^{-3}
	4	10				2.008×10^{-3}
		20				1.583×10^{-3}

Table 50: Comparison of maximum displacement and uplift-13 mass model, aspect ratio 4

Analysis method	No. of bearing n_b	Damping ratio [%]	Base shear coefficient	Max. u_1 [m]	Max. u_{13} [m]	Max. uplift z [m]
FE	2	10	0.198	0.603	0.782	1.669×10^{-3}
		20	0.148	0.451	0.590	1.451×10^{-3}
	3	10	0.198	0.603	0.790	2.592×10^{-3}
		20	0.147	0.450	0.595	2.182×10^{-3}
Response spectrum	2	10	0.186	0.567	0.713	1.789×10^{-3}
		20	0.153	0.466	0.587	1.474×10^{-3}
	3	10				2.683×10^{-3}
		20				2.211×10^{-3}

Table 51: Comparison of maximum displacement and uplift-19 mass model, aspect ratio 6

Analysis method	No. of bearing n_b	Damping ratio [%]	Base shear coefficient	Max. u_1 [m]	Max. u_{19} [m]	Max. uplift z [m]
FE	2	10	0.162	0.642	0.980	2.400×10^{-3}
		20	0.123	0.488	0.786	2.053×10^{-3}
	3	10	0.160	0.637	0.995	3.621×10^{-3}
		20	0.123	0.488	0.799	2.310×10^{-3}
Response spectrum	2	10	0.140	0.556	0.858	2.176×10^{-3}
		20	0.107	0.427	0.661	1.715×10^{-3}
	3	10				3.263×10^{-3}
		20				2.573×10^{-3}

Considering the required size of the rubber bearings and clearance around the buildings, all models with 10 % damping are not practical. Design standards such as [10] specified the limit in the shear strain and the compression stress of the isolator rubber bearing concerning the safety against buckling. Tada explains [85] those limitation in details and suggested that the maximum shear displacement of the base-isolation building should be below the radius of the smallest bearings to secure the safety against buckling as a rule of thumb. Also the performance of the seismic isolation

of the taller models with 13 and 19 masses is not ideal judging from relatively large shear deformation within the superstructures.
Except the tallest model with 19 masses, the response spectrum analysis delivers fair results in spite of rather simplified analysis assumptions. The horizontal response obtained by the response spectrum analysis for the 19-mass model is really poor with more than 10 cm difference in displacement in comparison with FE results. For the calculation of the uplift, however, difference is largely insignificant. Those values marked with yellow and green are ones that exceed the original deformation of the bearings amounting to 2 mm due to the dead load of superstructure. In other words those bearings carry tensile force, which means that the tensile force is carried by the spring. The simple response spectrum analysis failed to predict only one case of the critical uplifting by 0.3 mm. If the criterion (7.1) is applied for those yellow-marked FE cases, the following limit aspect ratios are obtained.

Table 52: Comparison of maximum displacement and uplift-19 mass model, aspect ratio 6

Model	Aspect ratio H_s/B_s	Damping ratio [%]	Base shear coefficient	Limit aspect ratio by criterion (7.1)	Verification
19-mass, B_s=20 m, n_b=4	3	10	0.163	6.1	fulfilled !
13-mass, B_s=10 m, n_b=3	4	10	0.198	3.4	violated
13-mass, B_s=10 m, n_b=3	4	20	0.147	4.5	fulfilled !
19-mass, B_s=10 m, n_b=2	6	10	0.162	6.2	fulfilled !
19-mass, B_s=10 m, n_b=2	6	20	0.123	8.1	fulfilled !
19-mass, B_s=10 m, n_b=3	6	10	0.160	4.2	violated
19-mass, B_s=10 m, n_b=3	6	20	0.123	5.4	violated

In the same table under "verification", the models with aspect ratios lower than the limit value calculated by the criterion (7.1) are indicated with the exclamation mark. Admittedly the simulation models prepared here may not be quite realistic. Nevertheless this result shows that the criterion (7.1) is only a rough estimation and if the middle to tall base-isolation building ought to be planned, the verification of uplifting should be performed by more accurate analytical methods. The simplified response spectrum analysis with the mode superposition analysis can provide fine estimation, even if not always as accurate as the time-history analysis. It should be also mentioned that for the all analyses in this Section, the ideal viscous damping is assumed which does not add its own stiffness to the structure. Other damping devices such as sliding friction dampers or metallic hysteresis dampers add their own stiffness to the structural one, which in general increases the chance of uplifting because the base shear coefficient is increased. For analysis of the structure with such dampers, the linear response spectrum method would not be adequate, even though its behaviour may be realized approximately by introducing the stiffness of the dampers to the stiffness of the bearing.

7.2.4 Influence of the vertical seismic force

In addition to the horizontal seismic forces, the vertical seismic component is always present, even though its influence is often regarded as negligible. As mentioned already, however the vertical seismic component can actually be significant near the active fault. The Christchurch earthquake of 2011 was caused by the slip of active faults and it occurred at the very shallow depth. Therefore the recorded vertical acceleration was far greater than the horizontal ones, see Fig. 117. The peak acceleration value of the vertical component was nearly 2g, two times of the gravitational

acceleration, which means that only this seismic component itself suffices to lift the building. Also note that the resonance natural period is very low and at the same time its range does not spread as wide as the horizontal component. EN 1998-1 defines, for instance, the natural period range of resonance from 0.05 to 0.15 s, which correspond to the natural frequency range from 6.7 to 20 Hz and the peak response of the Christchurch earthquake is also found within this range, approximately at 8.3 Hz. As discussed in Section 7.2.1, this frequency range overlaps the natural frequency of the vertical motion due to the bearing vertical stiffness. Therefore, it is suspected that this motion causes the high vertical acceleration measured on the seismically isolated building.

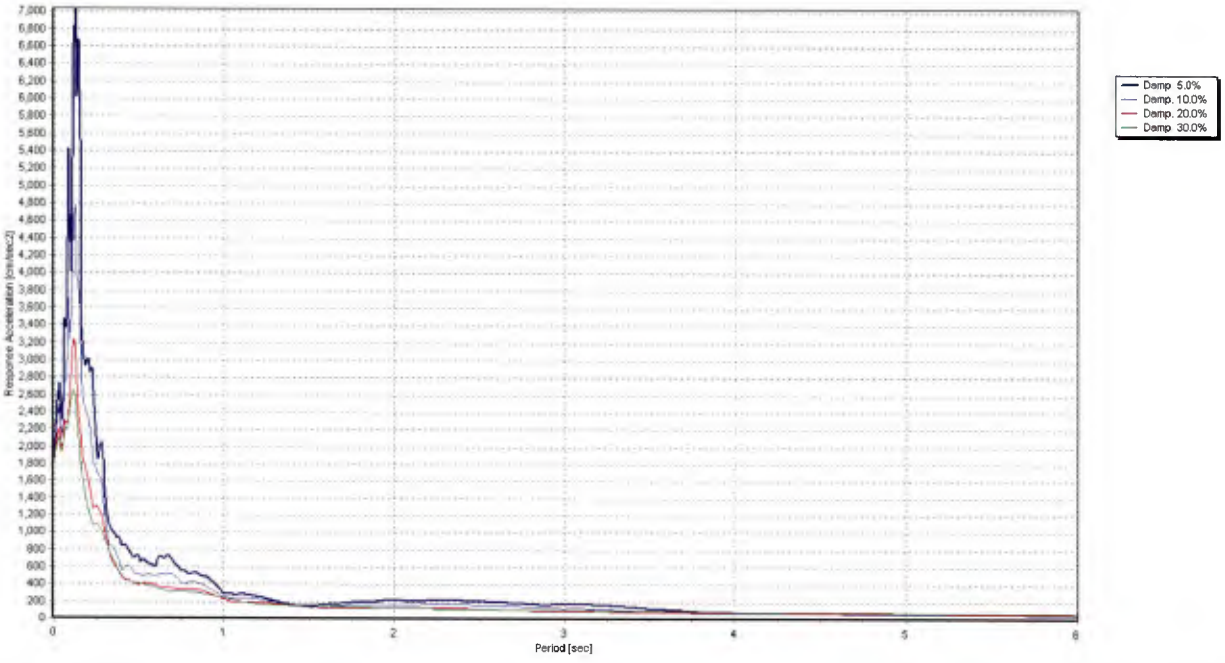

Figure 117: Linear acceleration spectrum of the UD component from 2011 Christchurch earthquake

The vertical seismic force can affect the amount of uplifting by another mechanism, namely P-Δ effect. This effect is already considered by the structure weight with the gravitational acceleration and the relative displacement between each floor and ground. Principally the same effect from the vertical ground acceleration should be taken into account. However the influence of this effect should be minimal since the rocking frequency (1st mode) of the superstructure lies generally out of this resonance frequency range. The lower and stiffer structures' possess a higher natural rocking frequency which increases the possibility of resonance somewhat but in such cases the effectiveness of the seismic isolation is high, which results in little structural deformation. Hence the P-Δ effect is again negligible.

FE analysis for the 13-mass-model of the aspect ratio 4 with three bearings is performed with the vertical seismic force in order to verify its influence on the uplifting of the bearings. 5 % and 20 % damping to their critical value are assumed in the vertical and horizontal displacement of bearings, respectively. The vertical seismic component of the same Christchurch earthquake is used, although its amplitude is reduced to 30 % of original value because in EN 1998-1 [13] it is recommended considering the 30 % of the vertical seismic effect when computed with the full horizontal seismic component in case of analysing the seismically isolated structure to which the peak vertical ground acceleration over 0.25g (2.5 m/s^2) is expected. Additionally the vertical stiffness of wall elements is varied while the vertical stiffness of bearings are kept constant so that a few variations of the natural frequencies due to the total vertical motion can be compared for its influence. They are summarized in Table 53 with each maximum uplift at the isolation layer and the maximum horizontal

displacement of the mass on top. The last variable is provided to see if the structural deformation is amplified by the P-Δ effect. Obviously the influence of this effect is negligible. The uplifting values are all increased by the vertical seismic forces and that increase is pronounced particularly for the model with lower vertical natural frequency as the frequency value approaches the peak resonance frequency of 8.3 Hz.

Table 53: Summary of the FE analysis with the vertical seismic force

Model	1	2	3
Vertical natural frequency of the superstructure [Hz]	33.72	40.56	50.85
Total vertical natural frequency [Hz]	9.321	9.886	10.350
Max. uplift [m]	3.695×10^{-3}	3.167×10^{-3}	3.148×10^{-3}
Max. horizontal displacement of the mass on top [m]	0.598	0.596	0.595

The time-vertical displacement curves of the left bearing are shown in Fig. 118. At approximately 3 seconds, this bearing carries tensile force for the first time. This tension force is not caused by the rocking motion but almost entirely by the vertical motion corresponding to Fig. 115 (b) alone because the middle bearing that should be subject to little rocking-induced tension appears to carry tensile force as well. Here only the structural stiffness is varied for comparison purpose but it is obvious that increasing the vertical stiffness of the bearing, hence enhancing the natural frequency of the vertical motion, can reduce the vertical displacement response more radically.

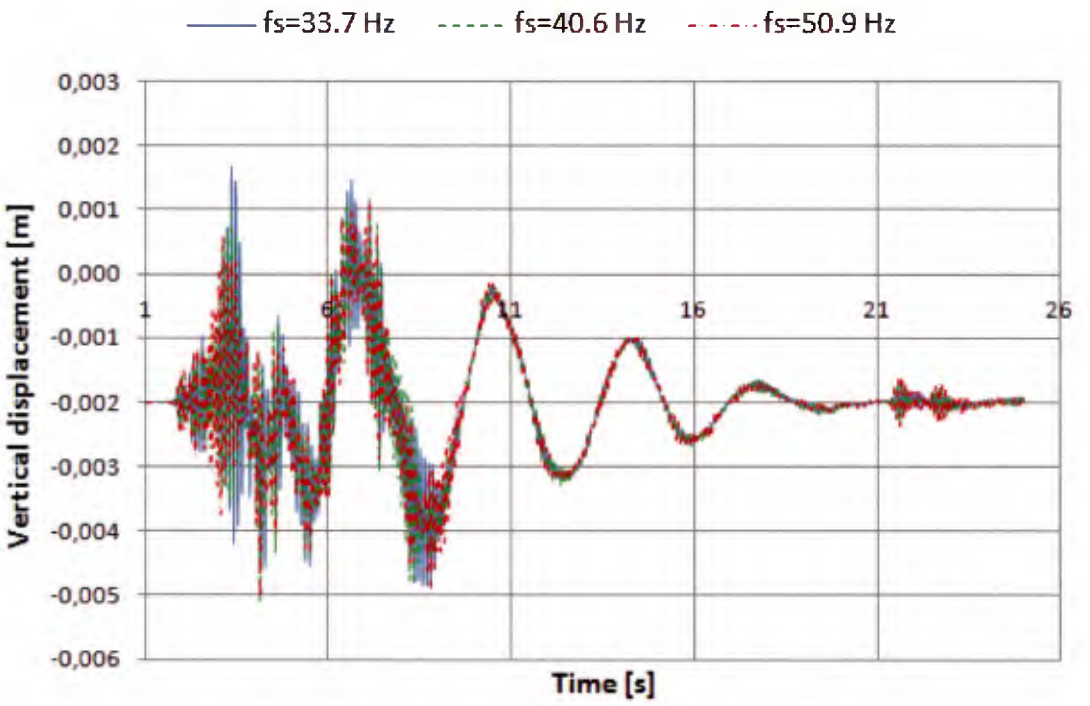

Figure 118: Comparison of vertical motions of the left bearing

Figure 119 shows two time-vertical acceleration plots of the model 1 from 1 to 10 s at the bottom and top mass. Overall the acceleration is increased at the top mass in comparison to the bottom floor, which is the same tendency observed in existing base-isolation structures, see Section 2.3. The peak

acceleration does not appear, however, at the top floor but at the bottom floor at approximately 6.2 s, although the vertical displacement is lower at this moment than the first peak value in spite of additional contribution of the rocking motion. By filtering this plot it becomes clear that the peak values of the bottom mass are related to the higher frequency mode, namely the solely structural vertical mode corresponding to Fig. 115 (c).

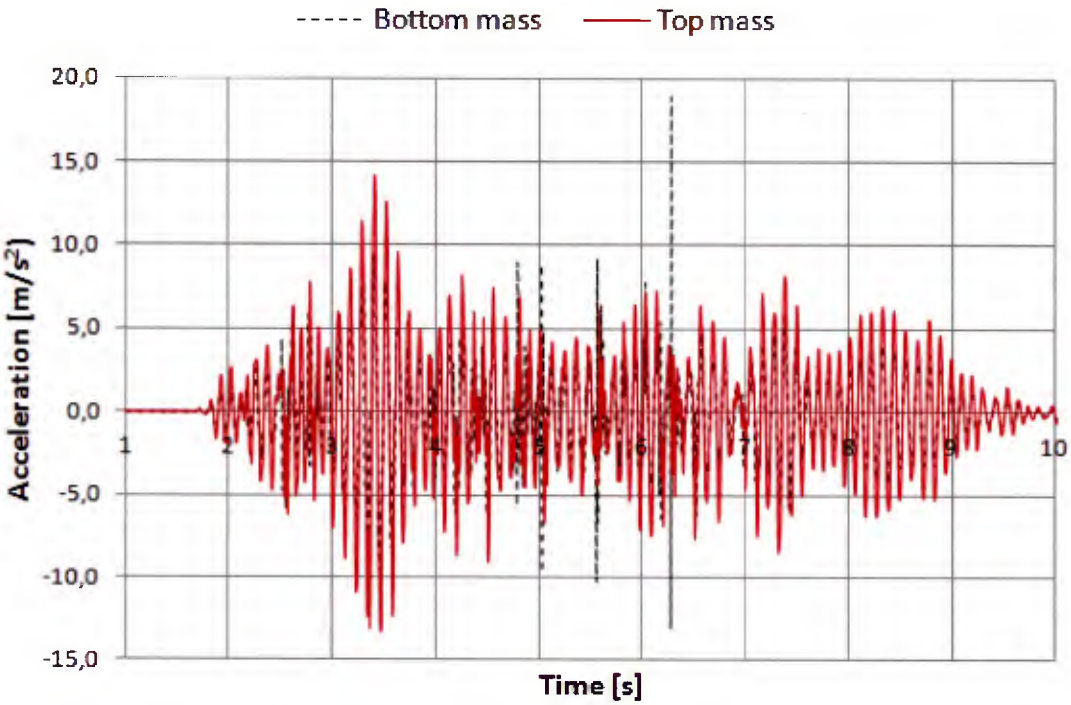

Figure 119: Time-acceleration plot of the model 1 at the bottom and top mass

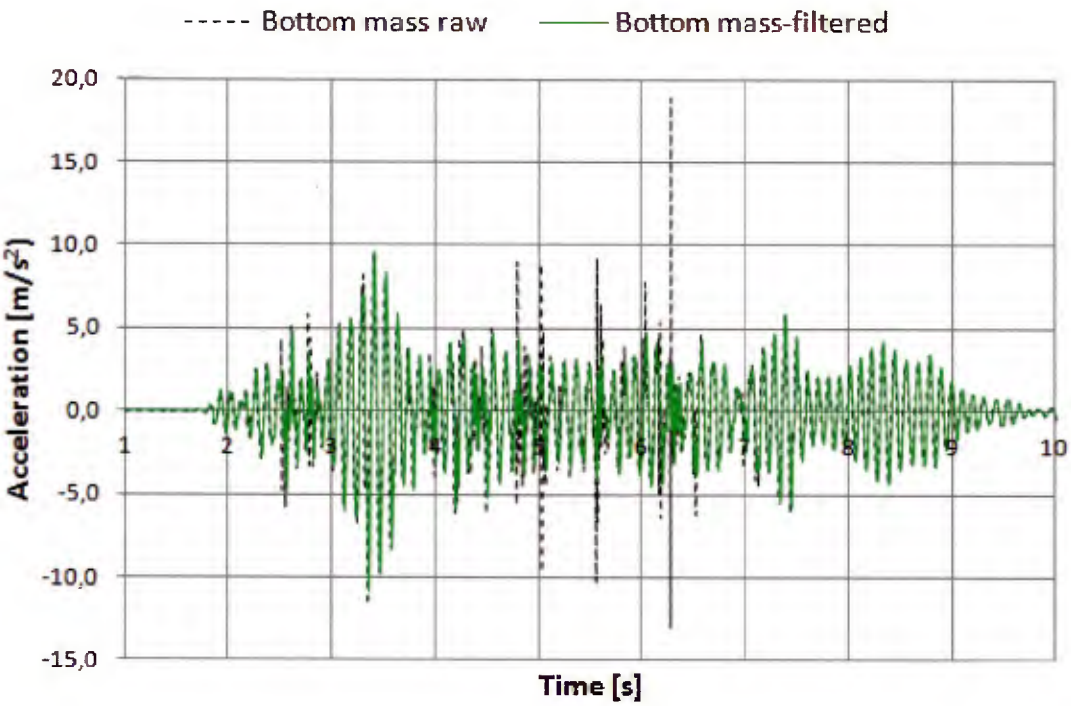

Figure 120: Raw and filtered time-acceleration plots of the model 1 at the bottom mass

Figure 120 shows the comparison of the raw and filtered time-acceleration plot. The Bessel low-pass filter function with the cut-off frequency of 30 Hz is adopted. All high peaks are successfully filtered out. Frequency as high as 30 Hz would not appear in displacement response and therefore its influence on the uplifting behaviour is negligible. At the actual measurement on the base-isolation building, this high-frequency-based acceleration would also appear on the higher floor. In this FE analysis the Rayleigh damping inevitably applies very high damping to the higher frequency modes and therefore this component is mostly eliminated in response.
Conclusions should not be drawn only by this analysis but assuming that the seismically isolated building is well-designed and that the structural deformation should be limited minimum, only the vertical deformation mode (a) and (b) in Fig. 115 should be taken into consideration. Then the uplifting can be possibly predicted again by the simple response spectrum analysis.

7.3 Consideration Of The Limitation In Tension And The Ultimate Dynamic Behaviour

In the final section of this Chapter, the theme 'reasonable tension limit' for the seismic isolator rubber bearing is briefly discussed taking all findings from Chapters 5 to 7 into consideration and also referring to the research of others. The limit tensile stress 2G for the seismic isolator rubber bearing seems to be widely accepted and provided that the first shape factor is sufficiently high, both experimental and numerical results support the suggested value because as a number of studies indicated, this value do correspond to the onset point of the cavitation phenomenon. Yet, as observed in test and numerical results, the tensile stiffness of rubber bearings reduces increasingly along with the strain only after rubber is fully cavitated. In other words, the rubber bearing still possesses an adequately high tensile stiffness up to the point that is named as the second softening phase in Chapter 6 for convenience. As the parametric study shows in Fig. 107, the onset of both first and second softening phases are delayed as the first shape factor increases and the tensile stress value at the onset of the second softening phase reaches almost as high as 3G for the tested bearing with its first shape factor higher than 20, which is common for the seismic isolator rubber bearing. Furthermore some research from Japan such as [120] [121] and the test results from Chapter 5 indicate that the shear and the compression stiffness of the bearing hardly deteriorate after cavities develop within rubber. All these facts point to the conclusion that the rubber bearing can be loaded up to the second softening phase without risking the stability of the whole structure during earthquake.
If the active fault lies in vicinity, the building planner needs to be well-aware of the danger of the vertical resonance due to the rubber bearings since in such a case the vertical acceleration can reach high enough that the superstructure is lifted only by the vertical seismic force. Provided that the geological characteristics and hence the response spectra in that region are known, it should be possible to adjust the vertical stiffness both of the structure itself and the bearing during the construction planning so that the worst scenario is avoided. Merely small adjustment of the stiffness may be adequately effective since the resonance frequency range is often rather narrow for the vertical seismic component.
In order to comprehend the influence of the damaged bearing on the dynamic structural behaviour, an attempt is made with the same numerical model used in Section 7.2.4. Here however, the vertical stiffness of the springs is defined with bilinear curve whose second inclination starts at the tensile stress of 1.2 MPa which corresponds to the value of 3G when the soft rubber material (G=0.4 MPa) is used. For the high-rise building, softer rubber material is commonly used because otherwise the long natural period of the seismic isolation cannot be achieved without increasing the bearing height which put the bearing in higher risk of the buckling. The time-vertical displacement curve on one of the end springs is shown in Fig. 121. For comparison the result of the original model with the linear

vertical springs is also presented in the same figure. Due to the softening, the peak vertical displacement of this bearing in tension is multiplied by the factor almost of six.

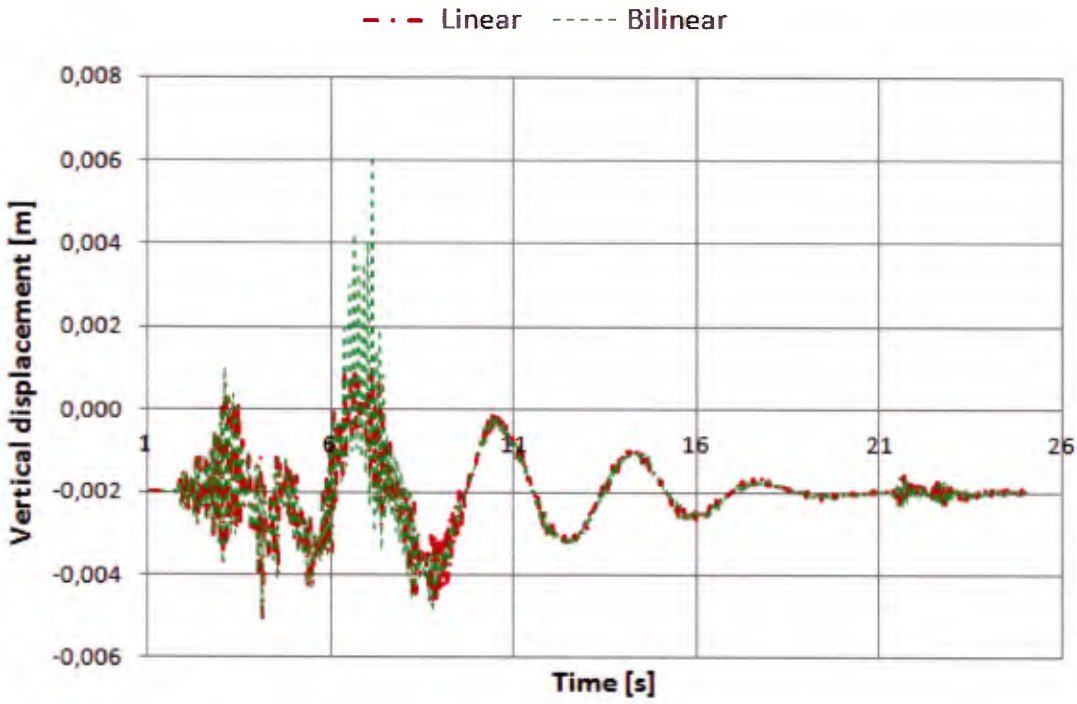

Figure 121: Time-vertical displacement curves of the model with linear and bilinear vertical springs

This result needs correction because no hardening in the compression stress range is taken into consideration in all simulations presented here. As another attempt, the stiffness of the vertical spring is defined as trilinear where the second stiffness in tension remains the same as the first model. Additionally the second stiffness in the compression whose onset is at approximately 15 MPa (equivalent to 3 mm vertical compression displacement). The comparison of time-vertical displacement curves of the models with bilinear and trilinear vertical springs are shown in Fig. 122. The compression stiffness of the vertical springs is multiplied by the factor of 1.5 beyond 15 MPa compression. This factor and the onset compression stress are selected randomly as it is not possible to generalize the properties of the isolator rubber bearings and the purpose of this analysis is merely to see how the compression hardening affects the overall dynamic behaviour. Logically the moment equilibrium at the isolation layer level has to be held by those three vertical springs and when the linear springs are considered the rotation centre coincides with the middle bearing. The rotation centre is shifted toward an end spring that carries the tensile force when the bilinear spring model is considered and in this case the middle spring contributes to the moment equilibrium by carrying compression force. From Fig. 121 it is observed that the maximal compression displacement remains unchanged regardless which spring type is adopted. This means that the contribution from the middle bearing fully compensates the loss of moment due to the low tensile stiffness. The softening is previously induced by only the rocking motion and after softening the displacement amplitude caused by the vertical seismic force is enlarged enormously. It is important that the structure does not lose its stability unless the tension-loaded bearing fails. Reference as well as test results shown in Chapters 4 to 5 provide us an optimistic impression that rubber bearings do carry tension without breaking up to relatively a high strain range. Then the cause of instability is not necessarily the tension failure but the compression buckling of the bearing on the other side due to doubly high loading on the less effective surface area reduced by large shear deformation.

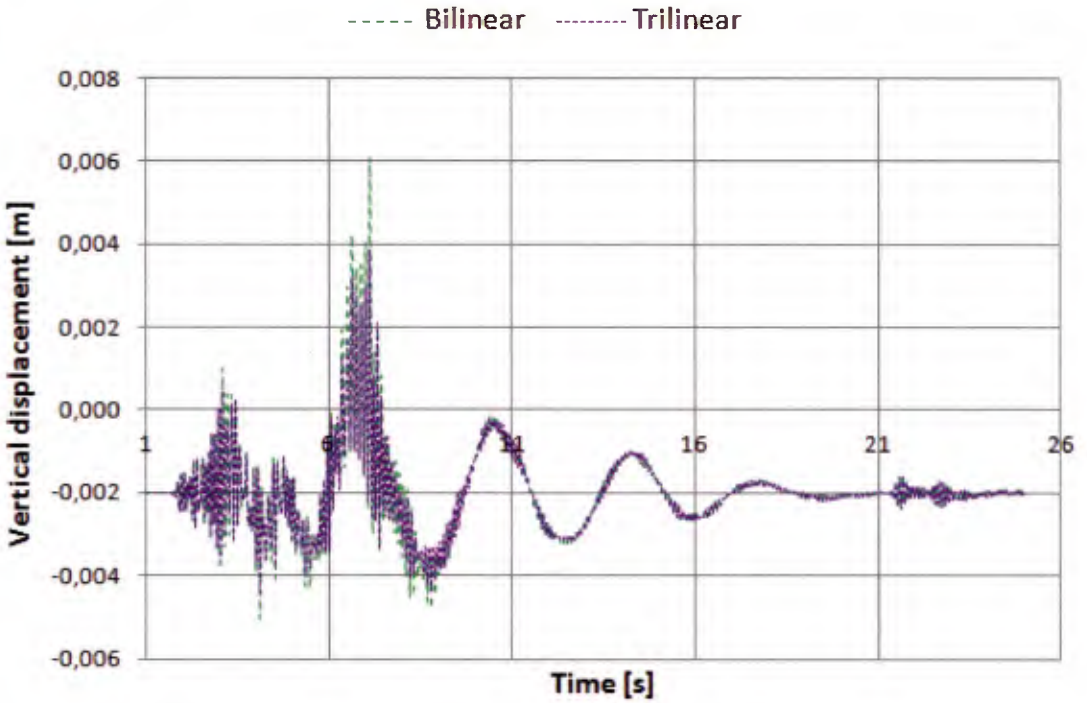

Figure 122: Time-vertical displacement curves of the model with bilinear and trilinear vertical springs

In case of the model with trilinear springs, the rotation centre is again shifted but this time in the other direction so that the contribution of the middle bearing is reduced and the softening in tension is compromised by the hardening in compression. Fig. 122 shows that the maximum compression displacement is reduced somewhat. The decrease in the maximum tension displacement is actually quite remarkable here. The change in the vertical stiffness in a higher stress range should have no influence on the purely vertical motion caused by the vertical seismic force and thus only the rocking motion is affected. This effect can be seen more clearly in the force-deformation curves of the vertical spring shown in Fig. 123. This raises the question if this hardening effect can be expected at all. The worst scenario in this example occurs when the both peaks of the rocking motion and the vertical motion superpose. At this moment the bearing also undergoes maximum shear strain, which means that the effective supporting area of the bearing is highly reduced. According to the evaluation formulae of international design standards, the vertical stiffness is proportional to the supporting area as explained in Chapter 3 and therefore it should be even softer rather than harder at the peak amplitude on the first sight and indeed the further sinking displacement is observed during test as the horizontal displacement approaches its peak. However as the compression test with shear deformation shown in [85], it is observed that the lower stiffness due to the reduction of the supporting area was observed with a small stress range and in a quite high stress range, the stiffness seems to converge to a certain value independent of the presence of shear deformation. In other words, the force-displacement curve is more nonlinear when shear deformation is accompanied. Explanation of this phenomenon can also be found from the FE analysis shown in [85]. Pressure starts concentrating along the compression strut as shear deformation increases. This region of high pressure concentration may be small but rubber there resists significantly harder than the other region due to its material nonlinearity. This compensates more or less for the influence of reduction in the supporting area. In this sense the depiction of trilinear force-displacement curve seems more appropriate for the dynamic analysis of the seismically isolated buildings. If this was always the case, comprehending the hardening behaviour of the rubber bearing under compression is also an interesting topic in the view point of its

contribution to a reduction in undesired tension of bearings within a seismically isolated structural system. These benefits of hardening are not of much use in the example considered here because the vertical seismic force alone is enough to lift the whole structure and a large part of the tensile deformation is contributed by that simple up and down motion. For such cases, carefully tuning the stiffness of the vertical springs would be an effective remedy in order to reduce the vertical displacement response since it ensures that the natural frequency of the vertical motion is shifted further away from the peak resonance frequency the earthquake. The three-dimensional seismic isolation is hence possible to achieve but not for every case since the softer vertical springs may induce the resonance of some of rocking modes. For this reason, the three-dimensional seismic isolation often seems to be separately realized in the horizontal and the vertical directions.

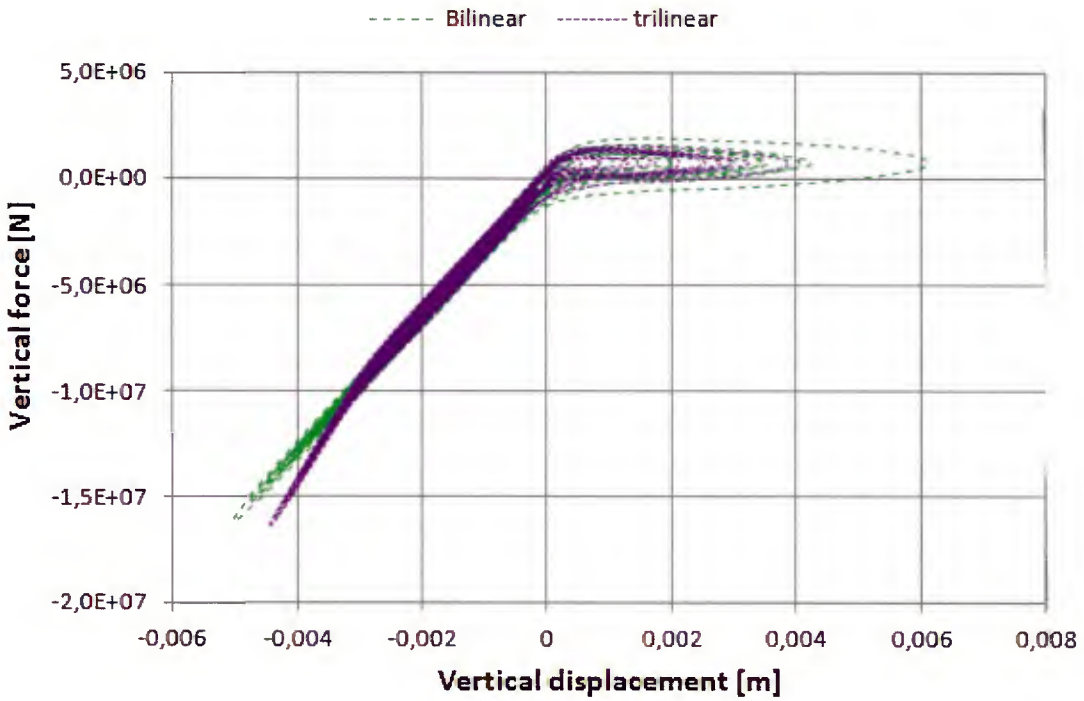

Figure 123: Comparison of the force-displacement curves of the different vertical springs

As already described repeatedly, more accurate representation of rubber bearings, for instances suggested by Koh et al. [5] or the modified model by Takaoka [8], is necessary for the analysis of the ultimate dynamic state of the seismically isolated buildings. In particular, the latter performed the whole series of numerical analysis with his detailed macro model and comparing with the shaking table test results, it was proven that his models could predict the dynamic structural behaviour at its ultimate state quite well. According to Takaoka's research, there is no significant difference in results between his model and the conventional model with the horizontal and vertical springs for predicting the instability due to the tension induced softening in bearings. Then by defining the skeleton curves of the vertical spring analogous to the horizontal one as well as its stiffness dependence on the horizontal displacement, the ultimate dynamic structural behaviour can be predicted even more precisely. Such a macro model is not commercially available FE software and therefore programming own Finite Element code is required in order to realize it. The aim in this Chapter is, however, roughly to comprehend the influence of the nonlinearity of the rubber bearings on the global structural system and hence this chapter will conclude without going into details of the modified macro model.

8 SUMMARY

Among the increasing applications of the seismic isolation, high-rise buildings are not currently an exception. Due to their aspect ratio, overturning moment has been an obstacle for the realization of the seismically isolated high-rise building, since the conventional seismic isolator bearings are not able to bear tensile force. The rubber isolator bearings that have been most commonly employed for seismic isolation are known to be capable of carrying a little tensile force but their tension capacity has not been utilized in practice because of the cavitation phenomenon which occurs when the rubber bearing is subjected to a certain degree of tension. The development of cavities is linked to the immediate softening of the bearing and this phenomenon has been known quite a while but research associated with rubber bearing is rarely found. In this dissertation, therefore, the rubber isolator bearings are investigated for their capacity against tensile force and the mechanism of cavitation phenomenon as well as the consequence of cavitation was sought for theoretically, analytically and experimentally.

As for the mechanism of cavitation, a number of researchers in the material science field have worked on it already and generally it is agreed that cavities are developed if the rubber contains microscopic voids of certain size such as air holes and is subjected to the hydrostatic pressure of 5G/2, where G is the shear modulus of the rubber material. The former condition can largely be taken for granted for rubber bearings. The latter condition as well has been experimentally proven for instance by [98]. However as pointed out by Hou and Abeyarante [114], the required pressure for cavitation would be higher if the balance in purely hydrostatic pressure condition is not held. Comparing with the results of uniaxial tension cases, slight differences in the cavity-induced softening behaviour of the bearing are frequently observed in the majority of the offset tension tests, i.e. a shift of the cavitation onset or the degree of softening. A part of reason for this change is the internal rotation of the bearing as explained by Kelly [106] but it can be explained mainly by the theory of Hou. He derived a new cavitation criterion, so-called cavitation instability surface, by applying the principle of the virtual work to the solid spherical body with a spherical void in it. Referring to other research and observing the result of the experiment carried out for this dissertation, such a fine cavitation criterion may not be needed since the differences in the softening behaviour are often minor. However, an implementation in FE analysis is necessary since the FE analysis of the rubber subjected to tension and shear will over- or underestimate the cavity-induced pressure if a single constant pressure value is set as the damage criterion. Once cavitation is triggered, the degree of softening is controlled by reducing the bulk modulus, which is the method introduced in [97], due to its simplicity. It can be so interpreted that rubber becomes highly compressible or "expandable" porous media. Based on the observation of FE and test results, the second softening phase is suggested and introduced to the implemented cavitation damage model additionally. Right after the onset of cavitation until fully cavitated state, the degree of softening is relatively mild but when enough cavities spread over the rubber body, they may expand its size elastically instead of developing further cavities. In this second phase, the degree of softening is high and the stiffness may reduce nearly to zero, although in many cases it can be stretched further without break. If a uniaxial tension test is conducted for a single small rubber disc glued between two steel plates as in laminate rubber bearings, necessary parameters for this two phase softening model such as the second critical volume change ratio or the degrees of two softening can be obtained. Then with those parameters, it should be possible to simulate the tensile load-carrying behaviour of a much larger rubber body as well. In Chapter 6 those parameters of the implemented cavitation model were obtained by adjusting the FE results to the uniaxial tension tests of the isolator rubber bearings. With the same parameters, the force-deformation relationship obtained by the offset tension tests was successfully predicted. This damage model can be integrated to the most of the hyperelastic material models, although strictly speaking only Neo-Hookean and Arruda-

Boyce models are appropriate because the cavitation instability surface is derived from the Neo-Hookean body and the Arruda-Boyce model is the expansion of the Neo-Hookean model. Judging from the simulation results obtained in Chapter 6, it is recommended integrating the cavitation criterion with these two material models. A reasonable representation of three axial stress condition plays a key role in this damage criterion and as explained in [144], Mooney-Rivlin model would generate a poor combination of principal stresses if only the simple tension or shear test for the is used for curve-fitting to obtain material parameters as in the case of the present research. Involving the higher terms of Mooney-Rivlin formulation would also cause the instability. In fact, all those material models provided almost identical simulation results of the simple tension test of a rubber pad, and the Mooney-Rivlin material failed to predict the behaviour of the rubber bearing under shear and tensile force. Arruda-Boyce material is recommended due to its simplicity and stability. It requires less material parameters than the other well-known hyperelastic material models and yet quite reasonable simulation results were obtained for all deformation modes corresponding to the bearing tests in Chapter 5 if curve-fitting were performed properly. It is recommended doing curve-fitting in the very low strain range first in order to obtain the accurate initial shear modulus that is the crucial parameter for both Arruda-Boyce formulation and the implemented cavitation criterion.
In Chapter 7 an attempt was made to comprehend the response of the bearings in the global structural system by means of the FE dynamic analysis and the linear response spectrum analysis with the mode superposition. A simple criterion (7.1) has been used as a rule of thumb to ensure that bearings carry no tension. However by comparing the results of two different analysis methods mentioned above it is found out that it underestimates the limit aspect ratio when the examined structure is tall and slim due to the increasing response contribution from the other deformation modes. Both analysis methods were presented for the verification to each other and they served their purposes. Especially it is noteworthy that the latter method is simple to implement and the computation is inexpensive. Nevertheless nearly equivalent approximation to the FE dynamic analysis is obtained by that. Therefore this useful analysis method can be recommended to compute the amount of uplift or the overturning moment.
FE dynamic analysis was then further performed with one of the same global model but this time with the vertical seismic motion. It was often observed in the seismic response records of the seismically isolated structures that the vertical acceleration response increased toward the top of the building. The purpose of the FE analysis here is, first of all, to investigate the cause of this problem and then also to see if the vertical seismic force affects the rocking motion. For the first concern, the FE result exhibits the same tendency except that the peak acceleration value appeared at the ground mass rather than at the top mass. This phenomenon occurred because the vertical seismic force is applied not through the bearings but directly on the ground floor due to the technical difficulty. In reality the response of the higher deformation mode would nearly vanish if the difference in natural frequencies between the first and other modes is wide. That is also the case for the vertical motion of the seismically isolated structures since the vertical stiffness of the rubber bearings, although it is still sufficiently high to support the superstructure, is lower than the structural vertical stiffness. In other words the rubber bearings also take over the first vertical natural mode. Therefore the appearance of the peak acceleration at the ground mass is a consequence of the erroneous application point of loading only in the FE analysis but such high frequency hardly affects the building and is of no interest. In fact the measured responses with higher frequencies are often filtered out. By filtering the FE result and applying FFT, it becomes clear that the increase in the vertical acceleration response towards the top mass is a result of the resonance near the natural frequency obtained by the total stiffness of both rubber bearings and the structure. Ironically the isolator rubber bearings may bring the structure into resonance in the vertical motion, although it is still high-frequency response and it should not cause damage in structure for a short time loading. In that example the influence of the vertical seismic force on the rocking motion was not observed. It

is assumed that the frequency of the rocking motion is in general much lower than the dominant frequency of the vertical seismic motion and therefore the risk of the resonance is negligibly low. Then only the pure up-and-down motion would be the contribution of the vertical seismic force. If that is the case, again the linear response spectrum analysis would be adequate for the estimation of uplifting.

Finally, nonlinearity was introduced in the vertical springs and the same analysis was repeated in order to comprehend the impact of not only tension softening but also compression hardening of the rubber bearing. This was admittedly not a qualitative vertical stiffness of the rubber bearing, yet there were some important findings: 1) the structure did not lose its stability, although radical softening was induced and thereafter tension force was repeatedly carried by the bearing. 2) the tensile amplitude was radically reduced if the hardening in compression was considered. A number of the experiment results show that the rubber bearings do not fail until relatively high tensile strain after the cavity-induced softening occurs. The bearings may even show some hardening before its failure due to reaching the extensibility of its molecular chains and also to the crystallization. These facts indicate that seismically isolated buildings may survive even if tension over the design limit value, under which cavitation should not occur, had to be carried by the rubber bearings during earthquake. As for the second point, it is beneficial to consider the hardening property of the rubber bearings since it definitely reduces the deformation induced by the overturning moment. In reality, however, it is difficult to estimate how much of hardening can be expected because no qualitative evaluation formula regarding the compression modulus including hardening is available. In [85] some results of the offset compression tests of the isolator rubber bearings are shown and they indicate indeed that the compression stiffness is lower in the low strain range when shear deformation is present since the effective supporting area is reduced but it exhibits higher degree of hardening so that the compression stiffness seems to converge eventually to a certain value no matter whether the shear deformation is present or not. If the rubber bearings with the high first shape factor are used, hardening may not be expected much because then the compression modulus is highly dominated by the material constant E_b, namely the bulk modulus. Nevertheless, the stiffness is generally higher in such cases and it in turn may reduce the rocking response. Or even more simply the benefit of the higher stiffness on the compression side can be realized by additional compression springs along the edge of the structure, which are activated only by the excessive rocking motion. These compression springs could be again some elastomeric bearings with the low-friction sliding top surface, for instance. These elements can replace the often elaborate tension anchoring construction and reduce the rocking motion of the structure effectively.

9 REFERENCE

[1] Kelly, T.E. (2001). Base Isolation of Structures-Design Guidelines, Holmes Consulting Group Ltd, New Zealand.

[2] Naeim, F. and Kelly, M.J. (1999). Design of Seismic Isolation Structures, John Wiley & Sons, Inc., New York, USA

[3] Higashino, M. and Okamoto, S. (2006). Response Control and Seismic Isolation of Buildings, Taylor & Francis, Oxon, UK

[4] Mano, T. (2010). Numerical and experimental analysis of the load-carrying behaviour of laminated elastomeric bearings as seismic isolators, Festschrift zum 60. Geburtstag von Univ.-Prof. Dr.-Ing. Ingbert Mangerig, pp. 191-198.

[5] Koh, G.C. and Kelly, M.J. (1988). A simple mechanical model for elastomeric bearings used in base isolation, Journal of Mechanical Science, Vol. 30, No. 12, pp. 933-943.

[6] Hino, J., Yoshitomi, S., Tsuji, M. and Takewaki, I.(2008). Bound of aspect ratio of base-isolated buildings considering nonlinear tensile behaviour of rubber bearing, Structural Engineering and Mechanics, 30 (3).

[7] Takaoka, E. and Takenaka, Y. (2009). Ultimate behaviour analyses of base-isolated buildings considering buckling and tensile characteristics of laminated rubber bearings (in Japanese), Annual technical report of Kashima Corporation, Vol. 57

[8] Takaoka, E. (2009). Study of the ultimate behaviour of base-isolated buildings considering the failure of laminated rubber bearings (in Japanese), PhD Thesis, Kyoto University, Japan.

[9] European Committee for Standardization (CEN), Structural bearings - Part3: Elastomeric bearings, EN 1337-3:2005

[10] European Committee for Standardization (CEN), Anti-Seismic Devices, EN 15129:2009

[11] AASHTO LRFD Bridge Design Specifications, 2007

[12] Japan Road Association, Japanese specifications for highway bridges bearings, April, 2004

[13] European Committee for Standardization (CEN), Eurocode 8: Design of structures for earthquake resistance – Part 1: General rules, seismic actions and rules for buildings, EN 1998-1:2006, April, 2006

[14] Japan Road Association, Japanese specifications for highway bridges-Part 5: Earthquake resistance design, March, 2004

[15] MCEER, Recommended LRFD Guidelines for the Seismic Design of Highway Bridges - Part I Specifications, November, 2001

[16] Chopra, A.K. (2000). Dynamics of Structures. 2nd Edition, Prentice Hall, USA.f

[17] Skinner, R.I., Robinson, W.H. and McVerry, G.H. (1993). An Introduction to Seismic Isolation, John Wiley & Sons Ltd, UK.

[18] Homepage of Maurer + Söhne Germany, http://www.maurer-soehne.de

[19] Mangerig, I., Mano, T. and Nothaft, R. (2011). Measurement report on Maurer Sliding Material (MSM) test. Test report for the company Maurer+Söhne GmbH, Munich, Germany.

[20] Zayas V.A., Low S.S. and Mahin S.A. (1987). The FPS Earthquake Resisting System: Experimental Report, UCB/EERC-87/01, Earthquake Engineering Research Centre, University of California, Berkley, the USA.

[21] Symans, M.D., Charney, F.A., Whittaker, A. S., Constantinou, M.C., Kircher, C.A., Johnson, M.W. and McNamara R.J. (2008). Energy Dissipation Systems for Seismic Applications: Current Practice and Recent Developments, Journal of Structural Engineering, Volume 134, No. 1, pp. 3-21.

[22] Kelly, T.E. (2001). In-Structure Damping and Energy Dissipation-Design Guidelines, Holmes Consulting Group Ltd, New Zealand.
[23] EN 1998-2:2005, Eurocode 8: Design of structures for earthquake resistance – Part 2: Bridges, June, 2006
[24] Douglass, P.T. and Duflot, P. (2000). Fluid Viscous Dampers Used for Seismic Energy Dissipation in Structures, http://taylordevices.eu/pdfs/seismic%20applications.pdf, July 2011
[25] Douglass, P.T. and Constantinou, M.C. (2000). Fluid Dampers for Applications of Seismic Energy Dissipation and Seismic Isolation, http://taylordevices.com/Tech-Paper-archives/literature-pdf/42-FluidDampers.pdf, July 2010
[26] Symas, M.D. and Constantinou, M.C. (1998). Passive Fluid Viscous Damping Systems for Seismic Energy Dissipation, ISET Journal of Earthquake Technology, Vol. 35, pp. 185-206.
[27] Constantinou, M.C., Whittaker, A.S., Kalpakidis, Y., Fenz, D.M. and Warn G.P. (2007). Performance of Seismic Isolation Hardware under Service and Seismic Loading, Technical Report MCEER, The USA.
[28] Markis, N. (1998). Viscous Heating of Fluid Dampers. I: Small-Amplitude Motions, Journal of Engineering Mechanics, Vol. 124, No. 11, pp. 1210-1216.
[29] Markis, N., Roussos, Y., Whittaker, A.S. and Kelly J.M. (1998). Viscous Heating of Fluid Dampers. II: Large-Amplitude Motions, Journal of Engineering Mechanics, Vol. 124, No. 11, pp. 1217-1223, November.
[30] Shao, D., Pall, A. and Soli, B. (2006). Friction dampers for seismic upgrade of a 14-story patient tower with a 36-foot tall soft-story, Proceedings of the 8th US National Conference on Earthquake Engineering, San Francisco, The USA, No. 90.
[31] Suzuki, K., Watanabe, A. and, Saeki, E. (2005). Development of U-shaped Steel Damper for Seismic Isolation System, Nippon Steel Technical Report No.92, Japan.
[32] Aiken, I.D. (2006). Energy Dissipation Devices, 100th Anniversary Earthquake Conference Commemorating the 1906 San Francisco Earthquake, CA, The USA.
[33] Aiken, I.D., Nims, D.K., Whittaker, A.S. and Kelly, J.M. (1993). Testing of Passive Energy Dissipation Systems, Earthquake Spectra, Vol. 9, No. 3, Earthquake Engineering Research Institute California, USA.
[34] Black, C.J., Markis, N. and Aiken, I.D. (2004). Component Testing, Seismic Evaluation and Characterization of Buckling-Restrained Braces, Journal of Structural Engineering, Vol. 130, No. 6, pp. 880-894.
[35] Wen-Hsiung, L. and Chopra, A.K. (2002). Earthquake response of elastic SDF systems with non-linear fluid viscous dampers, Earthquake Engineering and Structural Dynamics, Vol. 31, pp. 1623-1642.
[36] Martelli, A. (2006). Modern seismic protection systems for civil and industrial structures, Structural Assessment Monitoring and Control (SAMCO) Final Report.
[37] Martelli, A. (2011). On the Need for Reliable Seismic Input Assessment for Optimized Design and Retrofit of Seismically Isolated Civil and Industrial Structures, Equipment, and Cultural Heritage, Pure and Applied Geophysics, Vol. 168, Issue 1-2, pp. 217-235.
[38] Robinson, W.H. (1982). Lead-Rubber Hysteretic Bearings Suitable for Protecting Structures during Earthquakes, Earthquake Engineering and Structural Dynamics, Vol. 10, pp. 593-604.
[39] Bailey, J. and Allen E. (1991). Seismic isolation retrofitting of the Salt Lake City and County Building, Nuclear Engineering and Design, Vol. 127, pp. 367-374.
[40] Zhou, F.L., Yang, Z., Liu, W.G. and Tan, P. (2004). New Seismic Isolation for Irregular Structure with the Largest Isolation Building Area in the World, 13th World Conference on Earthquake Engineering, No.2349, Vancouver, Canada.

[41] Smirnov, V., Eisenberg, J. and Vasil'eva, A. (2004). Seismic Isolation of Buildings and Monuments. Recent Development in Russia, 13th World Conference on Earthquake Engineering, No.966, Vancouver, Canada.
[42] Melkumyan, M.G. (2008). Seismic Experience Accumulated in Armenia, 14th World Conference on Earthquake Engineering, Beijing, China.
[43] Zekioglu, A., Darama, H. and Erkus, B. (2009). Performance-Based Seismic Design of a Large Seismically Isolated Structure: Istanbul Sabiha Göcken International Airport Terminal Building, SEAOC 2009 Convention Proceedings, California, USA, pp. 409-427.
[44] Seki, M., Vacareanu, R. and Chesca, A.B. (2008). Analtical Study on the Application of Seismic Isolation Technology to the Vulnerable Building in Romania, 14th World Conference on Earthquake Engineering, Beijing, China.
[45] Tohoku Chapter-Disaster Committee-Architectural Institute of Japan, (2005) "Measured seismic responses of buildings during the 2005 Miyagi earthquake in Japan (in Japanese)", http://www.disaster.archi.tohoku.ac.jp/Saigai/tohoku/20050816/tatemonokiroku.pdf, May 2010.
[46] Morita, K. and Takayama, M. (2008). Performance of seismic isolated buildings due to 2005 west off Fukuoka earthquake in Japan, Proceedings of the 14th World Conference on Earthquake Engineering, Beijing, China.
[47] Kashima, T., Itou, A. and Fujita, H. (2004). Dynamic behavior of a 9-story base-isoltated building during the 2003 off Tokachi earthquake, Japan, Proceedings Third UJNR Workshop on Soil-Structure Interaction, California, The USA.
[48] Kent, J.A. (2007). *Kent and Riegel's Handbook of Industrial Chemistry and Biotechnology.* 11th Edition, Vol. 1, Springer Science+Business Media, LLC., New York, The USA.
[49] Seymour, R.B. and Carraher, C.E. (1998). Polymer Chemistry. 2nd Edition, MARCEL DEKKER, INC., New York, USA, 1988
[50] Röthemeyer, F. and Sommer F. (2006). Kautschuk Technologie. 2nd Edition, Carl Hanser Verlag München Wien, Germany.
[51] Gent, A.N. (2001). Engineering with Rubber. 2nd Edition, Hanser Publisher, Munich.
[52] Payne, A.R. (1974). Hysteresis in rubber vulcanisates, Journal of Polymer Science, Symposium No. 48, pp. 169-196.
[53] Payne, A.R. (1962). The dynamic properties of carbon black-loaded natural rubber vulcanisates-Part I, Journal of Applied Polymer Science, Vol. VI, Issue No. 19, pp. 57-63.
[54] Payne, A.R. (1965). Effect of dispersion on the dynamic properties of filler-loaded rubbers, Journal of Applied Polymer Science, Vol. 9, pp. 2273-2284.
[55] Payne, A.R. and Whittaker, R.E. (1971). Low strain dynamic properties of filled rubbers, Rubber Chemistry and Technology, Vol. 44, pp. 440-479.
[56] Vieweg, S., Unger, G., Heinrich, G. and Donth, E. (1999). Comparison of dynamic shear properties of styrene-butadiene vulcanisates filled with carbon black or polymeric fillers, Journal of Applied Polymer Science, Vol. 73, pp. 495-503.
[57] Einstein, A. (1906). Eine neue Bestimmung der Moleküldimensionen, Annalen der Physik, Volume 324, Issue 2, pp. 289-306.
[58] Einstein, A. (1911). Berichtigung zu meiner Arbeit: Eine neue Bestimmung der Moleküldimensionen, Annalen der Physik, Volume 339, Issue 3, pp. 591-592.
[59] Guth, E. and, Gold, O. (1938). On the hydrodynamical theory of the viscosity of suspensions, Physical Review, Vol. 53, pp. 322.
[60] Smallwood, H.M. (1944). Limiting law of the reinforcement of rubber, Journal of Applied Physics, Vol. 15, pp. 758-766.
[61] Guth, E. (1945). Theory of filler reinforcement, Journal of Applied Physics, Vol. 16, pp. 20-25.

[62] Kraus, G. (1984). Mechanical losses in carbon-black-filled rubbers, Journal of Applied Polymer Science: Applied Polymer Symposium, Vol. 39, pp. 75-92.
[63] Holt, W.L. (1931). Behavior of Rubber under Repeated Stresses, Industrial and Engineering Chemistry, Vol. 23 No. 12, pp. 1471-1475.
[64] Mullins, L. (1957). Theoretical Model for the Elastic Behavior of Filler-Reinforced Vulcanised Rubbers, Rubber Chemistry and Technology, Vol. 30, Issue 2, pp. 555-571.
[65] Mullins, L. (1969). Softening of Rubber by Deformation, Rubber Chemistry and Technology, Vol. 42, Issue 1, pp. 339-362.
[66] Mullins, L. (1948). Effect of Stretching on the Properties of Rubber, Rubber Chemistry and Technology, Vol. 21, pp. 281-300.
[67] Diani, J., Fayolle, B. and Gilormini, P. (2009). A Review of the Mullins Effect, European Polymer Journal, Vol. 45, pp. 601-612, 2009
[68] Bueche, F. (1960). Molecular Basis for the Mullins Effect, Journal of Applied Polymer Science, Vol. IV No. 10, pp. 107-114.
[69] Houwink, R. (1956). Slipping of Molecules during the Deformation of Reinforced Rubber, Rubber Chemistry and Technology, Vol. 29, pp. 888-893.
[70] Dannenberg, E.M. and Brennan, J.J. (1966). Strain Energy as a Criterion for Stress Softening in Carbon-Black-Filled Vulcanisates, Rubber Chemistry and Technology, Vol. 39, pp. 597-608.
[71] Harwood, J.A.C., Mullins, L. and Payne, A.R. (1965). Stress Softening in Natural Rubber Vulcanisates. Part II. Stress Softening Effect in Pure Gum and Filler Loaded Rubbers, Journal of Applied Polymer Science, Vol. 9, pp. 3011-3021.
[72] Harwood, J.A.C. and, Payne, A.R. (1966). Stress Softening in Natural Rubber Vulcanisates. Part III. Carbon Black-Filled Vulcanisates, Journal of Applied Polymer Science, Vol. 10, pp. 315-324.
[73] Mullins, L. and Tobin, N.R. (1965). Stress Softening in Rubber Vulcanisates. Part I. Use of a Strain Amplification Factor to Describe the Elastic Behavior of Filler-Reinforced Vulcanised Rubber, Journal of Applied Polymer Science, Vol. 9, pp. 2993-3009.
[74] Bueche, F. (1961). Mullins Effect and Rubber-Filler Interaction, Journal of Applied Polymer Science, Vol. V, Issue No. 10, pp. 271-281.
[75] Harwood, J.A.C. and Payne, A.R. (1966). Stress Softening in Natural Rubber Vulcanisates. Part IV. Unfilled Vulcanisates, Journal of Applied Polymer Science, Vol. 10, pp. 1203-1211.
[76] Flory, P.J. (1947). Thermodynamics of crystallization in high polymers. I. Crystallization induced by stretching, The Journal of Chemical Physics, Vol. 15, No. 6, pp. 397-408.
[77] Flory, P.J. (1953). Principles of polymer chemistry, Cornell University Press, Ithaca New York the USA.
[78] Toki, S., Fujimaki, T. and Okuyama, M. (2000). Strain-induced crystallization of natural rubber as detected real-time by wide-angle X-ray diffraction technique, Polymer, Vol. 41, pp. 5423-5429.
[79] Andrews, E.H. (1964). Crystalline morphology in thin films of natural rubber, II. Crystallization under strain, Proceedings of the Royal Society of London. Series A, Mathematical and Physical, London, UK, Vol. 277, No. 1371, pp. 562-570.
[80] Andrews, E.H., Owen, P.J. and Singh, A. (1971). Microkinetics of lamellar crystallization in a long chain polymer, Proceedings of the Royal Society of London. Series A, Mathematical and Physical, London, UK, Vol. 324, No. 1556, pp. 79-97.
[81] Poompradub, S., Tosaka, M., Kohiya, S., Ikeda, Y. and Toki, S.: (2005). Mechanism of strain-induced crystallization in filled and unfilled natural rubber vulcanisates, Journal of Applied Physics, Vol. 97, pp. 103529(1)-103529(9).

[82] Rault, J., Marchal, J., Judeinstein, P. and Albouy, P.A. (2006). Stress-induced crystallization and reinforcement in filled natural rubber: ^{2}H NMR study, Macromolecules, Vol. 39, No. 24, pp. 8356-8368.

[83] Chenal, J., Gauthier, C., Chazeau, L., Guy, L. and Bomal, Y. (2006). Parameters governing strain induced crystallization in filled natural rubber, Polymer, Vol. 48, pp. 6893-6901.

[84] Haringx, J.A. (1948&1949). On highly compressible helical springs and rubber rods, and their application for vibration-free mountings, Philips Research Reports, Vol. 3 and 4, Eindhoven, Netherland.

[85] Tada, E., Takayama, M. et al. (1997). 4 byoumenshin eno michi-the way to the 4 second-period base isolation (in Japanese). 2nd Edition, Rikoutosyo (Riko publisher), Tokyo, Japan.

[86] Recommendation for the design of base isolated buildings. 3rd Edition (in Japanese), Architectural Institute of Japan, December 2001.

[87] Lindley, P.B. (1964). Engineering design with natural rubber, Malayan Rubber Fund Board, The Natural Rubber Producers' Research Association, Technical bulletin No. 8, London, Great Britain.

[88] Gent, A.N. and Lindley, P.B. (1959). The compression of bonded rubber blocks, Proceedings of the Institution of Mechanical Engineers, London, UK, Vol. 173, pp. 111-122.

[89] Block, T. (2010). Verdrehwiderstände bewehrter Elastomerlager, PhD Thesis, die Ruhr-Universität Bochum.

[90] Rejcha, C.: (1964). Design of elastomeric bearings, Journal of the Prestressed Concrete Institute, Vol. 9, pp. 62-78.

[91] Kelly, M.J. (1993). Earthquake-Resistant Design with Rubber, Springer-Verlag London, UK.

[92] Gent, A.N. and Meinecke, E.A. (1970). Compression, bending, and shear of bonded rubber blocks, Polymer Engineering and Science, Vol. 10, No. 1, pp. 48-53.

[93] Constantinou, M.C., Kartoum, A. and Kelly, J.M. (1992). Analysis of compression of hollow circular elastomeric bearings", Engineering Structures, Vol.14, pp.103-111.

[94] Mangerig, I., Mano, T. and Distl, J. (2012). Finite Element Analysis of the Elastomeric Ring Bearing, Proceedings of the 9th German-Japanese Bridge Symposium, Kyoto, Japan.

[95] Pond, T.J. (1995). Cavitation in bonded natural rubber cylinder repeatedly loaded in tension, Journal of Natural Rubber Research, 10: pp. 14-25, 1995.

[96] Gent, A.N. and Lindley, P.B. (1958). Internal rupture of bonded rubber cylinders in tension, Proceedings of the Royal Society of London, Series A, London, UK, Vol. 249, No. 1257, pp. 195-205.

[97] Dorfmann, A. and Burtscher, L.S. (2000). Aspects of cavitaion damage in seismic bearings, Journal of Structural Engineering Vol. 126, No. 5, 72, pp. 573-579.

[98] Gent, A.N. and Tompkins, D.A. (1969). Nucleation and growth of gas bubbles in elastomers, Journal of Applied Physics, Vol.40, No. 6, pp.2520-2525.

[99] Gent, A.N. and Wang, C. (1991). Fracture mechanics and cavitation in rubber-like solids, Journal of Material Science, Vol. 26, pp. 3392-3395.

[100] Gent, A.N. and Tompkins, D.A. (1969). Surface energy for small holes or particles in elastomers, Journal of Polymer Science: Part A-2, Vol. 7, pp. 1483-1488.

[101] Notomi, M., Shimosaka, H., Shimoda, H., Suzuki, S. and Yoshizwa, T. (2002). Void Nucleation of Rubber Material for Seismic Isolation Due to tension Load, Transactions of the Japan Society of Mechanical Engineers, Vol. 68, pp.744-749.

[102] Shoji, M. and Saito, K. (2002). Seismic performance of a laminated rubber bearing under extreme shear deformation subjected tension or compression stress, 11th Japan Earthquake Symposium, Japan, pp. 1725-1728.

[103] Nishio, K., Ishihara, T., Yanagisawa, N., Matsubayashi, Y. and Fujinami, T. (1997) Study on

tensile performance of base isolation devices – Part 2 (in Japanese), Summaries of technical papers of Annual Meeting Architectural Institute of Japan, B-2, Structures II, Structural dynamics nuclear power plants, pp.529-530.

[104] Uryu, M., Kondo, T. and Hashimura, H. (2002). Experimental study on the tensile characteristics of natural rubber bearings – Part 6 (in Japanese), Summaries of technical papers of Annual Meeting Architectural Institute of Japan, B-2, Structures II, Structural dynamics nuclear power plants, pp.491-492.

[105] Kelly, M.J. (2003). Tension Buckling in Multilayer elastomeric bearings, Journal of Engineering Mechanics, Vol. 129, No. 12, pp. 1363-1368.

[106] Kelly, M.J. and Takhirov, M.S. (2007). Tension buckling in multilayer elastomeric isolation bearings, Journal of Mechanics of Material and Structures, Vol. 2, No. 8, pp. 1591-1605.

[107] Kikuchi, M., Kitamura, Y., Hayashi, S., Kawashima, K., Sakaguchi, T. and Yamada, C. (1999). Mechanical characteristics of elastomeric seismic isolation bearings under tension (in Japanese), Journal of Structural and Construction Engineering, Architectural Institute of Japan, No. 524, pp. 57-64.

[108] Muramatsu, Y., Kitamura, I., Nishikawa, I., Kawabata, M., Takayama, T. and Kimura, Y. (2001). Tensile property of large-sized natural rubber bearing (in Japanese), Journal of Technology and Design, Architectural Institute of Japan, No. 12, pp. 53-56.

[109] Kato, R., Oka, K. and Takayama, M. (2003). The tensile tests of natural rubber bearings focused on the effect of the steel flange plates, ASME Pressure Vessel and Piping Conference, Paper No. PVP2003-2105, Ohio, the USA, pp. 81-88.

[110] Furuta, T., Araki, S. and Kanamori, S. (2005). Finite element analysis of shear-tensile characteristics of natural rubber bearings, Journal of Structural Engineering, Vol. 51B, pp. 231-236.

[111] Hara, T., Tajima, J., Fukazawa, K., Mochizuki, M. and Tachibana, M. (1998). Experimental Study on Tensile Performance and Shearing Performance under Tensile Force of High Damping Rubber Bearings Part 4 and 5, Annual Meeting Architectural Institute of Japan, Japan, pp. 1137-1142.

[112] Bayraktar, E., Isac, N., Bessri, K. and Bathias, C. (2008). Damage mechanism in natural (NR) and synthetic rubber (SBR): nucleation, growth and instability of the cavitation, Fatigue & Fracture of Engineering Materials & Structures, Vol. 31, pp. 184-196.

[113] Holzapfel, G.A. (2000). Nonlinear Solid Mechanics-A Continuum Approach for Engineering, John Wiley & Sons, LTD, West Sussex, England.

[114] Hou, H.S. and Abeyarante, R. (1992). Cavitation in elastic and elastic-plastic solids, Journal of Mechanics and Physics of Solids, Vol. 26, No. 3, pp. 571-592.

[115] Hou, H.S. (1990). Cavitation instability in solids, PhD Thesis, Massachusetts Institute of Technology, USA.

[116] Chang, Y.W., Gent, A.N. and, Padovan, J. (1992). Expansion of a cavity in a rubber block under unequal stresses, International Journal of Fracture, Vol. 60, pp. 283-291.

[117] Ganghoffer, J.F. and Schultz, J. (1995). Expansion of a cavity in a rubber block under stress: application of the asymptotic expansion method to the analysis of the satility and bifurcation conditions, International Journal of Fracture, Vol. 72, pp. 1-20.

[118] Fond, C. (2001=. Cavitation criterion for rubber materials: A review of void-growth models, Journal of Polymer Science: Part B: Polymer Physics, Vol. 39, pp. 2081-2096.

[119] Skacel, P. and Bursa, J. (2005). Computational modelling of spherical cavity behaviour in rubber-like solids, Mechanical Science Forum, Vol. 482, pp. 323-326.

[120] Iwabe, N., Kani, N., Takayama, M., Morita, K. and Wada, A. (1999). Experimental Study on the Tension Capacity in the Displaced Position of Elastomeric isolators Part 1 to 3 (written in Japanese), Annual Meeting Architectural Institute of Japan, Japan, pp.559-564.

[121] Uno, Y., Sumimura, T. and Kanai, H. (2003). Research regarding the horizontal characteristics of various elastomeric bearings under tension influence (written in Japanese), JSCE Journal of Earthquake Engineering, Vol. 27, No. 190, pp. 1-4.
[122] Otsuka, H., Kuriki, S. and Ikenaga, M. (2022). Experimental Study on Ultimate Characteristics of Lead Rubber Bearing under Tensile Force, Journal of Structural Engineering, Vol. 48A, pp. 843-850.
[123] Matsushima, C., Notomi, M., Shimosaka, H., Shimoda, H., Suzuki S. and Yoshizawa, T. (2004). Low Cycle Fatigue by Shear Load of Rubber Material for Base Isolation, Transactions of Annual Meeting of the Japan Society of Mechanical Engineers, Vol. 1, pp. 123-124.
[124] Brown, L. (2006). Physical Testing of Rubber. 4th Edition, Springer Science+Business Media, Inc., the USA.
[125] Sussman, T. and Bathe, K.J. (1987). A finite element formulation for nonlinear incompressible elastic and inelastic analysis, Computers & Structures, Vol. 26, No. 1/2, pp. 357-409.
[126] Bathe, K.J. (1996). Finite Element Procedure, Prentice-Hall, Inc., New Jersey, the USA.
[127] Felippa, C.F. Nonlinear Finite Element Methods, Lecture script of the Department of Aerospace Engineering Sciences University of Colorado at Boulder, the USA.
[128] Guth, E. and Mark, H. (1934). Zur innermolekularen Statistik, insbesondere bei Kettenmolekühlen I, Monatshefte für Chemie und verwandte Teile anderer Wissenschaften, Vol. 65, Issue 1, pp. 93-121.
[129] Kuhn, V.W. (1934). Über die Gestalt fadenförmiger Moleküle in Lösungen, Kolloid-Zeitschrift, Vol. 68, Issue 1, pp. 2-15.
[130] Treloar, L.R.G. (1975). The Physics of Rubber Elasticity. 3rd Edition, Clarendon Press, Oxford, UK.
[131] Ogden, R.W. (1972). Large deformation isotropic elasticity – on the correlation of theory and experiment for incompressible rubberlike solids, Proceedings of the Royal Society of London. Series A, Mathematical and Physical Sciences, London, UK, Vol. 326, pp. 565-584.
[132] Flory, P.J. and Rehner, J. (1943). Statistical Theory of Chain Configuration and Physical Properties of High Polymers, Annals of the New York Academy of Science, Vol. 44, Issue 4, pp. 419-429.
[133] Arruda, E.M. and Boyce, M.C. (1993). A three-dimensional constitutive model for the large stretch behavior of rubber elastic materials, Journal of Mechanical and Physical Solids, Vol. 41, pp. 389-412.
[134] Boyce, M.C. and Arruda, E.M. (2000). Constitutive models of rubber elasticity: A review, Rubber Chemistry and Teschnology, Vol. 73, pp. 504-522.
[135] Kuhn, V.W. and Grün, F. (1942). Beziehungen zwischen elastischen Konstanten und Dehnungsdopeelbrechung hochelastischer Stoffe, Kolloid-Zeitschrift, Vol. 101, Issue 3, pp. 248-271.
[136] Furuta, T., Araki, S. and Kanamori, S. (2005). Finite Element Analysis for Shear-Tensile Characteristics of Natural Rubber Bearings (written in Japanese), Journal of Structural Engineering. B, Architectural Institute of Japan, Vol. 51B, pp. 231-236.
[137] Mangerig, I. and Mano, T. (2009). Tension Capacity of Elastomeric Bearings, Proceedings of the 8th Japanese-German Bridge Symposium, Munich, Germany, pp. 45-46.
[138] ADINA R&D, Inc., (2012). Theory and the modeling guide. Vol. 1, Watertown MA, the USA.
[139] ISO 37:2011-12, Rubber, vulcanised or thermoplastic – Determination of tensile stress-strain properties, December 2012

[140] DIN 53504:2009, Prüfung von Kautschuk und Elastomeren - Bestimmung von Reißfestigkeit, Zugfestigkeit, Reisdehnung und Spannungswerten im Zugversuch, October 2009

[141] Newmark, N.M. and Rosenblueth, E. (1971). Fundamentals of Earthquake Engineering, Prentice-Hall, Inc., New Jersey, the USA.

[142] Petersen, C. (2000). Dynamik der Baukonstruktionen, Friedr. Vieweg & Sohn Verlagsgesellschaft mbH, Braunschweig/Wiesbaden, Deutschland.

[143] Nakai, H. and Kobayashi, H. (1999). Doboku kozobutsuno shindou kaiseki (Vibration analysis of constructions, written in Japanese). 2nd Edition, Morikita Publishing Co., Ltd., Tokyo.

[144] Zheng, H. (2008). On the predictive capability and stability of rubber material models. Master thesis, School of Engineering, Massachusetts Institute of Technology, the USA.

[145] Dorfmann, A. (2003). Stress softening of elastomers in hydrostatic tension, Acta Mechanica 165, pp. 117-137.

[146] Martelli, A. and Fomi, M. (2008). Prevention and mitigation of seismic risk of strategic, public and residential constructions, cultural heritage and industrial plants and components by means of seismic isolation and energy dissipation in Italy and worldwide, http://www.assisi-antiseismicsystems.org/Territorial/GLIS/Glisnews/GN11/G11_Applica_World.pdf, June 2010

[147] Höfer, P. (2009). Dynamische Eigenschaften technischer Gummiwerkstoffe, Verlag Dr. Hut, München, Germany.

Appendix A – Results of the initial property tests

Property Test - Type 1-01 Bearing

Compression Test

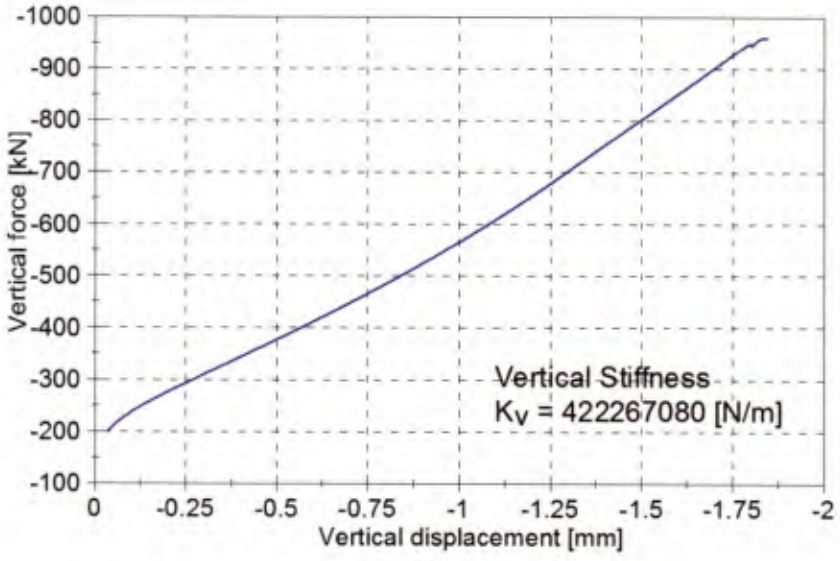

Property Test - Type 1-01 Bearing

Compression Shear Test - Cycle 9

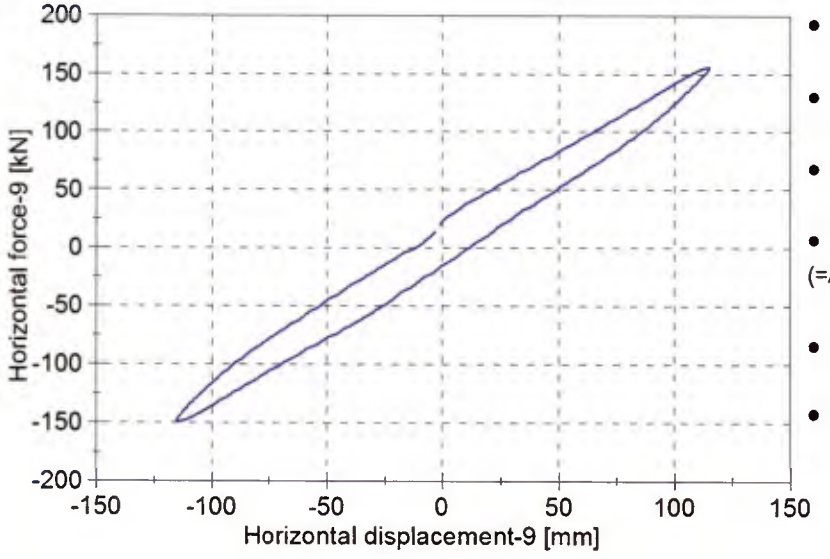

- Amplitude
  d_X = 0.1151 [m]
- Vertical Force
  N_S = -959000 [N]
- Max. Velocity
  v_{max} = 48.8 [mm/s]
- Dissipated Energy
  (=Area of the Hysteresis Loop)
  A_h = 6.2451 [kJ]
- Damping Coefficient
  c = 360000 [Ns/m]
- Horizontal Stiffness
  K_h = 1320000 [N/m]

Property Test - Type 1-02 Bearing

Compression Test

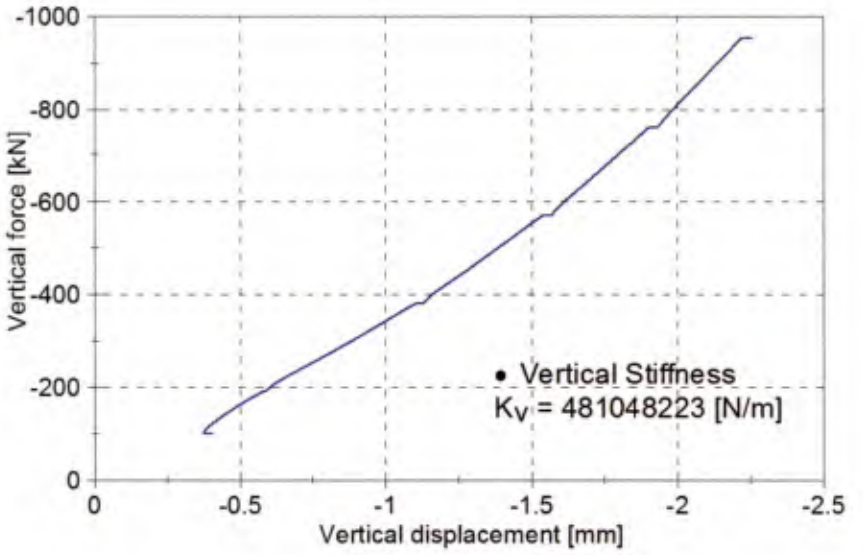

Property Test - Type 1-02 Bearing

Compression Shear Test - Cycle 9

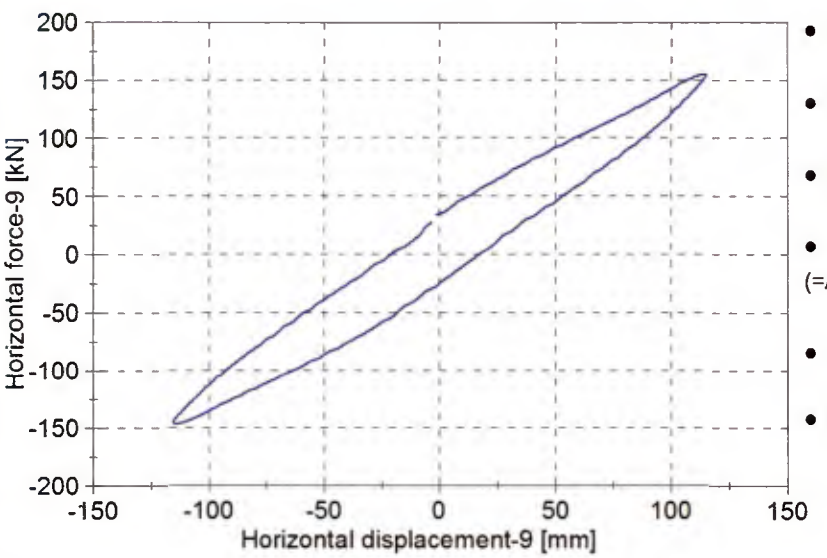

- Amplitude
  d_X = 0.1153 [m]
- Vertical Force
  N_S = -1005000 [N]
- Max. Velocity
  v_{max} = 48.4 [mm/s]
- Dissipated Energy
  (=Area of the Hysteresis Loop)
  A_h = 8.9583 [kJ]
- Damping Coefficient
  c = 514000 [Ns/m]
- Horizontal Stiffness
  K_h = 1300000 [N/m]

Property Test - Type 1-03 Bearing

Compression Test

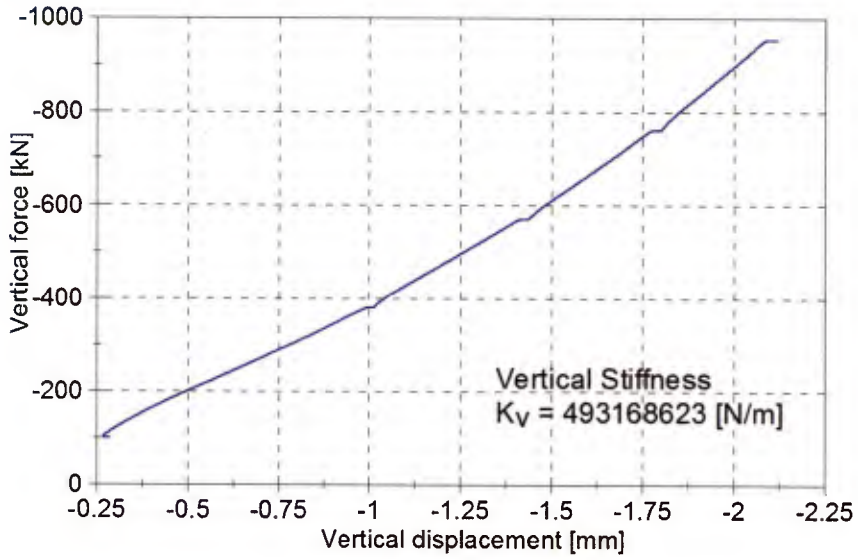

Property Test - Type 1-03 Bearing

Compression Shear Test - Cycle 9

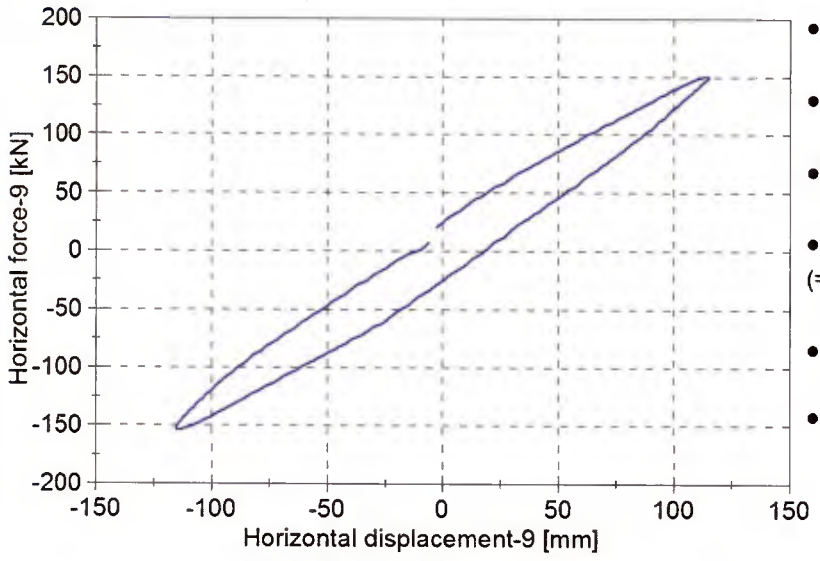

- Amplitude
  d_X = 0.1152 [m]
- Vertical Force
  N_S = -954000 [N]
- Max. Velocity
  v_{max} = 48.3 [mm/s]
- Dissipated Energy
  (=Area of the Hysteresis Loop)
  A_h = 7.643 [kJ]
- Damping Coefficient
  c = 439000 [Ns/m]
- Horizontal Stiffness
  K_h = 1310000 [N/m]

Property Test - Type 1-04 Bearing

Compression Test

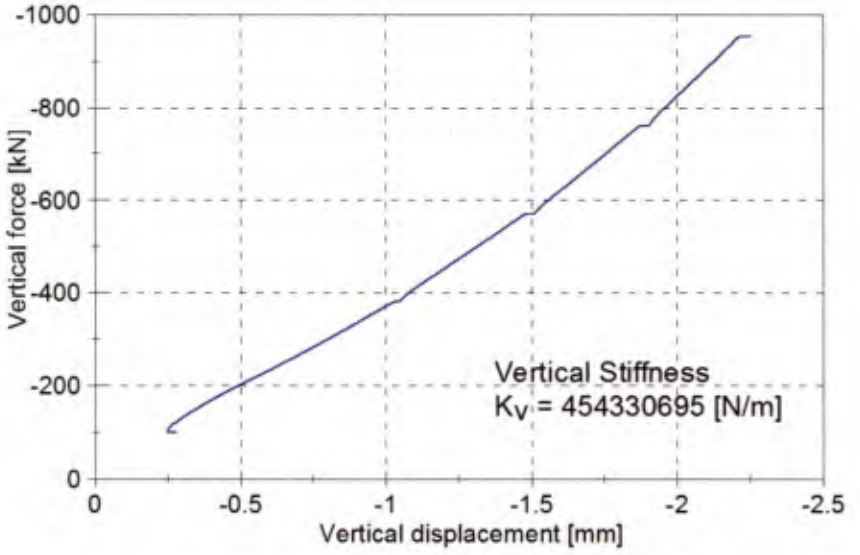

Property Test - Type 1-04 Bearing

Compression Shear Test - Cycle 9

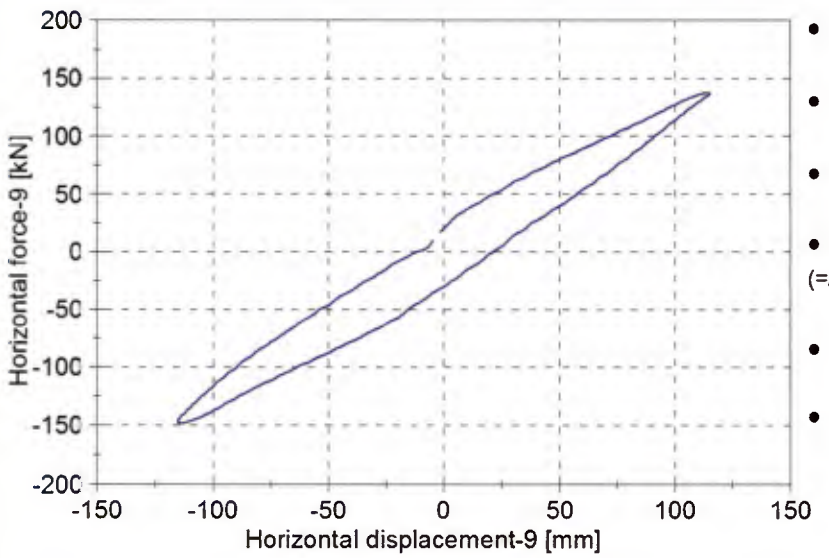

- Amplitude
  d_X = 0.1153 [m]
- Vertical Force
  N_S = -954000 [N]
- Max. Velocity
  v_{max} = 48 [mm/s]
- Dissipated Energy
  (=Area of the Hysteresis Loop)
  A_h = 7.6335 [kJ]
- Damping Coefficient
  c = 438000 [Ns/m]
- Horizontal Stiffness
  K_h = 1230000 [N/m]

Property Test - Type 1-05 Bearing

Compression Test

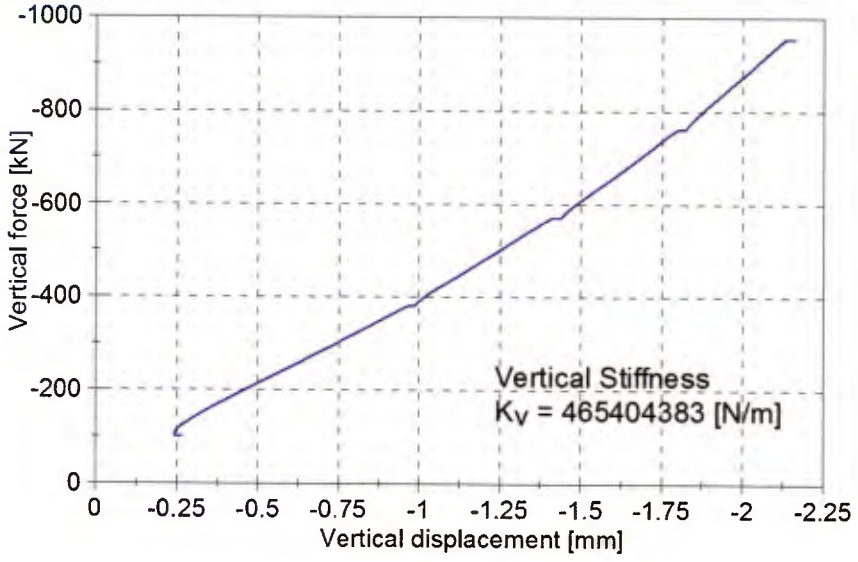

Property Test - Type 1-05 Bearing

Compression Shear Test - Cycle 9

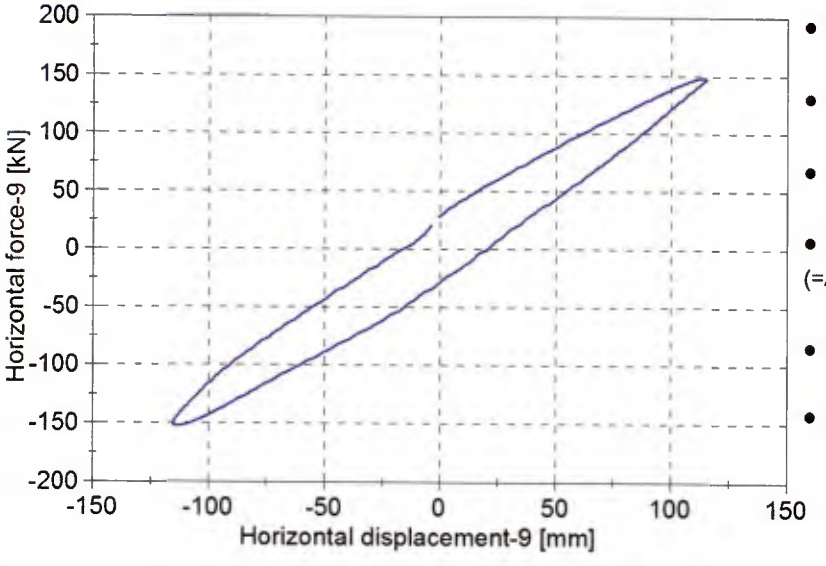

- Amplitude
  d_X = 0.1153 [m]
- Vertical Force
  N_S = -955000 [N]
- Max. Velocity
  v_{max} = 48.5 [mm/s]
- Dissipated Energy
  (=Area of the Hysteresis Loop)
  A_h = 8.5951 [kJ]
- Damping Coefficient
  c = 493000 [Ns/m]
- Horizontal Stiffness
  K_h = 1290000 [N/m]

Property Test - Type 1-06 Bearing

Compression Test

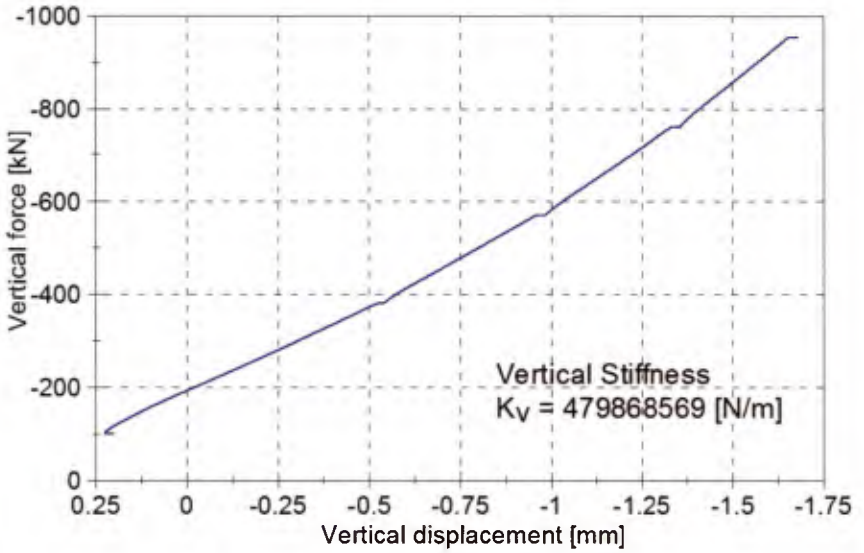

Property Test - Type 1-06 Bearing

Compression Shear Test - Cycle 9

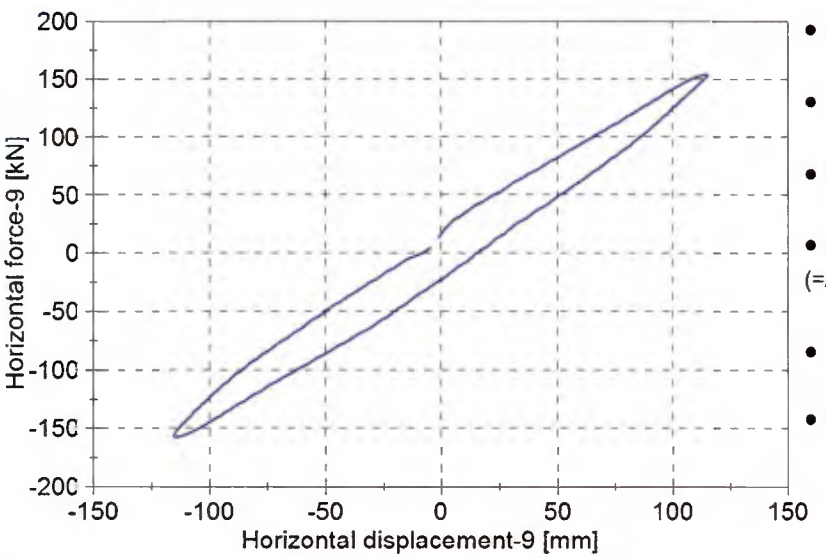

- Amplitude
  d_X = 0.1153 [m]
- Vertical Force
  N_S = -955000 [N]
- Max. Velocity
  v_{max} = 47.3 [mm/s]
- Dissipated Energy
  (=Area of the Hysteresis Loop)
  A_h = 6.5438 [kJ]
- Damping Coefficient
  c = 376000 [Ns/m]
- Horizontal Stiffness
  K_h = 1340000 [N/m]

Property Test - Type 1-07 Bearing

Compression Test

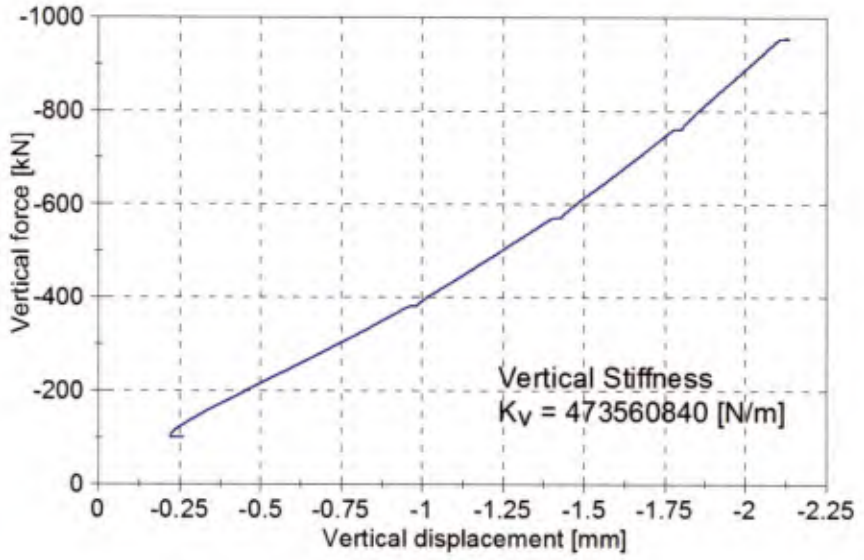

Property Test - Type 1-07 Bearing

Compression Shear Test - Cycle 9

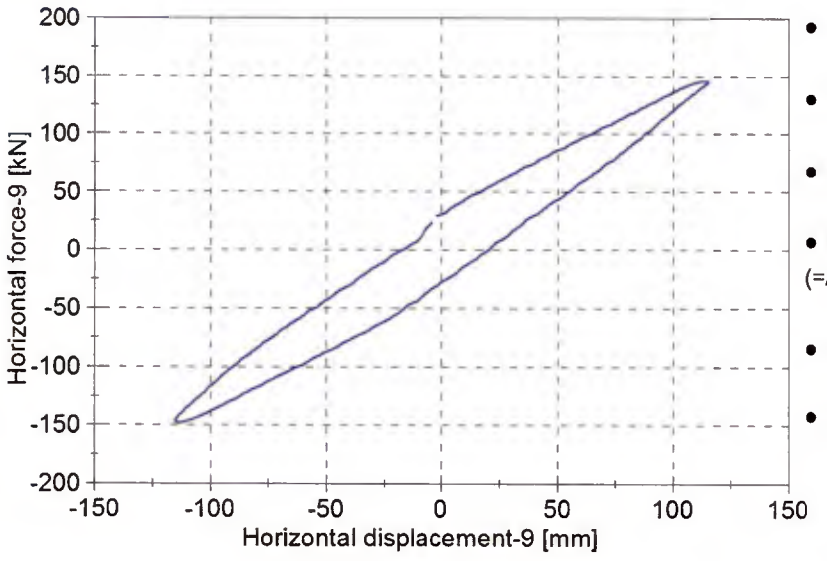

- Amplitude
  d_X = 0.1153 [m]
- Vertical Force
  N_S = -955000 [N]
- Max. Velocity
  v_{max} = 48.8 [mm/s]
- Dissipated Energy
  (=Area of the Hysteresis Loop)
  A_h = 8.4019 [kJ]
- Damping Coefficient
  c = 482000 [Ns/m]
- Horizontal Stiffness
  K_h = 1260000 [N/m]

Property Test - Type 1-08 Bearing

Compression Test

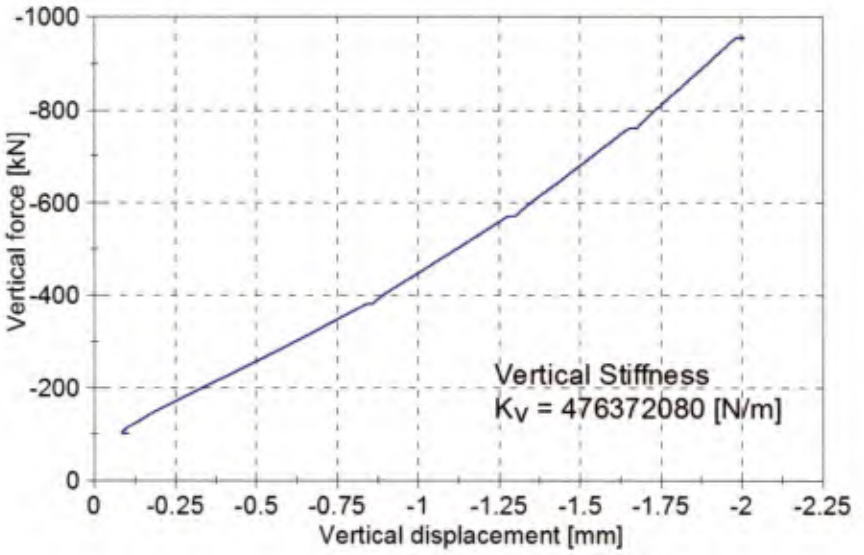

Property Test - Type 1-08 Bearing

Compression Shear Test - Cycle 9

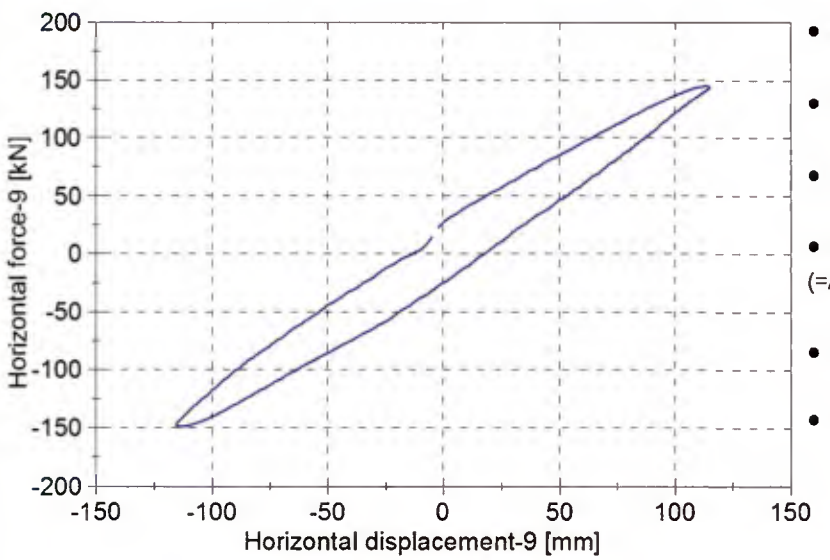

- Amplitude
  d_X = 0.1153 [m]
- Vertical Force
  N_S = -955000 [N]
- Max. Velocity
  v_{max} = 48.2 [mm/s]
- Dissipated Energy
  (=Area of the Hysteresis Loop)
  A_h = 7.6265 [kJ]
- Damping Coefficient
  c = 438000 [Ns/m]
- Horizontal Stiffness
  K_h = 1260000 [N/m]

Property Test - Type 1-09 Bearing

Compression Test

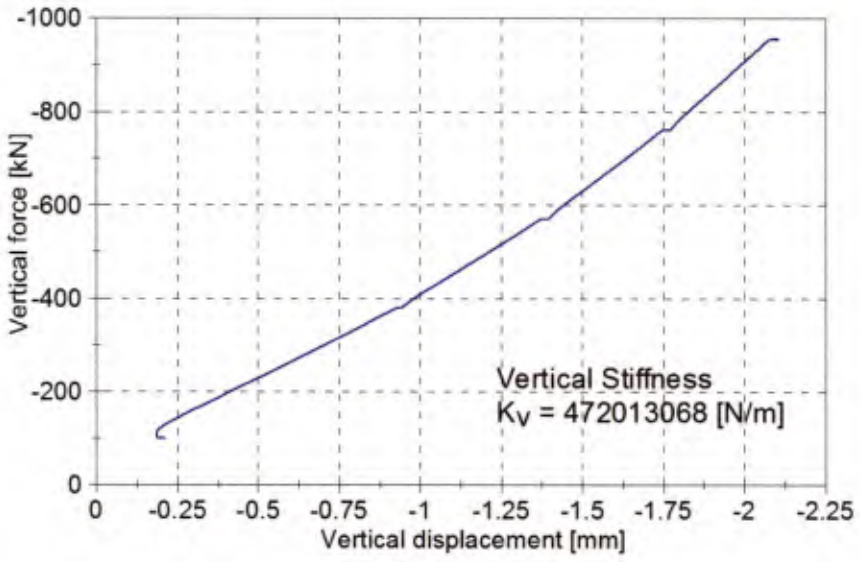

Property Test - Type 1-09 Bearing

Compression Shear Test - Cycle 9

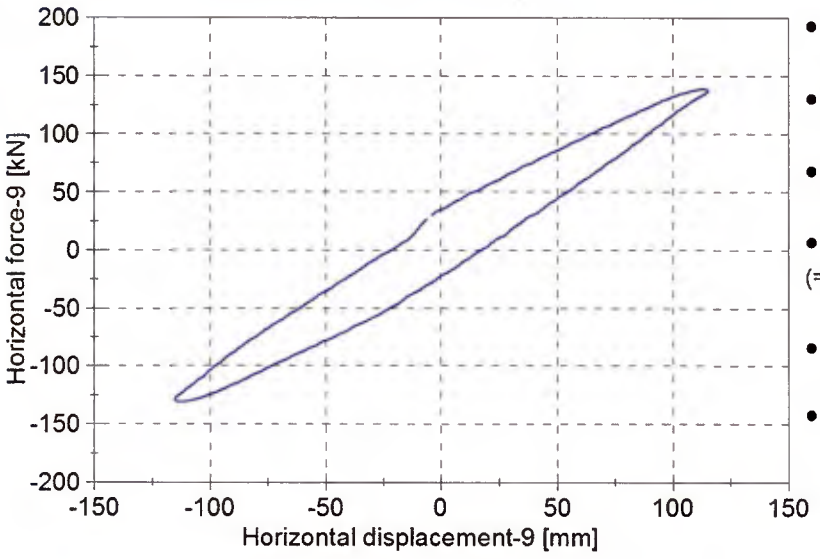

- Amplitude
  d_X = 0.1153 [m]
- Vertical Force
  N_S = -955000 [N]
- Max. Velocity
  v_{max} = 48.4 [mm/s]
- Dissipated Energy
  (=Area of the Hysteresis Loop)
  A_h = 8.2237 [kJ]
- Damping Coefficient
  c = 472000 [Ns/m]
- Horizontal Stiffness
  K_h = 1160000 [N/m]

Property Test - Type 2-01 Bearing

Compression Test

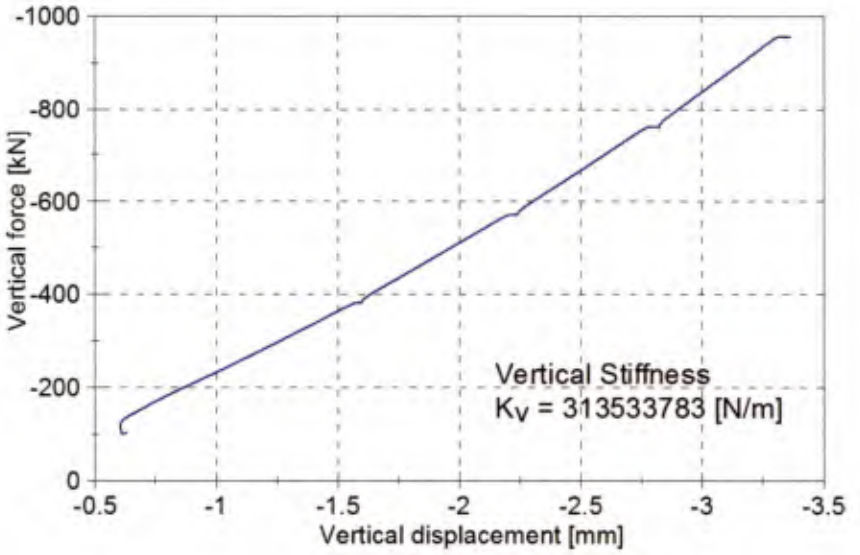

Property Test - Type 2-01 Bearing

Compression Shear Test - Cycle 9

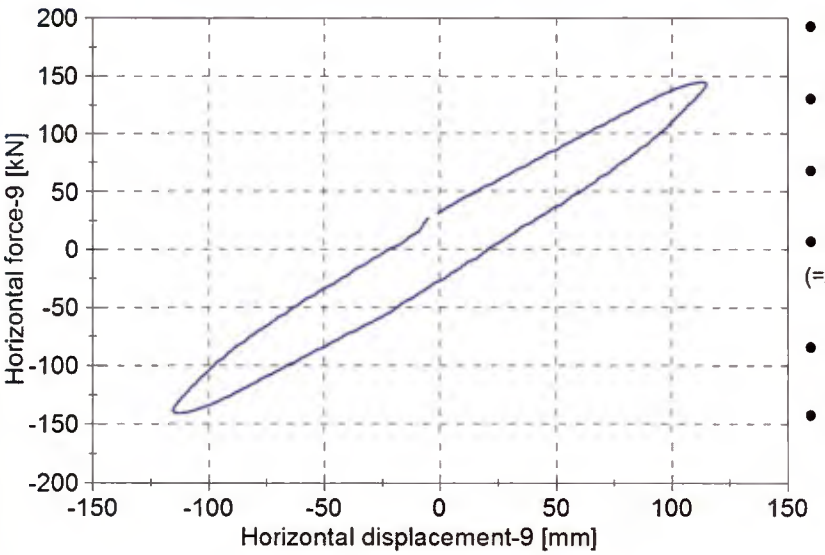

- Amplitude
  d_X = 0.1153 [m]
- Vertical Force
  N_S = -955000 [N]
- Max. Velocity
  v_{max} = 47.9 [mm/s]
- Dissipated Energy
  (=Area of the Hysteresis Loop)
  A_h = 9.5642 [kJ]
- Damping Coefficiert
  c = 94000 [Ns/m]
- Horizontal Stiffness
  K_h = 1220000 [N/m]

Property Test - Type 2-02 Bearing

Compression Test

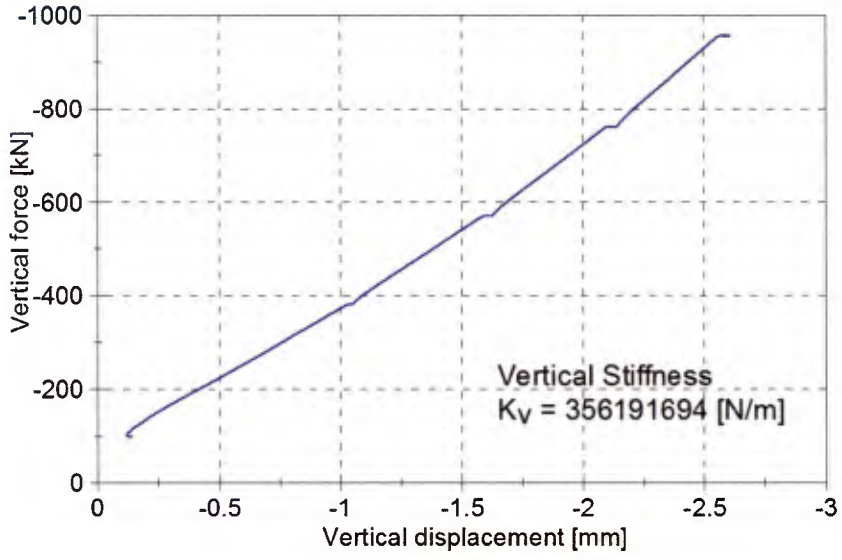

Property Test - Type 2-02 Bearing

Compression Shear Test - Cycle 9

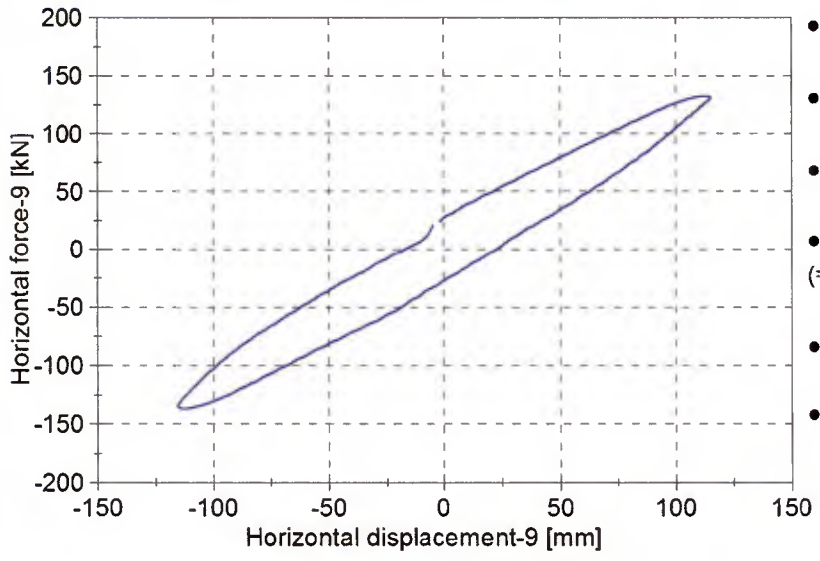

- Amplitude
  d_X = 0.1153 [m]
- Vertical Force
  N_S = -955000 [N]
- Max. Velocity
  v_{max} = 48.6 [mm/s]
- Dissipated Energy
  (=Area of the Hysteresis Loop)
  A_h = 8.81 [kJ]
- Damping Coefficient
  c = 92000 [Ns/m]
- Horizontal Stiffness
  K_h = 1150000 [N/m]

Property Test - Type 2-03 Bearing

Compression Test

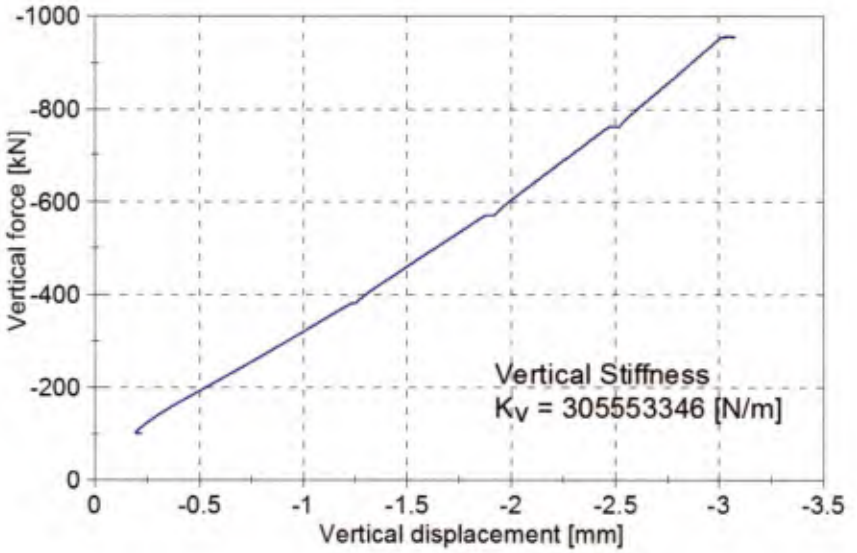

Property Test - Type 2-03 Bearing

Compression Shear Test - Cycle 9

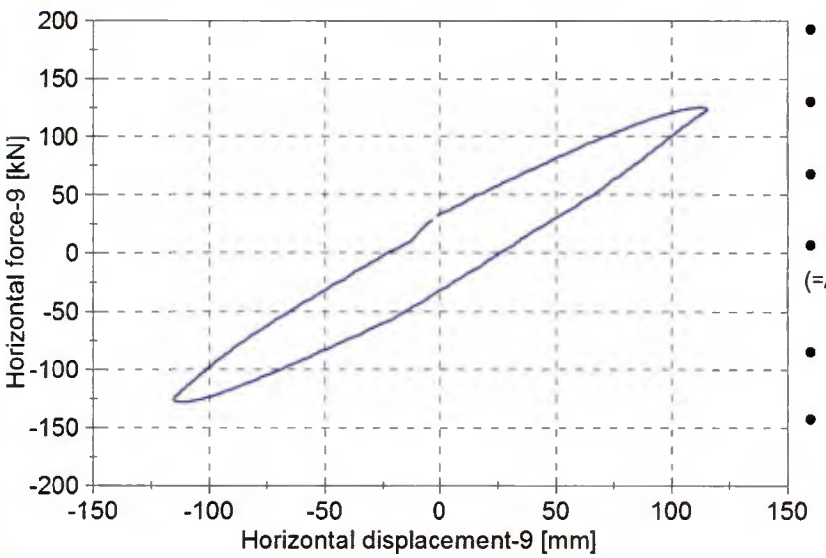

- Amplitude
  d_X = 0.1153 [m]
- Vertical Force
  N_S = -955000 [N]
- Max. Velocity
  v_{max} = 48.8 [mm/s]
- Dissipated Energy
  (=Area of the Hysteresis Loop)
  A_h = 9.9627 [kJ]
- Damping Coefficient
  c = 110000 [Ns/m]
- Horizontal Stiffness
  K_h = 1080000 [N/m]

Property Test - Type 2-04 Bearing

Compression Test

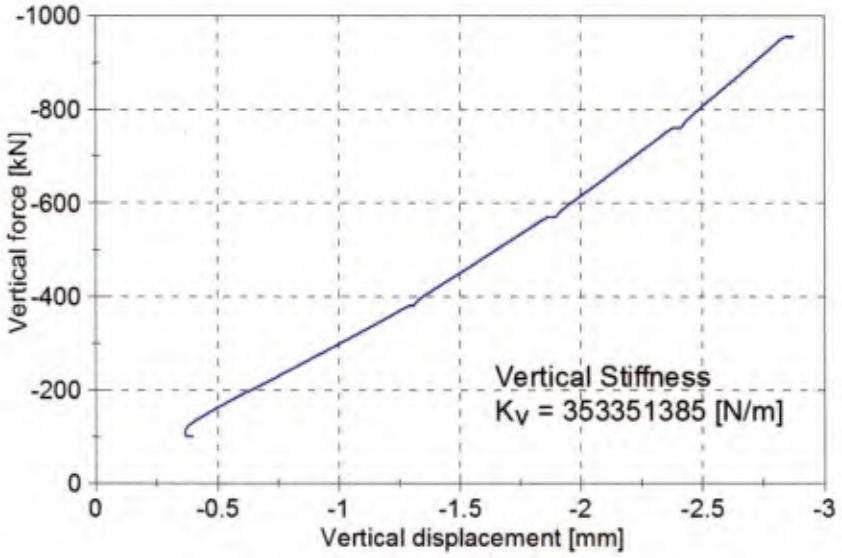

Property Test - Type 2-04 Bearing

Compression Shear Test - Cycle 9

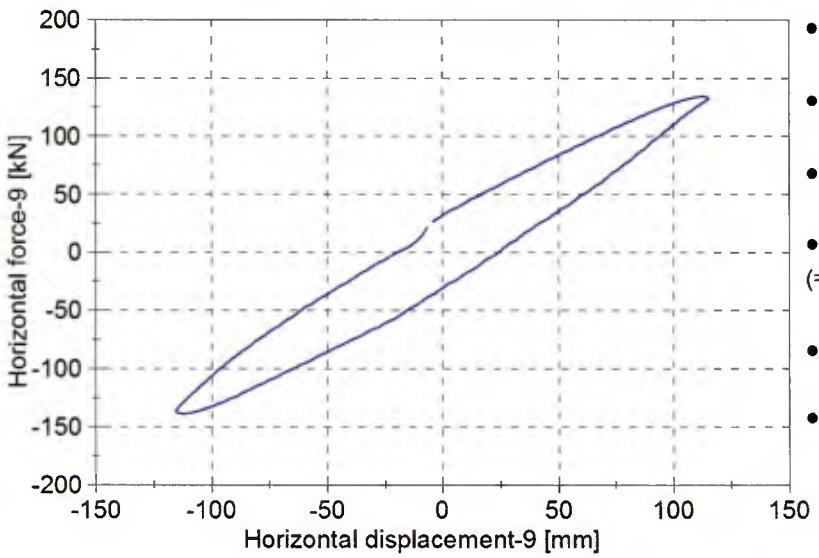

- Amplitude
  d_X = 0.1153 [m]
- Vertical Force
  N_S = -955000 [N]
- Max. Velocity
  v_{max} = 48.4 [mm/s]
- Dissipated Energy
  (=Area of the Hysteresis Loop)
  A_h = 9.4985 [kJ]
- Damping Coefficient
  c = 98000 [Ns/m]
- Horizontal Stiffness
  K_h = 1160000 [N/m]

Property Test - Type 2-05 Bearing

Compression Test

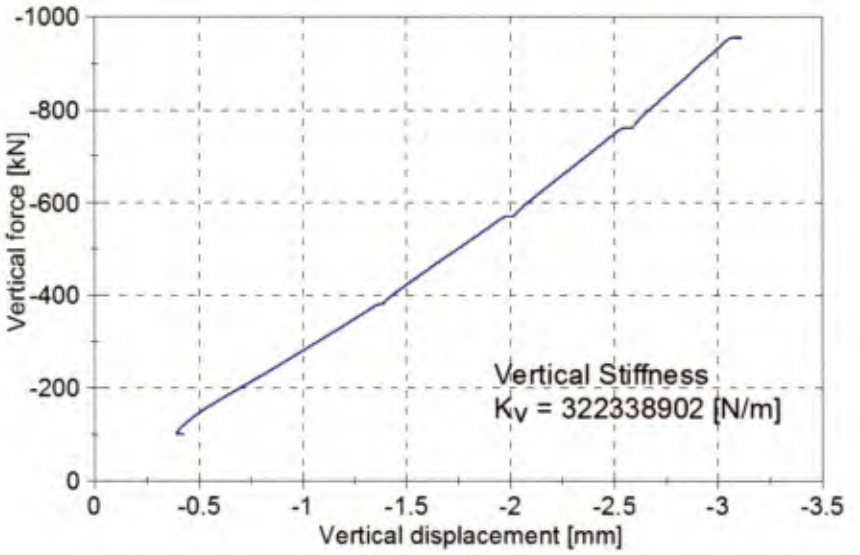

Property Test - Type 2-05 Bearing

Compression Shear Test - Cycle 9

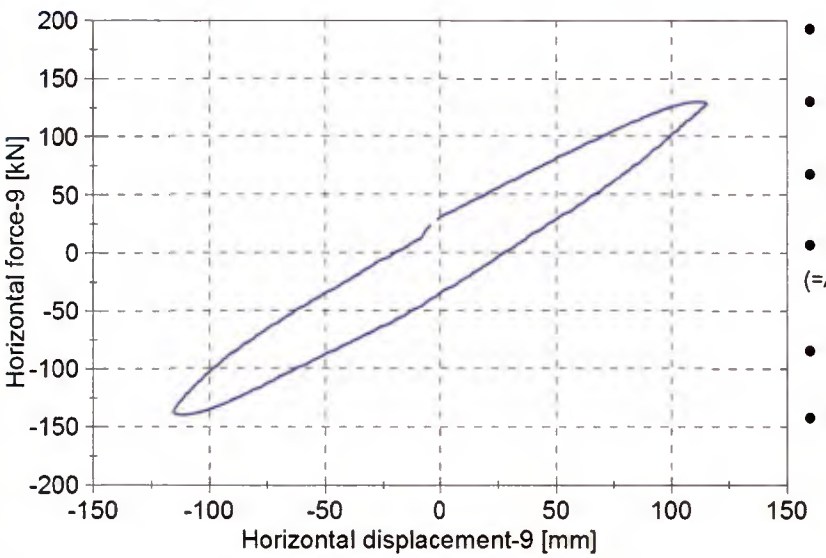

- Amplitude
  d_X = 0.1153 [m]
- Vertical Force
  N_S = -955000 [N]
- Max. Velocity
  v_{max} = 48.8 [mm/s]
- Dissipated Energy
  (=Area of the Hysteresis Loop)
  A_h = 10.3215 [kJ]
- Damping Coefficient
  c = 107000 [Ns/m]
- Horizontal Stiffness
  K_h = 1150000 [N/m]

Property Test - Type 2-06 Bearing

Compression Test

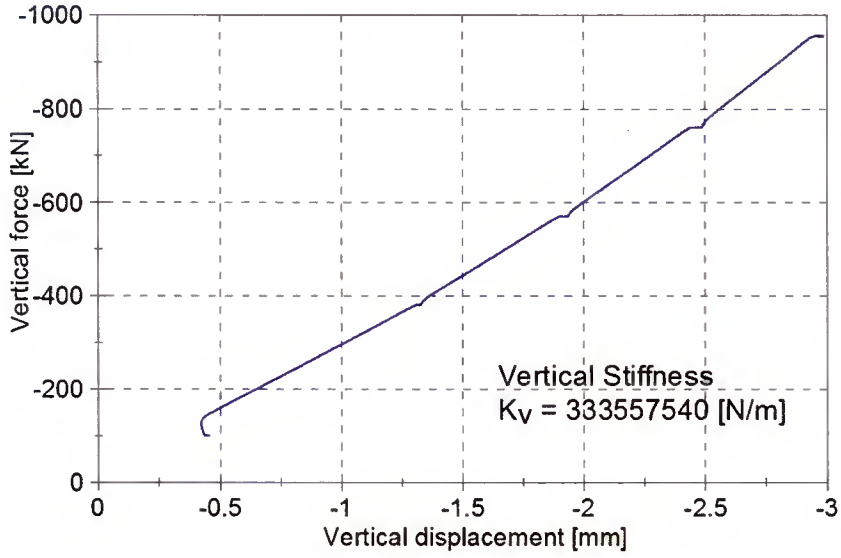

Property Test - Type 2-06 Bearing

Compression Shear Test - Cycle 9

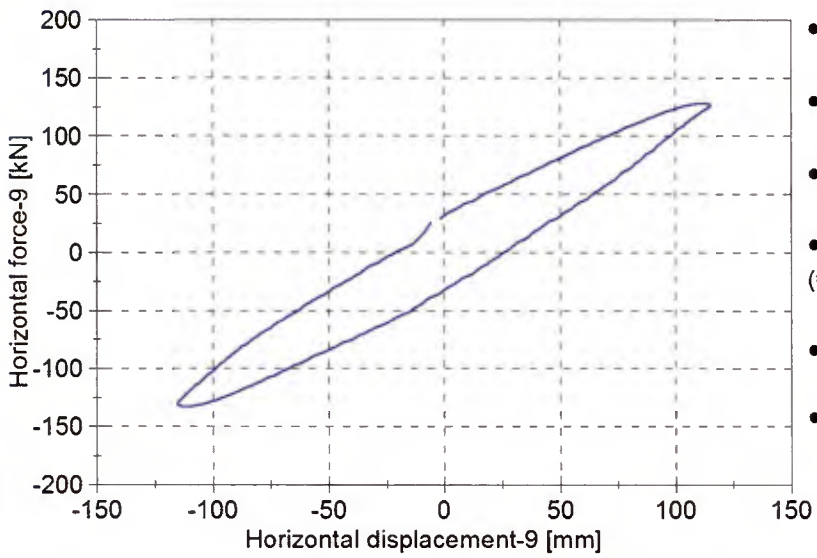

- Amplitude
  d_X = 0.1153 [m]
- Vertical Force
  N_S = -955000 [N]
- Max. Velocity
  v_{max} = 47.3 [mm/s]
- Dissipated Energy
  (=Area of the Hysteresis Loop)
  A_h = 9.4944 [kJ]
- Damping Coefficient
  c = 101000 [Ns/m]
- Horizontal Stiffness
  K_h = 1120000 [N/m]

Appendix B – Force-displacement plots of the tension / offset tension test

Type 1-01 Bearing

Uniaxial Tension Test

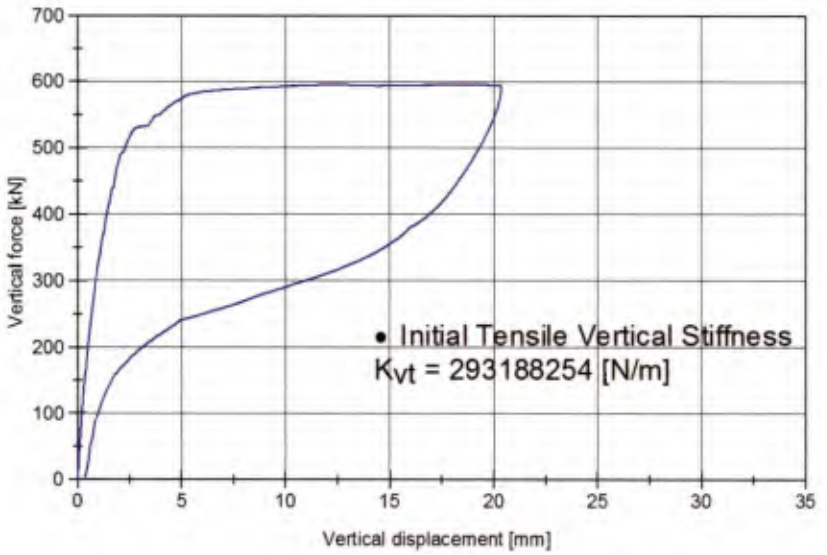

Type 1-02 Bearing

Uniaxial Tension Test

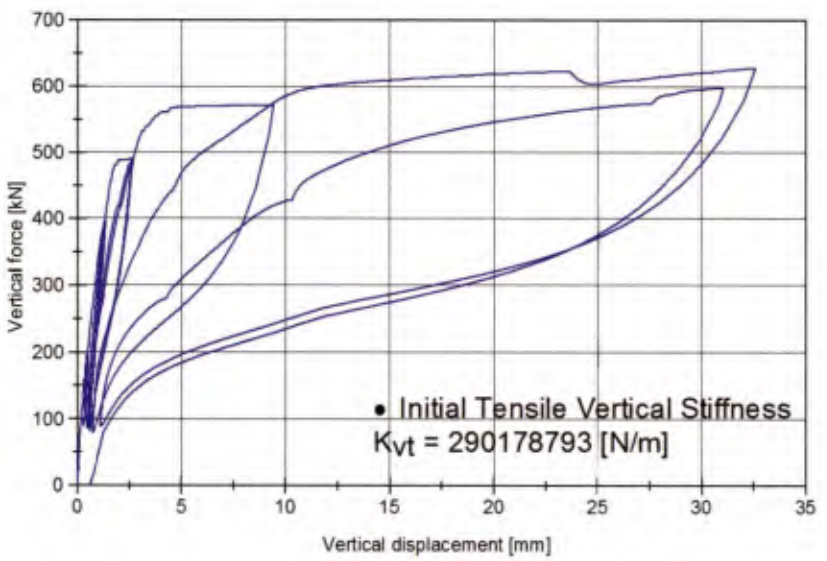

Type 1-03 Bearing

Uniaxial Tension Test

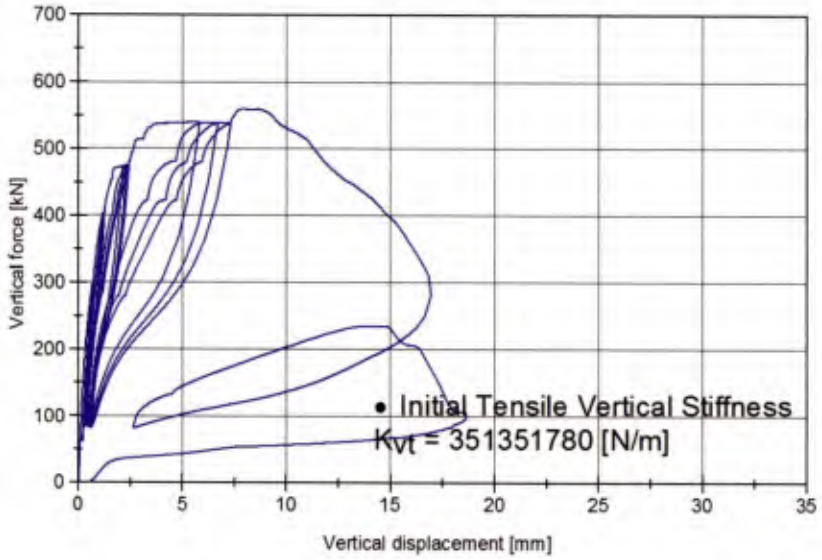

Type 1-04 Bearing

Uniaxial Tension Test

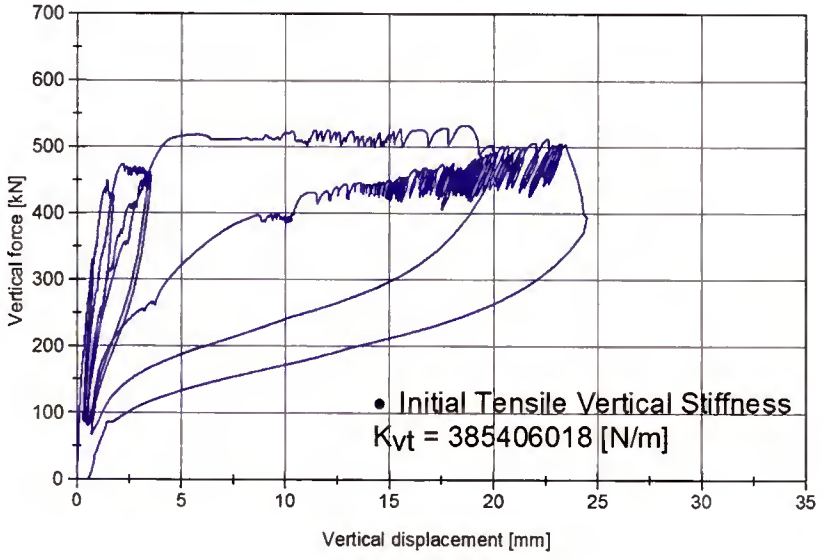

Type 1-05 Bearing

Uniaxial Tension Test

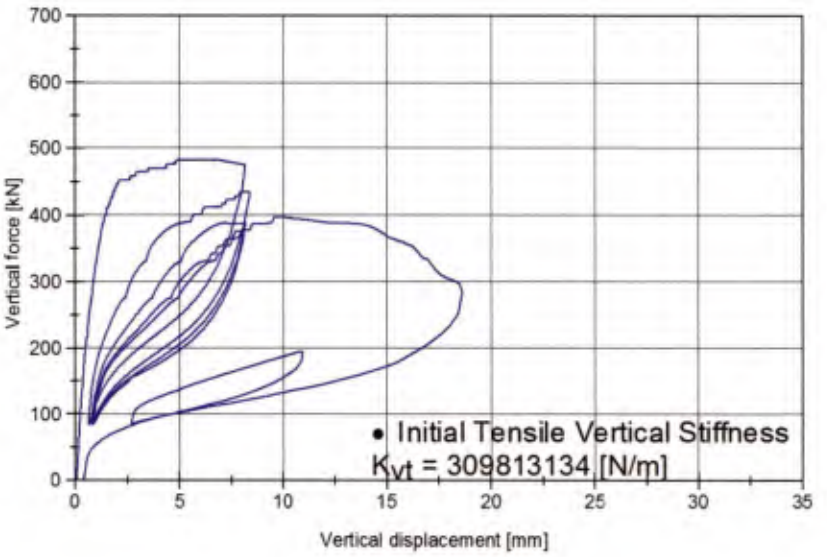

Type 1-06 Bearing

Uniaxial Tension Test

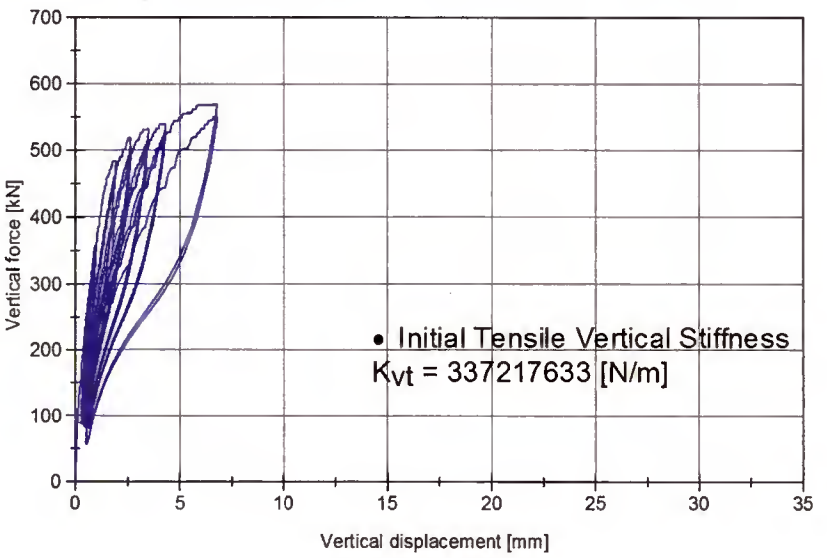

Type 1-07 Bearing

Tension and Shear Test

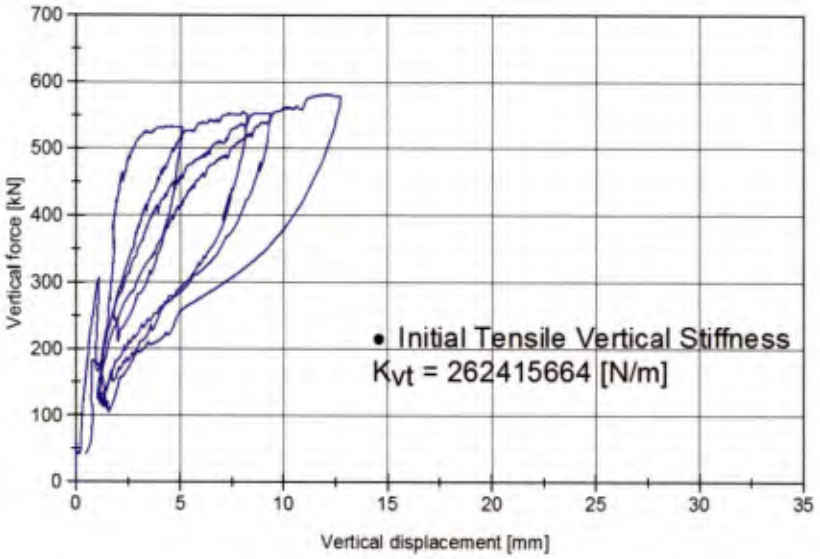

Type 1-08 Bearing

Tension and Shear Test

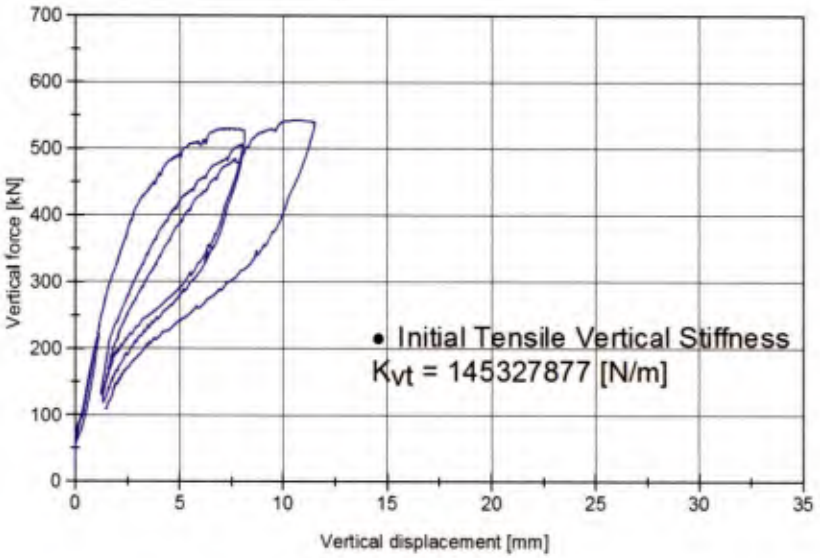

Type 1-09 Bearing

Tension and Shear Test

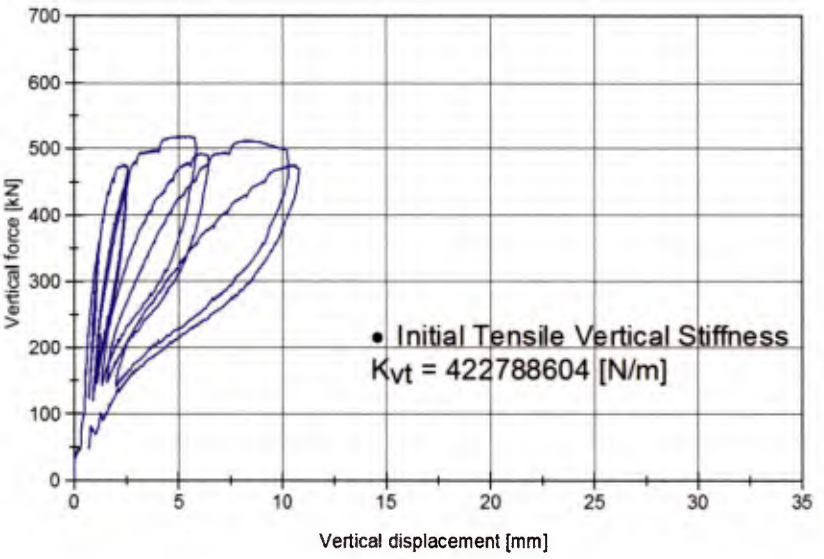

Type 2-01 Bearing

Uniaxial Tension Test

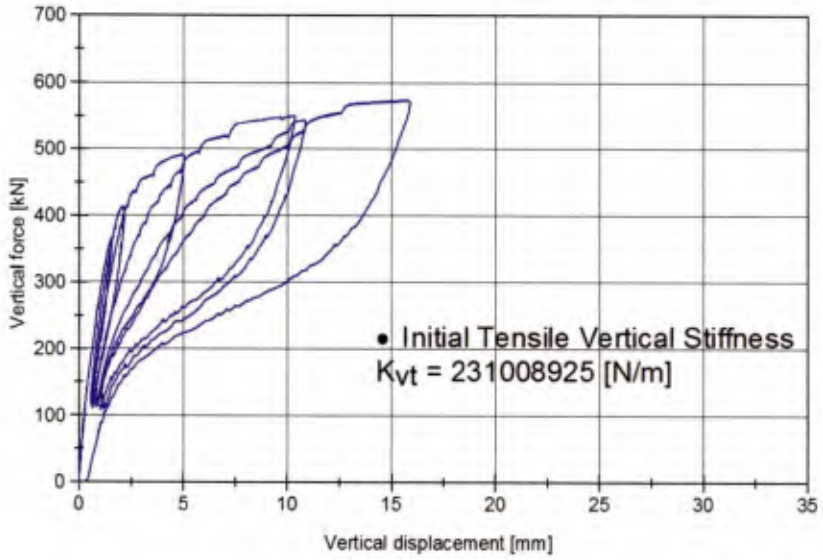

Type 2-02 Bearing

Uniaxial Tension Test

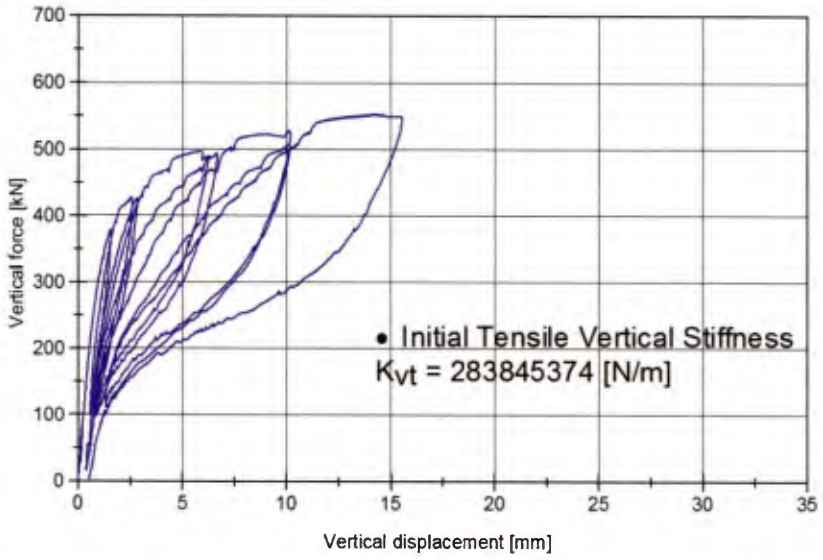

Type 2-03 Bearing

Uniaxial Tension Test

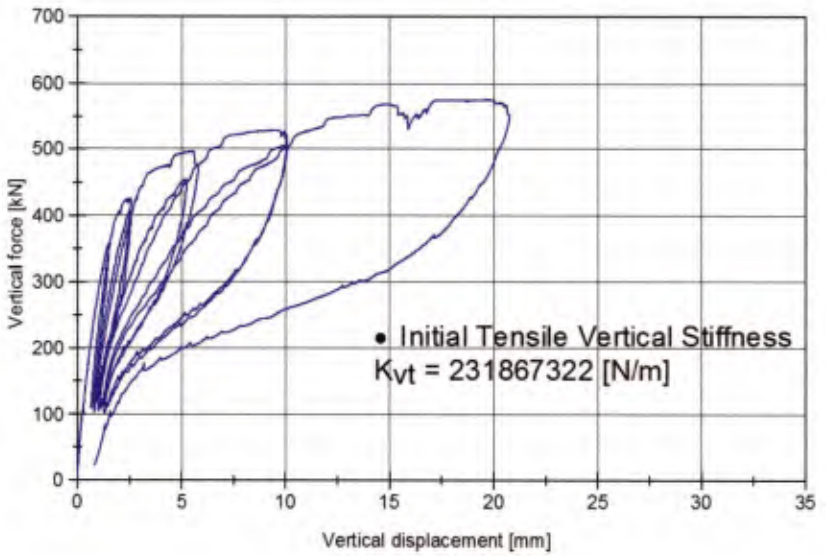

Type 2-04 Bearing

Tension and Shear Test

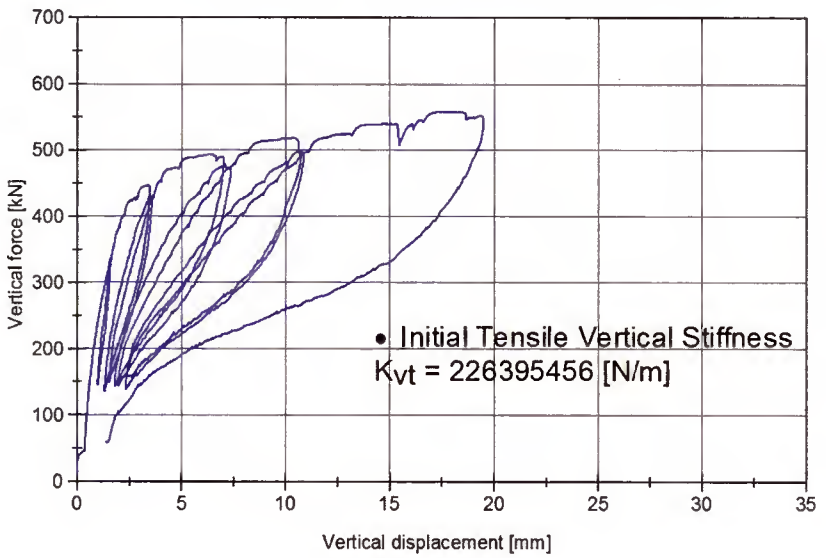

Type 2-05 Bearing

Tension and Shear Test

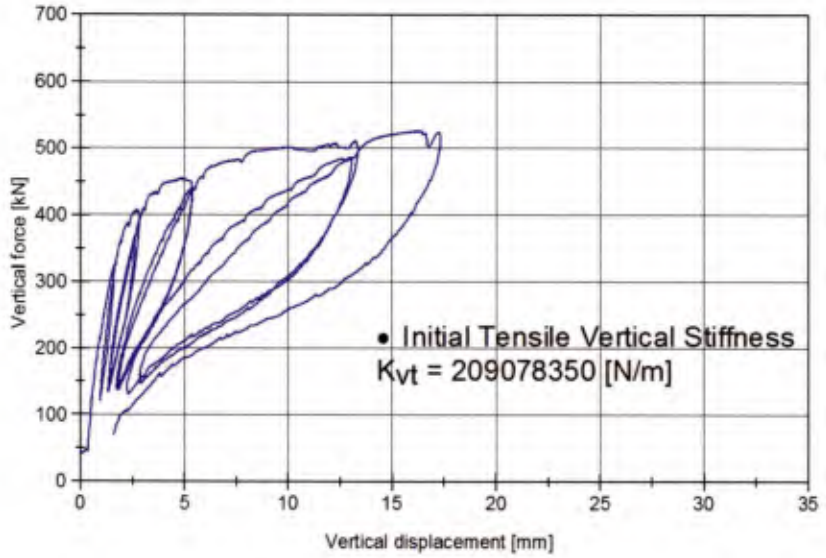

Type 2-06 Bearing

Tension and Shear Test

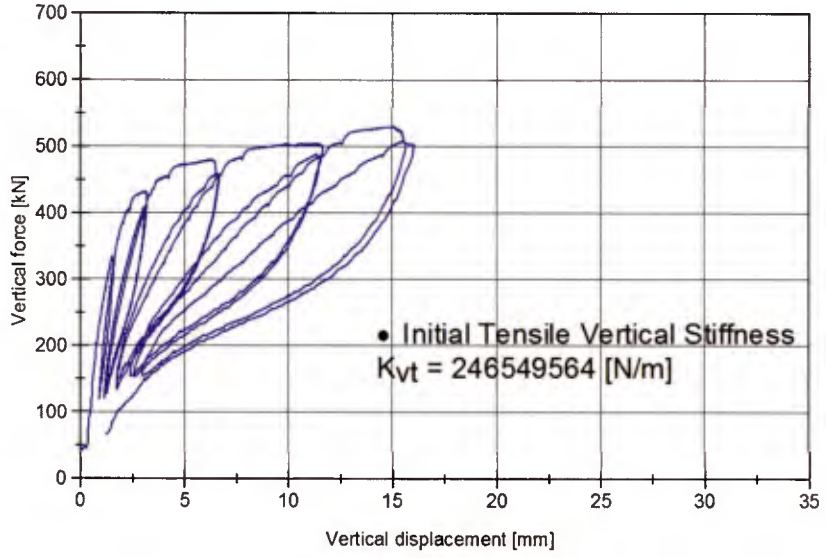

Appendix C – Results of the repeated property tests

Property Test - Type 1-01 Bearing

Compression Test

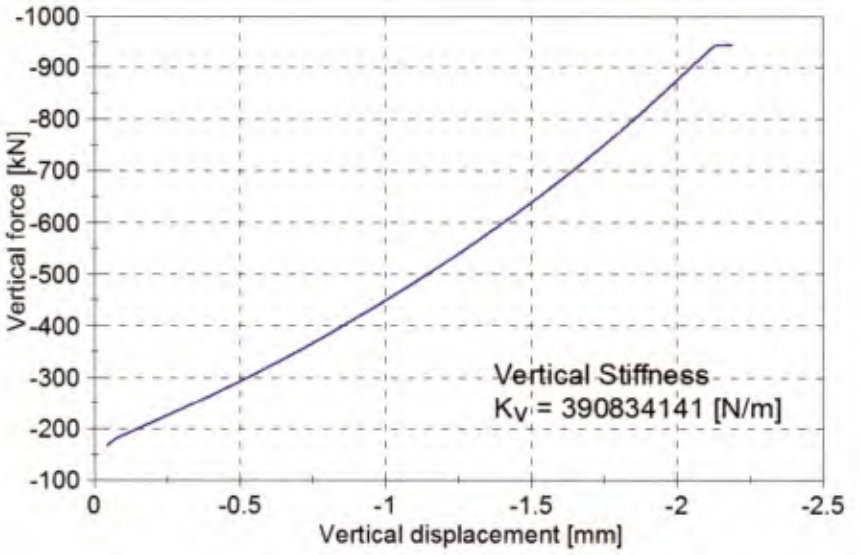

Property Test - Type 1-01 Bearing

Compression Shear Test - Cycle 9

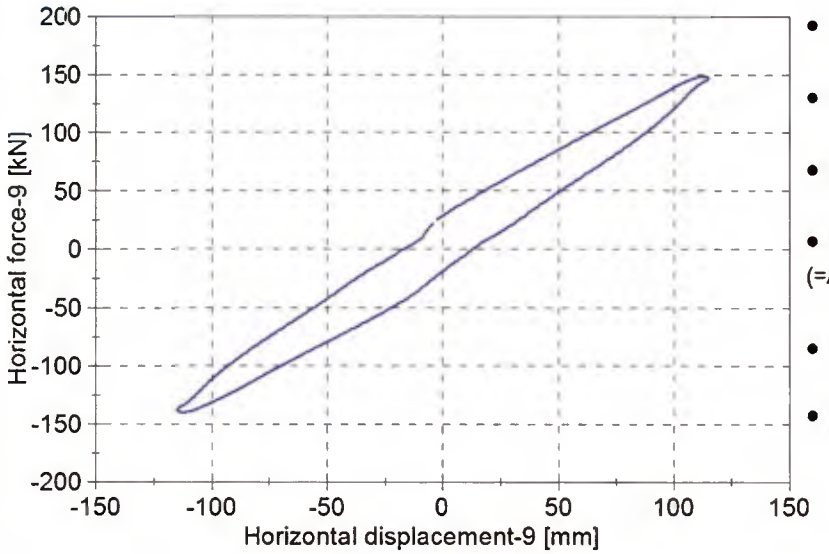

- Amplitude
  d_X = 0.1151 [m]
- Vertical Force
  N_S = -945000 [N]
- Max. Velocity
  v_{max} = 24.4 [mm/s]
- Dissipated Energy
  (=Area of the Hysteresis Loop)
  A_h = 7.2926 [kJ]
- Damping Coefficient
  c = 840000 [Ns/m]
- Horizontal Stiffness
  K_h = 1240000 [N/m]

Property Test - Type 1-02 Bearing

Compression Test

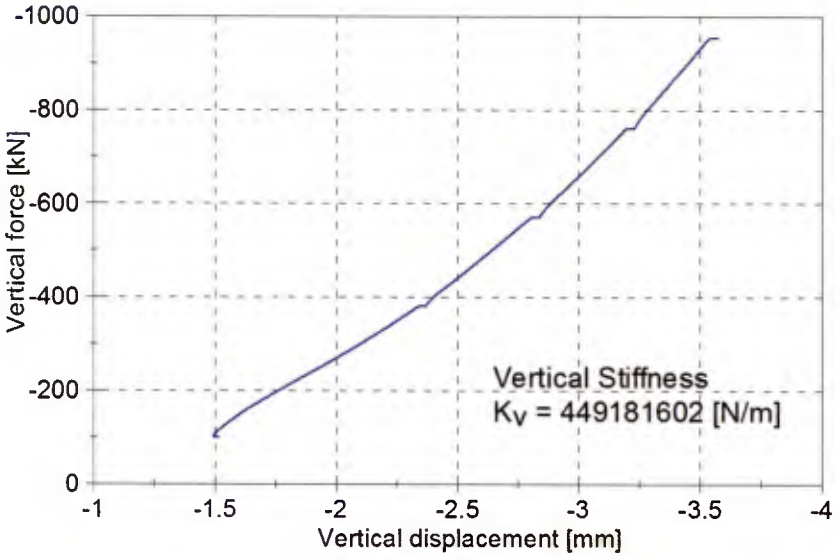

Property Test - Type 1-02 Bearing

Compression Shear Test - Cycle 9

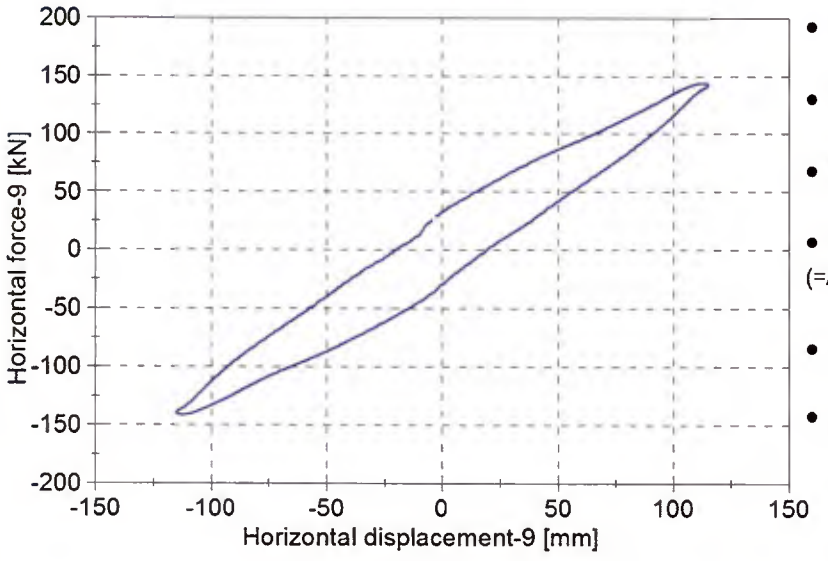

- Amplitude
  d_X = 0.115 [m]
- Vertical Force
  N_S = -955000 [N]
- Max. Velocity
  v_{max} = 24.2 [mm/s]
- Dissipated Energy
  (=Area of the Hysteresis Loop)
  A_h = 8.8842 [kJ]
- Damping Coefficient
  c = 1025000 [Ns/m]
- Horizontal Stiffness
  K_h = 1230000 [N/m]

Property Test - Type 1-04 Bearing

Compression Test

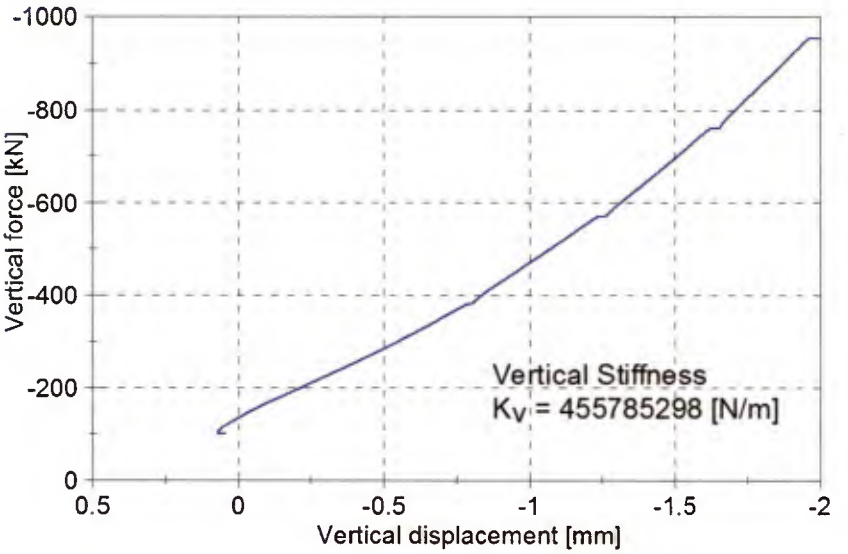

Property Test - Type 1-04 Bearing

Compression Shear Test - Cycle 9

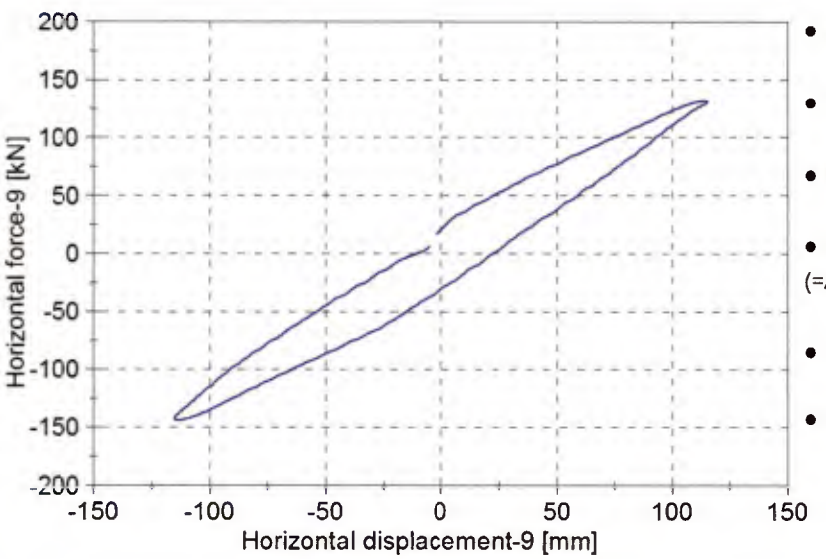

- Amplitude
  d_X = 0.1153 [m]
- Vertical Force
  N_S = -955000 [N]
- Max. Velocity
  v_{max} = 48.3 [mm/s]
- Dissipated Energy
  (=Area of the Hysteresis Loop)
  A_h = 7.5865 [kJ]
- Damping Coefficient
  c = 435000 [Ns/m]
- Horizontal Stiffness
  K_h = 1180000 [N/m]

Property Test - Type 1-05 Bearing

Compression Test

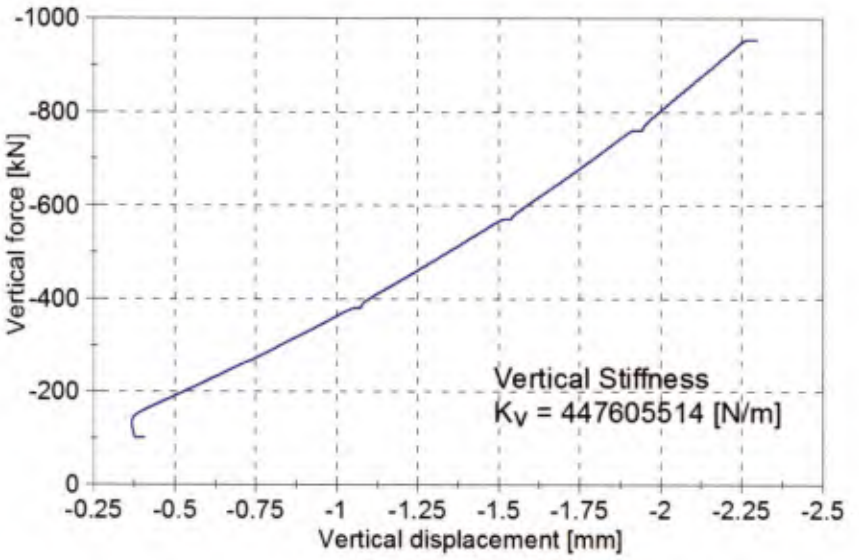

Property Test - Type 1-05 Bearing

Compression Shear Test - Cycle 9

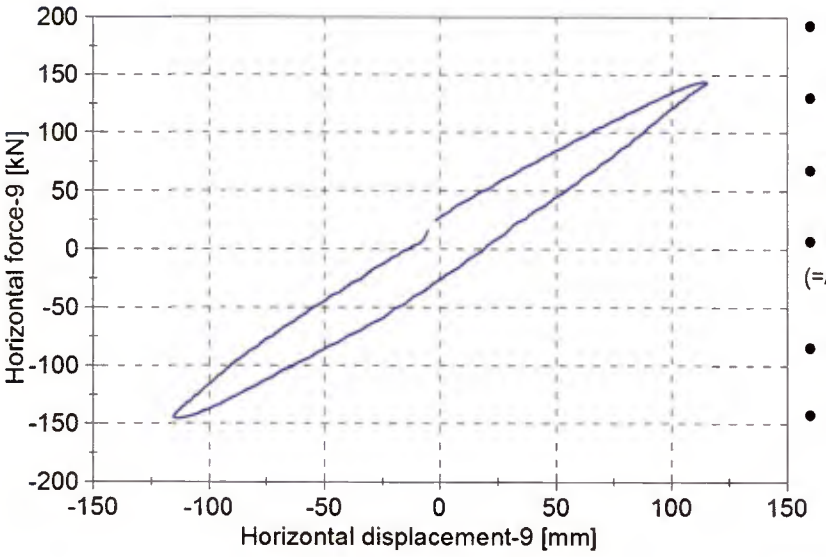

- Amplitude
  d_X = 0.1153 [m]
- Vertical Force
  N_S = -955000 [N]
- Max. Velocity
  v_{max} = 48.8 [mm/s]
- Dissipated Energy
  (=Area of the Hysteresis Loop)
  A_h = 7.639 [kJ]
- Damping Coefficient
  c = 438000 [Ns/m]
- Horizontal Stiffness
  K_h = 1240000 [N/m]

Property Test - Type 1-06 Bearing

Compression Test

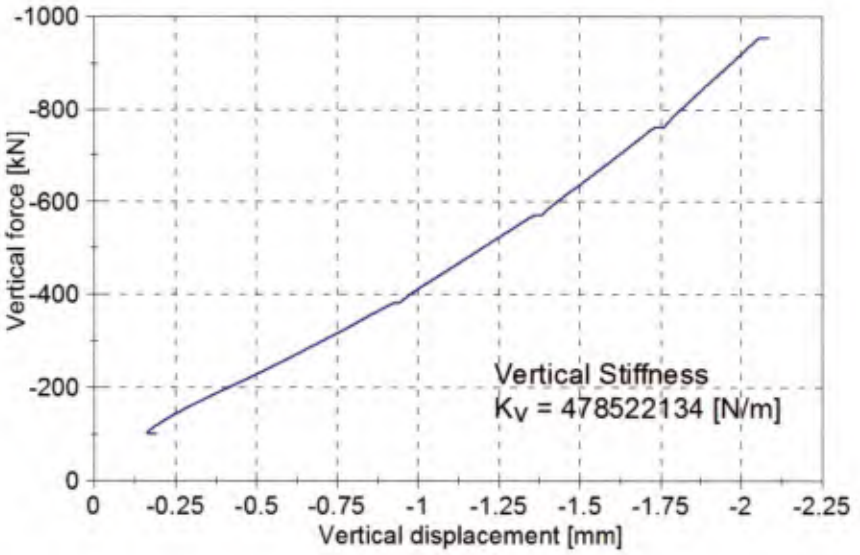

Property Test - Type 1-06 Bearing

Compression Shear Test - Cycle 9

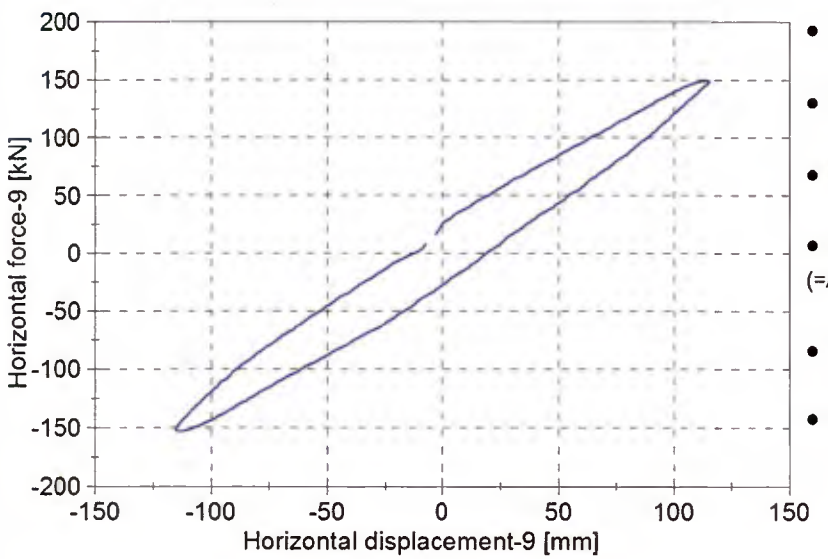

- Amplitude
  d_X = 0.1153 [m]
- Vertical Force
  N_S = -955000 [N]
- Max. Velocity
  v_{max} = 47.4 [mm/s]
- Dissipated Energy
  (=Area of the Hysteresis Loop)
  A_h = 7.8851 [kJ]
- Damping Coefficient
  c = 453000 [Ns/m]
- Horizontal Stiffness
  K_h = 1300000 [N/m]

Property Test - Type 1-07 Bearing

Compression Test

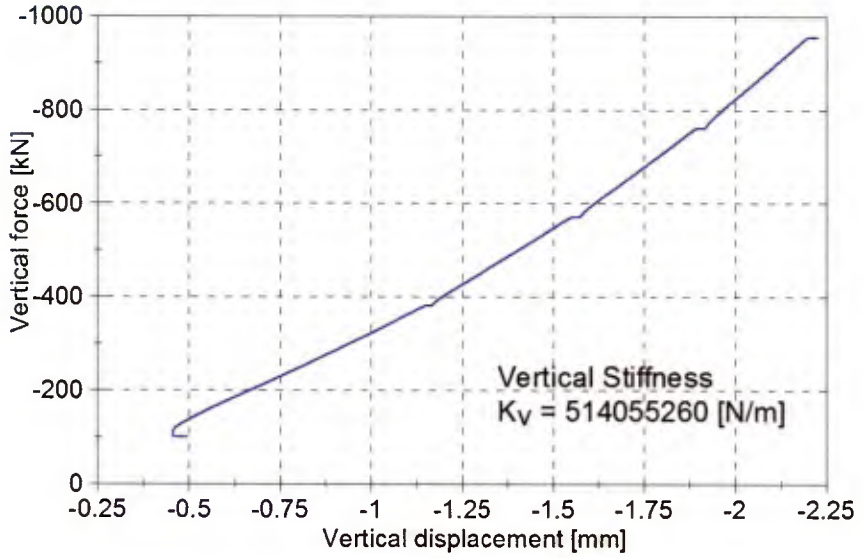

Property Test - Type 1-07 Bearing

Compression Shear Test - Cycle 9

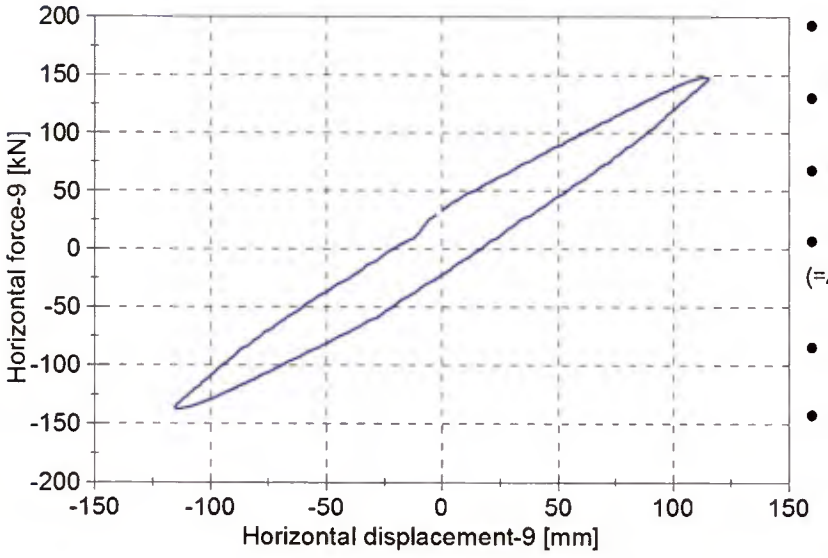

- Amplitude
  d_X = 0.1153 [m]
- Vertical Force
  N_S = -955000 [N]
- Max. Velocity
  v_{max} = 48.1 [mm/s]
- Dissipated Energy
  (=Area of the Hysteresis Loop)
  A_h = 8.287 [kJ]
- Damping Coefficient
  c = 476000 [Ns/m]
- Horizontal Stiffness
  K_h = 1230000 [N/m]

Property Test - Type 1-08 Bearing

Compression Test

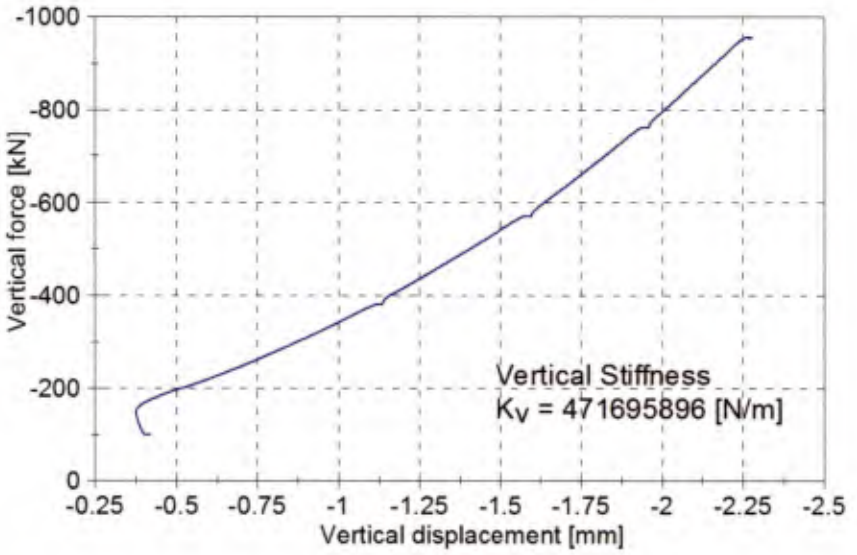

Property Test - Type 1-08 Bearing

Compression Shear Test - Cycle 9

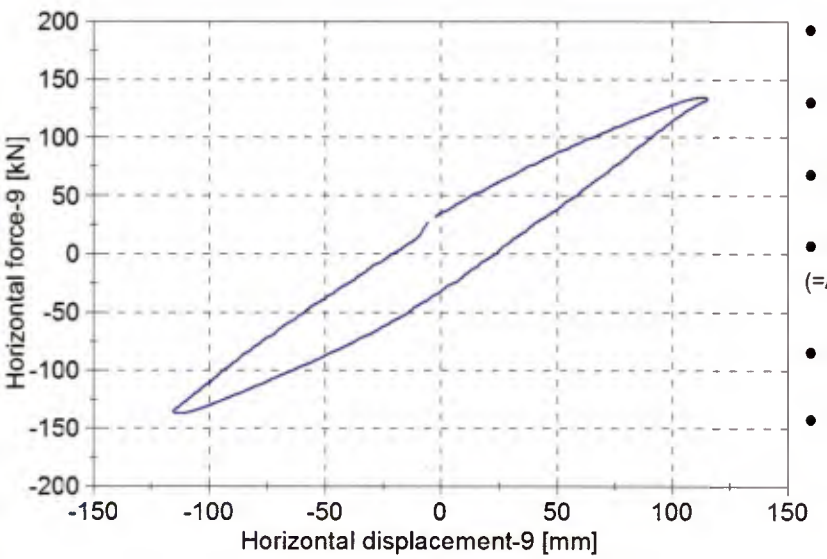

- Amplitude
  d_X = 0.1153 [m]
- Vertical Force
  N_S = -955000 [N]
- Max. Velocity
  v_{max} = 48.9 [mm/s]
- Dissipated Energy
  (=Area of the Hysteresis Loop)
  A_h = 9.0572 [kJ]
- Damping Coefficient
  c = 520000 [Ns/m]
- Horizontal Stiffness
  K_h = 1160000 [N/m]

Property Test - Type 1-09 Bearing

Compression Test

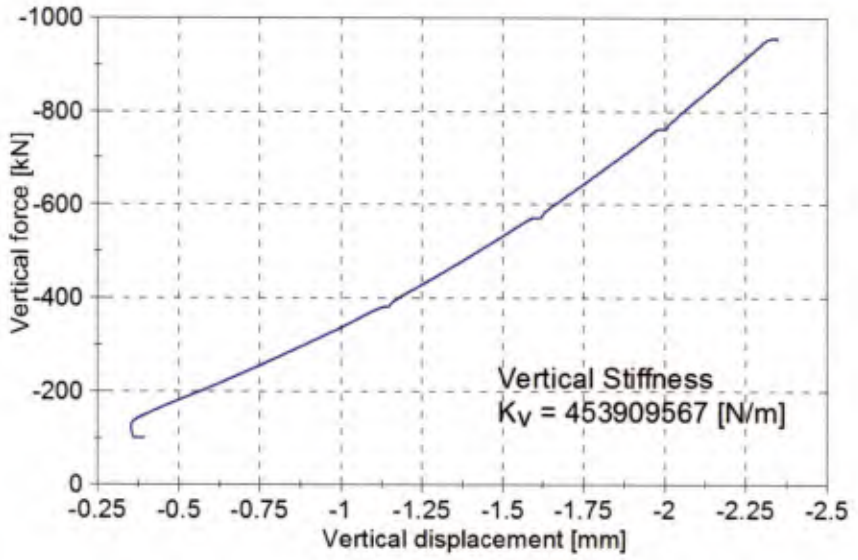

Property Test - Type 1-09 Bearing

Compression Shear Test - Cycle 9

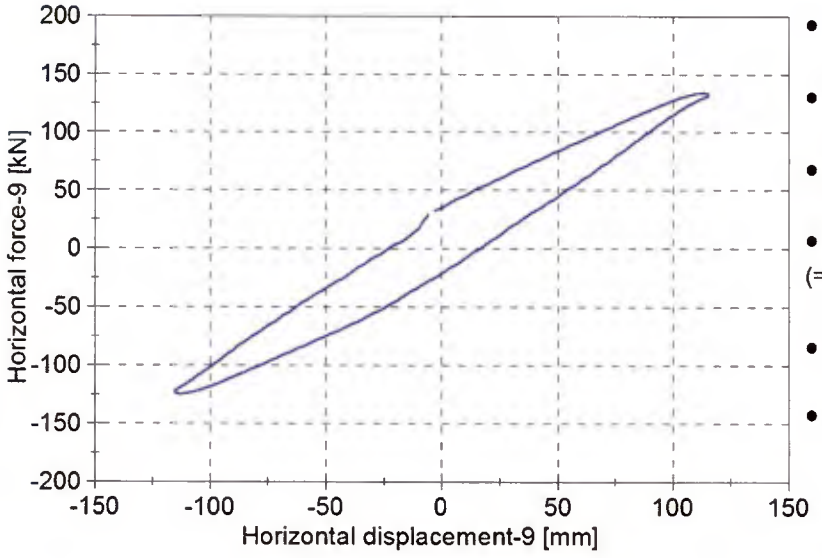

- Amplitude
  d_X = 0.1153 [m]
- Vertical Force
  N_S = -955000 [N]
- Max. Velocity
  v_{max} = 48.4 [mm/s]
- Dissipated Energy
  (=Area of the Hysteresis Loop)
  A_h = 7.539 [kJ]
- Damping Coefficient
  c = 433000 [Ns/m]
- Horizontal Stiffness
  K_h = 1110000 [N/m]

Property Test - Type 2-01 Bearing

Compression Test

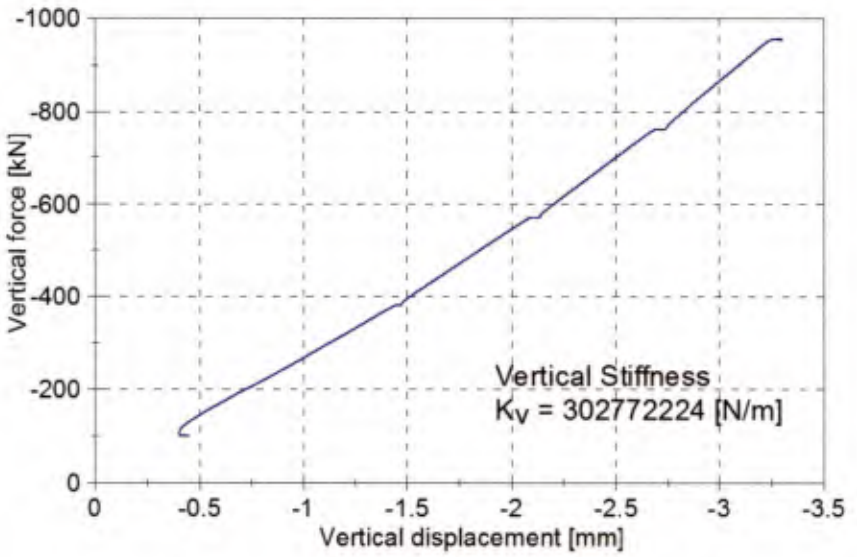

Property Test - Type 2-01 Bearing

Compression Shear Test - Cycle 9

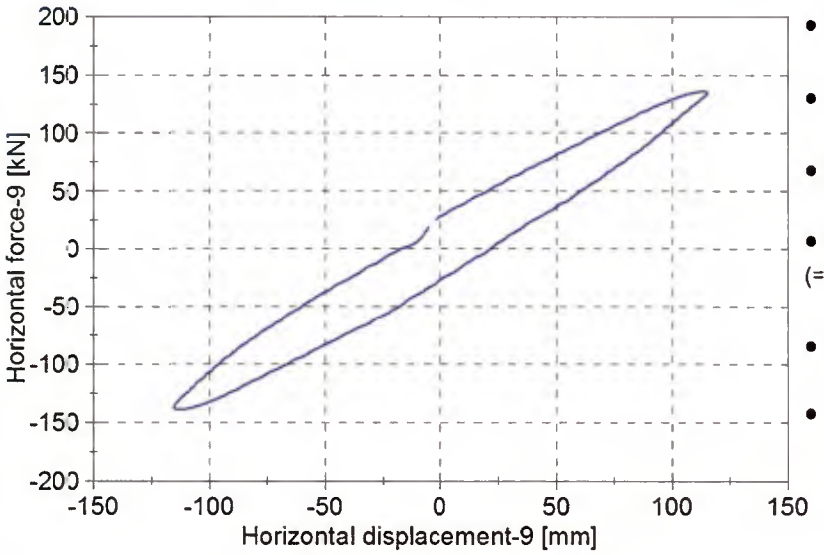

- Amplitude
  d_X = 0.1153 [m]
- Vertical Force
  N_S = -955000 [N]
- Max. Velocity
  v_{max} = 48.1 [mm/s]
- Dissipated Energy
  (=Area of the Hysteresis Loop)
  A_h = 8.6521 [kJ]
- Damping Coefficient
  c = 88000 [Ns/m]
- Horizontal Stiffness
  K_h = 1180000 [N/m]

Property Test - Type 2-02 Bearing

Compression Test

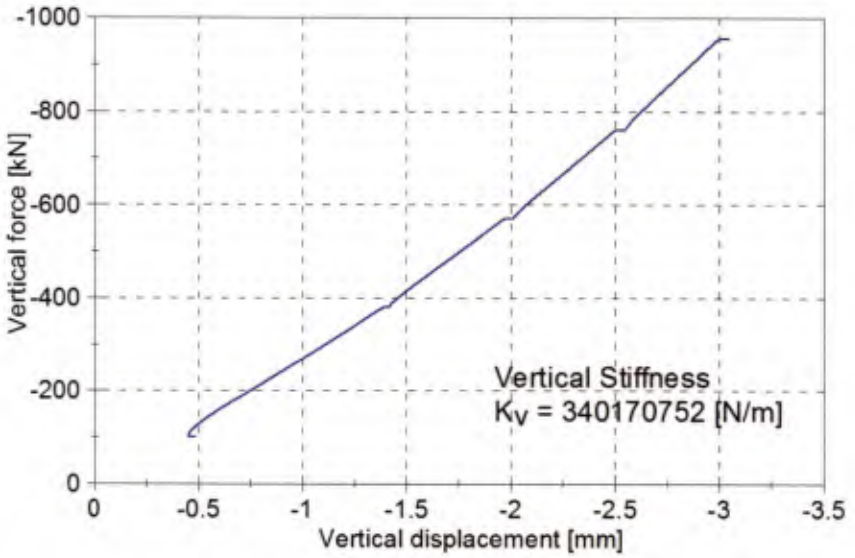

Property Test - Type 2-02 Bearing

Compression Shear Test - Cycle 9

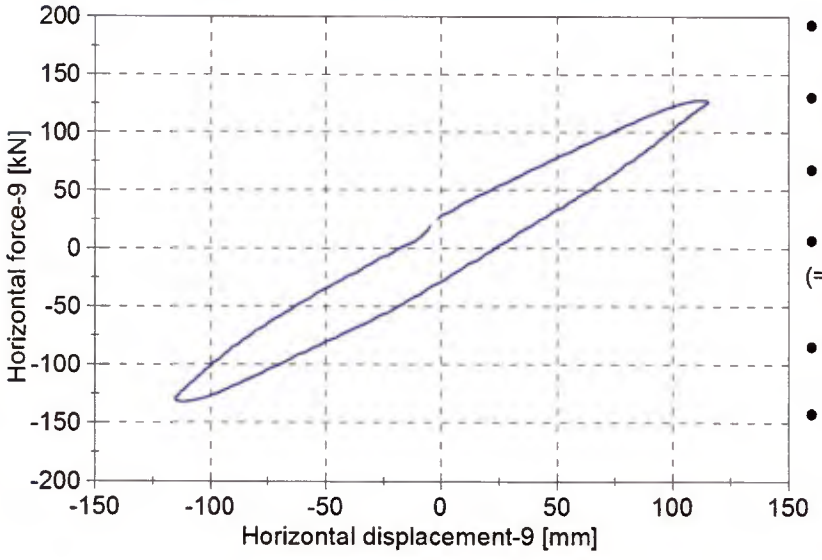

- Amplitude
  d_X = 0.1153 [m]
- Vertical Force
  N_S = -955000 [N]
- Max. Velocity
  v_{max} = 48.3 [mm/s]
- Dissipated Energy
  (=Area of the Hysteresis Loop)
  A_h = 8.7409 [kJ]
- Damping Coefficient
  c = 94000 [Ns/m]
- Horizontal Stiffness
  K_h = 1110000 [N/m]

Property Test - Type 2-03 Bearing

Compression Test

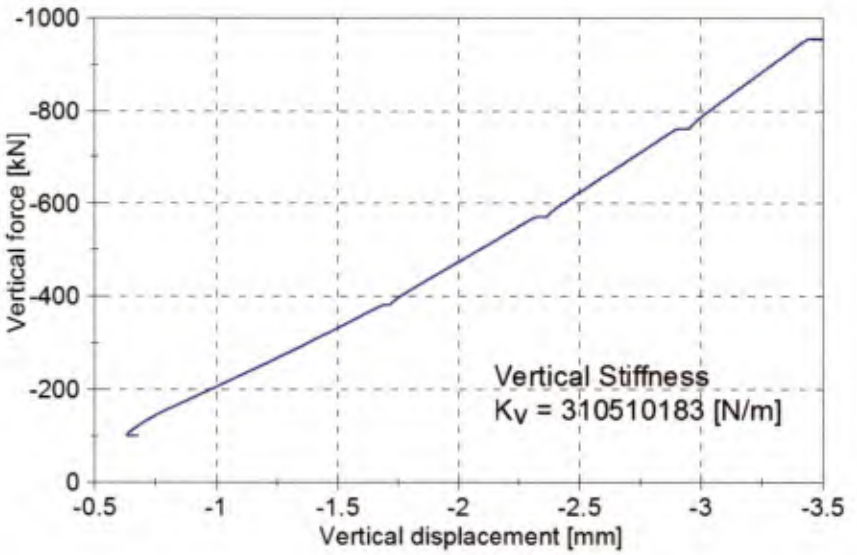

Property Test - Type 2-03 Bearing

Compression Shear Test - Cycle 9

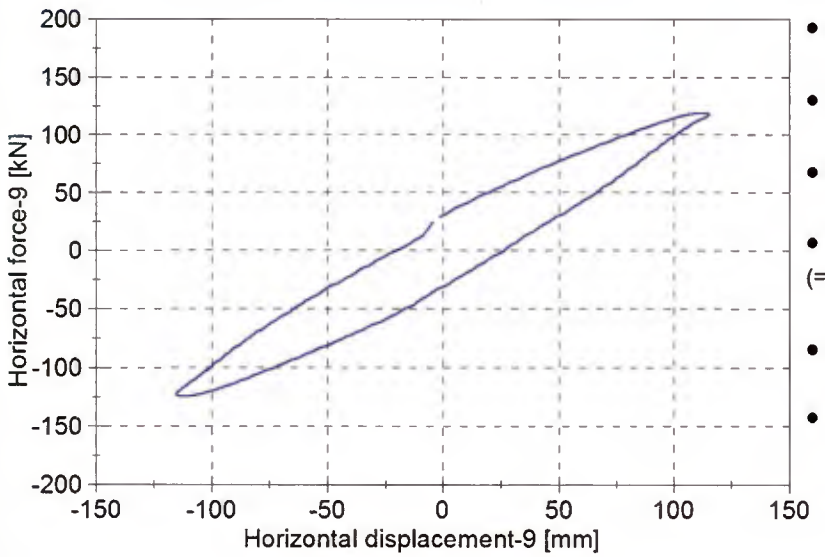

- Amplitude
  d_X = 0.1153 [m]
- Vertical Force
  N_S = -955000 [N]
- Max. Velocity
  v_{max} = 48.8 [mm/s]
- Dissipated Energy
  (=Area of the Hysteresis Loop)
  A_h = 8.9272 [kJ]
- Damping Coefficient
  c = 103000 [Ns/m]
- Horizontal Stiffness
  K_h = 1040000 [N/m]

Property Test - Type 2-04 Bearing

Compression Test

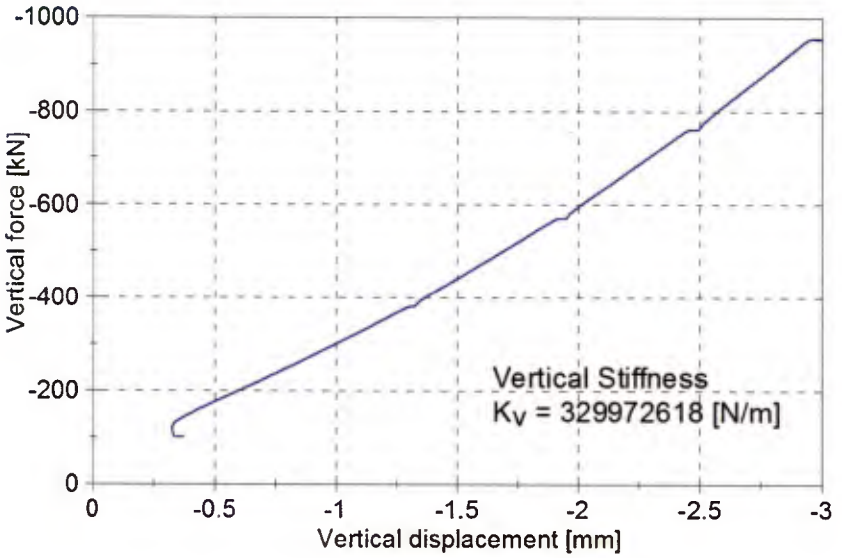

Property Test - Type 2-04 Bearing

Compression Shear Test - Cycle 9

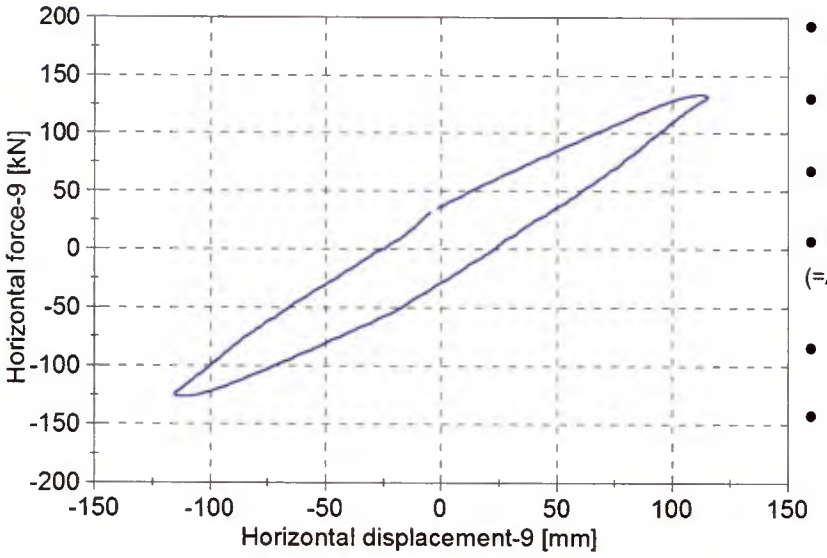

- Amplitude
  d_X = 0.1153 [m]
- Vertical Force
  N_S = -955000 [N]
- Max. Velocity
  v_{max} = 48.8 [mm/s]
- Dissipated Energy
  (=Area of the Hysteresis Loop)
  A_h = 9.5246 [kJ]
- Damping Coefficient
  c = 103000 [Ns/m]
- Horizontal Stiffness
  K_h = 1110000 [N/m]

Property Test - Type 2-05 Bearing

Compression Test

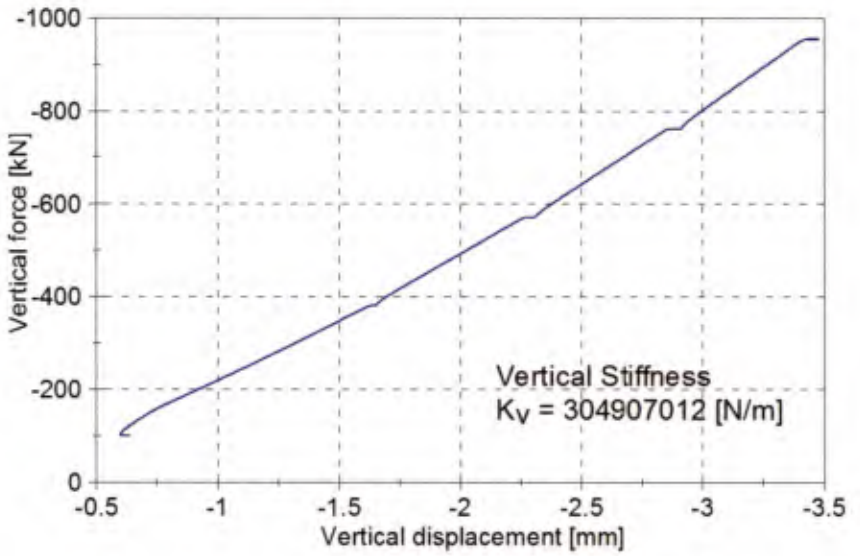

Property Test - Type 2-05 Bearing

Compression Shear Test - Cycle 9

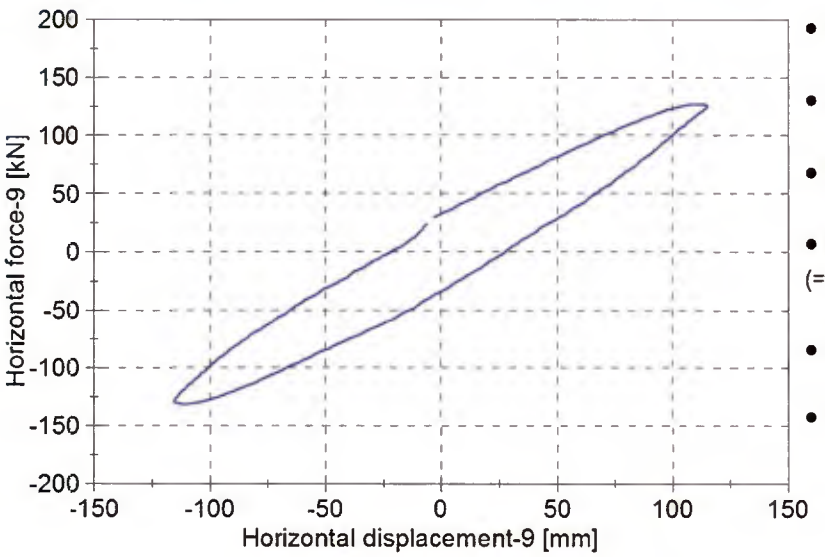

- Amplitude
  d_X = 0.1153 [m]
- Vertical Force
  N_S = -955000 [N]
- Max. Velocity
  v_{max} = 48.4 [mm/s]
- Dissipated Energy
  (=Area of the Hysteresis Loop)
  A_h = 10.2655 [kJ]
- Damping Coefficient
  c = 112000 [Ns/m]
- Horizontal Stiffness
  K_h = 1100000 [N/m]

Property Test - Type 2-06 Bearing

Compression Test

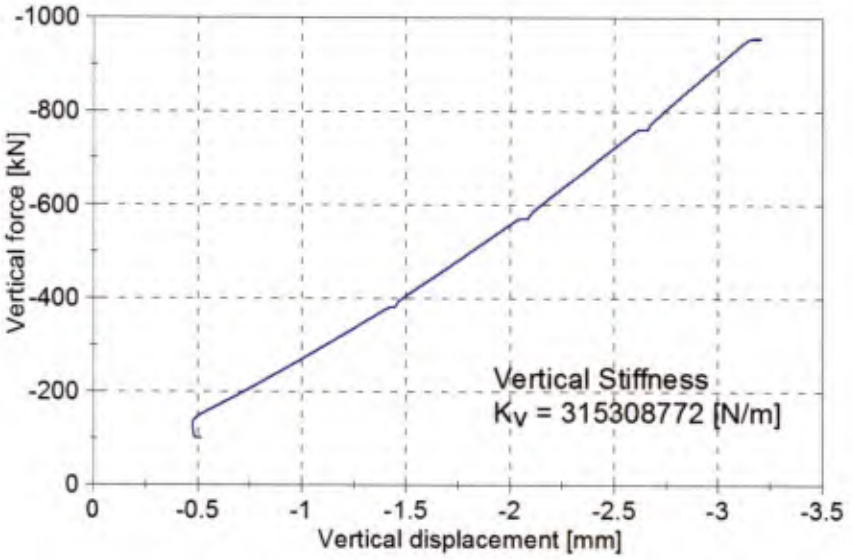

Property Test - Type 2-06 Bearing

Compression Shear Test - Cycle 9

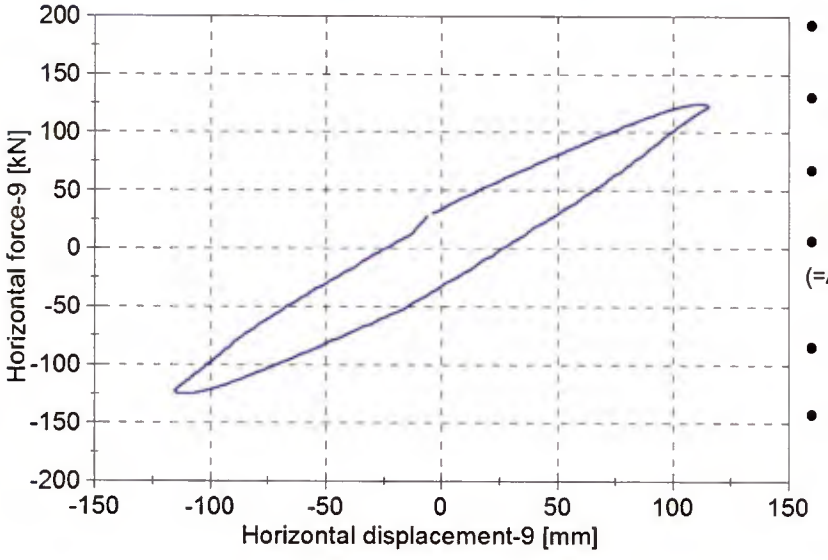

- Amplitude
  d_X = 0.1153 [m]
- Vertical Force
  N_S = -955000 [N]
- Max. Velocity
  v_{max} = 49 [mm/s]
- Dissipated Energy
  (=Area of the Hysteresis Loop)
  A_h = 9.9792 [kJ]
- Damping Coefficient
  c = 113000 [Ns/m]
- Horizontal Stiffness
  K_h = 1060000 [N/m]

Appendix D – Code of the modal superposition analysis in Chapter 7

```
Private Sub CommandButton1_Click()
'
Dim DOF, M, Ite As Integer
DOF = Range("B1").Value
Dim Mass(), Stiff(), StiffInv(), Temp(), IdMat(), Phi(), Ro() As Double
Dim MassS(), StiffInvS(), s(), x(), PhiM(), PhiMPhi() As Double
Dim x1(), x2(), y1(), y2() As Double
Dim OmegaN As Double
Dim Pi, Temp1, Temp2, Temp3, Comp, FacC, LastRo, Check As Double
Dim r(), LL(), Gamma() As Double
ReDim Mass(DOF, DOF), StiffInv(DOF, DOF), StiffInvS(DOF, DOF), x(DOF, DOF)
ReDim s(DOF, DOF), Phi(DOF, DOF), Ro(DOF), x1(DOF), x2(DOF), y1(DOF), y2(DOF)
ReDim Stiff(DOF, DOF), MassS(DOF, DOF), PhiM(DOF, DOF), PhiMPhi(DOF, DOF)
ReDim r(DOF), LL(DOF), Gamma(DOF), Temp(DOF, 2 * DOF), IdMat(DOF, DOF)
'
'Format
Range("F7:X46").ClearContents
Range("Z7:AR46").ClearContents
Range("H51:H70").ClearContents
Range("J51:J70").ClearContents
Range("L51:L70").ClearContents
Range("N51:N70").ClearContents
Range("P51:P70").ClearContents
Range("R51:R70").ClearContents
Range("B27:B46").ClearContents
'
'Calculate Isolation Stiffness
Pi = 3.14159265358979
Temp1 = 0
For i = 1 To DOF
   Temp1 = Temp1 + Cells(i + 6, 2)
Next i
Cells(27, 2) = Temp1 * 4 * (Pi / Cells(6, 2)) ^ 2
'Temp1 is the sum of all masses
'
'Vertical Stiffness
Cells(4, 2) = Temp1 * 9.8 / 0.002 / Cells(2, 4)
'
'Coarse estimation of the bearing's radius
Cells(4, 4) = Sqr(Temp1 * 9.8 / Cells(2, 4) / Cells(3, 4) / Pi) / 1000
'
'Determining the stiffness of the top floor, based on the period 0.5 sec
'If Cells(1, 2) > 7 Then
'   OmegaN = 10.472
'Else
'   OmegaN = 31.416
'End If
```

```
'
If DOF = 2 Then
   OmegaN = 2 * Pi / Cells(5, 2)
Else
   OmegaN = -1.221728 * DOF + 33.6851
End If
Cells(26 + DOF, 2) = OmegaN ^ 2 * Cells(6 + DOF, 2)
'
'Determining the stiffness of all other floors
FacC = Cells(26 + DOF, 2) / 100
Temp2 = ((Cells(5, 2) / (2 * Pi)) ^ 2) / Cells(8, 2)
Do
Temp3 = 0
   For i = 1 To DOF - 1
      Temp3 = Temp3 + 1 / (FacC * Cells(2, 2) / (DOF - 1) * (i - 1) _
      + Cells(26 + DOF, 2))
   Next i
   'MsgBox (Temp3)
   Comp = Abs(Temp2 / Temp3)
   FacC = FacC + Cells(26 + DOF, 2) / 100
Loop While Comp < 1
'
FacC = FacC - Cells(26 + DOF, 2) / 100
For i = DOF - 1 To 2 Step -1
   Cells(i + 26, 2) = Cells(26 + DOF, 2) + FacC * Cells(2, 2) _
   / (DOF - 1) * (DOF - i)
Next i
'
'Dunkerley's Estimation
Cells(48, 3) = Temp1 / Cells(27, 2)
Temp1 = 0
For i = 1 To DOF - 1
   Temp1 = Temp1 + Cells(i + 7, 2) / Cells(i + 27, 2)
Next i
Cells(48, 5) = Temp1
'
'Initializing in matrises
For i = 1 To DOF
   For j = 1 To DOF
      Cells(i + 7, j + 5) = 0
      Cells(i + 26, j + 5) = 0
      s(i, j) = 0
      PhiM(i, j) = 0
      PhiMPhi(i, j) = 0
   Next j
Next i
'Mass Matrix
For i = 1 To DOF
   Cells(i + 7, i + 5) = Cells(i + 6, 2)
```

```
Next i
'
For i = 1 To DOF
   For j = 1 To DOF
      Mass(i, j) = Cells(i + 7, j + 5)
   Next j
Next i
'
'Stiffness Matrix
For i = 1 To DOF - 1
   Cells(i + 26, i + 6) = -Cells(i + 27, 2)
   Cells(i + 26, i + 5) = Cells(i + 26, 2) + Cells(i + 27, 2)
Next i
Cells(DOF + 26, DOF + 5) = Cells(DOF + 26, 2)
Cells(DOF + 25, DOF + 5) = -Cells(DOF + 26, 2)
'
For i = 1 To DOF
   For j = 1 To DOF
      Cells(j + 26, i + 5) = Cells(i + 26, j + 5)
   Next j
Next i
'
For i = 1 To DOF
   For j = 1 To DOF
      Stiff(i, j) = Cells(i + 26, j + 5)
      Temp(i, j) = Cells(i + 26, j + 5)
      If i = j Then
         IdMat(i, j) = 1
      Else
         IdMat(i, j) = 0
      End If
   Next j
Next i
'
For i = 1 To DOF
   For j = DOF + 1 To 2 * DOF
      Temp(i, j) = IdMat(i, j - DOF)
   Next j
Next i
'
M = 0
Do
   l = 1
   For i = 2 + M To DOF
      For j = 2 * DOF To 1 Step -1
         Temp(i, j) = _
         Temp(i, j) - Temp(i - l, j) * Temp(i, i - l) / Temp(i - l, i - l)
      Next j
      l = l + 1
```

```
    Next i
    M = M + 1
Loop Until M = DOF - 1
'
M = 1
Do
    l = 1
    For i = DOF - M To 1 Step -1
        For j = 2 * DOF To 1 Step -1
            Temp(i, j) = _
            Temp(i, j) - Temp(i + l, j) * Temp(i, i + l) / Temp(i + l, i + l)
        Next j
        l = l + 1
    Next i
    M = M + 1
Loop Until M = DOF
'
For i = 1 To DOF
    For j = 2 * DOF To 1 Step -1
        Temp(i, j) = Temp(i, j) / Temp(i, i)
    Next j
Next i
'
For i = 1 To DOF
    For j = 1 To DOF
        StiffInv(i, j) = Temp(i, j + DOF)
    Next j
Next i
'
'    Range("F8:L14").Select
'    With Selection.Interior
'        .Pattern = xlSolid
'        .PatternColorIndex = xlAutomatic
'        .Color = 5296274
'        .TintAndShade = 0
'        .PatternTintAndShade = 0
'    End With
'
'Initializing arrays befor iteration
For i = 1 To DOF
    x1(i) = 1
    y1(i) = 0
    x2(i) = 0
    y2(i) = 0
Next i
'
'Calculation of the last mode
LastRo = 0.1
'
```

```
For i = 1 To DOF
   For j = 1 To DOF
      y1(i) = y1(i) + Mass(i, j) * x1(j)
   Next j
Next i
'
Do
   For i = 1 To DOF
      Temp1 = x2(i)
      For j = 1 To DOF
         x2(i) = x2(i) + y1(j) * StiffInv(i, j)
      Next j
      x2(i) = x2(i) - Temp1
   Next i
'
   For i = 1 To DOF
      Temp1 = y2(i)
      For j = 1 To DOF
         y2(i) = y2(i) + Mass(i, j) * x2(j)
      Next j
      y2(i) = y2(i) - Temp1
   Next i
'
   Ro(1) = 0
   Temp1 = 0
   For i = 1 To DOF
      Ro(1) = Ro(1) + x2(i) * y1(i)
      Temp1 = Temp1 + x2(i) * y2(i)
   Next i
   '
   For i = 1 To DOF
      y2(i) = y2(i) / (Temp1) ^ 0.5
   Next i
   '
   For i = 1 To DOF
      y1(i) = y2(i)
   Next i
   '
   Ro(1) = Ro(1) / Temp1
   Check = Abs(Ro(1) - LastRo) / Ro(1)
   LastRo = Ro(1)
   '
Loop While Check > 10 ^ -22
'MsgBox (Check)
'
Temp1 = 0
For i = 1 To DOF
   Phi(i, 1) = x2(i)
   Temp1 = Temp1 + x2(i) * y2(i)
```

```
Next i
For i = 1 To DOF
   Phi(i, 1) = Phi(i, 1) / (Temp1) ^ 0.5
Next i
'
'Building up the sweep matrix for the next modes
'
N = 1
'n=number of equations for the sweeping matrix
Do
   For i = 1 To DOF
      s(i, i) = 1
   Next i
   '
   l = 1
   For i = 1 To N
      For j = 1 To DOF
         x(i, j) = Mass(j, j) * Phi(j, l)
      Next j
      l = l + 1
   Next i
   '
      'For i = 1 To DOF
      '   For j = 1 To DOF
      '      Cells(i + 26, j + 15) = X(i, j)
      '   Next j
      'Next i
      '
   If N = 1 Then
      For i = 2 To DOF
         s(1, i) = -Mass(i, i) / Mass(1, 1) * Phi(i, 1) / Phi(1, 1)
      Next i
      s(1, 1) = 0
      '
   Else
      'Triangulizing X matrix
      M = 0
      Do
         l = 1
         For i = 2 + M To N
            For j = DOF To 1 Step -1
               x(i, j) = _
               x(i, j) - x(i - l, j) * x(i, i - l) / x(i - l, i - l)
            Next j
            l = l + 1
         Next i
         M = M + 1
      Loop Until M = N - 1
      '
```

```
    'Diagonalizing X matrix
    M = 1
    Do
      l = 1
      For i = N - M To 1 Step -1
        For j = DOF To 1 Step -1
          x(i, j) = x(i, j) - x(i + l, j) * x(i, i + l) / x(i + l, i + l)
        Next j
        l = l + 1
      Next i
      M = M + 1
    Loop Until M = N
    '
    For i = 1 To N
      For j = DOF To 1 Step -1
        x(i, j) = x(i, j) / x(i, i)
      Next j
    Next i
    '
    For i = 1 To N
      For j = N To DOF
        s(i, j) = -x(i, j)
      Next j
    Next i
    '
    For i = 1 To DOF
      For j = 1 To N
        s(i, j) = 0
      Next j
    Next i
    '
  End If
'
  For i = 1 To DOF
    For j = 1 To DOF
      MassS(i, j) = 0
      StiffInvS(i, j) = 0
    Next j
  Next i
'
  For i = 1 To DOF
    For j = 1 To DOF
      For l = 1 To DOF
        MassS(i, j) = MassS(i, j) + Mass(i, l) * s(l, j)
        StiffInvS(i, j) = StiffInvS(i, j) + StiffInv(i, l) * s(l, j)
      Next l
    Next j
  Next i
'
```

```
'Initializing arrays before iteration
   For i = 1 To DOF
      x1(i) = 1
      y1(i) = 0
      x2(i) = 0
      y2(i) = 0
   Next i
'
'Start iteration for all previous modes
'
   LastRo = 0.1
'
   For i = 1 To DOF
      For j = 1 To DOF
         y1(i) = y1(i) + MassS(i, j) * x1(j)
      Next j
   Next i
'
   Ite = 1
   Do
      For i = 1 To DOF
         Temp1 = x2(i)
         For j = 1 To DOF
            x2(i) = x2(i) + y1(j) * StiffInvS(i, j)
         Next j
         x2(i) = x2(i) - Temp1
      Next i
'
      For i = 1 To DOF
         Temp1 = y2(i)
         For j = 1 To DOF
            y2(i) = y2(i) + MassS(i, j) * x2(j)
         Next j
         y2(i) = y2(i) - Temp1
         'MsgBox (y2(i))
      Next i
'
      Ro(N + 1) = 0
      Temp1 = 0
      For i = 1 To DOF
         Ro(N + 1) = Ro(N + 1) + x2(i) * y1(i)
         Temp1 = Temp1 + x2(i) * y2(i)
      Next i
   '
      If Temp1 < 0 Then
         Exit Do
      End If
      '
      For i = 1 To DOF
```

```
      y2(i) = y2(i) / (Temp1) ^ 0.5
    Next i
  '
    For i = 1 To DOF
      y1(i) = y2(i)
    Next i
    Ro(N + 1) = Ro(N + 1) / Temp1
    Check = Abs(Ro(N + 1) - LastRo) / Ro(N + 1)
    LastRo = Ro(N + 1)
    'MsgBox (Check)
    Ite = Ite + 1
    If Ite > 5000 Then
      Exit Do
    End If
  Loop While Check > 10 ^ -20
'  MsgBox (Check)
'
  If Temp1 < 0 Then
    Exit Do
  End If
  '
  Temp1 = 0
  For i = 1 To DOF
    Phi(i, N + 1) = x2(i)
    Temp1 = Temp1 + x2(i) * y2(i)
  Next i
  'MsgBox (Temp1)
  For i = 1 To DOF
    Phi(i, N + 1) = Phi(i, N + 1) / (Temp1) ^ 0.5
  Next i
'
  N = N + 1
Loop Until N = DOF
'
'For i = 1 To DOF
'   For j = DOF To 1 Step -1
'      Phi(j, i) = Phi(j, i) / Phi(1, i)
'   Next j
'Next i
'
'Output shape modes and Omega values
l = 7
For i = 1 To 3
  For j = 1 To DOF
    Cells(j + 50, i + l) = Phi(j, i)
  Next j
  Cells(48, i + l) = Ro(i)
  l = l + 1
Next i
```

```
'
'Building up the effective mass matrix
For i = 1 To DOF
   For j = 1 To DOF
      PhiM(i, j) = Phi(j, i) * Mass(j, j)
      Cells(i + 7, j + 25) = PhiM(i, j)
   Next j
Next i
'
For i = 1 To DOF
   For j = 1 To DOF
      PhiMPhi(i, j) = 0
   Next j
   LL(i) = 0
Next i
'
For i = 1 To DOF
   For j = 1 To DOF
      For l = 1 To DOF
         PhiMPhi(i, j) = PhiMPhi(i, j) + PhiM(j, l) * Phi(l, i)
      Next l
      Cells(i + 26, j + 25) = PhiMPhi(i, j)
   Next j
Next i
'
'Influence vector, all values are set to 1
For i = 1 To DOF
   r(i) = 1
   Cells(i + 50, 14) = r(i)
Next i
'
For i = 1 To DOF
   For j = 1 To DOF
      LL(i) = LL(i) + r(j) * PhiM(i, j)
   Next j
   Cells(i + 50, 16) = LL(i)
Next i
'
For i = 1 To DOF
   If PhiMPhi(i, i) = 0 Then
      Exit For
   End If
   Gamma(i) = LL(i) / PhiMPhi(i, i)
   Cells(i + 50, 18) = Gamma(i)
Next i
'
End Sub
-----------------------------------------------------------------------------------------------------------------
Private Sub CommandButton2_Click()
```

```
'
Dim DOF, k As Integer
DOF = Range("B1").Value
Dim T(), u(), s(), f(), SRSS(), SumS(), SumF() As Double
Dim V, M, DeltaM, Alpha As Double
ReDim T(3), u(DOF, DOF), s(DOF, DOF), f(DOF, DOF)
ReDim SRSS(DOF), SumS(DOF), SumF(DOF)
'
'Format
Range("H75:H140").ClearContents
Range("J75:J140").ClearContents
Range("L75:L140").ClearContents
Range("N75:N140").ClearContents
'
T(1) = 2 * 3.14159265 / Range("H49").Value
T(2) = 2 * 3.14159265 / Range("J49").Value
T(3) = 2 * 3.14159265 / Range("L49").Value
'
For i = 71 To 670
   Comp = T(3) - Cells(i, 1)
   If Comp < 0.01 Then
      'Always 5% damping is assumed
      Range("L74").Value = Cells(i, 2) / 100
      Exit For
   End If
Next i
'
For j = i To 670
   Comp = T(2) - Cells(j, 1)
   If Comp < 0.01 Then
      'Always 5% damping is assumed
      Range("J74").Value = Cells(j, 2) / 100
      Exit For
   End If
Next j
'
For k = j To 670
   Comp = T(1) - Cells(k, 1)
   If Comp < 0.01 Then
      If Range("H73").Value = 5 Then
         Range("H74").Value = Cells(k, 2) / 100
      ElseIf Range("H73").Value = 10 Then
         Range("H74").Value = Cells(k, 3) / 100
      ElseIf Range("H73").Value = 20 Then
         Range("H74").Value = Cells(k, 4) / 100
      ElseIf Range("H73").Value = 30 Then
         Range("H74").Value = Cells(k, 5) / 100
      Else
         MsgBox "Not defined!"
```

```
      End If
      Exit For
   End If
Next k
'
'Output deformation
l = 8
For i = 1 To 3
   For j = 1 To DOF
      u(j, i) = Cells(j + 50, l) * Cells(74, l) _
         * Cells(i + 50, 18) / Cells(48, l)
      Cells(j + 74, l) = u(j, i)
   Next j
   l = l + 2
Next i
'
For i = 1 To DOF
   For j = 1 To 3
      SRSS(i) = SRSS(i) + u(i, j) ^ 2
   Next j
   SRSS(i) = Sqr(SRSS(i))
   Cells(i + 74, 14) = SRSS(i)
Next i
'
'Diagram
ActiveSheet.ChartObjects("Diagramm 1").Activate
ActiveChart.PlotArea.Select
ActiveChart.SeriesCollection(1).XValues = "='MDOF-inv2'!N75:N" & 74 + DOF
ActiveChart.SeriesCollection(1).Values = "='MDOF-inv2'!F75:F" & 74 + DOF
'
'Output modal masses
l = 8
For i = 1 To 3
   For j = 1 To DOF
      s(j, i) = _
      Cells(j + 50, l) * Cells(j + 7, j + 5) _
      * Cells(i + 50, 18)
      Cells(j + 95, l) = s(j, i)
   Next j
   l = l + 2
Next i
'
For i = 1 To DOF
   For j = 1 To 3
      SumS(i) = SumS(i) + s(i, j)
   Next j
   Cells(i + 95, 14) = SumS(i)
Next i
'
```

```
'Output modal forces
l = 8
For i = 1 To 3
   For j = 1 To DOF
      f(j, i) = s(j, i) * Cells(74, l)
      Cells(j + 116, l) = f(j, i)
   Next j
   l = l + 2
Next i
'
For i = 1 To DOF
   For j = 1 To 3
      SumF(i) = SumF(i) + f(i, j)
   Next j
   Cells(i + 116, 14) = SumF(i)
Next i
'
'Output base shear Vb1, Vb2, Vb3
l = 0
For i = 1 To 3
   For j = 1 To DOF
      V = V + f(j, i)
   Next j
   Cells(117, 17 + l) = V
   l = l + 2
   V = 0
Next i
'
'Output total base shear SRSS
V = (Cells(117, 17)) ^ 2 + (Cells(117, 19)) ^ 2 + (Cells(117, 21)) ^ 2
V = Sqr(V)
Cells(118, 17) = V
'
'Base shear coefficient
For i = 1 To DOF
   Alpha = Alpha + Cells(i + 6, 2)
Next i
'
Alpha = V / Alpha / 9.8
Cells(119, 17) = Alpha
'
'Output moment
h = Cells(7, 4)
l = 0
For i = 1 To 3
   For j = 1 To DOF
      If j = 1 Then
         M = M + f(j, i) * h
      Else
```

```
            M = M + f(j, i) * (j - 1) * ((Cells(2, 2)) / (DOF - 1) + h)
        End If
    Next j
    Cells(120, 17 + l) = M
    l = l + 2
    M = 0
Next i
'
M = (Cells(120, 17)) ^ 2 + (Cells(120, 19)) ^ 2 + (Cells(120, 21)) ^ 2
Cells(121, 17) = Sqr(M)
'
'Output Delta moment
DeltaM = 0
For i = 2 To DOF
    DeltaM = DeltaM + (SRSS(i) - SRSS(1)) * Cells(i + 7, 2) * 9.8
Next i
'
Cells(121, 23) = DeltaM
'
'Uplift
If Cells(2, 4) = 2 Or Cells(2, 4) = 3 Then
    Cells(122, 17) = Cells(121, 17) / Cells(3, 2)
ElseIf Cells(2, 4) = 4 Then
    Cells(122, 17) = 12 / 13 * Cells(121, 17) / Cells(3, 2)
ElseIf Cells(2, 4) = 5 Then
    Cells(122, 17) = 4 / 5 * Cells(121, 17) / Cells(3, 2)
Else
    MsgBox ("No. of spring should be L.E. 5")
End If
'
'Uplift with delta effect
If Cells(2, 4) = 2 Or Cells(2, 4) = 3 Then
    Cells(122, 25) = Cells(121, 25) / Cells(3, 2)
ElseIf Cells(2, 4) = 4 Then
    Cells(122, 25) = 12 / 13 * Cells(121, 25) / Cells(3, 2)
ElseIf Cells(2, 4) = 5 Then
    Cells(122, 25) = 4 / 5 * Cells(121, 25) / Cells(3, 2)
Else
    MsgBox ("No. of spring should be L.E. 5")
End If
'
End Sub
```

0	584.7362093	584.736209	584.7362093	584.736209
0.02	718.868226	683.134726	645.1225605	625.835287
0.03	754.8988266	705.218492	644.6770425	618.880764
0.04	764.5267004	652.126097	603.7822451	579.748268
0.05	832.5274198	728.289382	639.3281739	599.751016
0.06	661.6616827	693.990831	676.2873655	651.287986
0.07	923.919671	794.962499	716.464366	684.624946
0.08	889.1939964	815.217495	728.6937434	707.586548
0.09	1129.834416	878.015833	758.3794914	733.250658
0.1	1164.863003	928.312575	815.9909932	763.556074
0.11	1114.149802	946.242563	856.5332424	790.878505
0.12	1110.062856	995.235761	889.1729016	812.391751
0.13	1248.29421	1053.94036	913.5541673	827.68333
0.14	998.5253742	1006.63187	930.963412	836.327794
0.15	1197.659936	1103.55181	952.9788712	837.936458
0.16	1506.147588	1238.12095	967.7035446	828.482058
0.17	1581.687819	1287.50389	955.9643012	804.792061
0.18	1627.352825	1272.69498	912.162357	766.519641
0.19	1577.370506	1192.34076	840.2447063	716.377426
0.2	1432.191385	1052.10419	748.7786944	673.653175
0.21	1263.878232	973.652798	702.8434119	662.097926
0.22	1202.425222	930.189176	683.3617436	649.578263
0.23	1106.642915	859.065186	679.1719524	636.810889
0.24	1023.338211	794.878848	686.8659316	624.443383
0.25	939.9056383	825.368198	690.4117356	617.156617
0.26	999.5440945	843.875946	688.2151427	611.694957
0.27	1006.663135	842.163742	679.8458509	603.373935
0.28	968.7650957	821.165265	666.4590263	592.524461
0.29	908.9016069	787.929926	648.629591	579.589178
0.3	848.7344091	750.202286	627.7440251	565.476168
0.31	830.7347054	712.356102	605.1194336	554.314674
0.32	762.8282005	675.974943	581.7312016	547.103182
0.33	743.6943936	640.873415	558.2277679	540.709157
0.34	695.586624	606.158561	535.0572754	535.316062
0.35	658.8586939	597.08903	519.7865329	531.013973
0.36	660.9972673	599.53094	518.7491636	527.794718
0.37	695.1193141	604.702837	522.0559029	525.574117
0.38	733.7511276	609.055978	528.6755092	523.859453
0.39	757.9465083	608.519538	536.9374474	522.248671
0.4	762.9909083	618.241421	544.9889663	520.323133
0.41	848.8157543	665.574366	551.2226134	517.859708
0.42	914.5071016	696.592053	554.2659861	514.621374
0.43	937.1930818	708.460235	553.2760419	510.248703
0.44	920.4877276	702.321815	548.4966855	504.987515
0.45	872.6956873	681.081226	540.0186791	498.633264
0.46	803.166204	649.68376	528.5505097	491.562491
0.47	722.0456026	612.895266	514.8447527	483.623016
0.48	640.2853803	575.324853	499.8544826	475.06352
0.49	568.9437576	540.419881	484.003598	466.207654
0.5	535.9317406	509.742447	467.5297956	456.437058
0.51	542.7867299	485.640857	451.1211592	447.324719
0.52	549.1864358	487.941194	434.9622208	438.204066
0.53	567.2203413	507.803137	439.2284876	429.228219
0.54	593.7257009	526.540854	448.3628752	420.53505
0.55	618.3385446	542.868458	456.5126444	416.989736
0.56	640.3866428	557.475227	463.5554859	420.278487
0.57	659.431948	569.529396	469.1328247	422.967431

meff1	2802205.484	meff2	41679.9422	meff3	4417.12364	get responses!	
Damping (%)	10						
ü1 (m/s^2)	1.388456679	ü2 (m/s^2)	8.57809488	ü3 (m/s^2)	5.66392855		
0	**u1**	0.553283474	**u2**	0.05084325	**u3**	0.00355773	**SRSS (square** 0.55562604
1		0.568809771		0.05168086		0.00351839	0.57116359
2		0.584503721		0.05186691		0.00332661	0.58680989
3		0.600364505		0.05131851		0.00297234	0.60256117
4		0.616390902		0.04994775		0.00245135	0.61841615
5		0.632581177		0.0476617		0.00176716	0.63437663
6		0.648932923		0.04436252		0.00093315	0.65044819
7		0.665442856		0.03994774		-2.501E-05	0.66664085
8		0.682106499		0.03431072		-0.00106671	0.68296972
9		0.698917735		0.0273415		-0.00213343	0.69945558
10		0.715868107		0.01892812		-0.00314568	0.71612521
11		0.73294571		0.00895877		-0.00399993	0.73301137
12		0.75013332		-0.00267442		-0.00456586	0.75015198
13		0.767405058		-0.01606893		-0.00468456	0.76758757
14		0.784719898		-0.03129952		-0.00416899	0.78535492
15		0.802007631		-0.04839275		-0.00280998	0.80347122
16		0.819133424		-0.06726581		-0.00039634	0.82189075
17		0.835784268		-0.08754058		0.00321972	0.84036246
18		0.850904365		-0.10766941		0.00783244	0.85772507
	s1	116482.8379	**s2**	18228.1087	**s3**	6085.3877	**Sum** 140796.334
		119751.5911		18528.4052		6018.09085	144298.087
		123055.6402		18595.1035		5690.06984	147340.814
		126394.8131		18398.4939		5084.09162	149877.399
		129768.8525		17907.057		4192.95491	151868.864
		133177.393		17087.4726		3022.67372	153287.539
		136619.9282		15904.664		1596.13267	154120.725
		140095.7663		14321.8932		-42.7793952	154374.88
		143603.9651		12300.9335		-1824.57321	154080.325
		147143.2367		9802.36007		-3649.15941	153296.437
		150711.8006		6786.02808		-5380.58156	152117.247
		154307.1504		3211.86031		-6841.75771	150677.253
		157925.6602		-958.823444		-7809.77105	149157.066
		161561.8812		-5760.96611		-8012.79195	147788.123
		165207.1766		-11221.3705		-7130.92705	146854.879
		168846.7652		-17349.5643		-4806.39265	146690.808
		172452.2606		-24115.8532		-677.921933	147658.485
		175957.7647		-31384.6773		5507.22771	150000.315
		179141.0006		-38601.1831		13397.1505	153936.968
	f1	161731.3744	**f2**	156362.446	**f3**	34467.2011	**Sum** 352561.021
		166269.8966		158938.418		34086.0366	359294.351
		170857.4256		159510.562		32228.1491	362596.137
		175493.7224		157824.026		28795.9317	362113.681
		180178.4301		153608.434		23748.5971	357535.461
		184911.0409		146577.962		17120.208	348609.21
		189690.8519		136431.717		9040.38141	335162.95
		194516.9025		122854.559		-242.299438	317129.162
		199387.8845		105518.574		-10334.2523	294572.207
		204302.0098		84085.5747		-20668.5782	267719.006
		209256.8063		58211.1927		-30475.2295	236992.769

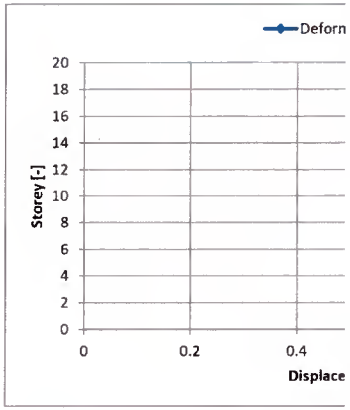

Vb1 (N)	3890740.92	Vb2 (N)	
Vb_total (N)	3907214.07		
Base shear	0.13989309		
M1 (Nm)	141182700	M2 (Nm)	
M_total (Nm)	147805003		
uplift f (N)	7390250.16		
uplift z (m)	0.0010584		
total z (m)	0.0009416		

DOF	19			get mode shapes!
H (m)	60	No.Bearing	2	
B (m)	20	stress (Mpa)	14	
kv (N/m)	6982500000	Radius (m)	0.563483905	
Ts1 (s)	1.2			
Tb (s)	4			
mb (kg)	150000	Heightb	0.4	
m1 (kg)	150000	Height1		
m2 (kg)	150000	Height2		
m3 (kg)	150000	Height3		
m4 (kg)	150000	Height4		
m5 (kg)	150000	Height5		
m6 (kg)	150000	Height6		
m7 (kg)	150000	Height7		
m8 (kg)	150000	Height8		
m9 (kg)	150000	Height9		
m10 (kg)	150000	Height10		
m11 (kg)	150000	Height11		
m12 (kg)	150000	Height12		
m13 (kg)	150000	Height13		
m14 (kg)	150000	Height14		
m15 (kg)	150000	Height15		
m16 (kg)	150000	Height16		
m17 (kg)	150000	Height17		
m18 (kg)	150000	Height18		

					M	150000	0	0	0	0	0	0	0	0	0	0	0	0
						0	150000	0	0	0	0	0	0	0	0	0	0	0
						0	0	150000	0	0	0	0	0	0	0	0	0	0
						0	0	0	150000	0	0	0	0	0	0	0	0	0
						0	0	0	0	150000	0	0	0	0	0	0	0	0
						0	0	0	0	0	150000	0	0	0	0	0	0	0
						0	0	0	0	0	0	150000	0	0	0	0	0	0
						0	0	0	0	0	0	0	150000	0	0	0	0	0
						0	0	0	0	0	0	0	0	150000	0	0	0	0
						0	0	0	0	0	0	0	0	0	150000	0	0	0
						0	0	0	0	0	0	0	0	0	0	150000	0	0
						0	0	0	0	0	0	0	0	0	0	0	150000	0
						0	0	0	0	0	0	0	0	0	0	0	0	150000
						0	0	0	0	0	0	0	0	0	0	0	0	0
						0	0	0	0	0	0	0	0	0	0	0	0	0
						0	0	0	0	0	0	0	0	0	0	0	0	0
						0	0	0	0	0	0	0	0	0	0	0	0	0
						0	0	0	0	0	0	0	0	0	0	0	0	0
						0	0	0	0	0	0	0	0	0	0	0	0	0
kb (N/m)	7032093.136					247205882.7	-240173789.6	0	0	0	0	0	0	0	0	0	0	0
ks1 (N/m)	240173789.6	I1	0.010589673		K	-240173789.6	467187371.5	-227013581.9	0	0	0	0	0	0	0	0	0	0
Ks2 (N/m)	227013581.9	I2	0.010009417			0	-227013581.9	440866956.2	-213853374	0	0	0	0	0	0	0	0	0
Ks3 (N/m)	213853374.3	I3	0.009429161			0	0	-213853374.3	414546541	-200693167	0	0	0	0	0	0	0	0
Ks4 (N/m)	200693166.6	I4	0.008848905			0	0	0	-200693167	388226126	-187532959	0	0	0	0	0	0	0
Ks5 (N/m)	187532959	I5	0.008268649			0	0	0	0	-187532959	361905710	-174372751	0	0	0	0	0	0
Ks6 (N/m)	174372751.3	I6	0.007688393			0	0	0	0	0	-174372751	335585295	-161212544	0	0	0	0	0
ks7 (N/m)	161212543.7	I7	0.007108137			0	0	0	0	0	0	-161212544	309264880	-148052336	0	0	0	0
Ks8 (N/m)	148052336	I8	0.006527881			0	0	0	0	0	0	0	-148052336	282944464	-134892128	0	0	0
Ks9 (N/m)	134892128.4	I9	0.005947625			0	0	0	0	0	0	0	0	-134892128	256624049	-121731921	0	0
Ks10 (N/m)	121731920.7	I10	0.005367369			0	0	0	0	0	0	0	0	0	-121731921	230303634	-108571713	
Ks11 (N/m)	108571713.1	I11	0.004787113			0	0	0	0	0	0	0	0	0	0	-108571713	203983219	-954
Ks12 (N/m)	95411505.45	I12	0.004206857			0	0	0	0	0	0	0	0	0	0	0	-95411505.4	177
Ks13 (N/m)	82251297.8	I13	0.0036266			0	0	0	0	0	0	0	0	0	0	0	0	-822
Ks14 (N/m)	69091090.15	I14	0.003046344			0	0	0	0	0	0	0	0	0	0	0	0	
Ks15 (N/m)	55930882.5	I15	0.002466088			0	0	0	0	0	0	0	0	0	0	0	0	
Ks16 (N/m)	42770674.85	I16	0.001885832			0	0	0	0	0	0	0	0	0	0	0	0	
Ks17 (N/m)	29610467.21	I17	0.001305576			0	0	0	0	0	0	0	0	0	0	0	0	
Ks18 (N/m)	16450259.56	I18	0.00072532			0	0	0	0	0	0	0	0	0	0	0	0	

Dunkerley's Estimation	Isolation	0.40528473	structure	0.0360036	Iteration Estimation	Omega1^2	1.94874b37	Omega2^2	20.5025487	Omega3^2	64.5865094
	Omega1^2	2.26609208	Omega2^2	27.7749997		Omega1	1.395975061	Omega2	4.52797402	Omega3	8.03657324
	Omega1	1.50535447	Omega2	5.27019921							

Phi1	0.00033231	Phi2	-0.00013146	Phi3	7.5955E-05	r	1	L	1199.14674
	0.000341635		-0.00013362		7.5115E-05		1		-45.0878604
	0.000351061		-0.0001341		7.1021E-05		1		8.26987346
	0.000360587		-0.00013269		6.3457E-05		1		-2.75184658
	0.000370213		-0.00012914		5.2335E-05		1		0.04662298

Gamma 233
-924
534
-369
217

Verzeichnis der in dieser Schriftenreihe erschienenen Hefte

96/1 **Gebbeken, N.:** *Zur Untersuchung des linearen Tragverhaltens von Faserverbundkonstruktionen mittels numerischer Methoden*

97/1 **Rötzer, J.:** *Ein Beitrag zur Berechnung von Stahlbetontragwerken unter hohen Dehnungsgeschwindigkeiten und hohen Drücken*

97/2 **Gebbeken, N.; Wanzek, T.; Petersen, C:** *„Semi-rigid" Verbindungen – Versuche an „T-stubs". Versuchsbericht*

97/3 **Jian, Y.:** *Tragverhalten dünner rechteckiger Stahlplatten mit großen Verformungen unter Berücksichtigung der Membranwirkung*

97/4 **Reif, F.:** *Mittels geregelter harmonischer Endpunktverschiebung induzierte räumliche Seilschwingungen.*

97/5 **Wei, Y.:** *Influences of Creep, Shrinkage and Steel Relaxation on Structural Behaviour.*

97/6 **Wurzer, O.:** *Zur Tragfähigkeit von Betondübeln.*

97/7 **Wanzek, T.:** *Zu Theorie, Numerik und Versuchen verformbarer Anschlusskontruktionen.*

97/8 **Gebbeken, N.; Rothert, H.; Wanzek, T.:** *Zur Theorie und Finite-Element-Berechnung des Tragverhaltens von verformbaren (semi-rigid) Anschlusskonstruktionen im Stahlbau.*

99/1 **Böge, G.:** *MAKROS – Pre- und Postprozessing für Finite Elemente – AutoCAD-Erweiterung zur Generierung von FE-Modellen.*

00/1 **Gebbeken, N.:** *Beiträge zur Begabungs-, Bildungs- und Hochschulpolitik.*

00/2 **Bettin, I.; Urrutia Galicia, J.C.; Gebbeken, N.:** *On the analysis of vertical circular cylindrical tanks under earthquake excitation at its base.*

00/3 **Gebbeken, N.:** *Wörterbuch Bauwesen Englisch-Deutsch Deutsch-Englisch.*

00/4 **Ruppert, M.:** *Zur numerischen Simulation von hochdynamisch beanspruchten Betonstrukturen.*

00/5 **Sauer, M.:** *Adaptive Kopplung des netzfreien SPH-Verfahrens mit finiten Elementen zur Berechnung von Impaktvorgängen.*

01/1 **Zapfe, C.:** *Trag- und Verformungsverhalten von Verbundträgern mit Betondübeln zur Übertragung der Längsschubkräfte.*

01/2 **Urrutia-Galicia, J. L.:** *Contributions to Applied Mathematics in Engineering*

01/3 **Gebbeken, N.:** *Wörterbuch Bauwesen Englisch-Deutsch Deutsch-Englisch ergänzte und überarbeitete 2. Auflage*

02/1 **Matias León, J.C.:** *Ein Beitrag zur Wirkung von Wellen und Schockwellen in Tragwerken*

02/2 **Bosl, R.:** *Zum Nachweis des Trag- und Verformungsverhaltens von Wandscheiben aus Brettlagenholz*

02/3 **Fischer, O.; Heinen, A.H.; Thalheim, J.-U.:** *Nichtlineare räumliche Seilschwingungen*

02/4 **Paulke, S.:** *Ein Beitrag zur Herleitung und Lösung nichtlinearer, thermomechanisch gekoppelter Grundgleichungen für Schalentragwerke*

02/5 **Mangerig, I.; Zapfe, C.:** *Nachweisverfahren und Sanierungsmöglichkeiten für Stahlträgerdecken mit Betonausfachung*

03/1 **Gebbeken, N.:** *Wörterbuch Bauwesen Englisch-Deutsch Deutsch-Englisch erheblich ergänzte Auflage, 3. Auflage*

03/2 **Urrutia-Galicia, J.L.:** *„The Best Manifold Theory", In Frequency Interpretation of Time Dependent Functions, An Application To Seismic Engineering.*

03/3 **Gebbeken, N.; Bletzinger, K.-U.; Rothert, H.:** *Hrsg. Aktuelle Beiträge aus Baustatik und Computational Mechanics*

03/4 **Gebbeken, N.; Dittrich, G.; Mueller-Hagen, S.:** *Zur Verwendung und Berechnung von Fahnenblechanschlüssen*

04/1 **Weiß, J.:** *Vereinfachte Integration von Fachwissen in Computerprogramme am Beispiel eines Planungssystems für die Bauindustrie*

04/2 **Thalheim, J.-U.:** *Nichtlineare Seilschwingungen und Stabilitätsanalysen für Seilbewegungen*

04/3 **Gebbeken, N.:** *Wörterbuch Bauwesen Englisch-Deutsch Deutsch-Englisch ergänzte Auflage, 4. Auflage*

04/4 **Greulich, S.:** *Zur numerischen Simulation von Stahlbeton- und Faserbetonstrukturen unter Detonationsbeanspruchung.*

04/5 **Ehrlich, I.:** *Impactverhalten schwach gekrümmter Strukturen aus faserverstärkten Kunststoffen*

05/1 **Lichte, U.:** *Klimatische Temperatureinwirkungen und Kombinationsregeln bei Brückenbauwerken*

05/2 **Petersen, C.:** *Studien zum Einsatz von Erdbebenschutzsystemen*

06/1 **Kustermann, A.; Keuser, M.; Zimbelmann R. K.; Grimm, R.:** *Hochfeste Bindemittel und Zuschlagstoffe für hochfeste Betone unterschiedlicher Güte" für Schutzanlagen der militärischen Sonderinfrastruktur*

06/2 **Bludau, Ch.; Keuser, M.; Kustermann, A.; Thienel K.-Ch.:** *Schutzplatten aus hochfestem Beton (Abschlussbericht)*

06/3 **Purainer, R.; Keuser, M.:** *Versuche an Stahlbetonscheiben und –platten unter Zugbeanspruchung*

06/4 **Gebbeken, N.; Keuser, M.; Klaus, M.; Mangerig, I.; Thoma, K.: (Hrsg.):** *2. Workshop „BAU-PROTECT" Sicherheit der baulichen Infrastruktur vor außergewöhnlichen Einwirkungen*

07/1 **Gollwitzer, T.:** *Finite Stabelemente für mehrteilige nachgiebige Verbundquerschnitte zur Berechnung von Brettrippenschalen*

08/1 **Urrutia-Galicia, J.L.:** *Contributions to Applied Mathematics in Engineering*

08/2 **Gebbeken, N.; Thoma, K. (Hrsg.):** *3. Workshop „BAU-PROTECT" Sicherheit der baulichen Infrastruktur vor außergewöhnlichen Einwirkungen*

09/1 **Hartmann, T.:** *Zur mesomechanischen Modellierung von Beton und ihrer Anwendung zur makromechanischen Modellbildung*

10/1 **Baumhauer, A.:** *Beurteilung geschädigter Brückenbauwerke unter Berücksichtigung unscharfer Tragwerksparameter*

10/2 **Bierbrauer, K.:** *Ein Beitrag zur Ermittlung der Biegetragfähigkeit bestehender Stahlbetonbrücken unbekannter Eigenschaften*

10/3 **Rüdiger, L.:** *Tragverhalten von Stahlbetonplatten unter Berücksichtigung der Steifigkeitsänderung im gerissenen Zustand*

10/4 **Fuchs, M.:** *Stahlbetonbauteile nach außergewöhnlichen Einwirkungen – Schadensquantifizierung und Instandsetzung*

10/5 **Braml, T.:** *Zur Beurteilung der Zuverlässigkeit von Massivbrücken auf der Grundlage der Ergebnisse von Überprüfungen am Bauwerk*

10/6 **Festschrift** *zum 60. Geburtstag von Univ.-Prof. Dr.-Ing. Ingbert Mangerig*

10/7 **Seel, U.:** *Der konzeptionelle Entwicklungswandel von Flughafenterminal-gebäuden in der Gegenüberstellung zur Entstehungsgeschichte des Flughafens München*

11/1 **Retze, U.:** *Beispielhafte Untersuchung zum Einsatz von Monitoringmethoden an einer Brücke*

11/2 **Burger, S.:** *Untersuchungen zum Ermüdungsverhalten von Betondübeln im Verbundbau*

11/3 **Kroyer, R.:** *Instationäres Temperatur- und Strukturverhalten von Stabwerkstrukturen*

11/4 **Urrutia-Galicia, J. L.:** *Contributions to Applied Mathematics in Engineering III*

11/5 **Köck, B.:** *Barocke Dachwerke: Konstruktion und Tragverhalten*

12/1 **Teich, M.:** *Interaktionen von Explosionen mit flexiblen Strukturen*

12/2 **Beucher, S.:** *Zur aktiven Temperierung von Brückenfahrbahnen*

12/3 **Döge, T.:** *Zur Reflexion von Luftstoßwellen an nachgiebigen Materialien und Baustrukturen*

12/4 **Festschrift** *zum 60. Geburtstag von Univ.-Prof. Dr.-Ing. Manfred Keuser*

12/5 **Gebbeken, N.; Klaus, M.; Thoma, K. (Hrsg.):** *5. Workshop „BAU-PROTECT" Sicherheit der baulichen Infrastruktur vor außergewöhnlichen Einwirkungen*

12/6 **Linse, T.:** *Materialmodelle für Mörtel und Ziegel für die diskrete Modellierung von Mauerwerk unter dynamischen Einwirkungen*

13/1 **Haese, A.:** *Beitrag zur Bemessung scheibenbeanspruchter Stahl-Glas-Elemente*

14/1 **Wensauer, R.:** *Zum Einfluss hochdynamischer Einwirkungen auf das Verbundverhalten von Stahlbeton*

14/2 **Lenner, R.:** *Safety Concept and Partial Factors for Military Assessment of Existing Concrete Bridges*

14/3 **Pfeiffer, E.; Rödig, P.:** *Lebenszyklusbegleitende Nutzbarkeit digitaler Bauwerksinformationen*

16/1 **Herrmann, T.:** *Untersuchungen zu punktgestützten Verglasungen mit Senkkopfhaltern*

17/1 **Ampunant, P.:** *Numerische Untersuchungen zur Druck-Sog-Belastung auf Lärmschutzwände an Hochgeschwindigkeitsstrecken der Bahn*

17/2 **Michal, M.:** *Verbund von Beton und Bewehrung unter hochdynamischen Beanspruchungen*

17/3 **Friedl, R.:** *Grundlagenorientierte theoretische und experimentelle Untersuchungen zum Schwingungsverhalten einer modifizierten Schwenktraversendehnfuge sowie zu fahrbahnunebenheitsinduzierten Radkraftschwankungen von Straßenfahrzeugen im Hinblick auf die daraus resultierende Streuung messtechnisch erfasster Fahrzeuggewichte*

17/4 **Niederwald, M.:** *Zum Einfluss der viskoelastischen Eigenschaften des beschichteten Bewehrungsmaterials auf das Zugtragverhalten von carbonbewehrtem Beton*

18/1 **Mano, T.:** *Numerical and experimental analysis of the load-carrying behaviour of laminated elastomeric bearings as seismic isolators*